NEW INVESTIGATIONS OF NITRIC OXIDE, NITRITE AND HYPONITRITE INTERACTIONS WITH HEME/COPPER ASSEMBLIES

by
Shabnam Hematian

A dissertation submitted to Johns Hopkins University in conformity with the requirements for the degree of Doctor of Philosophy

Baltimore, Maryland

August, 2015

Abstract

Our long-time niche in synthetic biological inorganic chemistry has been to design ligands and generate coordination complexes of copper and/or iron ions, those reacting with dioxygen (O_2) and/or nitrogen oxides (e.g., nitric oxide ($NO_{(g)}$), nitrite (NO_2^-), and hyponitrite ($N_2O_2^{2-}$)). The purpose of investigation of synthetic models is to elucidate fundamental aspects of the chemistry, here metal/small-molecule adduct formation, structure, spectroscopy and correlation to structure, electronic-structure/bonding, reactivity and mechanism of action.

As inspiration for the work presented in this dissertation, we turn to mitochondrial cytochrome *c* oxidase (C*c*O) which is responsible for dioxygen consumption and also regarded as the key target for $NO_{(g)}$ and nitrite within mitochondria. The very same binuclear active site is also capable of reductive coupling of two $NO_{(g)}$ molecules to generate nitrous oxide (N_2O) where a heme and/or copper coordinated hyponitrite ($N_2O_2^{2-}$) moiety has been postulated (or even detected in some protein chemistry) as an intermediate in the reaction. Our synthetic heme/Cu assemblies possess redox activity toward these small molecules of biological interest.

Chapter 1 provides an overview of our recent advances in studying synthetic heme/Cu complexes with respect to the design and synthetic generation of O_2-adducts to elucidate fundamental aspects of the O_2-reduction and subsequent O–O cleavage process as well as our new investigations on closely related heme/Cu constructs capable of mediating nitrite ion reduction to $NO_{(g)}$ or the reverse, oxidation of $NO_{(g)}$ to nitrite.

In chapter 2, we first introduce a synthetic heme/Cu assembly that in its partially reduced form facilitates nitrite reduction to $NO_{(g)}$, while the fully oxidized form of the same assembly, a μ-oxo heme-Fe^{III}−O−Cu^{II}(L) complex, oxidizes $NO_{(g)}$ to nitrite.

Chapter 3 probes the key factors involved in the nitrite reductase chemistry wherein the nature of the heme and/or the copper ligand were synthetically modified. The ferrous heme is the reductant, but its reducing ability does not influence the overall reaction rate. It is proposed that the nitrite to cupric ion binding dictates how nitrite coordinates to the ferrous heme, via a *N*- or *O*-atom, which influences the overall kinetics.

To elucidate the molecular mechanism of $NO_{(g)}$ oxidase chemistry, in Chapter 4, detailed spectroscopic and kinetic studies using various μ-oxo heme-Fe^{III}−O−Cu^{II}(L) compounds were performed. The experimental results are in excellent agreement with theoretical calculations, revealing the nature of intermediates and key mechanistic steps.

In Chapter 5, the first example of a cupric hyponitrite compound is reported. From X-ray analysis, a *trans*-geometry for the hyponitrite moiety is confirmed. The first example of a synthetic heme/Cu hyponitrite intermediate is described. Warming the intermediate to room temperature results in clean formation of the corresponding μ-oxo heme-Fe^{III}−O−Cu^{II}(L) complex and N_2O is released stoichiometrically.

Advisor: Professor Kenneth D. Karlin

Ira Remsen Chair of Chemistry

Thesis Committee:

Professor David P. Goldberg

Professor John P. Toscano

Acknowledgments

I would like to express my sincere appreciation and thanks to my advisor Professor Kenneth D. Karlin for his continuous support and tremendous mentorship throughout my graduate career. I have learned a great deal of science from him and could not have imagined having a better advisor for my PhD study. Without his supervision and constant help this dissertation would not have been possible.

I would also like to thank my committee members, professor David P. Goldberg and professor John P. Toscano for serving as my committee members. I also want to thank them for their support, valuable discussions, and accessibility over the past few years. I would especially like to thank professor Davar M. Boghaei for introducing me to the field of bioinorganic chemistry during my master's study and as well for his support on the way. I am grateful to our collaborators, professor Ivana Ivanovic-Burmazovic and her research group at University of Erlangen-Nuremberg as well as professor Edward I. Solomon and members of the Solomon lab for their useful discussions and taking samples coming from my projects and carrying out spectroscopic or other investigations.

My heartfelt thanks go to my fellow labmates, all of the past and present members of the Karlin research group, for providing a supportive and encouraging research environment. I would specifically like to thank Dr. Zakaria Halime, Dr. Ryan Peterson, and Dr. Mark Schopfer who played important roles in my scientific development. It was lucky for me to start graduate school with the company of a very helpful chemist, Dr. Jung Yoon Lee, who also joined the Karlin lab in the autumn of 2010 as well as to share our new glovebox with two highly motivated jovial students, Jeffrey Liu and David Quist.

Working with such a great group of people made my time in the lab a very enjoyable experience. I only overlapped for a very short time with our new postdoctoral fellow, Dr. Gayan Wijeratne, who is a great scientist and careful experimentalist and will continue working on the project discussed in Chapter 5.

A special thank you to Jean Goodwin, Meghan Carter, and Rosalie Elder for all the administrative help. I also thank the wonderful staff in the Chemistry Department for always being helpful and friendly. In particular, I would like to thank Maxime Siegler, our crystallographer who helped with obtaining X-ray structures of many new compounds over the past 5 years. I also thank my friends (too many to list here but you know who you are!) for providing support and friendship that I needed to strive towards my goals. I would like to thank my very best friend, Farahnaz Tavakoli, for visiting me all the way from Germany every year and being supportive throughout my time here.

Most importantly, none of this would have been possible without the love and continuous support of my family. Words cannot express how grateful I am to my mother, Shamisa Taherian, for all the sacrifices she has made on my behalf. Very special thanks to my one and only brother for always being there for me. I would also like to express my heartfelt appreciation to my wonderful grandparents, aunt and uncle who have believed in me and supported me all along the way.

Finally, I appreciate the financial support from NIH that funded the research discussed in this dissertation. I would also like to thank to Department of Chemistry of the Johns Hopkins University for their financial support granted through *William Hooper Grafflin* fellowship.

Table of Contents

Chapter 4: Nitrogen Oxide Atom-Transfer Redox Chemistry; Mechanism of $NO_{(g)}$ to Nitrite Conversion Utilizing μ-oxo Heme-Fe^{III}–O–Cu^{II}(L) Constructs

Chapter 1: Synthetic Heme/Copper Assemblies: Toward an Understanding of Cytochrome *c* Oxidase Interactions with Dioxygen and Nitrogen Oxides

Chapter 2: Heme/Copper Assembly Mediated Nitrite and Nitric Oxide Interconversion

Chapter 3: Nitric Oxide Generation from Heme/Copper Assembly Mediated Nitrite Reductase Activity

.

Chapter 4: Nitrogen Oxide Atom-Transfer Redox Chemistry; Mechanism of $NO_{(g)}$ to Nitrite Conversion Utilizing μ-oxo Heme-Fe^{III}–O–Cu^{II}(L) Constructs

Chapter 5: A Heme/Copper Hyponitrite Species, a Possible Intermediate during Nitric Oxide Reductive Coupling Catalyzed by Cytochrome *c* Oxidase (C*c*O)

Chapter 1:

Synthetic Heme/Copper Assemblies: Toward an Understanding of Cytochrome *c* Oxidase Interactions with Dioxygen and Nitrogen Oxides

This work was co-authored with the following authors and is published under the following citation:

Shabnam Hematian, Isaac Garcia-Bosch, and Kenneth D. Karlin

Acc. Chem. Res. **2015***, 48* (8), 2462−2474

Abstract:

Our long-time niche in synthetic biological inorganic chemistry has been to design ligands and generate coordination complexes of copper or iron ions or both, those reacting with dioxygen (O_2) or nitrogen oxides (e.g., nitric oxide ($NO_{(g)}$) and nitrite (NO_2^-)) or both. As inspiration for this work, we turn to mitochondrial cytochrome *c* oxidase, which is responsible for dioxygen consumption and is also the predominant target for $NO_{(g)}$ and nitrite within mitochondria. In this Account, we highlight recent advances in studying synthetic heme/Cu complexes in two respects. First, there is the design, synthesis, and characterization of new O_2 adducts whose further study will add insights into O_2 reductive cleavage chemistry. Second, we describe how related heme/Cu constructs reduce nitrite ion to $NO_{(g)}$ or the reverse, oxidize $NO_{(g)}$ to nitrite. The reactions

of nitrogen oxides occur as part of C*c*O's function, which is intimately tied to cellular O_2 balance.

We had first discovered that reduced heme/Cu compounds react with O_2 giving μ-oxo heme-FeIII−O−CuII(L) products; their properties are discussed. The *O*-atom is derived from dioxygen, and interrogations of these systems led to the construction and characterization of three distinctive classes of heme−peroxo complexes, two high-spin and one low-spin species. Recent investigations include a new approach to the synthesis of low-spin heme−peroxo−Cu complexes, employing a "naked" synthon, where the copper ligand denticity and geometric types can be varied. The result is a collection of such complexes; spectroscopic and structural features (by DFT calculations) are described. Some of these compounds are reactive toward reductants/protons effecting subsequent O−O cleavage. This points to how subtle improvements in ligand environment lead to a desired local structure and resulting optimized reactivity, as known to occur at enzyme active sites.

The other sector of research is focused on heme/Cu assemblies mediating the redox interplay between nitrite and $NO_{(g)}$. In the nitrite reductase chemistry, the cupric center serves as a Lewis acid, while the heme is the redox active center providing the electron. The orientation of nitrite in approaching the ferrous heme center and *N*-atom binding are important. Also, detailed spectroscopic and kinetic studies of the $NO_{(g)}$ oxidase chemistry, in excellent agreement with theoretical calculations, reveal the intermediates and key mechanistic steps. Thus, we suggest that both chemical and biochemical heme/Cu-mediated nitrite reductase and $NO_{(g)}$ oxidase chemistry require *N*-atom binding to a ferrous heme along with cupric ion *O*-atom coordination, proceeding

via a three-membered O−Fe−N chelate ring transition state. These important mechanistic features of heme/Cu systems interconverting $NO_{(g)}$ and nitrite are discussed for the first time.

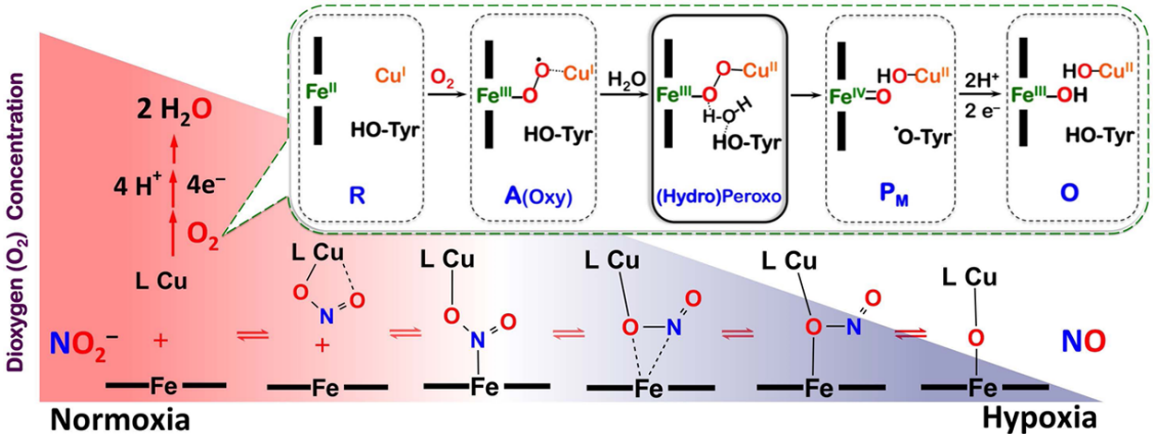

1. Introduction

Mitochondrial cytochrome c oxidase (C*c*O) is the terminal component of the respiratory chain that carries out the enzymatic four-electron reduction of dioxygen (O_2) to water (H_2O). This enzyme is essential to respiration, providing the energy to pro- duce a proton gradient across the membrane, which supplies the driving force for ATP synthesis. The binding of O_2 and its subsequent reduction to water take place at the C*c*O binuclear active site consisting of heme-a_3 and Cu_B ligated by three histidine residues with a unique linkage of one histidine to a nearby tyrosine residue. During catalytic turnover, the Fe^{II}/Cu^{I} center binds and reduces O_2, sequentially forming superoxide (**A**), (hydro)peroxide, and ferryl (**PM**, after O−O cleavage, thought to be assisted by tyrosine H atom injection) intermediates (Figure 1), followed by stepwise protonation−reduction giving water and regenerating the Fe^{II}/Cu^{I} site.[1−3] The O−O bond reductive cleavage event is a crucial but complicated process; it depends on electron transfer and protonation steps, and its full understanding has implications well beyond C*c*O.[4]

This same heme-a_3/Cu_B binuclear center is also a major site of respiratory regulation as it interacts with nitrite (NO_2^-) and nitric oxide ($NO_{(g)}$) to modulate cellular O_2 balance (Figure 1). In tissues experiencing hypoxia, when the O_2 concentration decreases below physiological levels,[5] nitrite serves as an acceptor for accumulating electrons at the C*c*O binuclear active site, and the enzymatic one-electron reduction of nitrite (NO_2^-) takes place generating nitric oxide. The $NO_{(g)}$ produced by C*c*O reversibly interacts with the same center and, thus, decreases its affinity to O_2 reduction resulting in cellular O_2 accumulation. Some of mitochondrially produced $NO_{(g)}$ also participates in the up-regulation of hypoxic nuclear genes (hypoxic signaling).[5,6] In turn, at

mitochondrial sites recovering from hypoxia, local accumulation of O_2 progressively triggers one-electron oxidation of $NO_{(g)}$ back to NO_2^- ion, the latter held in reserve to be reconverted when needed. This process serves as an adaptive mechanism eliminating $NO_{(g)}$-mediated respiratory inhibition.[7,8]

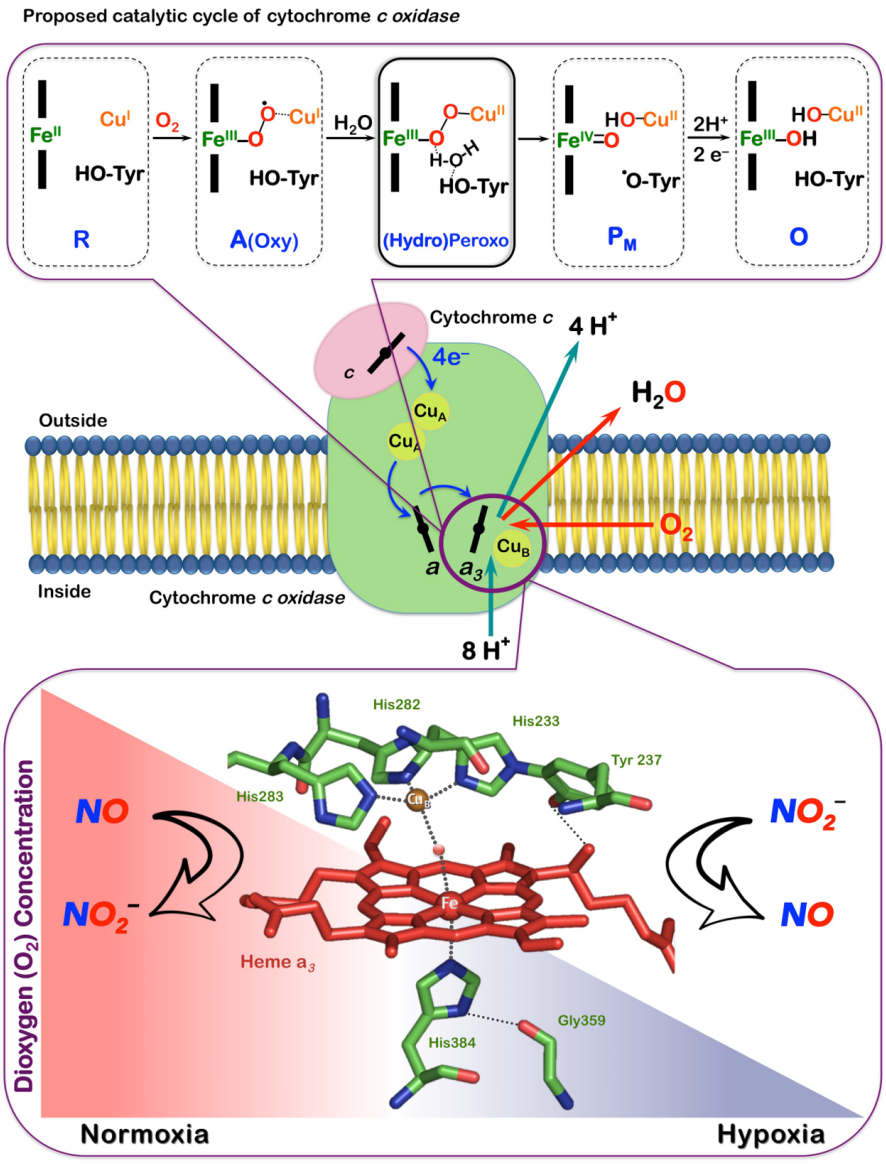

Figure 1. Cytochrome *c* oxidase reduces dioxygen via the proposed intermediates shown (*top*). This heme-a_3/Cu_B binuclear active site also functions in $NO_2^-/NO_{(g)}$ interconversion in a regulatory role modulating O_2 balance (*bottom*).

In this Account, we describe our recent findings on both subjects. A great emphasis has been placed on design and generation of relevant O_2 adducts, that is, heme-Fe−(O_2^{2-})−Cu(L) complexes, as a segue to future chemistries involving the critical O−O cleavage process. We also highlight our investigations on the interconversion of $NO_{(g)}$ and nitrite mediated by heme/Cu assemblies. Our work is thus aimed at introducing synthetic heme/Cu binuclear systems capable of performing chemical transformations of relevant small molecules, those occurring at the C*c*O active site. Our goal is to provide fundamental insights into essential factors contributing to these redox processes.

2. Initial Work on Heme-$Fe^{II}\cdots Cu^{I}$(L)/O_2 Chemistry: Fe−oxo−Cu Complexes

Our initial attempts at modeling the C*c*O heme-a_3/Cu_B dioxygen chemistry led to discovery of μ-oxo heme-Fe^{III}−O−Cu^{II}(L) compounds forming from reaction of O_2 with equimolar quantities of the corresponding reduced heme and copper mono-nuclear complexes; the μ-oxo ligand derives from O_2. Interestingly, despite the known substantial thermodynamic stability of μ-oxo iron dimer heme-Fe^{III}−O−Fe^{III}-heme, here such μ-oxo heme-Fe^{III}−O−Cu^{II}(L) complexes are the kinetically stable products, which can also be generated by acid−base reaction of oxidized metal complexes, that is, reaction of heme-Fe^{III}−OH and [(L)Cu^{II}] plus a base.[9,10]

Chart 1. Molecular Structures of μ-oxo [(Porphyrinate)Fe^{III}–O–Cu^{II} (L)]$^+$ Complexes.[a]

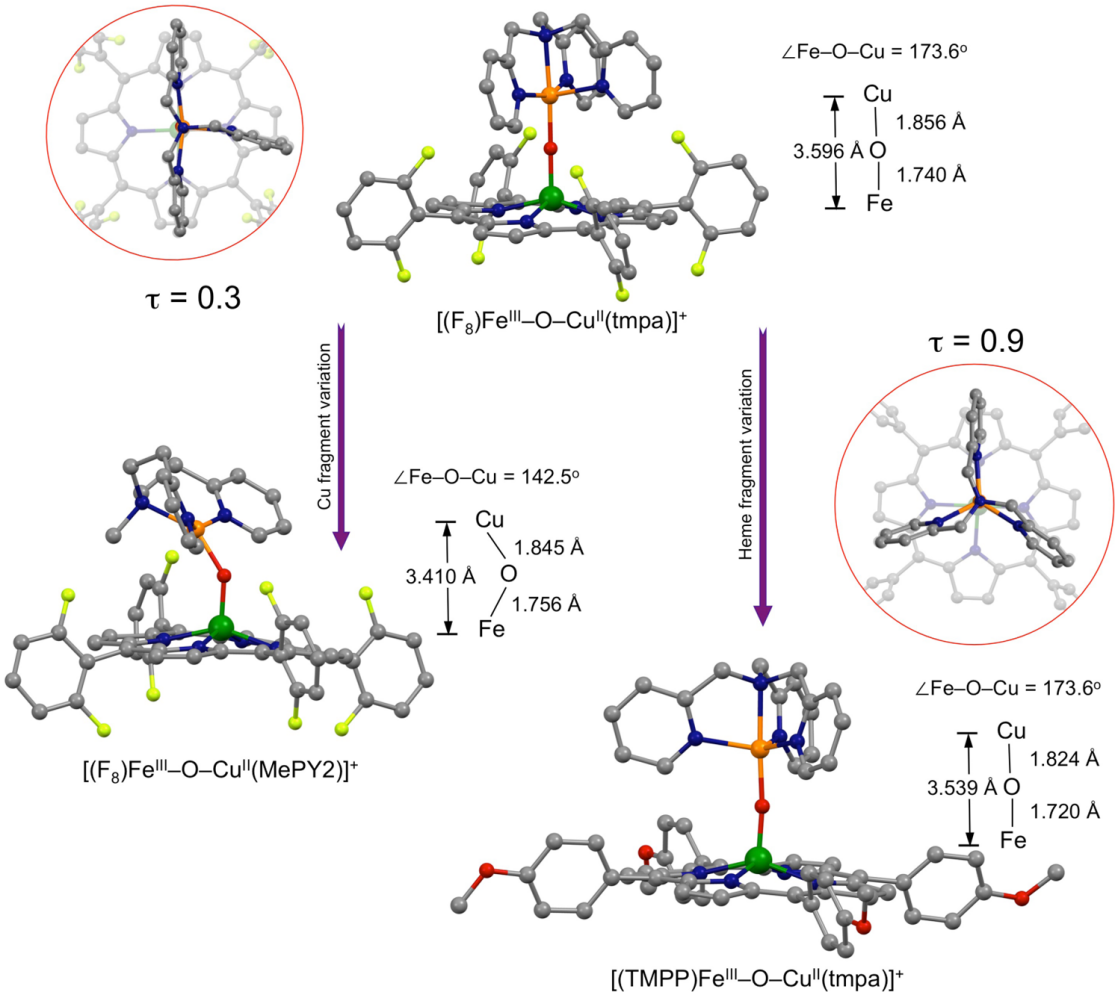

[a]Abbreviations: tmpa, tris(2-pyridylmethylamine); MePY2, bis(2-pyridyl-ethyl)methylamine; F_8, tetrakis(2,6-difluorophenyl)-porphyrinate(2−); TMPP, tetrakis(4-methoxyphenyl)porphyrinate(2−).

We recently added new crystal structures, [(TMPP)Fe^{III}–O–Cu^{II}(tmpa)]$^+$ and [(F8)Fe^{III}–O–Cu^{II}($MePY_2$)]$^+$ (Chart 1), to our library of such compounds, which conform to previous findings in that the Fe–O–Cu core in the former compound with its tetradentate chelate for the cupric center, TMPA, is near-linear while the latter complex bearing a tridentate copper(II) ligand, MePY2, has a very bent μ-oxo moiety (Chart 1).

They also exhibit the very red-shifted Soret bands (λ_{max} = 443 and 438 nm, respectively) characteristic of the μ-oxo compounds relative to that of classical high-spin ferric hemes, probably due to a weaker affinity of Cu(II) for the bridging oxo and thus the greater degree of π charge donation available onto the ferric center by the oxo group. Also, $[(TMPP)Fe^{III}–O–Cu^{II}(tmpa)]^{+}$ is the first example of the heme-$Fe^{III}–O–Cu^{II}(L)$ class that contains the strongly donating TMPP porphyrinate. Notably, comparison of $[(TMPP)Fe^{III}–O–Cu^{II}(tmpa)]^{+}$ and its closely related analog $[(F_8)Fe^{III}–O–Cu^{II}(tmpa)]^{+}$, in which only the porphyrinate identity varies, reveals that the cupric centers adopt very different geometries; for the former, the tmpa-Cu N_4O ligation occurs within a nearly perfect trigonal bipyramidal (TBP) geometry (τ = 0.9), while for the latter, the copper center adjusts to a distorted square pyramidal (SP) coordination (τ = 0.3, Chart 1). Steric constraints imposed by o-fluorine substi- tuents of the meso-phenyl groups on the attached porphyrin ring in the F_8 ligand dictate structural properties of the cupric center resulting in deviation from the normal TBP geometry seen for $[(tmpa)Cu^{II}(X)]^{n+}$ (X = H_2O, MeCN, $Cl^{–}$, or $NO_2^{–}$) compounds.[11]

In all μ-oxo compounds, the bridging oxo moiety is very basic and can be reversibly protonated to give the protonated acid− base partner, heme-$Fe^{III}–(OH)–Cu^{II}(L)$. For some cases corresponding μ-hydroxo analogues have been characterized and pK_a values reported.[12,13] In general, protonation of the Fe−O−Cu core results in bending and rehybridization of the bridging oxygen moiety, accompanied by bond elongation.

3. High-Spin Heme−Peroxo−Copper Complexes

In view of our interest in studying the C*c*O active-site O_2-reduction chemistry (Figure 1), Fe/Cu/O_2 intermediates preceding the formation of μ-oxo heme-Fe^{III}−O−Cu^{II}(L) compounds have been primary targets for study. A first generation example is the metastable heme−peroxo−copper complex $[(F_8)Fe^{III}–(O_2^{2–})–Cu^{II}(tmpa)]^+$ (**HS-TMPA**, Scheme 1), formed from O_2 bubbling through cold solutions of a 1:1 mixture of $[(tmpa)Cu^{I}(MeCN)]^+/(F_8)Fe^{II}$.[14] Structural and spectroscopic studies on **HS-TMPA** provided evidence for a bridging peroxide unit bound in a side-on fashion to the high-spin iron(III) center and end-on to the copper(II) center.[15] Key observations were as follows: (i) ^{2}H-NMR spectroscopy revealed that **HS-TMPA** possesses anti-ferromagnetically coupled (through the peroxide bridge) high- spin iron(III) and copper(II) ions, leading to an S = 2 system; (ii) resonance Raman spectroscopic (rRaman) measurements identified O−O, Fe−O, and Cu−O vibrations (Scheme 1); (iii) X-ray absorption fine structure (EXAFS) provided Cu−O, Fe−O, and Fe···Cu contributions at 1.87, 1.94, and 3.72 Å. These spectroscopic/structural features correspond to data from the only crystallographically characterized heme−peroxo−copper system.[16]

Scheme 1.

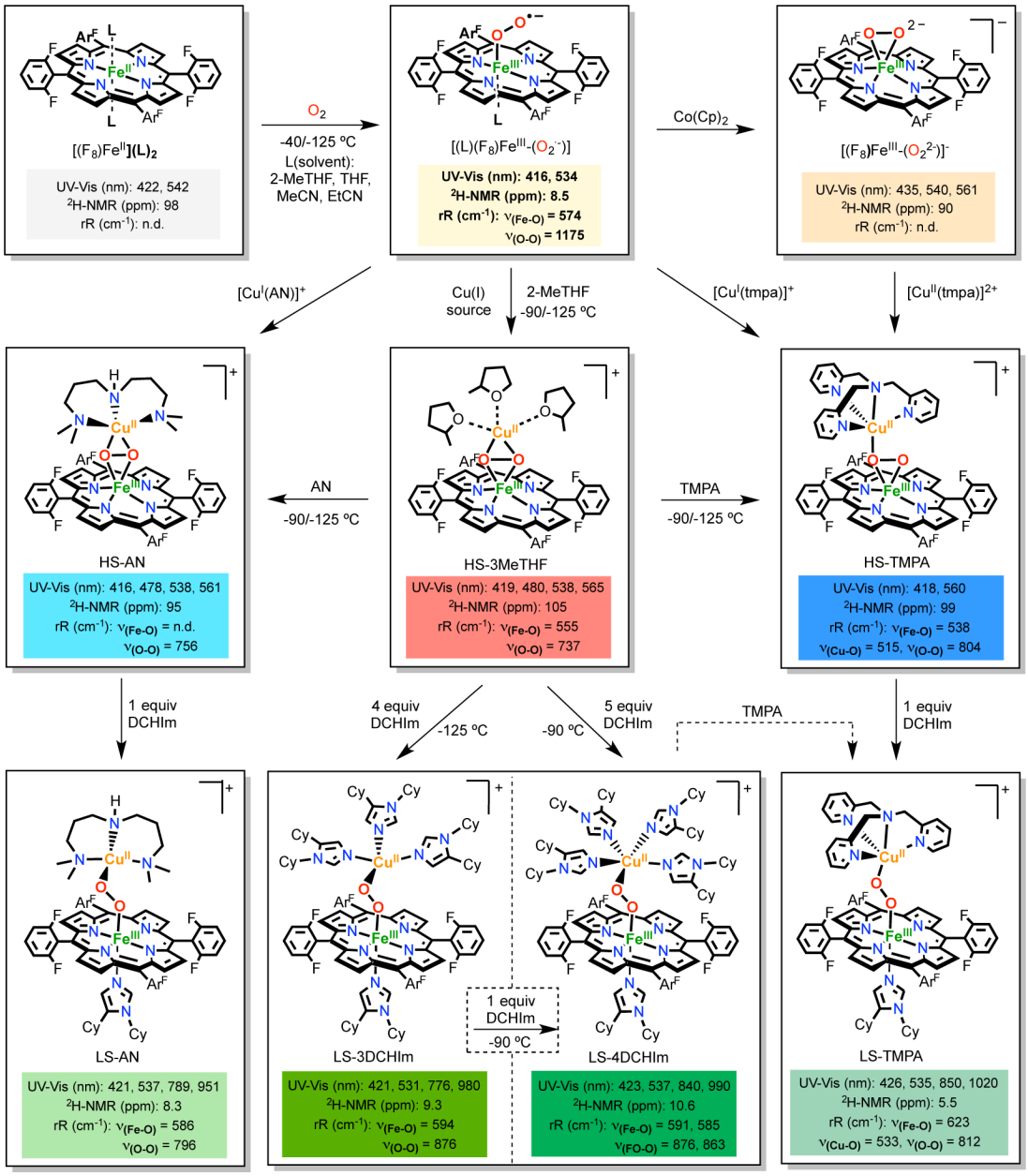

As to the formation of **HS-TMPA**, stopped-flow UV−vis measurements revealed an iron(III)−superoxo intermediate $[(L)(F_8)Fe^{III}–(O_2^{\bullet-})]$ (L = solvent, that is, EtCN) initially formed. Indeed, addition of 1 equiv of $[(tmpa)Cu^{I}(MeCN)]^{+}$ to this leads to

HS-TMPA. Scheme 1 depicts alternative synthetic routes giving **HS-TMPA**. With the expectation that significant (or even small) ligand variations can dramatically alter structure and other properties, we also synthesized heme−(O_2)−copper assemblies using tridentate chelates for copper. A well-studied example is $[(F_8)Fe^{III}–(O_2^{2–})–Cu^{II}(AN)]^+$ (**HS-AN**, AN is 3,3′-iminobis(*N,N*-dimethylpropylamine), Scheme 1; EXAFS, Fe···Cu = 3.63 Å). Further analyses led to the conclusion that **HS-AN** and other analogs with tridentate ligands for copper possess a side-on peroxide coordination mode (i.e., μ-η^2:η^2) to both metal ions (Scheme 1).[17,18]

4. Low-Spin Heme−Peroxo−Copper Complex, LS-AN

A crucial advance for our research came when we reported the generation of the low-spin (LS) [(DCHIm)$(F_8)Fe^{III}$-$(O_2^{2–})$-Cu(AN)] (**LS-AN**),[19] likely a close analogue of the putative heme−peroxo−copper species formed in C*c*O. Addition of an axial ligand (DCHIm = 1,5-dicyclohexylimidazole) to **HS-AN** leads to the new species **LS-AN**, which presented unusually strong low-energy UV−vis features (Scheme 1). A change in the spin-state is associated with an alternation in the bridging mode of the peroxide ligand, forming an end-on $Fe^{III}–(\mu$-$\eta1$:$\eta1$-$O_2^{2–})–Cu^{II}$ core. ^{2}H-NMR spectroscopy indicates an overall S = 0 spin-state, derived from antiferromagnetic coupling of a low-spin Fe(III) (S = 1/2) to the S = 1/2 Cu(II). Two isotope-sensitive features at 796 and 586 cm^{-1} are assigned to O−O and Fe−O vibrations, respectively, based on rRaman. Note the large change in $\nu_{O–O}$ in comparing high- and low-spin AN analogs. EXAFS measurements on **LS-AN** give Cu−O, Fe−O, and Fe···Cu distances of 1.98, 1.81, and 4.01 Å, respectively.

Relative to **HS-AN**, a shortening of the Fe−O bond (1.94 vs 1.81 Å) and elongation of the Fe···Cu distance (3.72 vs 4.01 Å) pro- vide for the new end-on peroxide bridging mode in **LS-AN** (Scheme 1).

5. "Naked" Fe−Peroxo−Cu Synthon for New Low-Spin Compounds

We recently explored a new synthetic approach,[20] following a discovery leading to the high-spin complex $[(F_8)Fe^{III}–(O_2^{2–})–Cu^{II}(MeTHF)_3]^+$ (**HS-3MeTHF**, Scheme 1), a "naked" synthon as a starting point for the generation of an array of heme−peroxo−copper assemblies. Addition of $[Cu^{I}(MeCN)_4][B(C_6F_5)_4]$ to a solution of $[(MeTHF)(F_8)Fe^{III}–(O_2^{\bullet–})]$ at low temperatures (−90 to −125 °C) leads to the clean formation of **HS-3MeTHF**, formulated as possessing a side-on $Fe^{III}–(\mu\text{-}\eta^2\text{:}\eta^2\text{-}\ O_2^{2–})–Cu^{II}$ core with three solvent molecules surrounding the copper(II) center, due to its spectroscopic similarities with **HS-AN**, see Scheme 1 for spectroscopic data.

The utility of **HS-3MeTHF** is illustrated by its use in generation of a new low-spin complex $[(DCHIm)(F_8)Fe^{III}–(O_2^{2–})–Cu^{II}(tmpa)]^+$ (**LS-TMPA**, Scheme 1). Addition of 1 equiv of the free ligand TMPA to the **HS-3MeTHF** gives **HS-TMPA** by replacement of the labile solvent ligands to copper. A further step comes from addition of 1 equiv of DCHIm to **HS-TMPA**, giving the new compound **LS-TMPA**. Like **LS-AN**, **LS-TMPA** also possesses unusual low-energy UV−vis features (Scheme 1). ^{2}H-NMR spectroscopy confirmed the change in spin-state, as the pyrrole signal shifted from 99 ppm for **HS-TMPA** (S = 2) to 5 ppm for **LS-TMPA** (S = 0). The change in the spin state is again linked to alteration in the peroxide coordination mode. The data given in

Scheme 1 shows that O−O, Fe−O, and Cu−O stretching frequencies for **LS-TMPA** are systematically higher than those for **HS-TMPA**, especially the ν_{Fe-O} value. This appears to be the first case in which the effect of changing the spin state on all relevant vibrations, O−O, Fe−O, and Cu−O, could be evaluated.[20]

Most interestingly, we found that simple monodentate ligand donors such as imidazoles, native C*c*O active-site ligands, could be added to the solvato "naked" complex **HS-3MeTHF** to generate new low-spin heme−(O_2)−copper assemblies. Addition of excess of DCHIm to **HS-3MeTHF** at −125 °C led to the formation of a new species with UV−vis features very similar to those found for **LS-AN**. Titration experiments provided evidence that 4 equiv of DCHIm were required for its formation, formulating the new low-spin peroxo as $[(DCHIm)(F_8)Fe^{III}-(O_2^{2-})-Cu^{II}(DCHIm)_3]^+$ (**LS-3DCHIm**) with one imidazole ligand coordinated to the heme and three coordinated to the cupric ion. ^{2}H-NMR spectroscopic characterization corroborated the S = 0 complex ground state, while rRaman revealed the existence of a particularly high O−O stretching vibration, $\nu_{O-O} = 876$ cm^{-1} (Scheme 1).[20]

When **LS-3DCHIm** is warmed to −90 °C in the presence of excess DCHIm, a new species with shifted UV−vis features forms (Scheme 1). The same species is also obtained when 5 equiv of DCHIm are added to **HS-3MeTHF** generated at −90 °C. Cooling this new complex with four imidazole donors for the copper ion, $[(DCHIm)(F_8)Fe^{III}-(O_2^{2-})-Cu^{II}(DCHIm)_4]^+$ (**LS-4DCHIm**, Scheme 1) does not lead to the reversible formation of **LS-3DCHIm**; thus, **LS-4DCHIm** is the thermodynamic product, formed after the generation of the kinetic product, **LS-3DCHIm**. ^{2}H-NMR spectroscopy indicates that these two complexes are distinctly different (Scheme 1).

However, **LS-4DCHIm** has distinctive but surprisingly similar vibrational features to those found for **LS-3DCHIm**, $\nu_{Fe-O} = 594$ cm^{-1} and $\nu_{O-O} = 876$ cm^{-1}; coordination of an extra imidazole does not induce dramatic changes in the Fe−O and O−O bond strengths. Interestingly, the compounds **LS-3DCHIm** and **LS-4DCHIm** can also be used as starting material for the generation of other low-spin compounds. In fact, addition of 1 equiv of TMPA to **LS-3DCHIm** or **LS-4DCHIm** results in imidazole ligand displacement, giving **LS-TMPA**.[20]

6. Structural Variations and Comparison of Heme−Peroxo−Copper Cores

As described above, we have synthesized a series of heme−peroxo−Cu(L) complexes with varying ligands (L) to Cu(II) ion and observed that spectroscopic parameters for L = TMPA vs AN vs (3 or 4) DCHIm exhibit distinctive differences. Thus, there are clear differences in structure and bonding (electronic structure) among the compounds. With Ed Solomon's group at Stanford University, DFT calculations have been carried out in order to determine finer details concerning structural and vibrational characteristics of these compounds.20 One focus was to compare and contrast the (**HS-AN**)/(**LS-AN**) pair. We see that axial base coordination (DCHIm) promotes isomerization of the side-on Fe^{III}−(μ-η^2:η^2-O_2^{2-})−Cu^{II} core in **HS-AN**, giving an end-on Fe^{III}−(μ-η^1:η^1-O_2^{2-})−Cu^{II} structure in **LS-AN**, responsible for the change in spin-state. A significant reorganization of the peroxo core has occurred, as evidenced by the increased Fe···Cu distance (+0.36 Å) and shortened Fe−O (−0.20 Å), O−O (−0.06 Å), and Cu−O

(−0.09 Å) bond lengths (Figure 2). These changes stem from (i) the transition to an end-on geometry in which the Fe and Cu ions bind only one oxygen atom and (ii) the low-spin nature of heme-iron(III). The O−O distance shortening is small but can be explained by an increase in O_2^{2-} (π^*) donation into the Fe(d_z^2) orbital, which increases the O−O bond strength. Similarly, DFT calculations on the (**HS-TMPA**)/(**LS-TMPA**) pair lead to similar observed trends (Figure 2).[20] DCHIm coordination as a heme axial ligand produces rearrangement of the peroxo core with a notorious increase in the Fe−Cu distance (+0.77 Å) but shortened Fe−O (−0.20 Å) and O−O (−0.06 Å) distances (Figure 2, bottom right). However, in this case, only a slight change in the geometry around copper center is observed (Cu−O distance shortened 0.02 Å), which is explained by the retention of the peroxide coordination mode (i.e., end-on to Cu) upon heme-Fe spin change.

We have previously mentioned21 that heme−peroxo−copper reactivity is enhanced in the low-spin-state. Thus, comparison of **LS-AN** and **LS-TMPA** is worthy of discussion. They both possess end-on Fe^{III}–(μ-η^1:η^1-O_2^{2-})−Cu^{II} low-spin cores; however, their structural differences (Figure 2) are prominent. A significantly greater Fe···Cu distance (+0.50 Å) and much larger ∠Cu−O−O (+22°) are found for **LS-TMPA**. As shown before, these variances are also reflected in the complexes' distinctive spectroscopic features (UV−vis, rRaman). Ongoing computational studies will include analyses of **LS-3DCHIm** vs **LS-4DCHIm** and comparison to the other low-spin complexes. These complexes possess the same ν_{O-O} values (876 cm^{-1}; vide supra), but this frequency is much higher (>64 cm^{-1}) than what is found for **LS-AN** or **LS-TMPA**.[20]

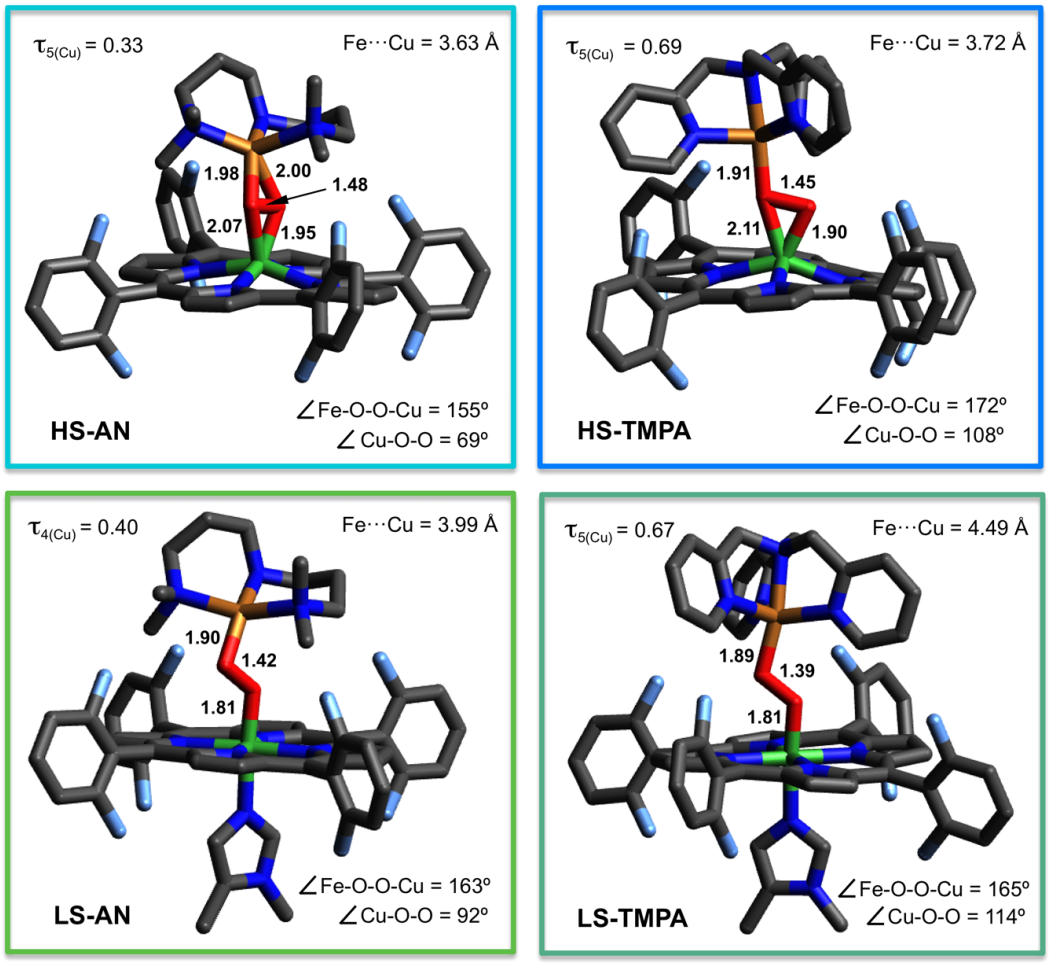

Figure 2. DFT optimized structures for **HS-AN**, **LS-AN**, **HS-TMPA**, and **LS-TMPA** complexes. Adapted with permission from ref 20. Copyright 2015 American Chemical Society.

As seen from the structural and spectroscopic information displayed in Scheme 1 and Figure 2, significant variations are observed as a function of the nature of the specific ligand to copper ion and the heme spin state. Peroxo-bridged heme/Cu species are possible C*c*O reaction intermediates forming between **Oxy** and **PM** (Figure 1);[19,20,22,23] we regard them as a near ideal starting point for studying O−O reductive cleavage reactivity.[24] Further, initial studies reveal that **LS-3DCHIm** and **LS-4DCHIm**, along with other compounds (Scheme 1), possess markedly different behavior with respect to

O−O cleavage upon protonation or reduction. Our long-term goal is to understand these reactivity differences in terms of heme−peroxo−Cu complex structure and bonding variations, and the results will impact C*c*O chemistry and other processes where O−O reductive cleavage occurs (see Introduction).

7. Initial Work on Nitrite and $NO_{(g)}$ Interconversion

In biological systems, the production of $NO_{(g)}$ as a signaling agent, for example, in smooth muscle cell relaxation, is critically important. Aside from $NO_{(g)}$ synthesis by cytochrome P-450 like NO-synthases, which produce $NO_{(g)}$ via L-arginine oxidative chemistry,[25] nitrite also serves as a critical $NO_{(g)}$ source (also see below). The cellular balance of $NO_{(g)}$ is very tightly regulated and mechanisms for its removal include $NO_{(g)}$-reductase (NOR), coupling $NO_{(g)}$ molecules to give N_2O, and $NO_{(g)}$-dioxygenase (NOD), producing nitrate as a benign $NO_{(g)}$ oxidation product.[25] $NO_{(g)}$ is also "removed" via oxidation to nitrite, to later be converted back to nitric oxide when needed. The blood copper protein ceruloplasmin oxidizes $NO_{(g)}$ to nitrite,[26] as does cytochrome c oxidase.

In fact, our heme/Cu assemblies as heme-a_3/Cu_B C*c*O active-site models not only are capable of O_2 reduction but also possess redox activity toward nitrogen oxides including nitrite and $NO_{(g)}$ interconversions. To help shed light on the molecular mechanism of this redox interplay between these two molecules and the roles that the metal centers may play, we have employed our binuclear synthetic systems. In our initial report,[27] we introduced a synthetic heme/Cu assembly that in its partially reduced form facilitates nitrite reduction to $NO_{(g)}$. Thus, addition of the cupric−nitrite complex

[(tmpa)$Cu^{II}(NO_2)$]$^+$ to 2 equiv of the ferrous heme $(F_8)Fe^{II}$ (λ_{max} = 421 nm) resulted in formation of a one-to-one mixture of the ferrous heme−nitrosyl complex $(F_8)Fe^{II}(NO)$ (λ_{max} = 399 nm) and the μ-oxo compound $[(F_8)Fe^{III}–O–Cu^{II}(tmpa)]^+$ (λmax = 435 nm, Scheme 2), readily confirmed by UV−vis, EPR, and IR (ν_{NO} = 1688 cm^{-1}) spectroscopies. Here, the second equivalent of ferrous heme was not involved in the redox chemistry and only trapped the $NO_{(g)}$ produced. Our electrochemical measurements showed that in this heme/Cu assembly, the cuprous complex [(tmpa)Cu^{I}(MeCN)]$^+$ (−0.42 V vs $Fc^{+/0}$) is a chemically stronger reductant compared with the ferrous heme $(F_8)Fe^{II}$ (−0.20 V vs $Fc^{+/0}$). However, based on our control experiments, neither of these reduced compounds, nor the combination of the two, is capable of reducing nitrite to $NO_{(g)}$. Thus, our initial study[27] highlighted two primary findings: (i) the ferrous heme is the redox active center providing the electron, (ii) while the cupric center serves as a Lewis acid facilitating nitrite (N−O) bond cleavage. This overall chemical transformation can also be viewed as one-electron reduction of nitrite (formally NO^+), which accompanies a transfer of an oxygen atom derived from the nitrite, finally forming an oxo-bridge $Fe^{III}–O–Cu^{II}$ product.

Interestingly, in turn, we showed that the fully oxidized form of the same assembly as a μ-oxo compound $[(F_8)Fe^{III}–O–Cu^{II}(tmpa)]^+$ (λ_{max} = 435 nm) could oxidize $NO_{(g)}$ back to nitrite (Scheme 2).[27] Addition of $NO_{(g)}$ to the μ-oxo complex $[(F_8)Fe^{III}–O–Cu^{II}(tmpa)]^+$ resulted in reformation of the cupric−nitrite complex [(tmpa)$Cu^{II}(NO_2)$]$^+$; the reduced heme $(F_8)Fe^{II}$ formed from this $NO_{(g)}$ oxidase chemistry is trapped by a second equivalent of $NO_{(g)}$ to give $(F_8)Fe^{II}(NO)$ (λ_{max} = 399 nm). The results of product analysis using UV−vis, EPR, and IR spectroscopies and capillary electrophoresis (nitrite analysis, 95% yield) confirmed the nature of the products and

proposed stoichiometric reaction. For comparison, the μ-hydroxo complex $[(F_8)Fe^{III}–(OH)–Cu^{II}(tmpa)]^{2+}$ was also tested for "$NO_{(g)}$ oxidase" chemistry, but addition of $NO_{(g)}$ resulted in no nitrite production; the μ-oxo complex $[(F_8)Fe^{III}– O–Cu^{II}(tmpa)]^{+}$ is unique in its ability to effect this redox and oxo transfer reaction.

Scheme 2. Heme/Cu-Assembly-Mediated Interconversion of Nitrite and Nitric Oxide.

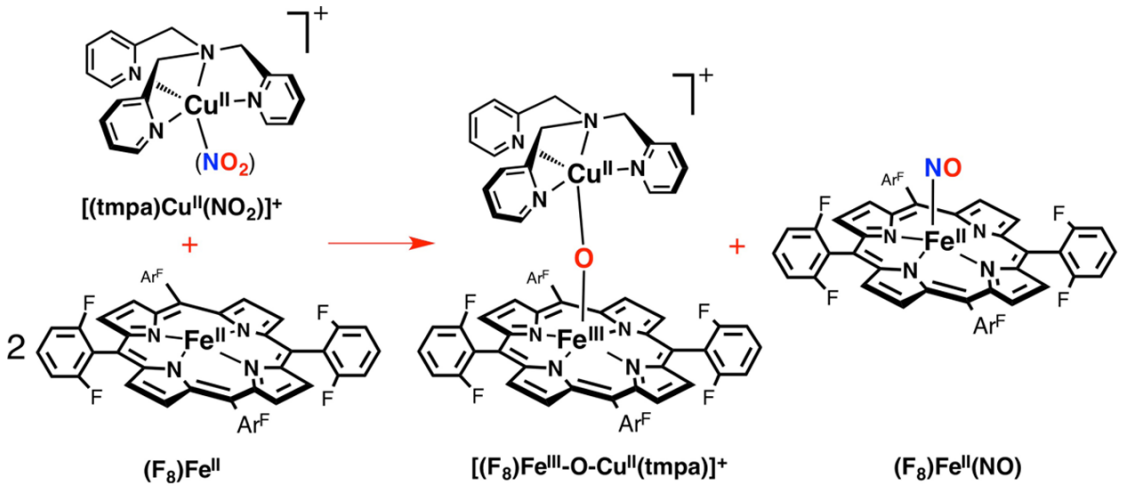

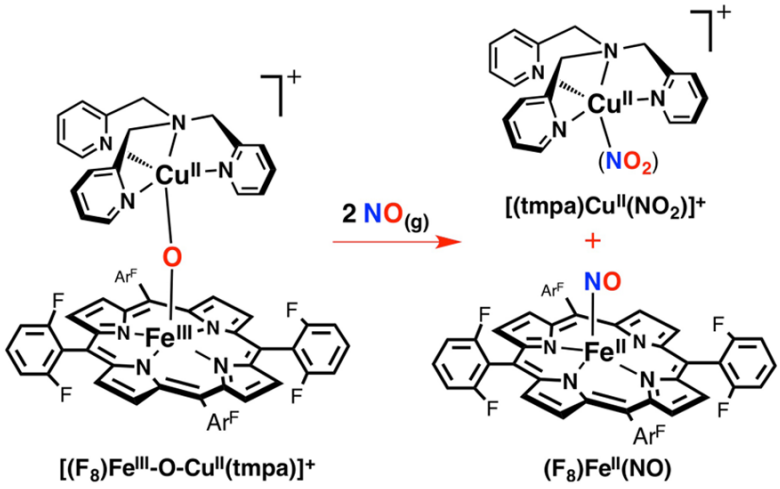

8. Investigation on Nitrite Reductase Chemistry Mediated by Heme/Cu Assemblies

To further investigate the key factors involved in the nitrite reductase chemistry, the nature of the heme or the copper ligand or both were synthetically modified (Scheme 3).[28]

Scheme 3. Nitrite Reductase Chemistry Mediated by Heme/Cu Assemblies.[a]

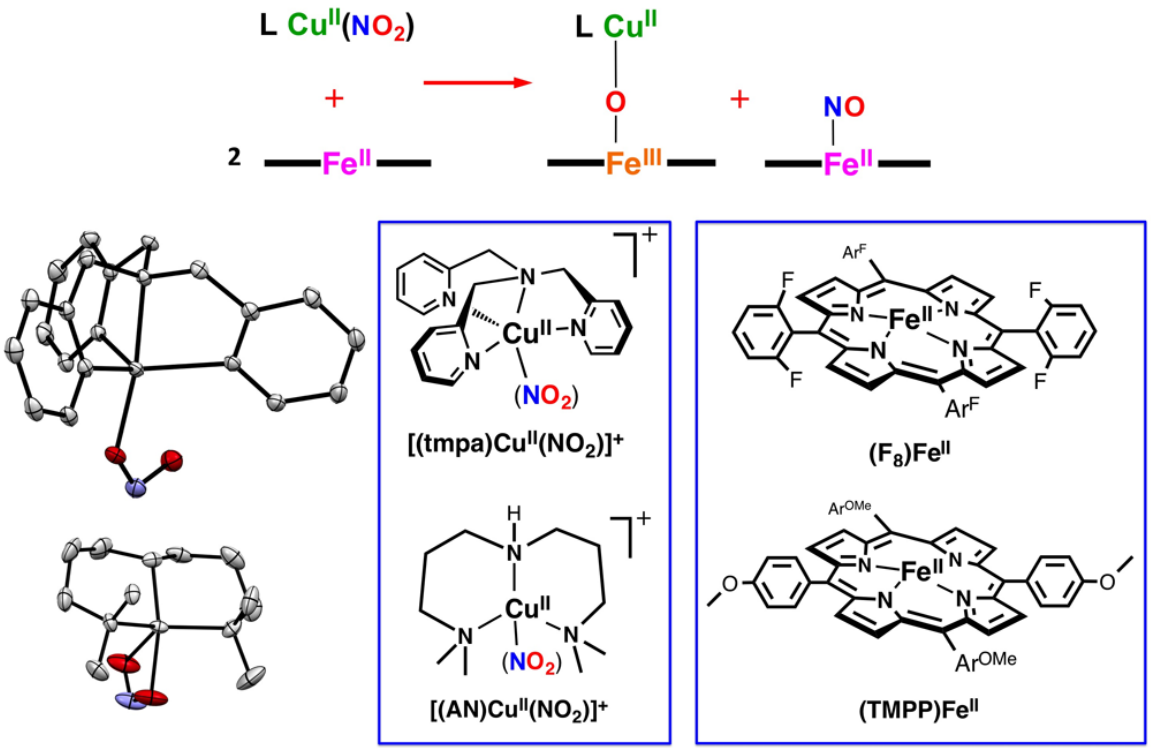

[a](*top*) General reaction equation. (*bottom*) Structures of copper and heme complexes used in our study.

8.1. Pophyrinate Variation

Toward a better understanding of the role of the reducing ability of the ferrous heme center, a different tetraarylporphyrinate bearing strong electron-donating peripheral groups, TMPP, was employed, and its reactivity was compared with the Fe^{II}/Cu^{II}–nitrite "parent" reaction, the combination of $[(tmpa)Cu^{II}(NO_2)]^+$ and $(F_8)Fe^{II}$, where the heme possesses electron-withdrawing peripheral substituents.[28] Product analysis confirmed the same overall redox reaction, converting nitrite to $NO_{(g)}$, thus generating a one-to-one mixture of the μ-oxo compound $[(TMPP)Fe^{III}–O–Cu^{II}(tmpa)]^+$ (λ_{max} = 443 nm) and ferrous heme nitrosyl complex $(TMPP)Fe^{II}(NO)$ (λ_{max} = 410 nm).

Notably, on the basis of UV−vis monitoring of the disappearance of the Soret band for the ferrous heme, the reaction proceeds at about the same rate as for the Fe^{II}/Cu^{II}–nitrite "parent" reaction, pointing to the fact that even with the greater electron-donating ability of the ferrous heme $(TMPP)Fe^{II}$, the nitrite reduction reaction is not accelerated.

8.2. Influence of Copper Coordination Environment on Nitrite Reduction

In order to examine the effect of differing modes of coordination of nitrite to the cupric center, we employed $[(AN)Cu^{II}(NO_2)](CF_3SO_3)$, having a tridentate alkylamine chelate rather than a tetradentate pyridyl-alkylamine ligand, as in $[(tmpa)Cu^{II}(NO_2)]$-$[B(C_6F_5)_4]$ (Scheme 3).[28] As revealed by X-ray crystallography, these two cupric–nitrite complexes exhibit different binding modes of nitrite to the copper center, *O,O′*- bidentate

binding in the former and *O*-unidentate coordination in the latter (note that the outer *O*-atom is very accessible). Reactions of both cupric−nitrite complexes with either ferrous-heme leads to the same overall redox reaction reducing nitrite to $NO_{(g)}$. Interestingly, we observed that when $[(AN)Cu^{II}(NO_2)]^+$ was reacted with either $(F_8)Fe^{II}$ or $(TMPP)Fe^{II}$, the rate of ferrous heme disappearance was roughly twice as fast as the reaction of the same heme with the $[(tmpa)Cu^{II}(NO_2)]^+$. Thus, faster reduction of nitrite to $NO_{(g)}$ occurs when the nitrito ligand is coordinated in bidentate vs unidentate fashion to the cupric center. We concluded that this difference in nitrite coordination mode leads to differing approaches of the cupric−nitrite compound to the reduced heme (i.e., the reduction center) to transiently form a bridged ferrous heme−(nitrite)−cupric complex. For $[(AN)Cu^{II}(NO_2)]^+$, having *O,O′*-bidentate nitrite ligation, one could anticipate a facile approach of a nitrite nitro- gen atom to the ferrous heme, leading to a nitro (*N*-ligated) mode of coordination (Figure 3), perhaps in the rate-determining step.

This can be followed by an intramolecular electron transfer from the ferrous heme to the bridging nitrite generating a bridged hydronitrite radical (NO_2^{2-}) assembly, which rapidly converts to $NO_{(g)}$ and a kinetically stable μ-oxo (O^{2-}) complex $[(porphyrinate)Fe^{III}-O-Cu^{II}(AN)]^+$ (F_8 or TMPP porphyrinate).[28]

Another possibility is that in both cases, using $[(tmpa)Cu^{II}(NO_2)]^+$ or $[(AN)Cu^{II}(NO_2)]^+$, NO_2^- binding to the ferrous heme must occur through the nitrogen atom in order to lead to a productive reaction, that is, resulting in nitrite (N−O) bond cleavage and $NO_{(g)}$ formation. This would be consistent with the expectation that soft Fe(II) favors the softer *N*-atom coordination versus that hard *O*-atom of nitrite based on "hard−soft" acid−base principles. So, even for $[(tmpa)Cu^{II}(NO_2)]^+$, an effective reaction

may require a relatively slow nitrite group rearrangement or reorientation in order that the nitrogen atom can bind the ferrous heme. Such a rearrangement is not required for the nitrite bound in $[(AN)Cu^{II}(NO_2)]^+$; thus a faster reaction occurs, all consistent with the observations.

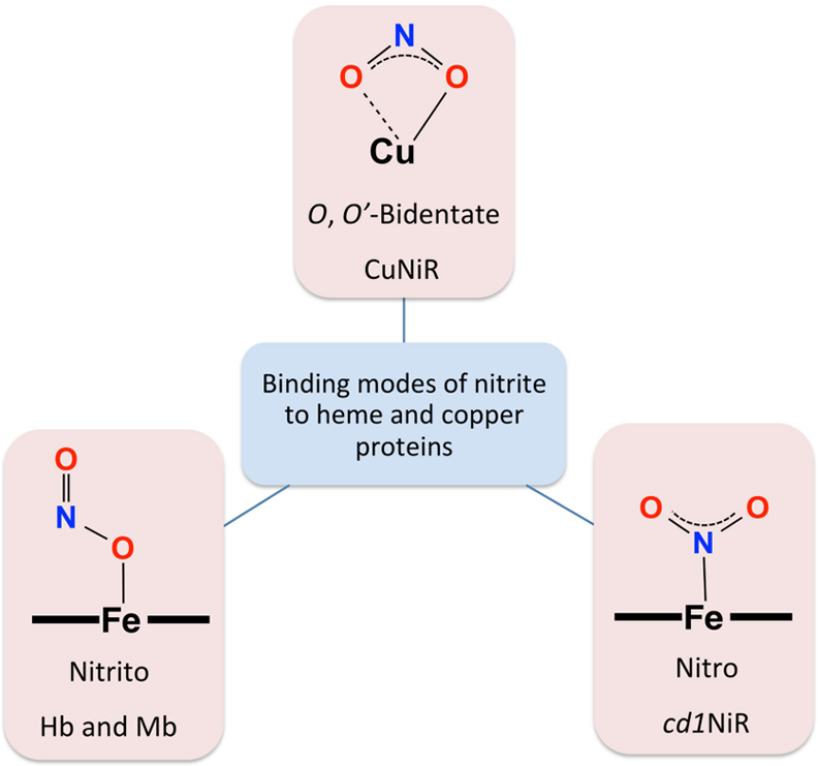

Figure 3. Binding modes of nitrite to heme and copper proteins.

In general, enzymatic nitrite reductase reactivity (i.e., one-electron reduction of nitrite to $NO_{(g)}$) has been ascribed to two classes of proteins, containing either copper (CuNiR) or heme (e.g., cd_1NiR, hemoglobin (Hb), and myoglobin (Mb)) as cofactor.[25,29,30] As Figure 3 illustrates, based on available crystal structure data, nitrite

binds to copper-containing NiRs in the *O,O′*-bidentate nitrito mode, while it coordinates to *cd*$_1$NiR via the *N*-unidentate nitro fashion. It has also been shown that nitrite binding to Hb or Mb occurs through an *O*-unidentate coordination (nitrito mode)[31,32] Interestingly, the interactions of nitrite with *ba*$_3$-C*c*O, with both heme and copper active-site ions, have been just recently studied by rRaman,[32] revealing the existence of a ferrous heme−nitro species not previously observed. This finding, thus, supports our original hypothesis or thought[28] that iron−nitrogen bond formation, as assisted by cupric center orienting or directing of the nitrite ion, is a crucial step in our heme/Cu assembly nitrite-reductase activity. Further support for this supposition is also provided through our detailed mechanistic study of the reverse reaction, that is, oxidation of $NO_{(g)}$ to nitrite, discussed below.

9. Mechanistic Study of Nitric Oxide Oxidase Chemistry Mediated by Heme/Cu Assemblies

As indicated in Scheme 3, we initially[27] described in the $Fe^{III}/Cu^{II}–NO_{(g)}$ "parent" reaction a fully oxidized heme/Cu assembly, in the form of the μ-oxo complex $[(F_8)Fe^{III}–O–Cu^{II}(tmpa)]^+$, which mediates the one-electron oxidation of $NO_{(g)}$ to nitrite. To expand on the initial study, we very recently reported a detailed mechanistic study[11] using different μ-oxo $[(porphyrinate)Fe^{III}–O–Cu^{II}(L)]^+$ complexes in which the heme or copper chelating ligand is modified (Scheme 4); ligand (L) for the cupric core was either a tripodal tetradentate pyridyl-alkylamine chelate or a related tridentate alkylamine ligand, and two different tetraarylporphyrinates were employed for the heme core, one with

electron-withdrawing peripheral substituents versus one with strong electron-donating groups.

Scheme 4. Variations of Heme/Cu Assemblies in $NO_{(g)}$ Oxidase Chemistry.

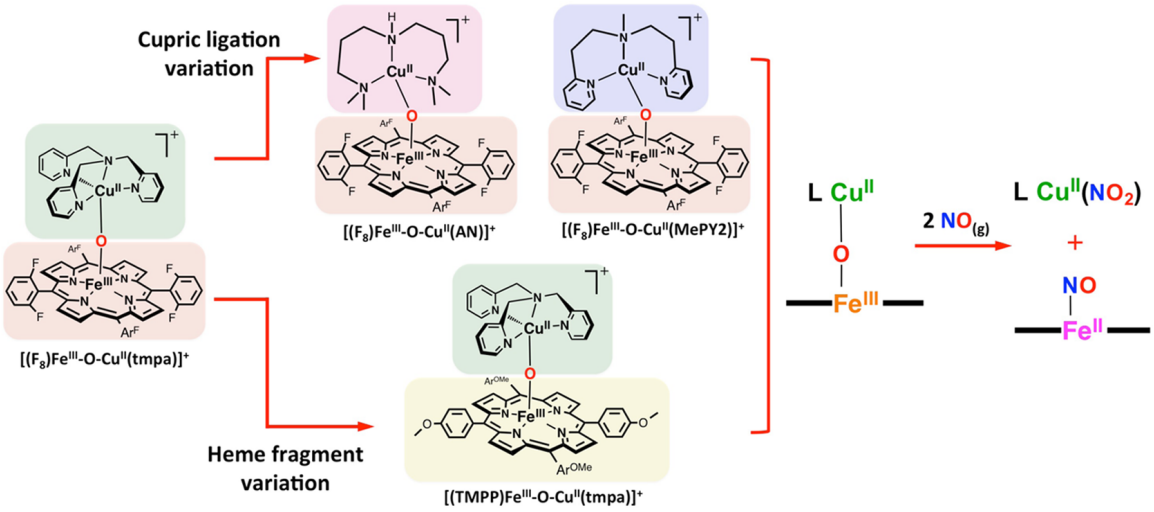

9.1. Copper Coordination Environment Variation

The effects of alterations in copper-ligand denticity and electronics were investigated by comparing the tetradentate chelate TMPA used in the Fe^{III}/Cu^{II}–$NO_{(g)}$ oxidase "parent" reaction with new tridentate ligands, L = AN and MePY2 (Scheme 4).[11] When the tridentate chelates were employed under the same experimental conditions, oxidation of $NO_{(g)}$ by μ-oxo $[(F_8)Fe^{III}–O–Cu^{II}(L)]^+$ ensued considerably faster than that for the parent analog, still yielding the Cu(II)−nitrite plus ferrous heme−nitrosyl products.

These observations can be justified based on two factors: (i) previous studies

reveal that for μ -oxo heme-Fe^{III}–O–Cu^{II}(L) complexes where L is the tridentate ligand AN or MePY2,[13] the bridging oxo ion is more basic than that for the tetradentate ligand, that is, L = TMPA,[12] and (ii) for tridentate ligands, there is a lack of steric hindrance, primarily because the Fe^{III}–O–Cu^{II} moiety is bent; further, the coordination number for the copper ion is only four, relative to pentacoordination in the TMPA analog, making the bridging oxo ion more accessible for addition of $NO_{(g)}$ (Chart 1 and Scheme 4).[11]

9.2. Impact of Peripheral Substituents of the Porphyrinate: Dynamics and Intermediates Involved in $NO_{(g)}$ Oxidase by Heme/Cu Assemblies

Modification of the nature of the porphyrinate employed in this chemistry has turned out to provide us with many new mechanistic insights.[11] A new μ-oxo complex, $[(TMPP)Fe^{III}–O–Cu^{II}(tmpa)]^{+}$, was synthesized and characterized, and in its reaction with $NO_{(g)}$ at RT, there was an instantaneous change (as followed by UV−vis monitoring), giving a mixture of species, which eventually all converted to the expected final products, $[(tmpa)Cu^{II}(NO_2)]^{+}$ and $(TMPP)Fe^{II}(NO)$.

When this reaction was repeated at −20 °C, a new inter- mediate (λ_{max} = 433 nm) was detected following addition of $NO_{(g)}$ to the solution of μ-oxo compound.[11] Later, this isosbestically converted to the final products in a first-order process (Scheme 5, $k_{dissoc.}$ = 6.7×10^{-3} s^{-1} at −20 °C, $\Delta H^{\ddagger}$ = 41.1 ± 0.1 kJ mol^{-1} and $\Delta S^{\ddagger}$ = −123 ± 2 J mol^{-1} K^{-1}). In cryospray ionization mass spectrometry (CSI-MS) measurements[33] at −60 °C, we could detect this new species, which presented itself as a manifold of intense peaks with maximum at *m/z* = 1217.2847, this corresponding to a *bis*-NO adduct of the initial μ-oxo

compound. With this observation, along with the further studies carried out (vide infra), we could conclude that sequential addition of two $NO_{(g)}$ molecules to the starting $[(TMPP)Fe^{III}–O–Cu^{II}(tmpa)]^{+}$ complex led to the *bis*-NO adduct, formulated as $[(NO)(TMPP)Fe^{II}–NO_2–Cu^{II}(tmpa)]^{+}$ complex.[11]

Scheme 5. Proposed Reaction Steps for $NO_{(g)}$ Oxidase Chemistry Mediated by μ-oxo Heme-Fe^{III}–O–Cu^{II}(L) Complexes Generating Nitrite.

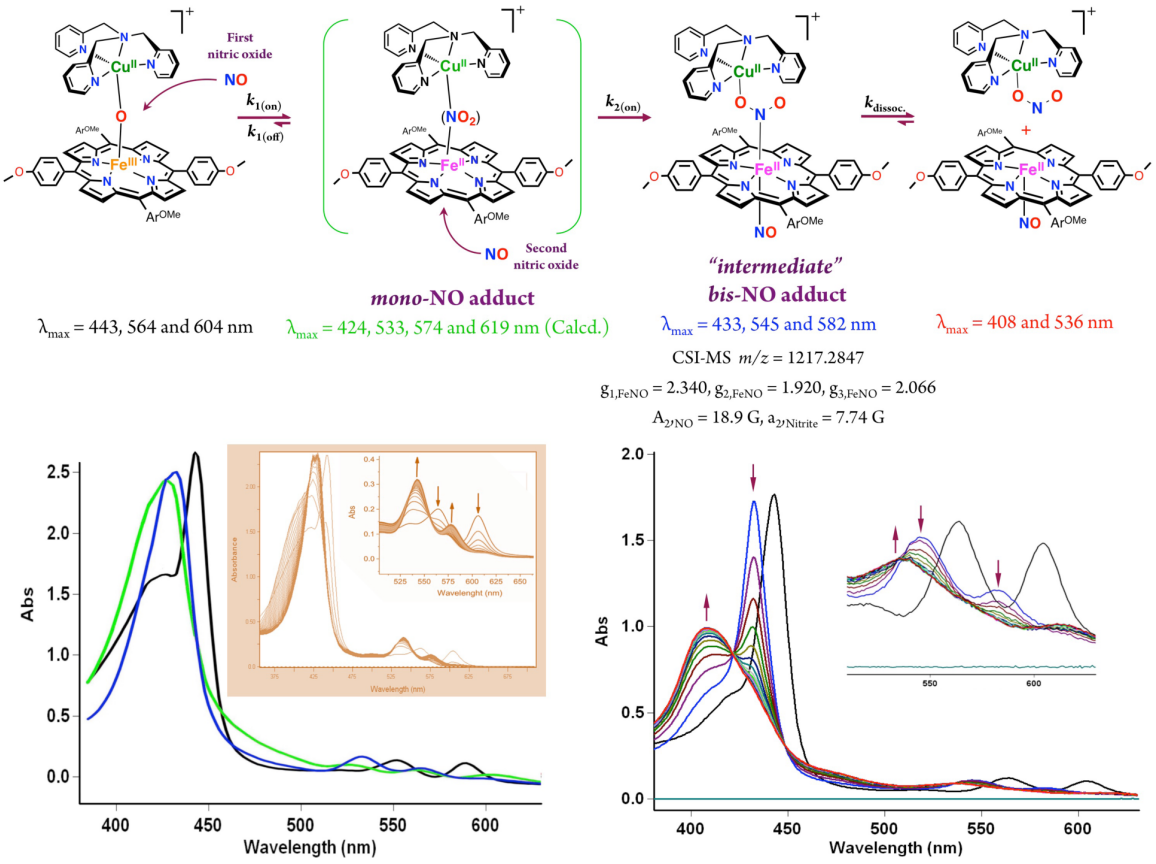

Adapted with permission from ref 11. Copyright 2015 American Chemical Society.

Low-temperature stopped-flow kinetic spectroscopic measurements[33] provided (full) spectral changes for the entire course of the reaction. From the analyses carried out, the spectrum of the *mono*-NO adduct, which forms prior to formation of the *bis*-NO intermediate, could be extracted (Scheme 5). We also determined corresponding observed rate constants for the addition of first ($k_{1(obs)}$) and the second ($k_{2(obs)}$) $NO_{(g)}$ molecules for a range of low temperatures down to −83 °C and different $NO_{(g)}$ concentrations (ranging between 0.28 to 2.3 mM).[11] At all temperatures, linear dependencies ($k_{(obs)} = k_{(on)}[NO] + k_{(off)}$) of the observed rate constants ($k_{1(obs)}$ and $k_{2(obs)}$) on $NO_{(g)}$ concentration were observed. An overview of the first and second $NO_{(g)}$ binding kinetics at different temperatures and thermodynamic parameters are given in Table 1. Notably, the binding of the second $NO_{(g)}$ is irreversible; addition of the first $NO_{(g)}$ to $[(TMPP)Fe^{III}–O–Cu^{II}(tmpa)]^+$ occurs about 1 order of magnitude faster than binding of the second $NO_{(g)}$ (Scheme 5, Table 1).[11,34]

Table 1. Binding Kinetics and Thermodynamics of First and Second $NO_{(g)}$ to $[(TMPP)Fe^{III}–O–Cu^{II}(tmpa)]^+$.

	First $NO_{(g)}$ binding				*Second* $NO_{(g)}$ binding	
T (°C)	$k_{1(on)}$ (M^{-1} s^{-1})		$k_{1(off)}$ (s^{-1})		$k_{2(on)}$ (M^{-1} s^{-1})	
-60	6,053 ± 186		2.61 ± 0.24		706 ± 20	
-67	5,061 ± 244		1.47 ± 0.32		637 ± 40	
-74	2,356 ± 69		1.07 ± 0.09		504 ± 40	
-83	1,184 ± 12		0.50 ± 0.01		*could not be determined*[11]	
	$\Delta H^{‡}_{(on)}$ (kJ mol^{-1})	$\Delta S^{‡}_{(on)}$ (J mol^{-1} K^{-1})	$\Delta H^{‡}_{(off)}$ (kJ mol^{-1})	$\Delta S^{‡}_{(off)}$ (J mol^{-1} K^{-1})	$\Delta H^{‡}_{(on)}$ (kJ mol^{-1})	$\Delta S^{‡}_{(on)}$ (J mol^{-1} K^{-1})
	24 ± 3	-64 ± 10	22 ± 2	-131 ± 9	7 ± 2	-155 ± 8
	$\Delta H°$ (kJ mol^{-1})		$\Delta S°$ (J mol^{-1} K^{-1})			
	2.0 ± 0.4		67 ± 15			

The small values of $\Delta H^{\ddagger}_{(on)}$ and negative activation entropies ($\Delta S^{\ddagger}_{(on)}$) observed are consistent with the associative nature of the $NO_{(g)}$ binding steps. The negligible activation enthalpy (7 ± 2 kJ mol^{-1}) for the binding of the second $NO_{(g)}$ points to an almost activation-less process. Together with the negative $\Delta S^{\ddagger}_{(on)}$ value, one can conclude that the rate-determining step does not involve bond breaking; instead, bond-making predominates. These data and conclusions are in excellent agreement with DFT studies[33] (Scheme 6), which also describe the sequential addition of $NO_{(g)}$ to the μ-oxo complex.[11]

The first $NO_{(g)}$ attacks the μ-oxo atom, leading to the *mono*-NO adduct (Scheme 6). According to DFT calculations, electron-transfer occurs here, formally from $NO_{(g)}$ to the heme, via transient formation of a "triangular" structure. Both the original μ-oxo atom and the $NO_{(g)}$-derived *N*-atom bind to the iron center (Scheme 6, TS1). The experimentally observed low activation enthalpy (24 ± 3 kJ/mol) and negative activation entropy derived from the kinetic studies are consistent with this sequence of events.[11]

As relevant to the addition of the second $NO_{(g)}$ molecule, the DFT results reveal that the SOMO of the *bis*-NO "intermediate" is predominantly localized on the Fe-porphyrin moiety, pointing to its ferrous character. Experimental evidence confirming the formulation and properties of the "intermediate" were obtained from (i) the fact that cooling the products, consisting of a 1:1 mixture of $(TMPP)Fe^{II}(NO)$ plus $[(tmpa)Cu^{II}(NO_2)]^{+}$, leads to association and reformation of the key 433 nm UV−vis feature of the "intermediate", where the nitrite bound to copper ion coordinates and thus forms a bridge to the ferrous heme−nitrosyl complex; (ii) analyses of EPR spectra of the "intermediate" indicate the presence of a six-coordinated ferrous-heme nitrosyl bearing a trans *N*-based ligand ($a_{2,Nitrite}$ = 7.74 G), all linked to an EPR active cupric species in a

TBP coordination environment.[11]

Scheme 6. Schematic Calculated Energy Profile for [(TMPP)Fe^{III}–O–Cu^{II}(tmpa)]$^{+}$ Reaction with $NO_{(g)}$.[a]

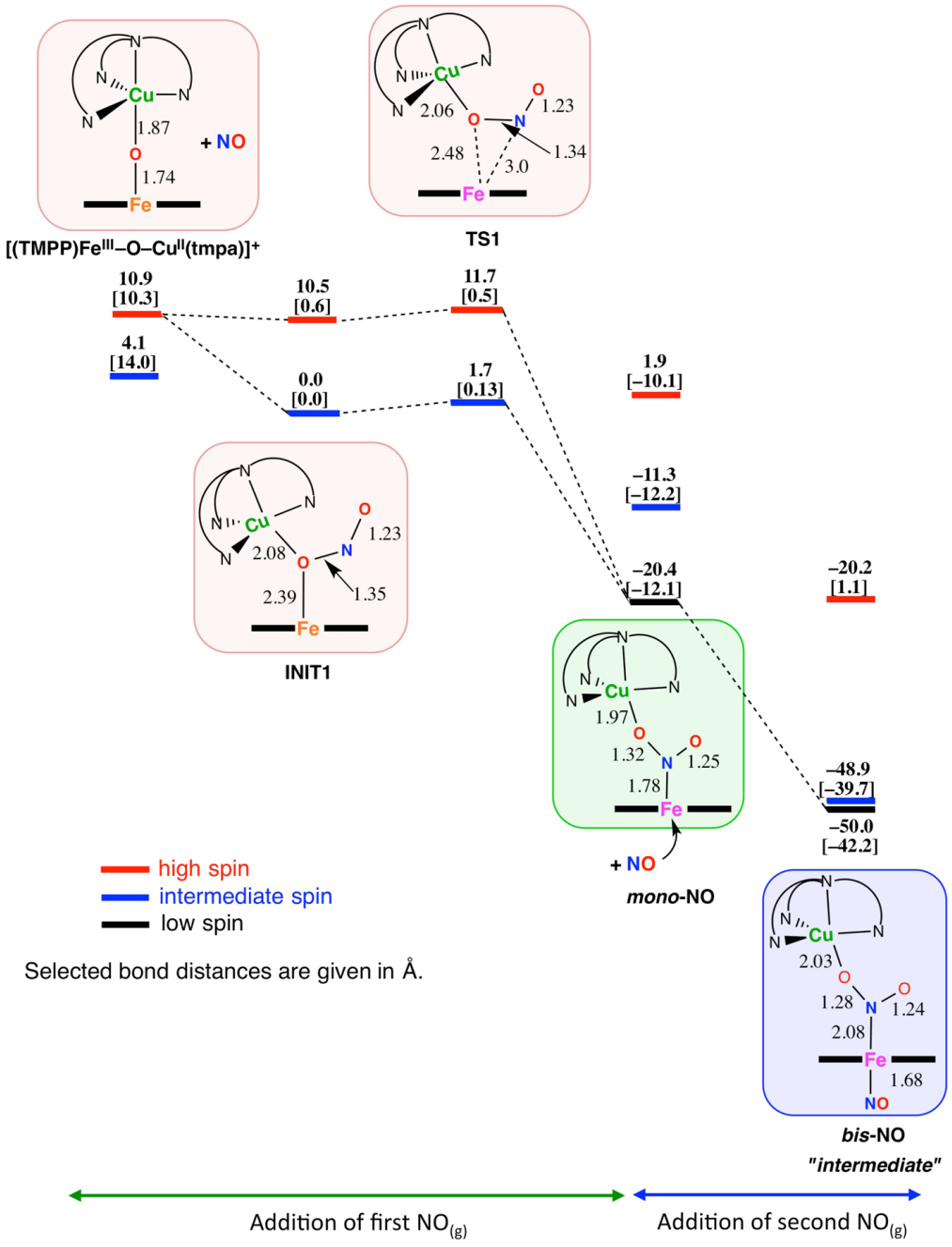

Adapted with permission from ref 11. Copyright 2015 American Chemical Society. [a]ΔE + ZPE in kcal mol^{-1} including solvent correction at both the BP86/6-31G(d) level and OLYP/6-311+G(d,p) level (given in brackets).

In the last step, the “intermediate”, undergoes dissociation in a first-order process to release the finally observed mononuclear adducts, the cupric−nitrite and ferrous heme−nitrosyl complexes.

10. Broader Perspectives on Nitrite and $NO_{(g)}$ Interconversion

From our broad investigations on nitrite/$NO_{(g)}$ redox interconversions mediated by heme/Cu centers, we conclude that both (bio)chemical transformations necessitate specific nitrite coordination, *N*-atom to ferrous-heme and *O*-atom to cupric ion. In fact, we believe that both chemical transformations proceed via the same intermediates.

Our proposed mechanism for nitrite reduction is represented by the forward (left-to-right) reaction in Scheme 7. For aerobic organisms, O_2 is the ultimate electron acceptor for cellular respiration. Under conditions of stress and when the O_2 concentration drops below a certain level, nitrite starts to compete with the residual O2 for reduction by the C*c*O binuclear active site, eventually generating $NO_{(g)}$. The $NO_{(g)}$ thus produced reversibly inhibits the oxygen reduction at the same center and allows for O_2 accumulation. Then, in this recovery from hypoxia, the reverse reaction consists of the same steps traversed backward; $NO_{(g)}$ is removed and converted back to nitrite for future use. Now, in normoxia, in the absence of $NO_{(g)}$, the C*c*O recovers its traditional function, that is, catalyzing the four- electron reduction of O_2 to water.

We note that the μ-oxo heme-Fe^{III}−O−Cu^{II}(L) complexes described here may not exactly represent C*c*O turnover inter- mediates or even resting-state structures. However,

these μ-oxo compounds should be thought of as representatives of actual enzyme active site heme/Cu entities, those involved in $NO_{(g)}$ oxidation chemistry, possibly a heme-Fe^{III}–OH···Cu^{II} or even a high-valent compound II type species, heme-Fe^{IV}=O···Cu.

Scheme 7.

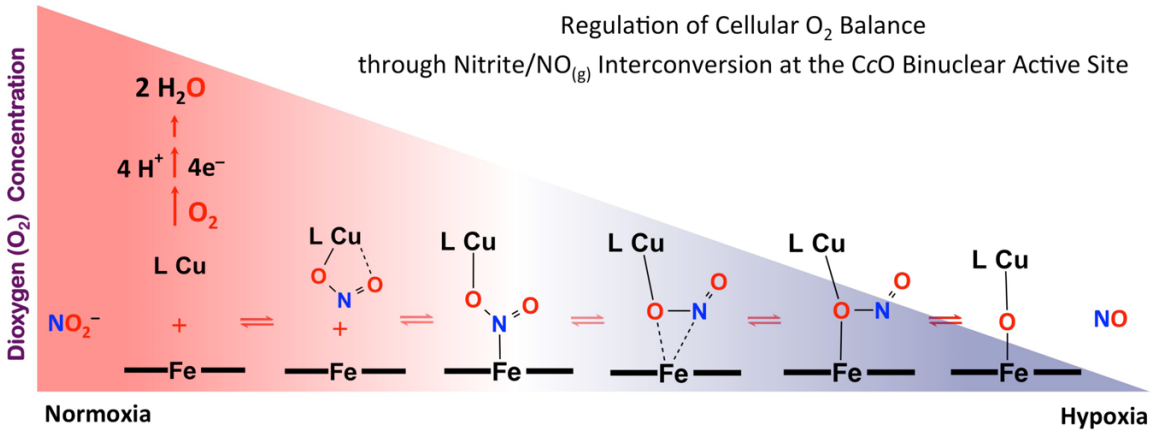

11. Summary and Outlook

In this Account, we have described our recent studies using synthetic heme/Cu assemblies, investigating their reactivity with dioxygen and nitrogen oxides. The work involves rational design and implementation of constructs mimicking basic aspects of the C*c*O active site, which allow for redox transformations of these small molecules (i.e., O_2, $NO_{(g)}$, and NO_2^-).

Our long time goals have been to study metal–dioxygen chemistry at heme/Cu

centers, because the details of O_2 ligation, resulting coordination geometry, and electronic structure require full elucidation. Because clean four-electron, four-proton O_2 reduction will depend on heme and Cu ligation, factors such as the exact juxtaposition of these two metal ions, redox potentials ($Fe^{III/II}$, $Fe^{IV/III}$, and $Cu^{II/I}$), relative basicity of O_2-derived fragments, and availability and pK_a of proton sources, study of these factors is critical in order to fully understand C*c*O fuel-cell chemistry, that is, the O−O cleavage process, that pervades all of (bio)chemistry. Here, we briefly summarized past and very recent findings, which have led to the novel chemistry presented, a new powerful synthetic approach to generate many kinds of (new) heme/Cu constructs, which will allow for the future approaches and studies mentioned here. We have succeeded in the synthesis of heme−O_2−Cu complexes possessing distinctively varying properties of ligation, structure, spectroscopic features, and bonding. We are poised to examine the intimate details of stoichiometric reductive O−O cleavage reactions as a function of those heme−peroxo−Cu complex properties versus reducing agent power and proton source pK_a.

As we have also shown here, the same or similar heme/Cu constructs are able to readily effect one-electron nitrite reduction or $NO_{(g)}$ oxidation, occurring through *O*-atom transfer redox reactions. Molecular level structural and mechanistic details of these biologically relevant processes have been determined. The chemistry involved in these two processes is closely related; detailed kinetic−thermodynamic and spectroscopic studies reveal that they both proceed by essentially the same (but in opposite direction) pathways and require the involvement of common intermediates (Scheme 7). Of course, in C*c*O, these reactions also involve protons; in our synthetic models, these are not needed because the metal ions instead capture *O*-atoms or ions. Nevertheless, the studies

here for the first time point to how these nitrogen oxide reactions can or do occur at heme/Cu centers and their relationship to dioxygen chemistry. These provide a basis for understanding the self-regulatory role of C*c*O in effecting cellular O_2 balance and its correlation to $NO_{(g)}$ and nitrite redox interplay with respect to hypoxia. Aside from further inquiries into heme/Cu/NO_x chemical systems, near-future goals include the interrogation of heme/Cu constructs for $NO_{(g)}$ reductive coupling, relevant to bacterial denitrification and $NO_{(g)}$ homeostasis.

12. References

(1) Yoshikawa, S.; Shinzawa-Itoh, K.; Nakashima, R.; Yaono, R.; Yamashita, E.; Inoue, N.; Yao, M.; Jei-Fei, M.; Libeu, C. P.; Mizushima, T.; Yamaguchi, H.; Tomizaki, T.; Tsukihara, T. *Science* **1998**, *280*, 1723.

(2) Kim, E.; Chufán, E. E.; Kamaraj, K.; Karlin, K. D. *Chem. Rev*. **2004**, *104*, 1077.

(3) Yoshikawa, S.; Shimada, A. *Chem. Rev.* **2015**, *115*, 1936.

(4) Solomon, E. I.; Heppner, D. E.; Johnston, E. M.; Ginsbach, J. W.; Cirera, J.; Qayyum, M.; Kieber-Emmons, M. T.; Kjaergaard, C. H.; Hadt, R. G.; Tian, L. *Chem. Rev.* **2014**, *114*, 3659.

(5) Castello, P. R.; David, P. S.; McClure, T.; Crook, Z.; Poyton, R. O. *Cell Metab.* **2006**, *3*, 277.

(6) Poyton, R. O.; Castello, P. R.; Ball, K. A.; Woo, D. K.; Pan, N. *Ann. N. Y. Acad. Sci.* **2009**, *1177*, 48.

(7) Nicholls, P.; Sharpe, M.; Torres, J.; Wilson, M. T.; Cooper, C. E. *Biochem. Soc. Trans.* **1998**, *26*, S323.

(8) Torres, J.; Sharpe, M. A.; Rosquist, A.; Cooper, C. E.; Wilson, M. T. *FEBS Lett.* **2000**, *475*, 263.

(9) Nanthakumar, A.; Fox, S.; Murthy, N. N.; Karlin, K. D.; Ravi, N.; Huynh, B. H.; Orosz, R. D.; Day, E. P.; Hagen, K. S.; Blackburn, N. J. *J. Am. Chem. Soc.* **1993**, *115*, 8513.

(10) Karlin, K. D.; Nanthakumar, A.; Fox, S.; Murthy, N. N.; Ravi, N.; Huynh, B. H.; Orosz, R. D.; Day, E. P. *J. Am. Chem. Soc.* **1994**, *116*, 4753.

(11) Hematian, S.; Kenkel, I.; Shubina, T. E.; Dürr, M.; Liu, J. J.; Siegler, M. A.; Ivanovic-Burmazovic, I.; Karlin, K. D. *J. Am. Chem. Soc.* **2015**, *137*, 6602.

(12) Fox, S.; Nanthakumar, A.; Wikström, M.; Karlin, K. D.; Blackburn, N. J. *J. Am. Chem. Soc.* **1996**, *118*, 24.

(13) Kopf, M.-A.; Neuhold, Y.-M.; Zuberbühler, A. D.; Karlin, K. D. *Inorg. Chem*. **1999**, *38*, 3093.

(14) Ghiladi, R. A.; Hatwell, K. R.; Karlin, K. D.; Huang, H.-w.; Moeñne-Loccoz, P.; Krebs, C.; Huynh, B. H.; Marzilli, L. A.; Cotter, R. J.; Kaderli, S.; Zuberbühler, A. D. *J. Am. Chem. Soc.* **2001**, *123*, 6183.

(15) Chufán, E. E.; Puiu, S. C.; Karlin, K. D. *Acc. Chem. Res.* **2007**, *40*, 563.

(16) Chishiro, T.; Shimazaki, Y.; Tani, F.; Tachi, Y.; Naruta, Y.; Karasawa, S.; Hayami, S.; Maeda, Y. *Angew. Chem. Int. Ed.* **2003**, *42*, 2788.

(17) Kim, E.; Shearer, J.; Lu, S.; Moeñne-Loccoz, P.; Helton, M. E.; Kaderli, S.; Zuberbühler, A. D.; Karlin, K. D. *J. Am. Chem. Soc.* **2004**, *126*, 12716.

(18) Chufán, E. E.; Mondal, B.; Gandhi, T.; Kim, E.; Rubie, N. D.; Moeñne-Loccoz, P.; Karlin, K. D. *Inorg. Chem.* **2007**, *46*, 6382.

(19) Kieber-Emmons, M. T.; Qayyum, M. F.; Li, Y.; Halime, Z.; Hodgson, K. O.; Hedman, B.; Karlin, K. D.; Solomon, E. I. *Angew. Chem. Int. Ed.* **2012**, *51*, 168.

(20) Garcia-Bosch, I.; Adam, S. M.; Schaefer, A. W.; Sharma, S. K.; Peterson, R. L.; Solomon, E. I.; Karlin, K. D. *J. Am. Chem. Soc.* **2015**, *137*, 1032.

(21) Halime, Z.; Kieber-Emmons, M. T.; Qayyum, M. F.; Mondal, B.; Gandhi, T.; Puiu, S. C.; Chufán, E. E.; Sarjeant, A. A. N.; Hodgson, K. O.; Hedman, B.; Solomon, E. I.; Karlin, K. D. *Inorg. Chem.* **2010**, *49*, 3629.

(22) Blomberg, M. R. A.; Siegbahn, P. E. M.; Wikström, M. *Inorg. Chem*. **2003**, *42*, 5231.

(23) Fee, J. A.; Case, D. A.; Noodleman, L. *J. Am. Chem. Soc.* **2008**, *130*, 15002.

(24) If one starts with a heme-Fe^{III}−superoxide Cu(I) species (a model for compound A, Figure 1), at least two electrons are still required (e.g., from Cu(I), the active site tyrosine, or iron) to cleave the O−O bond. Our peroxo complexes are at the stage of having one more electron (from Cu(I)); we are thus poised to study the O−O cleavage step. The ultimate goal is to determine what factors pertaining to (heme)Fe−O_2^- Cu ligation, structure and bonding, and electron reducing ability (E°) or proton acidity (pK_a) allow for (or not) O−O reductive cleavage without leakage of H_2O_2 or hydroxyl radical.

(25) Lehnert, N.; Berto, T. C.; Galinato, M. G. I.; Goodrich, L. E. The Role of Heme-Nitrosyls in the Biosynthesis, Transport, Sensing, and Detoxification of Nitric Oxide (NO) in Biological Systems: Enzymes and Model Complexes. In *The Handbook of Porphyrin Science*; Kadish, K. M.; Smith, K.; Guilard, R., Eds.; World Scientific: Singapore, 2011; *Vol. 14*, pp 1−247.

(26) Shiva, S.; Wang, X.; Ringwood, L. A.; Xu, X.; Yuditskaya, S.; Annavajjhala, V.; Miyajima, H.; Hogg, N.; Harris, Z. L.; Gladwin, M. T. *Nat. Chem. Biol.* **2006**, *2*, 486.

(27) Hematian, S.; Siegler, M. A.; Karlin, K. D. *J. Am. Chem. Soc.* **2012**, *134*, 18912.

(28) Hematian, S.; Siegler, M. A.; Karlin, K. D J. *Biol. Inorg. Chem.* **2014**, *19*, 515.

(29) Merkle, A. C.; Lehnert, N. *Dalton Trans.* **2012**, *41*, 3355.

(30) Maia, L. B.; Moura, J. J. G. *Chem. Rev.* **2014**, *114*, 5273.

(31)Yi,J.;Heinecke,J.;Tan,H.;Ford,P.C.;Richter-Addo,G.B. *J. Am. Chem. Soc.* **2009**, *131*, 18119.

(32) Loullis, A.; Noor, M. R.; Soulimane, T.; Pinakoulaki, E. *Chem. Commun.* **2015**, *51*, 286.

(33) Collaboration with the University of Erlangen-Nuremberg group. See ref 11.

(34) In the C*c*O active site, the heme possesses an axial proximal histidine ligand, which can be considered to be taking the place of the second $NO_{(g)}$ molecule in our synthetic system.

Chapter 2:

Heme/Copper Assembly Mediated Nitrite and Nitric Oxide Interconversion

---

This work was co-authored with the following authors and is published under the following citation:

Shabnam Hematian, Maxime A. Siegler, and Kenneth D. Karlin

J. Am. Chem. Soc. **2012**, *134*, 18912−18915

Abstract:

The heme-a_3/Cu_B active site of cytochrome *c* oxidase is responsible for cellular nitrite reduction to nitric oxide; the same center can return $NO_{(g)}$ to the nitrite pool via oxidative chemistry. Here, we show that a partially reduced heme/Cu assembly reduces NO_2^- ion, producing nitric oxide. The heme serves as the reductant, but the Cu^{II} ion is also required. In turn, a μ-oxo heme-Fe^{III}−O−Cu^{II} complex facilitates $NO_{(g)}$ oxidation to nitrite; the final products are the reduced heme and Cu^{II}−nitrito complexes.

1. Introduction

Nitrogen oxides (NO_x) are components of great interest in both biological and environmental sciences. Nitric oxide (NO) is an important cellular signaling molecule and a powerful vasodilator involved in many physiological and pathological processes.[1] Nitrite (NO_2^-) is the one-electron oxidized product of endogenous $NO_{(g)}$ metabolism. Recent studies indicate that nitrite plays a critical biological role by serving as a biochemical circulating reservoir for $NO_{(g)}$, in particular under conditions of physiologic hypoxia (low O_2 tensions; see also below) and ischemia. The nitrite-to- $NO_{(g)}$ conversion represents an important alternative source of $NO_{(g)}$ to the classical oxygen-dependent L-arginine-derived generation of $NO_{(g)}$ catalyzed by nitric oxide synthase (NOS).[2] Subsequently, suggested conserved roles for the $NO_2^-/NO_{(g)}$ pool in cellular processes include oxygen sensing and oxygen-dependent modulation of intermediary metabolism.[3] It is now considered that in order to stimulate $NO_{(g)}$ signaling, nitrite reductase activity occurs widely in differing cellular environments and is effected by a variety of proteins/enzymes, including hemes, those with molybdenum,[4] and what draws our current interest, cytochrome *c* oxidases (C*c*O's).[3,5]

The link between nitrite/$NO_{(g)}$ redox interconversion and O_2 sensing is thought to occur in mitochondria at the C*c*O binuclear heme-a_3/Cu_B center; C*c*O is the terminal enzyme of the mitochondrial respiratory chain. Here, molecular oxygen consumption (i.e., O_2 reduction to water) is down-regulated in hypoxia by increased $NO_{(g)}$ generation via C*c*O nitrite reductase activity, as reduced heme/Cu centers dominate when the O_2 concentration is low.[3a,4,6] The $NO_{(g)}$ thus generated inhibits C*c*O activity by reversibly binding to hemea3 in place of O_2, resulting in cellular O_2 accumulation (Figure 1).

Some of the $NO_{(g)}$ produced also participates in hypoxic signaling, the upregulation of nuclear genes needed in response to the inherent dangers of low cellular O_2 concentrations.[3]

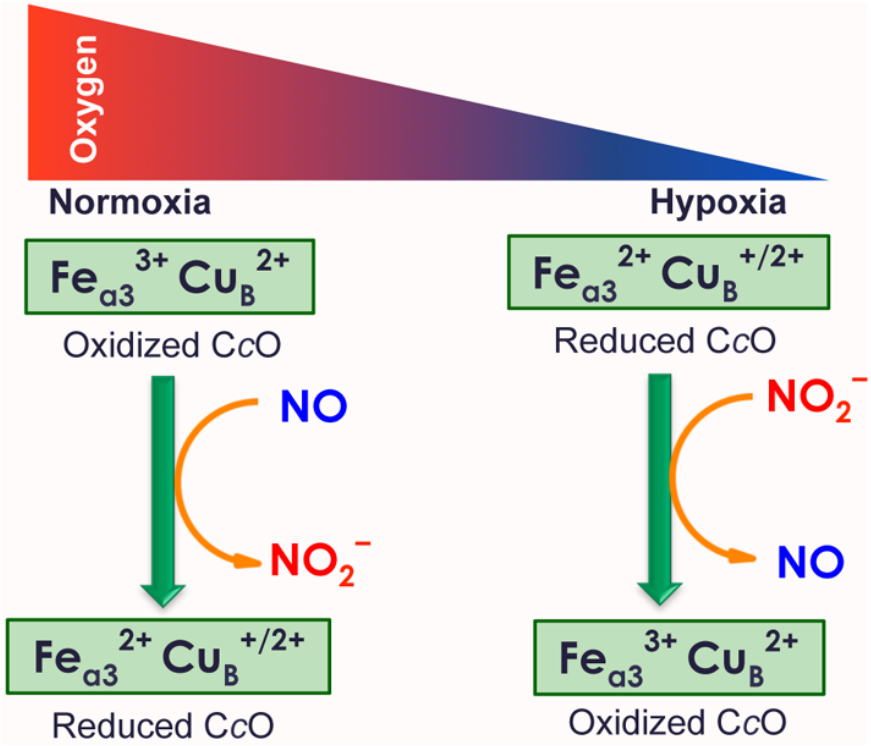

Figure 1. Cytochrome *c* oxidase (C*c*O) functioning in nitrite (NO_2^-)/nitric oxide (NO) interconversion as part of its role in regulation of O_2 balance. The availability of O_2 influences the redox state of the C*c*O containing the heme-a_3/Cu_B binuclear center.

In turn, in normoxia, high local O_2 concentrations do not allow nitrite to compete as an oxidant at the C*c*O binuclear center; thus, NO/O_2 binding is noncompetitive,[7] and heme-a_3/Cu_B oxidizes $NO_{(g)}$ back to nitrite (Figure 1) to rejoin the storage pool. $NO_{(g)}$ is thought to first attack oxidized Cu_B, formally giving CuI−NO^+; the latter hydrolyzes to nitrite.[8,9]

2. Heme/Copper Assemblies Interconverting Nitrite and Nitric Oxide

In this report, we describe a chemical system involving a heme/Cu assembly-mediated interconversion of these important nitrogen oxides. A partially reduced/oxidized state, with reduced heme and oxidized copper ion (i.e., $Fe^{II}\cdots Cu^{II}$) efficiently converts nitrite to $NO_{(g)}$. When a fully oxidized $Fe^{III}\cdots Cu^{II}$ heme/Cu complex is employed, $NO_{(g)}$ is readily oxidized to nitrite. The overall reactions are represented by eqs 1 and 2:

$$(P)Fe^{II}Cu^{II} + NO_2^- \rightarrow (P)Fe^{III}{-}O{-}Cu^{II} + NO_{(g)} \quad (1)$$

$$(P)Fe^{III}{-}O{-}Cu^{II} + NO_{(g)} \rightarrow (P)Fe^{II}Cu^{II} + NO_2^- \quad (2)$$

The nitrite reductase chemistry,[10] here however in a heme/Cu chemical system, consisted of the iron(II) complex $(F_8)Fe^{II}$ [F_8 ≡ tetrakis(2,6-difluorophenyl)-porphyrinate(2−)][11] and a preformed copper(II)−nitrito complex $[(tmpa)Cu^{II}(NO_2)]$-$[B(C_6F_5)_4]$ [tmpa ≡ tris(2-pyridylmethyl)amine]; the latter was synthesized by adding $AgNO_2$ to a chloride precursor $[(tmpa)Cu^{II}(Cl)][B(C_6F_5)_4]$, and its X-ray structure revealed an *O*-bound nitrito ligated Cu(II) ion (Scheme 1).[12]

When 2 equiv of $(F_8)Fe^{II}$ were mixed with 1 equiv of $[(tmpa)Cu^{II}(NO_2)]^+$ under a N_2 atmosphere in acetone at room temperature (RT), a reaction ensued, and on the basis of UV−vis, electron paramagnetic resonance (EPR), and IR spectroscopies, a 1:1 mixture of the heme−nitrosyl species $(F_8)Fe^{II}(NO)$ and the μ-oxo complex $[(F_8)Fe^{III}{-}O{-}Cu^{II}(tmpa)]^+$ were produced.[12] These products were readily identified, having been previously thoroughly characterized.[13] To determine whether the heme or the copper ion is the reductant in this one-electron process ($NO_2^- \rightarrow NO_{(g)}$), we also carried

out the reaction in which nitrite was added to the oxidized heme complex $[(F_8)Fe^{III}](SbF_6)$[13b] (binding of nitrite to the ferric heme[14] was indicated by a large UV−vis change)[12] and then the reduced complex $[(tmpa)Cu^{I}(MeCN)]^{+}$ [12,15] was added. In this case there was no reaction (Scheme 1), even over a period of days.[12] Control experiments showed that nitrite reacts only very slowly with $(F_8)Fe^{II}$ and not at all with $[(tmpa)Cu^{I}(MeCN)]^{+}$. Moreover, no nitrite reductase activity was observed for the fully reduced metal combination, nitrite plus $(F_8)Fe^{II}$ and $[(tmpa)Cu^{I}(MeCN)]^{+}$.[12]

Scheme 1. Heme/Copper Assembly-Mediated Reduction of Nitrite to Nitric Oxide.

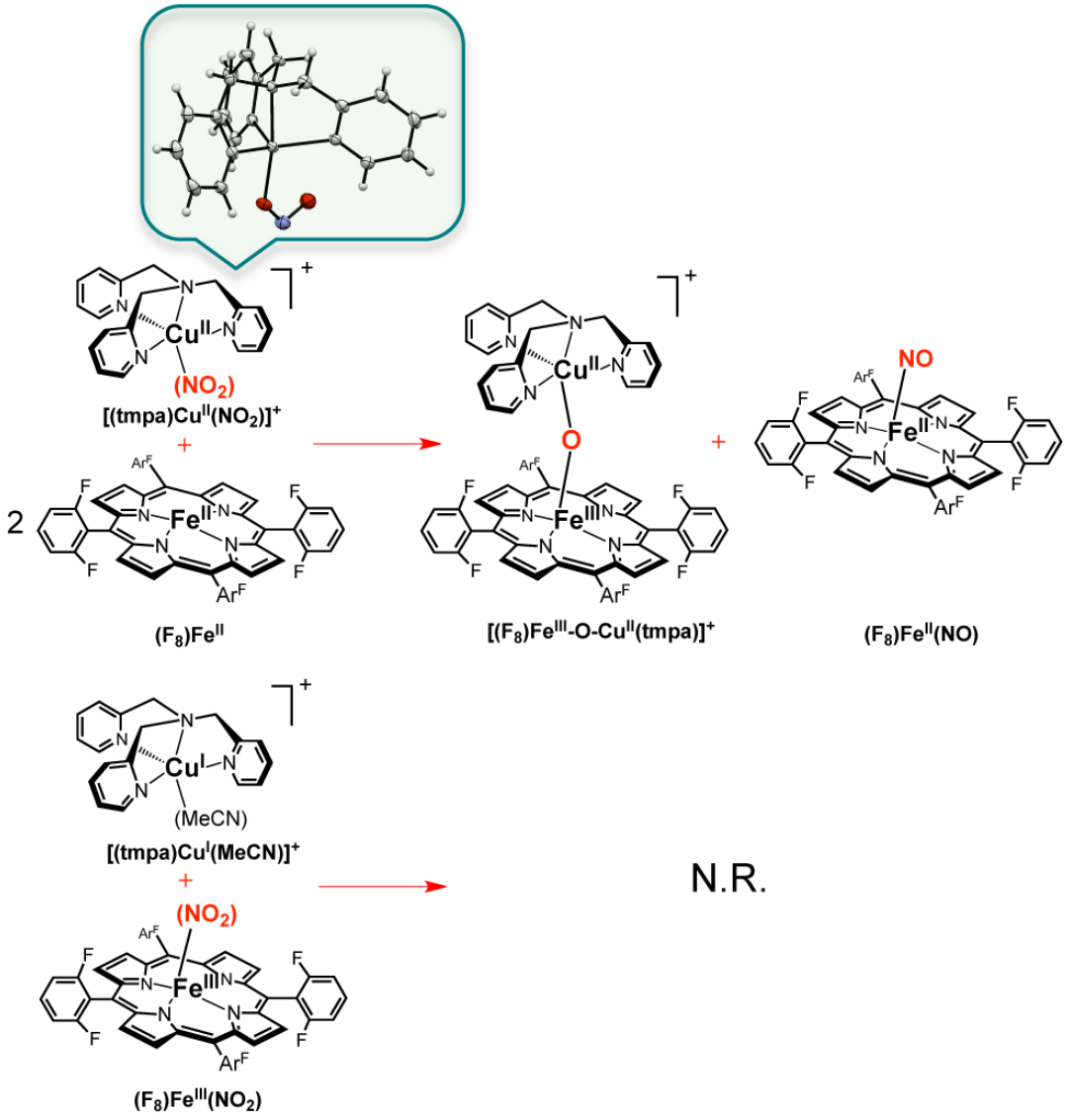

These observations indicate that the heme is the reductant in this heme/Cu nitrite reductase chemistry. The need for 2 equiv of $(F_8)Fe^{II}$ is due to the well-known high affinity of $NO_{(g)}$ to bind ferrous hemes.[16] The initially formed $NO_{(g)}$ reacts very rapidly with $(F_8)Fe^{II}$; thus, if the reaction were carried out with equimolar quantities of $(F_8)Fe^{II}$ and $[(tmpa)Cu^{II}(NO_2)]^+$, only half of the iron would be available to reduce nitrite, and the rest would trap the $NO_{(g)}$ as $(F_8)Fe^{II}(NO)$. The role of the Cu^{II} ion appears to be to provide a Lewis acid interaction with nitrite, facilitating NO_2^- (N−O) bond cleavage and stabilization of the resulting oxo anion via eventual formation of $[(F_8)Fe^{III}{-}O{-}Cu^{II}(tmpa)]^+$.

To demonstrate that heme/copper assemblies can mediate $NO_{(g)}$ oxidation to nitrite, as occurs biologically in order to remove excess $NO_{(g)}$ when it is not needed and return it to the nitrite pool (see above), we employed $[(F_8)Fe^{III}{-}O{-}Cu^{II}(tmpa)]^+$. Addition of $NO_{(g)}$ to this fully oxidized heterobinuclear complex led to rapid reaction (Scheme 2) and formation of nitrite, which bound to Cu(II); the $(F_8)Fe^{II}$ formed[17] in this redox reaction was trapped by a second equivalent of $NO_{(g)}$ to give $(F_8)Fe^{II}(NO)$. UV−vis (Figure 2) and IR (ν_{NO} = 1688 cm^{-1})[12] spectroscopies directly indicated nitrosyl complex formation. Nitrite analysis employing capillary electrophoresis revealed that this ion was produced in 95% yield.[12] EPR spectroscopy confirmed that a copper(II)−nitrito complex was produced (Figure 2); a sample taken from the reaction mixture was identical in all regards to that of an authentic sample of a 1:1 mixture of $(F_8)Fe^{II}(NO)$ and $[(tmpa)Cu^{II}(NO_2)]^+$.

It is important to explain why the reaction required 2 molar equiv of $NO_{(g)}$ (Scheme 2). The second equivalent was not involved in the redox chemistry but was

Scheme 2. Heme/Copper Assembly-Mediated Oxidation of Nitric Oxide to Nitrite.

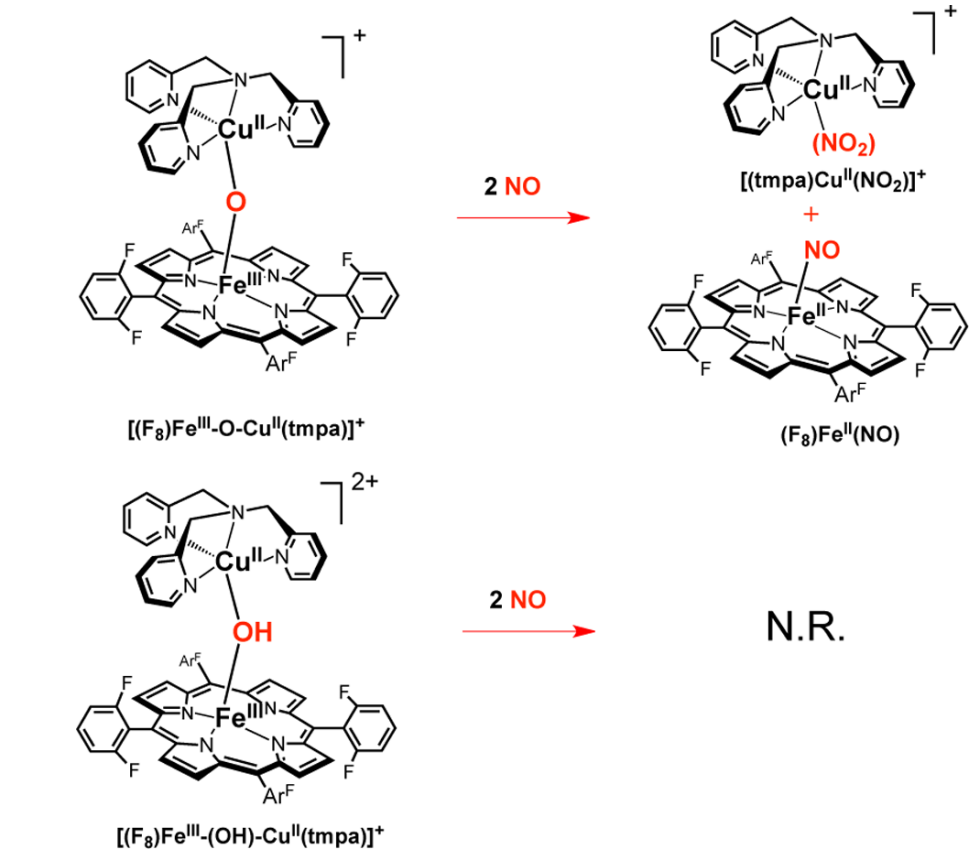

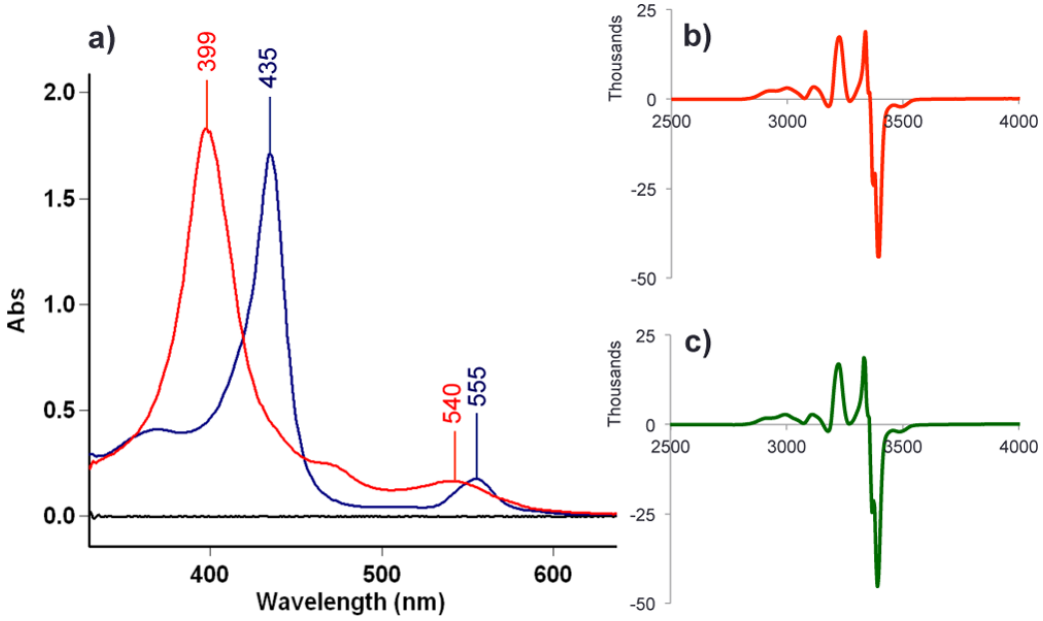

Figure 2. (a) UV−vis spectra of $(F_8)Fe^{III}$−O−Cu^{II}(tmpa)][$B(C_6F_5)_4$] (1) (blue) and $(F_8)Fe^{II}$(NO) generated from 1 + $NO_{(g)}$ (12 μM in acetone at RT) (red). (b, c) EPR spectra of (b) the products of the reaction of $(F_8)Fe^{III}$−O−Cu^{II}(tmpa)][$B(C_6F_5)_4$] and $NO_{(g)}$ (red) and (c) an authentic sample of a 1:1 mixture of $(F_8)Fe^{II}$(NO) and [(tmpa)Cu(NO_2)][$B(C_6F_5)_4$] (green). The EPR spectra were recorded at 20 K (1 mM in MeTHF).

needed to trap the free $(F_8)Fe^{II}$ produced by the $NO_{(g)}$ oxidase chemistry. When $(F_8)Fe^{II}$ is present, it effects the reverse reaction, namely, reduction of Cu(II)-bound nitrite to give $NO_{(g)}$ (Scheme 1). This was demonstrated as follows: When 25 mL of a 10 μM solution containing a mixture of $(F_8)Fe^{II}(NO)$ and $[(tmpa)Cu^{II}(NO_2)]^+$ produced by the reaction of $[(F_8)Fe^{III}–O–Cu^{II}(tmpa)]^+$ with excess $NO_{(g)}$ (green spectrum in Figure 3) was titrated with 25 mL of a 20 μM solution (i.e., 2 equiv) of $(F_8)Fe^{II}$, the product solution (red spectrum in Figure 3) contained ~5 μM $[(F_8)Fe^{III}–O–Cu^{II}(tmpa)]^+$ along with 10 μM $(F_8)Fe^{II}(NO)$; the spectral intensity was equivalent to that observed in the starting mixture because of dilution. This proves that the backward reaction can and does occur, that is, that $[(tmpa)Cu^{II}(NO_2)]^+$ reacts first with $(F_8)Fe^{II}$ in a 1:1 stoichiometry to give $NO_{(g)}$, which is then trapped by the second equivalent of $(F_8)Fe^{II}$.

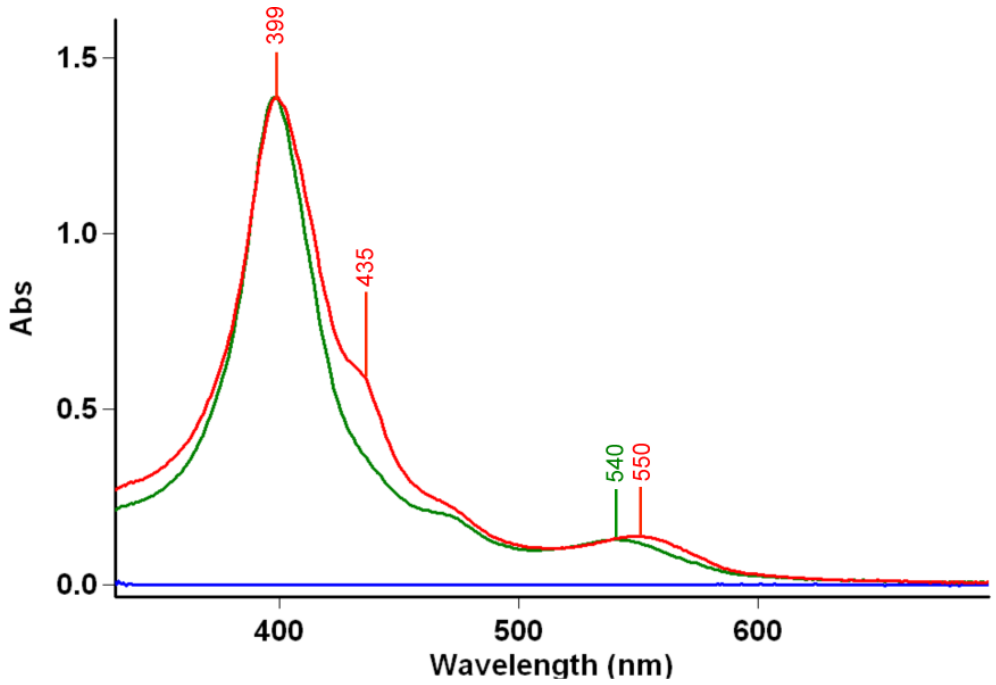

Figure 3. UV−vis spectra of a mixture of $(F_8)Fe^{II}(NO)$ (λ_{max} = 399 nm) and $[(tmpa)Cu^{II}(NO_2)]^+$ derived from the $NO_{(g)}$ oxidase chemistry before (green) and after (red) the addition of 2 equiv of $(F_8)Fe^{II}$. The red spectrum shows the presence of a 2:1 mixture of $(F_8)Fe^{II}(NO)$ and $[(F_8)Fe^{III}–O–Cu^{II}(tmpa)]^+$ (435 nm, sh). The new second equivalent of $(F_8)Fe^{II}(NO)$ was derived from the nitrite reductase chemistry described by Scheme 1. See the text for further explanation.

We also tested the μ-hydroxo complex $[(F_8)Fe^{III}-(OH)-Cu^{II}(tmpa)]^{2+}$ for "$NO_{(g)}$ oxidase" chemistry, but upon addition of $NO_{(g)}$, there was no nitrite production (Scheme 2).[12] Instead, very slow (hours) reductive nitrosylation[18] occurred, and all of the heme present was converted to $(F_8)Fe^{II}(NO)$. It is thus clear that the μ-oxo complex ($[(F_8)Fe^{III}-O-Cu^{II}(tmpa)]^{+}$ is efficient or at least special in its ability to effect a redox reaction (formally $Fe^{III} \rightarrow Fe^{II}$) that includes oxo transfer.[19]

3. Conclusion

In summary, this report has described new chemistry with heme/Cu assemblies and nitrogen oxide interconversion: nitrite reduction to nitric oxide can readily be effected with our heme/copper chemistry. The reduced heme is the source of the one electron required. The presence of Cu^{II} ion as a Lewis acid is crucial. While nitrite reduction to $NO_{(g)}$ is well-known to occur via heme proteins such as hemoglobin and myoglobin,[20] bacteria/fungal heme cd_1[21] or copper nitrite reductases,[22] and certain copper(I) complexes,[22a,23] it appears that the transformation with heme/Cu synthetic complexes has not been examined to date. We have shown here that both heme and Cu are required, at least in our system. It is notable that the heme is the reductant on the basis of the observed products; however, cyclic voltammetric determination of the redox potentials for the separate complexes $(F_8)Fe$ (−0.20 V vs Fc+/Fc)[12] and Cu(tmpa) (−0.42 V vs Fc+/Fc)[12] indicate the latter is a better reductant. For C*c*O, the opposite appears to be the case, as the heme-a_3 has a lower redox potential than does Cu_B.[24]

On the other hand, the heme is also the redox entity, as $[(F_8)Fe^{III}–O–Cu^{II}(tmpa)]^+$ effects oxidation of $NO_{(g)}$ to nitrite by oxo transfer (see above)[19] with reduction of $(F_8)Fe^{III}$. The closely related species $[(F_8)Fe^{III}–(OH)–Cu^{II}(tmpa)]^+$ and/or heme-only complexes do not enable this reaction. However, as already mentioned, it is the Cu_B in C*c*O that is thought to oxidize $NO_{(g)}$,[9] and it is well-known that $NO_{(g)}$ can react with Cu^{II} complexes,[25] affording nitrite. This may imply that in C*c*O it is a particular coordination environment, a specific structural and/or redox state, that is required for mediation of the $NO_{(g)}$ oxidase chemistry.

Further investigations will include our probing of the mechanisms of the reactions described in this report. For nitrite reduction, critical mechanistic components will certainly include the heme reductive capability and the nitrite–Cu binding mode (e.g., *O*- vs *O*,*O′*- vs *N*-bound). As our heme and Cu centers have switched redox capabilities compared with C*c*O, we also wish to change the heme or the Cu ligand to make the Cu center a better oxidant than the heme. For our heme/Cu $NO_{(g)}$ oxidation chemistry, we are uncertain about which metal is the real oxidant,[18] so further investigations are required; as is often the case, “the devil is in the details”.

4. References

(1) (a) Ignarro, L. J. Nitric Oxide as a Communication Signal in Vascular and Neuronal Cells. In *Nitric Oxide: Principles and Actions*; Lancaster, J., Ed.; Academic Press: New York, 1996; p 111. (b) Schopfer, M. P.; Wang, J.; Karlin, K. D. *Inorg. Chem.* **2010**, 49, 6267.

(2) (a) Samouilov, A.; Kuppusamy, P.; Zweier, J. L. *Arch. Biochem. Biophys.* **1998**, *357*, 1. (b) Dezfulian, C.; Raat, N.; Shiva, S.; Gladwin, M. T. *Cardiovasc. Res.* **2007**, *75*, 327.

(3) (a) Castello, P. R.; David, P. S.; McClure, T.; Crook, Z.; Poyton, R. O. *Cell Metab.* **2006**, *3*, 277. (b) Feelisch, M.; Fernandez, B. O.; Bryan, N. S.; Garcia-Saura, M. F.; Bauer, S.; Whitlock, D. R.; Ford, P. C.; Janero, D. R.; Rodriguez, J.; Ashrafian, H. *J. Biol. Chem.* **2008**, *283*, 33927.

(4) van Faassen, E. E.; Bahrami, S.; Feelisch, M.; Hogg, N.; Kelm, M.; Kim-Shapiro, D. B.; Kozlov, A. V.; Li, H.; Lundberg, J. O.; Mason, R.; Nohl, H.; Rassaf, T.; Samouilov, A.; Slama-Schwok, A.; Shiva, S.; Vanin, A. F.; Weitzberg, E.; Zweier, J.; Gladwin, M. T. *Med. Res. Rev.* **2009**, *29*, 683.

(5) (a) Sarti, P.; Giuffre, A.; Barone, M. C.; Forte, E.; Mastronicola, D.; Brunori, M. *Free Radic. Biol. Med.* **2003**, *34*, 509. (b) Gupta, K. J.; Igamberdiev, A. U. *Mitochondrion* **2011**, *11*, 537. (c) Sarti, P.; Forte, E.; Mastronicola, D.; Giuffre , A.; Arese, M. *Biochim. Biophys. Acta* **2012**, *1817*, 610. (d) Curtis, E.; Hsu, L. L.; Noguchi, A. C.; Geary, L.; Shiva, S. *Antioxid. Redox Signal.* **2012**, *17*, 951. (e) Toledo, J. C.; Augusto, O. *Chem. Res. Toxicol.* **2012**, *25*, 975. (6) Poyton, R. O.; Castello, P. R.; Ball, K. A.; Woo, D. K.; Pan, N. *Ann. N.Y. Acad. Sci.* **2009**, *1177*, 48.

(7) Mason, M. G.; Nicholls, P.; Wilson, M. T.; Cooper, C. E. *Proc. Natl. Acad. Sci. U.S.A.* **2006**, *103*, 708.

(8) (a) Antunes, F.; Boveris, A.; Cadenas, E. *Antioxid. Redox Signal.* **2007**, 9, 1569. (b) Torres, J.; Sharpe, M. A.; Rosquist, A.; Cooper, C. E.; Wilson, M. T. *FEBS Lett.* **2000**, *475*, 263.

(9) (a) The multicopper enzyme ceruloplasmin has also been shown to effect $NO_{(g)}$ oxidase ($NO_{(g)}$ →

NO_2^-) chemistry. (b) Shiva, S.; Wang, X.; Ringwood, L. A.; Xu, X.; Yuditskaya, S.; Annavajjhala, V.; Miyajima, H.; Hogg, N.; Harris, Z. L.; Gladwin, M. T. *Nat. Chem. Biol.* **2006**, *2*, 486. (c) Paradis, M.; Gagné, J.; Mateescu, M.-A.; Paquin, J. *Free Radic. Biol. Med.* **2010**, *49*, 2019.

(10) (a) Castiglione, N.; Rinaldo, S.; Giardina, G.; Stelitano, V.; Cutruzzola, F. *Antioxid. Redox Signal.* **2012**, *17*, 684. (b) Merkle, A. C.; Lehnert, N. *Dalton Trans.* **2012**, *41*, 3355.

(11) (a) Kopf, M.-A.; Neuhold, Y.-M.; Zuberbühler, A. D.; Karlin, K. D. *Inorg. Chem.* **1999**, *38*, 3093. (b) Ghiladi, R. A.; Kretzer, R. M.; Guzei, I.; Rheingold, A. L.; Neuhold, Y.-M.; Hatwell, K. R.; Zuberbühler, A. D.; Karlin, K. D. *Inorg. Chem.* **2001**, *40*, 5754.

(12) See the Supporting Information.

(13) (a) Wang, J.; Schopfer, M. P.; Sarjeant, A. A. N.; Karlin, K. D. *J. Am. Chem. Soc.* **2009**, *131*, 450. (b) Wang, J.; Schopfer, M. P.; Puiu, S. C.; Sarjeant, A. A. N.; Karlin, K. D. *Inorg. Chem.* **2010**, *49*, 1404.

(c) Karlin, K. D.; Nanthakumar, A.; Fox, S.; Murthy, N. N.; Ravi, N.; Huynh, B. H.; Orosz, R. D.; Day, E. P. *J. Am. Chem. Soc.* **1994**, *116*, 4753. (d) Fox, S.; Nanthakumar, A.; Wikström, M.; Karlin, K. D.; Blackburn, N. J. *J. Am. Chem. Soc.* **1996**, *118*, 24.

(14) (a) Finnegan, M. G.; Lappin, A. G.; Scheidt, W. R. *Inorg. Chem.* **1990**, *29*, 181. (b) Wyllie, G. R. A.; Scheidt, W. R. *Chem. Rev.* **2002**, *102*, 1067.

(15) Lucas, H. R.; Meyer, G. J.; Karlin, K. D. *J. Am. Chem. Soc.* **2010**, *132*, 12927.

(16) Cooper, C. E. *Biochim. Biophys. Acta* **1999**, *1411*, 290.

(17) By analogy to what has in the past been suggested for the enzyme reaction,8b nitric oxide attacks at the cupric center. Formally, this affords Cu^{I}–NO^{+}, to which oxo transfer occurs, along with electron transfer from Cu^{I} to Fe^{III} to give the Cu^{II}–nitrito complex and FeII, which is then trapped by a second $NO_{(g)}$ molecule. Separately, we can demonstrate that with the present complexes $[(tmpa)Cu^{I}(MeCN)]^{+}$

and [$(F_8)Fe^{III}$](SbF_6), the Cu^{I}-to-Fe^{III} electron transfer readily occurs in acetone (see the Supporting Information).

(18) (a) Ford, P. C. *Inorg. Chem.* **2010**, *49*, 6226. (b) Fernandez, B. O.; Lorkovic, I. M.; Ford, P. C. *Inorg. Chem.* **2003**, *42*, 2.

(19) Man, W.-L.; Lam, W. W. Y.; Ng, S.-M.; Tsang, W. Y. K.; Lau, T.-C. *Chem. —Eur. J.* **2012**, *18*, 138.

(20) (a) Doyle, R. P.; Pickering, R. A.; Deweert, T. M.; Hoekstra, J. W.; Pater, D. *J. Biol. Chem.* **1981**, *256*, 12393. (b) Gladwin, M. T.; Grubina, R.; Doyle, M. P. *Acc. Chem. Res.* **2009**, *42*, 157. (c) Shiva, S.; Huang, Z.; Grubina, R.; Sun, J. H.; Ringwood, L. A.; MacArthur, P. H.; Xu, X. L.; Murphy, E.; Darley-Usmar, V. M.; Gladwin, M. T. *Circ. Res.* **2007**, *100*, 654. (d) Yi, J.; Heinecke, J.; Tan, H.; Ford, P. C.; Richter-Addo, G. B. *J. Am. Chem. Soc.* **2009**, *131*, 18119.

(21) (a) Averill, B. A. *Chem. Rev.* **1996**, 96, 2951. (b) Zumft, W. G. *Microbiol. Mol. Biol. Rev.* **1997**, *61*, 533. (c) Lehnert, N.; Berto, T. C.; Galinato, M. G. I.; Goodrich, L. E. The Role of Heme−Nitrosyls in the Biosynthesis, Transport, Sensing, and Detoxification of Nitric Oxide (NO) in Biological Systems: Enzymes and Model Complexes. In *The Handbook of Porphyrin Science*; Kadish, K. M., Smith, K., Guilard, R., Eds.; World Scientific: Singapore, 2011; Vol. 14, pp 1−247.

(22) (a) Wasser, I. M.; de Vries, S.; Moënne-Loccoz, P.; Schröder, I.; Karlin, K. D. *Chem. Rev.* **2002**, 102, 1201. (b) Merkle, A. C.; McQuarters, A. B.; Lehnert, N. *Dalton Trans.* **2012**, *41*, 8047.

(23) (a) Hsu, S. C. N.; Chang, Y.-L.; Chuang, W.-J.; Chen, H.-Y.; Lin, I. J.; Chiang, M. Y.; Kao, C.-L.; Chen, H.-Y. *Inorg. Chem.* **2012**, *51*, 9297. (b) Kumar, M.; Dixon, N. A.; Merkle, A. C.; Zeller, M.; Lehnert, N.; Papish, E. T. *Inorg. Chem.* **2012**, *51*, 7004.

(24) (a) Nicholls, P.; Wrigglesworth, J. M. *Ann. N.Y. Acad. Sci.* **1988**, 550, 59. (b) Moskovitz, J. *Biochim. Biophys. Acta* **2005**, *1703*, 213.

(c) Gorbikova, E. A.; Vuorilehto, K.; Wikstrom, M.; Verkhovsky, M. I. *Biochemistry* **2006**, *45*, 5641.

(d) Belevich, I.; Bloch, D. A.; Belevich, N.; Wikstrom, M.; Verkhovsky, M. I. *Proc. Natl. Acad. Sci. U.S.A.* **2007**, *104*, 2685. (e) C*c*O metal center redox potentials are highly dependent on the redox states of the other metal cofactors as well as the pH/protonation state.

(25) (a) Tran, D.; Skelton, B. W.; White, A. H.; Laverman, L. E.; Ford, P. C. *Inorg. Chem.* **1998**, 37, 2505. (b) Kalita, A.; Kumar, P.; Deka, R. C.; Mondal, B. *Chem. Commun.* **2012**, *48*, 1251.

5. Supporting Information

5.1. Materials and Methods

Unless otherwise stated all solvents and chemicals used were of commercially available analytical grade. Dichloromethane (CH_2Cl_2), diethyl ether (Et_2O), and methanol (MeOH) were used after passing them through a 60 cm long column of activated alumina (Innovative Technologies, Inc.) under argon. Tetrahydrofuran (THF) and 2-Methyltetrahydrofuran (MeTHF) (Sigma, 673277, inhibitor free) were purified and dried by distillation from sodium/benzophenone ketyl under argon. Pentane and acetonitrile (MeCN) were dried by distillation over calcium hydride and acetone was freshly distilled from Drierite (anhydrous calcium sulfate) under argon prior to use. Dioxygen was dried by passing through a short column of supported P_4O_{10} (Aquasorb, Mallinkrodt). Nitrogen monoxide (NO) gas was obtained from Matheson Gases. Following methods previously described in the literature,1 nitric oxide was purified by passage through a series of two KOH columns and finally distilled at 195 K and then collected in an evacuated Schlenk flask (typically 50 mL) fitted with a septum. Addition of $NO_{(g)}$ to metal complex solutions was effected by transfer via a three-way long syringe needle. Preparation and handling of air sensitive compounds were performed under an argon atmosphere using standard Schlenk techniques or in an MBraun Labmaster 130 inert atmosphere (<1 ppm O_2, <1 ppm H_2O) drybox filled with nitrogen. Deoxygenation of solvents was effected by either repeated freeze/pump/thaw cycles or bubbling with argon for 45 - 60 min.

Elemental analyses were performed by Columbia Analytical Services (Tucson, AZ). UV–vis spectra were recorded on a Cary-50 Bio spectrophotometer equipped with a

fiber optic coupler (Varian). Spectrophotometer cells used were made by Quark Glass with column and pressure/vacuum side stopcock and 1 cm path length. ^{1}H-NMR spectra were acquired using a Bruker 400 MHz spectrometer. Chemical shifts were reported as δ values relative to an internal standard (Me4Si) and the residual solvent proton peak. Electron paramagnetic resonance (EPR) spectra were recorded on a Bruker EMX spectrometer controlled with a Bruker ER 041 X G microwave bridge operating at X-band (~9.4 GHz). Infrared spectra (IR) were obtained using a Thermo Scientific Nicolet Nexus 670 FT-IR spectrophotometer.

X-ray diffraction was performed at the X-ray diffraction facility at the Johns Hopkins University. All reflection intensities were measured at 110(2) K using a KM4/Xcalibur (detector: Sapphire3) with enhance graphite-monochromated Mo *K*α radiation (λ = 0.71073 Å) under the program CrysAlisPro (Versions 1.171.33.31 or 1.171.35.11, Agilent Technologies, 2011). The program CrysAlisPro (Versions 1.171.33.31 or 1.171.35.11, Agilent Technologies, 2011) was used to refine the cell dimensions. Data reduction was done using the program CrysAlisPro (Versions 1.171.33.31 or 1.171.35.11, Agilent Technologies, 2011). The structure was solved with the program SHELXS-97[2] and was refined on F^2 with SHELXL-97.[2] Analytical numeric absorption corrections based on a multifaceted crystal model were applied using CrysAlisPro (Versions 1.171.33.31 or 1.171.35.11, Agilent Technologies, 2011). The temperature of the data collection was controlled using the system Cryojet (manufactured by Oxford Instruments). The H atoms were placed at calculated positions using the instructions AFIX 23 or AFIX 43 with isotropic displacement parameters having values 1.2 times U_{eq} of the attached C atoms. The structure of $[(tmpa)Cu^{II}(Cl)][B(C_6F_5)_4]$ is

ordered. The structure of $[(tmpa)Cu^{II}(NO_2)][B(C_6F_5)_4]$ is found to be mostly ordered; the nitrite ion is disordered over two orientations. The occupancy factor of the major orientation refines to 0.875(5). $[(tmpa)Cu^{II}(Cl)][B(C_6F_5)_4]$, Fw = 1068.40, turquoise blue block, 0.49 × 0.20 × 0.16 mm^3, orthorhombic, *Pbca* (no. 61), a = 13.08228(15), b = 23.1771(3), c = 26.3615(3) Å, V = 7993.05(17) $Å^3$, Z = 8, D_x = 1.776 g cm^{-3}, μ = 0.747 mm^{-1}, abs. corr. range: 0.78−0.90. 50400 Reflections were measured up to a resolution of $(\sin \theta/\lambda)_{max}$ = 0.62 $Å^{-1}$. 7840 Reflections were unique (R_{int} = 0.055), of which 5584 were observed [$I > 2\sigma(I)$]. 622 Parameters were refined. $R1/wR2$ [$I > 2\sigma(I)$]: 0.0305/0.0665. R1/wR2 [all refl.]: 0.0525/0.0699. S = 0.932. Residual electron density found between −0.58 and 0.34 $eÅ^{-3}$. $[(tmpa)Cu^{II}(NO_2)][B(C_6F_5)_4]$, Fw = 1078.96, green block, 0.67 × 0.37 × 0.21 mm^3, orthorhombic, *Pbca* (no. 61), a = 13.3059(2), b = 22.9396(5), c = 26.0492(7) Å, V = 7951.1(3) $Å^3$, Z = 8, D_x = 1.803 g cm^{-3}, μ = 0.692 mm^{-1}, abs. corr. range: 0.711−0.894. 25595 Reflections were measured up to a resolution of $(\sin \theta/\lambda)_{max}$ = 0.62 $Å^{-1}$. 8030 Reflections were unique (R_{int} = 0.0356), of which 6640 were observed [$I > 2\sigma(I)$]. 659 Parameters were refined using 63 restraints. $R1/wR2$ [$I > 2\sigma(I)$]: 0.0317/0.0784. $R1/wR2$ [all refl.]: 0.0428/0.0833. S = 1.034. Residual electron density found between −0.58 and 0.39 e $Å^{-3}$.[2]

A capillary electrophoresis (CE) instrument from Beckman Coulter (P/ACE MDQ, Fullerton, CA) equipped with diode-array UV–vis detector was used to measure nitrite concentrations. Bare fused silica capillary (Polymicro Technologies, Phoenix, AZ) with 75 μm ID × 60 cm total length was used for separation. Capillary and sample board temperature was thermostatted to 25 ^oC during operation. Between experiments, the capillary was sequentially rinsed by flushing distilled, deionized water (DDW) for 0.5

min, 0.1 M NaOH for 1 min, DDW again for 1 min, and capillary electrolyte for 2.5 min. Samples were introduced into the capillary by hydrostatic injection using a pressure of 0.5 psi for 10 s at an applied negative potential of 25 kV, and UV detection at 220 nm. The background electrolyte consisted of 25 mM sodium phosphate (pH 7.0) and 0.5 mM tetradecyltrimethylammonium chloride (TTAC) electroosmotic flow modifier. Cyclic voltammetic measurements were undertaken in acetone solvent under argon at room temperature using a BAS 100B/W electrochemical analyzer with a glassy carbon working electrode and a platinum wire auxiliary electrode. Potentials were recorded versus an $Ag/AgNO_3$ reference electrode. Scans were run at 100 mV/s using ~0.1 M tetrabutylammonium hexafluorophosphate ($(Bu)_4N(PF_6)$) as the supporting electrolyte. The voltammograms are plotted versus the $Fe(Cp)_2^{+/0}$ potential which was measured as an external standard under the same elctrochemical cell conditions.

Tris(2-pyridylmethyl)amine (TMPA),[3] $[(tmpa)Cu^{II}(MeCN)](ClO_4)_2$,[4] $(F_8)Fe^{III}(OH)$,[5] $[(F_8)Fe^{III}(THF)_2](SbF_6)$,[4] $(F_8)Fe^{II}$,[6] and $[H(C_2H_5OC_2H_5)_2][B(C_6F_5)_4]$ (HBArF)[7] were synthesized and characterized following methods previously described in the literature. $[(F_8)Fe^{III}–O–Cu^{II}(tmpa)][B(C_6F_5)_4]$[8] was prepared by bubbling dry dioxygen through the 1:1 solution of $(F_8)Fe^{II}$ and $[(tmpa)Cu^{I}(MeCN)][B(C_6F_5)_4]$ in MeTHF for 2 min and the mixture was allowed to stir for 2 h at RT. The solvent was then removed under vacuum and solid was further dried under vacuum for additional 6 h. $[(F_8)Fe^{III}\text{-}(OH)\text{-}Cu^{II}(tmpa)][B(C_6F_5)_4]_2$[8] was synthesized by addition of 1 equiv HBArF to the $[(F_8)Fe^{III}–O–Cu^{II}(tmpa)][B(C_6F_5)_4]$ in MeTHF and solution was stirred for 10 min and then dried under vacuum for several hours.

5.2. Synthesis and Characterization of Copper Complexes

Synthesis of [(tmpa)Cu^{II}(Cl)][B(C$_6$F$_5$)$_4$]: $CuCl_2.2H_2O$ (171 mg, 1.00 mmol) and tmpa (290 mg, 1.00 mmol) were dissolved in 10 mL of MeCN followed by addition of five drops of water to form a clear blue solution. After stirring for 5 min, $K[B(C_6F_5)_4]$ (718 mg, 1.00 mmol) was added to the reaction mixture, causing a white precipitate to form. The reaction mixture was concentrated to dryness under reduced pressure leaving a crude residue, which was redissolved in diethyl ether, filtered, giving a turquoise blue solution. The solvent was then removed under reduced pressure and recrystallization of the resulting soild from hot MeOH/water afforded turquoise blue good-quality crystals suitable for X-ray structure determination. After vacuumdrying the crystals weighed 887 mg (83% yield). Anal. Calcd for $C_{42}H_{18}BClCuF_{20}N_4$: C, 47.22; H, 1.70; N, 5.24. Found: C, 47.43; H, 2.11; N, 5.03. UV–vis spectrum (Figure S1) in acetone (λ_{max}, nm (ε_{max}, $M^{-1}cm^{-1}$)): 961 (205); 745 (90, sh). EPR spectrum (Figure S2): X-band spectrometer (ν = 9.428 GHz) in MeTHF at 21 K: $g_{\|} \approx 2.004$, $A_{\|} \approx 70$ G, $g_{\perp} = 2.190$, $A_{\perp} = 96$ G. These data are typical for trigonal bipyramidal copper(II) structures.[10]

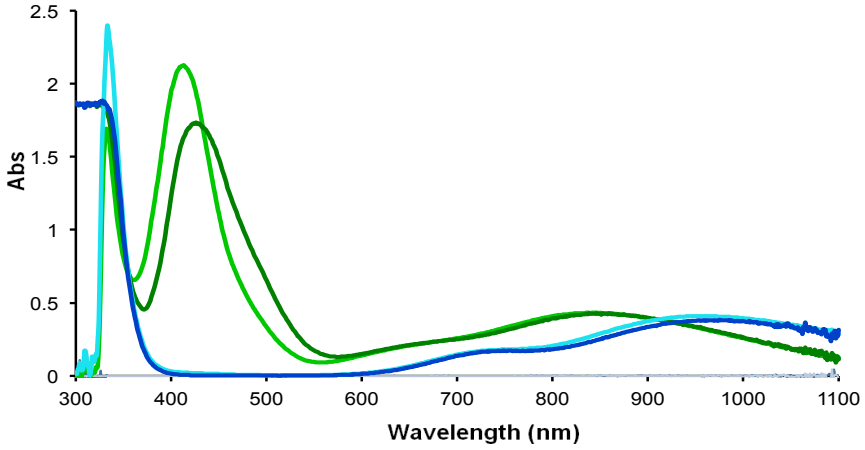

Figure S1. UV–vis spectra of [(tmpa)Cu^{II}(Cl)][B(C$_6$F$_5$)$_4$] in acetone (cyan) in MeTHF (dark blue) and [(tmpa)Cu^{II}(NO$_2$)][B(C$_6$F$_5$)$_4$] in acetone (light green, λ_{max} = 413 nm) in MeTHF (dark green, λ_{max} = 427 nm) (2mM).

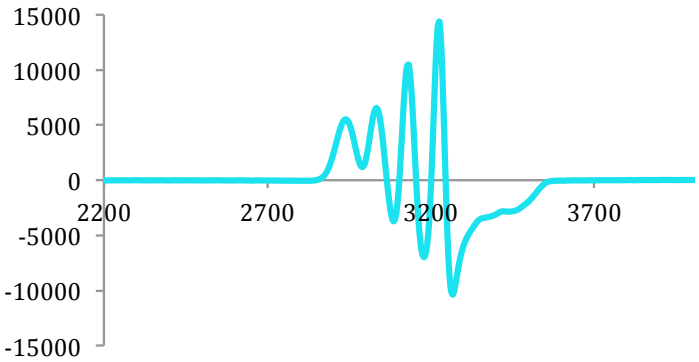

Figure S2. EPR spectrum of $[(tmpa)Cu^{II}(Cl)][B(C_6F_5)_4]$ (2mM) in MeTHF at 20 K.

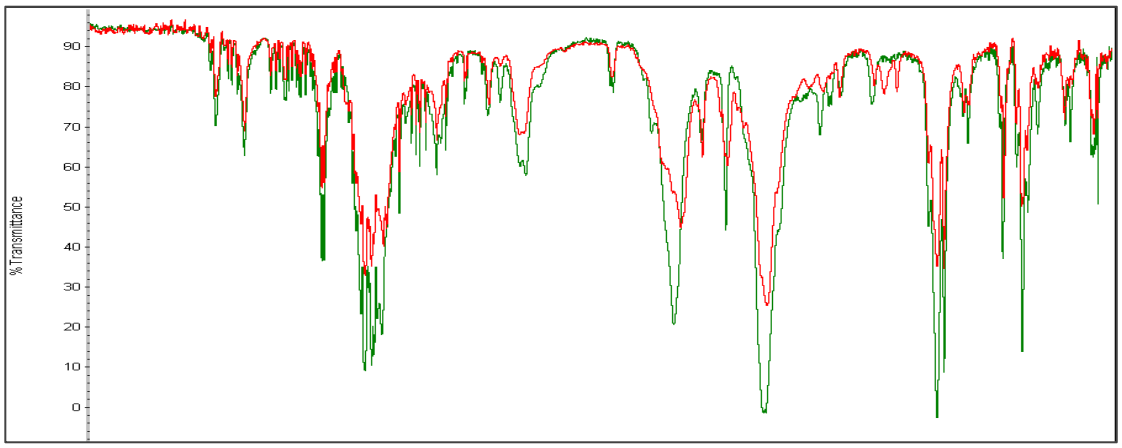

Figure S3. IR spectra (solid) comparison between the two Cu^{II} complexes: $[(tmpa)Cu^{II}(Cl)][B(C_6F_5)_4]$ (green) $[(tmpa)Cu^{II}(NO_2)][B(C_6F_5)_4]$ (red).

Crystal Structure of [(tmpa)Cu^{II}(Cl)][B(C$_6$F$_5$)$_4$]: A displacement ellipsoid plot (50% probability level) of the cationic fragment, $[(tmpa)Cu^{II}(Cl)]^+$, is presented in Figure S4. The structure is five-coordinate, with ligation to the three pyridyl and single aliphatic nitrogen atoms of the ligand (N(1), N(2), N(3) and N(4)), accompanied by an interaction of the cupric ion with the chloride ion (Cl1). Selected bond distances and angles are given in the Figure S4 caption. The geometry about the copper atom is trigonal bipyramidal (τ = 1)11 with the amine nitrogen N(2) and chloride ion occupying the axial positions and

the pyridyl nitrogens (N(1), N(3), N(4)) in the trigonal plane.

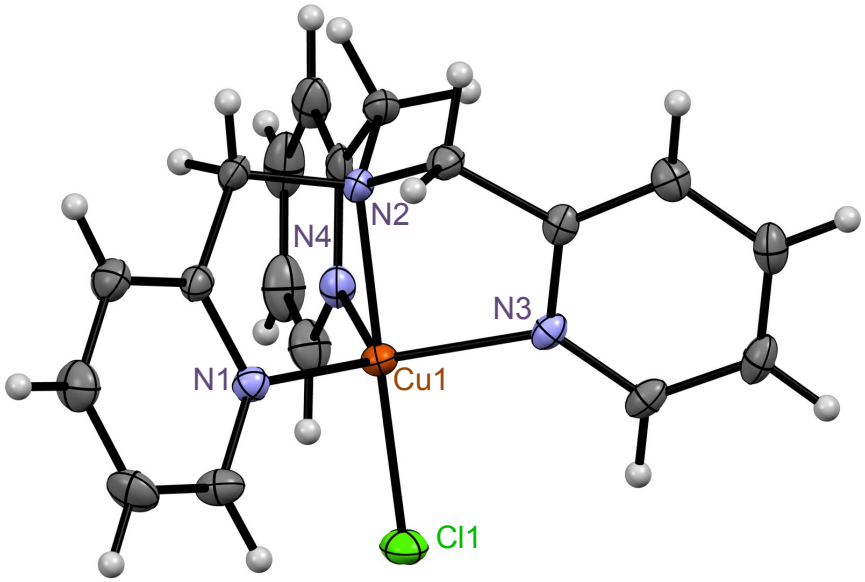

Figure S4. Displacement ellipsoid plot (50% probability level) of $[(tmpa)Cu^{II}(Cl)]^{+}$, showing the atom-labeling scheme. Relevant bond lengths (Å) and angles (deg): Cu–N(1), 2.074 (2); Cu-N(2), 2.045 (1); Cu–N(3), 2.078 (2); Cu–N(4), 2.052 (6); Cu–Cl(1), 2.221 (9); N(2)–Cu–N(4), 81.3 (8); N(2)–Cu–N(1), 81.0 (3); N(2)–Cu–N(3), 81.7 (1); N(4)–Cu–N(1), 121.5 (1); N(4)–Cu–N(3), 118.3 (7); N(1)–Cu–N(3), 113.4 (7); N(2)–Cu–C1(1), 178.3 (2); N(4)–Cu–Cl(1), 97.2 (1); N(1)–Cu–C1(1), 100.5 (1); N(3)–Cu–C1(1), 98.2 (1).

Synthesis of [(tmpa)Cu^{II}(NO$_2$)][B(C$_6$F$_5$)$_4$]: Silver nitrite (77 mg, 0.50 mmol) was added to $[(tmpa)Cu^{II}(Cl)][B(C_6F_5)_4]$ (534 mg, 0.50 mmol) in 10 mL of methanol resulting a green solution and precipitation of AgCl. The reaction mixture was sonicated for 5 min, and followed by filtration. Then, the filtrate was heated and gently recrystallized by slow addition of water yielding 421 mg (78%) of green crystals. Anal. Calcd for $C_{42}H_{18}BCuF_{20}N_5O_2$: C, 46.75; H, 1.68; N, 6.49. Found: C, 46.93; H, 2.25; N, 6.21. UV–vis spectrum (Figure S1) in acetone (λ_{max}, nm (ε_{max}, $M^{-1}cm^{-1}$)): 843 (216); 413 (1156) (A small bathochromic shift was observed for the latter spectral band in MeTHF (λ_{max} = 427 nm)). EPR spectrum (Figure S5): X-band spectrometer (ν = 9.426 GHz) in

MeTHF at 21 K: $g_{\|} = 1.992$, $A_{\|} = 84$ G, $g_{\perp} = 2.200$, $A_{\perp} = 102$ G. FT-IR spectrum (solid) (Figure S3): $\nu_{(N=O)} = 1435$, $\nu_{(N-O)} = 1076$, and $\delta_{(NO2)} = 813$ and 829 cm^{-1}. The infrared spectrum of $[(tmpa)Cu^{II}(NO_2)][B(C_6F_5)_4]$ is mainly characterized by the nitrite ligand vibrations. Although nitrite vibrations can only be assigned certainly by isotope labeling, they are tentatively attributed here through the spectra differences between $[(tmpa)Cu^{II}(NO_2)][B(C_6F_5)_4]$ and its chloride precursor.

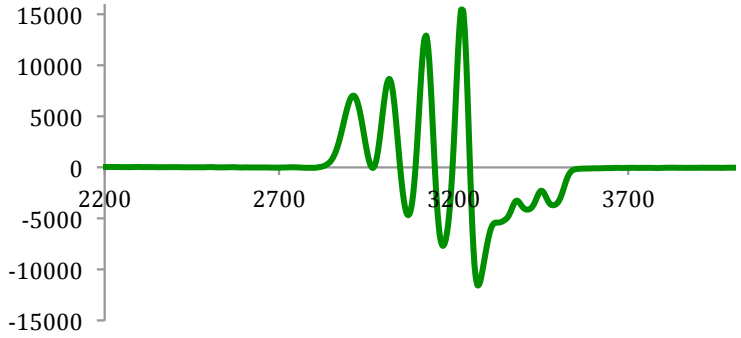

Figure S5. EPR spectrum of $[(tmpa)Cu^{II}(NO_2)][B(C_6F_5)_4]$ (2mM) in MeTHF at 20 K.

Crystal Structure of $[(tmpa)Cu^{II}(NO_2)][B(C_6F_5)_4]$***:*** The structure consists of isolated $[(tmpa)Cu^{II}(NO_2)]^+$ cations and $[B(C_6F_5)_4]^-$ counter anions. The copper centers are penta-coordinated by the *N*-donor atoms of tris(2-pyridylmethyl)amine ligand, and O(1) of a monodentate nitrito ligand. The structure of $[(tmpa)Cu^{II}(NO_2)]^+$ is, therefore, approximated by a trigonal bipyramidal geometry ($\tau = 0.9$), as shown by the data in Figure S6.

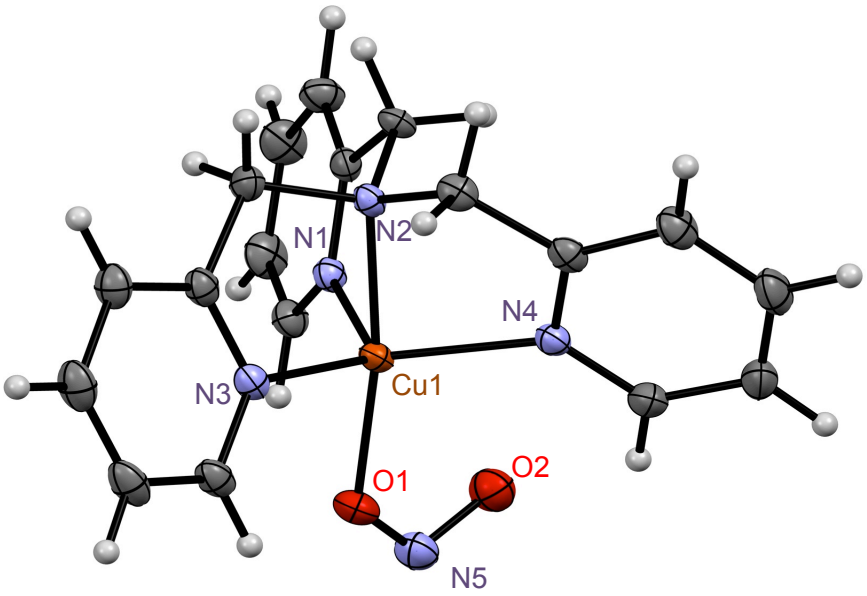

Figure S6. Displacement ellipsoid plot (50% probability level) of $[(tmpa)Cu^{II}(NO_2)]^+$, showing the atom-labeling scheme. The disorder observed for the nitrite ligand is not shown for the sake of clarity. Relevant bond lengths (Å) and angles (deg): Cu–N(1), 2.058 (2); Cu–N(2), 2.039 (9); Cu–N(3), 2.063 (5); Cu–N(4), 2.100 (7); Cu–O(1), 1.930 (9); O(1)–Cu–N(2), 170.6 (7); O(l)–Cu–N(1), 99.2 (0); N(2)–Cu–N(1), 81.3 (7); O(l)–Cu–N(3), 90.6 (9); N(2)–Cu–N(3), 81.0 (5); N(1)–Cu–N(3), 119.6 (6); O(1)–Cu–N(4), 107.3 (0); N(2)–Cu–N(4), 80.5 (2); N(1)–Cu–N(4), 115.9 (6); N(3)–Cu–N(4), 117.1 (5).

Synthesis of [(tmpa)Cu^I(MeCN)][B(C$_6$F$_5$)$_4$]: This synthesis followed a procedure similar to that reported earlier for a number of cuprous pyridyl-alkylamine compounds.[3,11] In a 100 ml Schlenk flask located in the drybox, 625 mg (0.69 mmol) of $[Cu^I(MeCN)_4][B(C_6F_5)_4]$[12] was dissolved in 7 ml THF. 200 mg (0.69 mmol) of tmpa ligand dissolved in approximately 3 ml of THF was added to the copper solution, resulting in an immediate color change from colorless to red-orange. This solution was allowed to stir for 25 min followed by addition of 60 ml of deoxygenated pentane to the solution resulting precipitation. The supernatant was decanted and the compound obtained was recrystallized from THF/Pentane. The precipitate formed was dried under vacuum to afford 642 mg of a bright yellow-orange solid. (87% yield). ^{1}H-NMR

(CD_3CN, 400 MHz; δ, ppm): 8.95 (br, 3H), 7.83 (m, 3H), 7.49 (br, 6H), 4.30 (vbr, 6H), 2.02 (s, 3H, CH_3CN).

5.3. Reaction of 2 $(F_8)Fe^{II}$ with $[(tmpa)Cu^{II}(NO_2)][B(C_6F_5)_4]$

In the drybox, $(F_8)Fe^{II}$ (10.0 mg, 0.012 mmol) was dissolved in 50 mL acetone in a 100 mL Schlenk flask equipped with a magnetic stir bar. Then $[(tmpa)Cu^{II}(NO_2)][B(C_6F_5)_4]$ (6.6 mg, 0.006 mmol) was added to the solution and after stirring for 1 h, the solvent was removed to yield a brown solid. During the reaction, 305 μL aliquots were withdrawn by syringe every 10 min, diluted with acetone to 5.0 mL, and a UV–vis spectrum was recorded (Figure S7). The formation of 1:1 mixture of the $(F_8)Fe^{II}(NO)$ and the μ-oxo complex $[(F_8)Fe^{II}–O–Cu^{II}(tmpa)]^+$ was observed based on UV–vis spectrum{λ_{max} = 399 and 435 (Soret), 555 nm}; these spectral parameters matched those of previous reports for these products. The EPR spectrum of the product mixture (Figure S8) gave signals for $(F_8)Fe^{II}(NO)$ which has a distinctive three-line hyperfine splitting and was consistent with the presence of a 1:1 mixture of $(F_8)Fe^{II}(NO)$ and $[(F_8)Fe^{III}–O–Cu^{II}(tmpa)]^+$; the latter is an EPR-silent species. EPR quantification in acetone at 20 K, employing authentic $[(tmpa)Cu^{II}(MeCN)](ClO_4)_2$ and $(F_8)Fe^{III}(OH)$ separately revealed the presence of trace amounts (< 5%) of free Cu^{II} and Fe^{III} species suggesting that majority of Cu^{II} and Fe^{III} ions were converted to the μ-oxo complex, i.e. one equiv Fe^{III} was produced corresponding to one equiv nitrite reduced. In addition, the IR spectrum of the solid product (Figure S9) displayed a N–O stretching frequency at 1688 cm^{-1} due to formation of $(F_8)Fe^{II}(NO)$. Similar reaction products were obtained

when instead $(Bu)_4N(NO_2)$ as nitrite source was used to carry out the reaction. In this reaction, 1 equiv tetrabutylammonium nitrite ($(Bu)_4N(NO_2)$) was added to the solution of $[(tmpa)Cu^{II}(MeCN)](ClO_4)_2$ in acetone and an immediate color change from blue to green was observed upon addition indicating rapid coordination of nitrite to Cu^{II} ion. The resulting green solution was then added to the solution of 2 equiv $(F_8)Fe^{II}$ in acetone followed by stirring for 1 h. The formation of the similar 1:1 product mixture of $(F_8)Fe^{II}(NO)$ and $[(F_8)Fe^{III}–O–Cu^{II}(tmpa)]^+$ was confirmed by UV–vis, EPR, and IR spectroscopies.

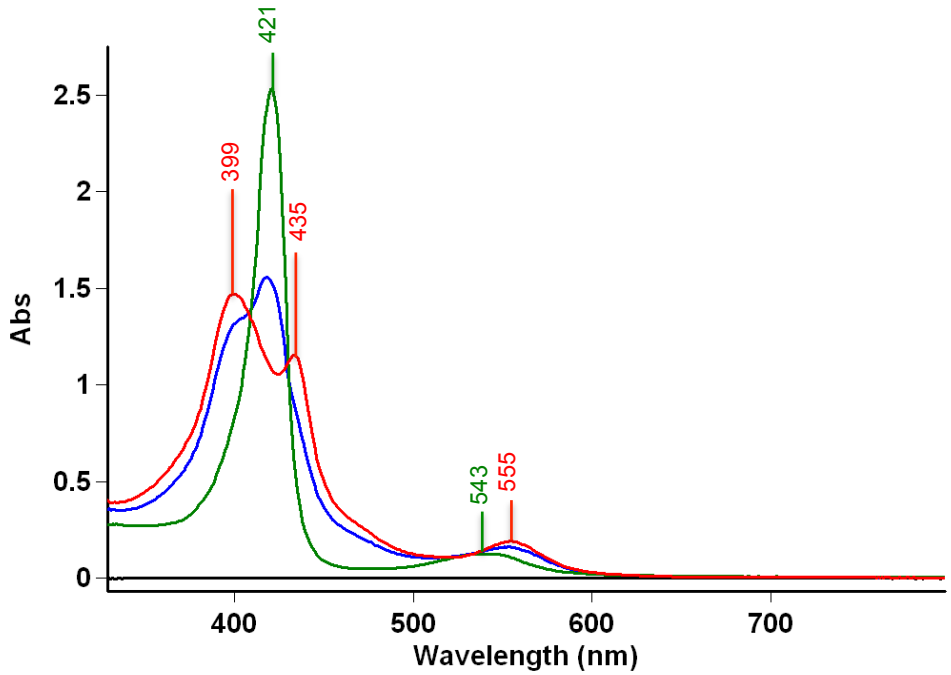

Figure S7. UV–vis spectra of $(F_8)Fe^{II}$ (10 μM) (green, λ_{max} = 421 (Soret), 543 nm) and reaction solution of $(F_8)Fe^{II}$ and ½$[(tmpa)Cu^{II}(NO_2)][B(C_6F_5)_4]$ after stirring for 10 min (15 μM) (blue) and 1 h (15 μM) (red, λ_{max} = 399, 435 (Soret), 555 nm) in acetone at RT.

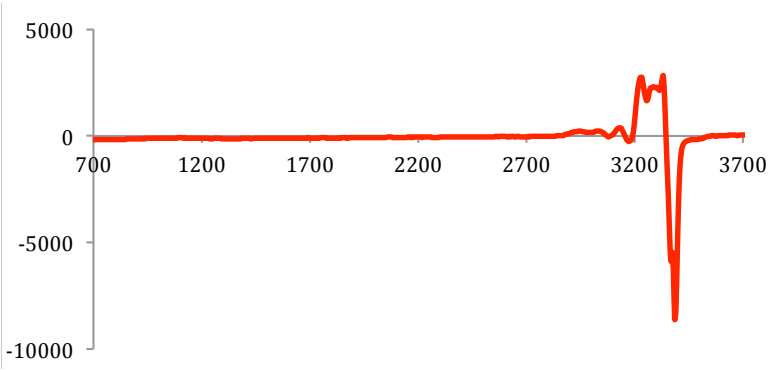

Figure S8. EPR spectrum of the reaction solution of $(F_8)Fe^{II}$ and ½[(tmpa)$Cu^{II}(NO_2)$][$B(C_6F_5)_4$] (2mM) in acetone at 20 K.

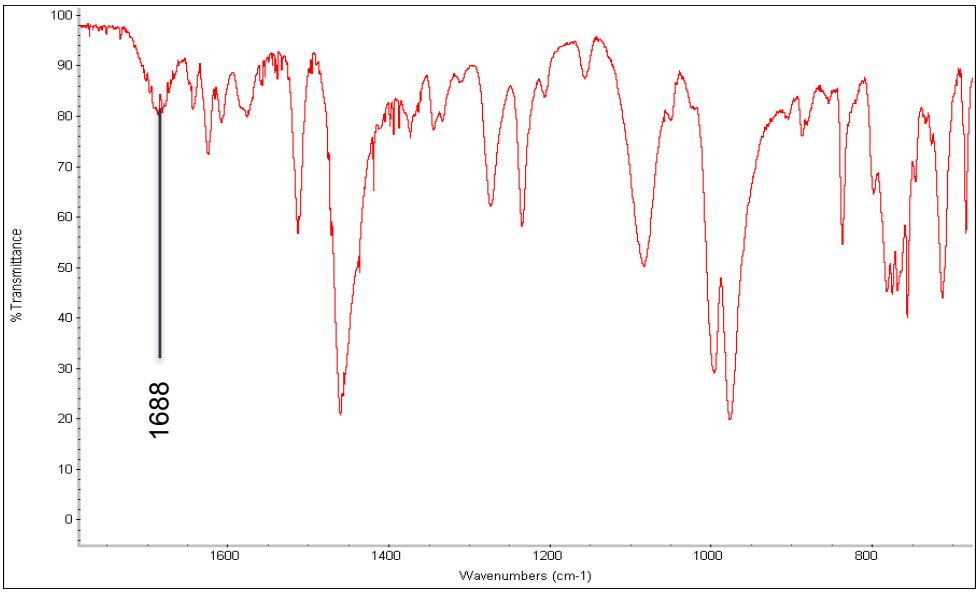

Figure S9. IR spectrum of the solid product of the reaction of $(F_8)Fe^{II}$ and ½[(tmpa)$Cu^{II}(NO_2)$]-[$B(C_6F_5)_4$].

5.4. Reaction of [$(F_8)Fe^{III}(THF)_2$](SbF_6) and Nitrite with [(tmpa)Cu^{I}(MeCN)]-[$B(C_6F_5)_4$]

[$(F_8)Fe^{III}(THF)_2$](SbF_6) (14.7 mg, 0.012 mmol) was dissolved in 50 mL deoxygenated acetone in a 100 mL Schlenk flask equipped with a magnetic stir bar.

$(Bu)_4N(NO_2)$ (3.6 mg, 0.012 mmol) was added to the solution resulting in a large UV–vis change assigned to the formation of $(F_8)Fe^{III}(NO_2)$ {λ_{max} = 405 (Soret), 567 nm} (Figure S10). After stirring for 10 min, reduced complex $[(tmpa)Cu^{I}(MeCN)][B(C_4F_6)_4]$ (13.2 mg, 0.012 mmol) was added to the solution and stirred for several hours. UV–vis spectra showed no significant change even after stirring for days. In order to prepare UV–vis samples, 305 µL aliquots were withdrawn by syringe and diluted with acetone to 5.0 mL (15 µM). UV–vis spectra showed no significant change even after stirring for days indicating no nitrite reduction proceeded (Figure S10).

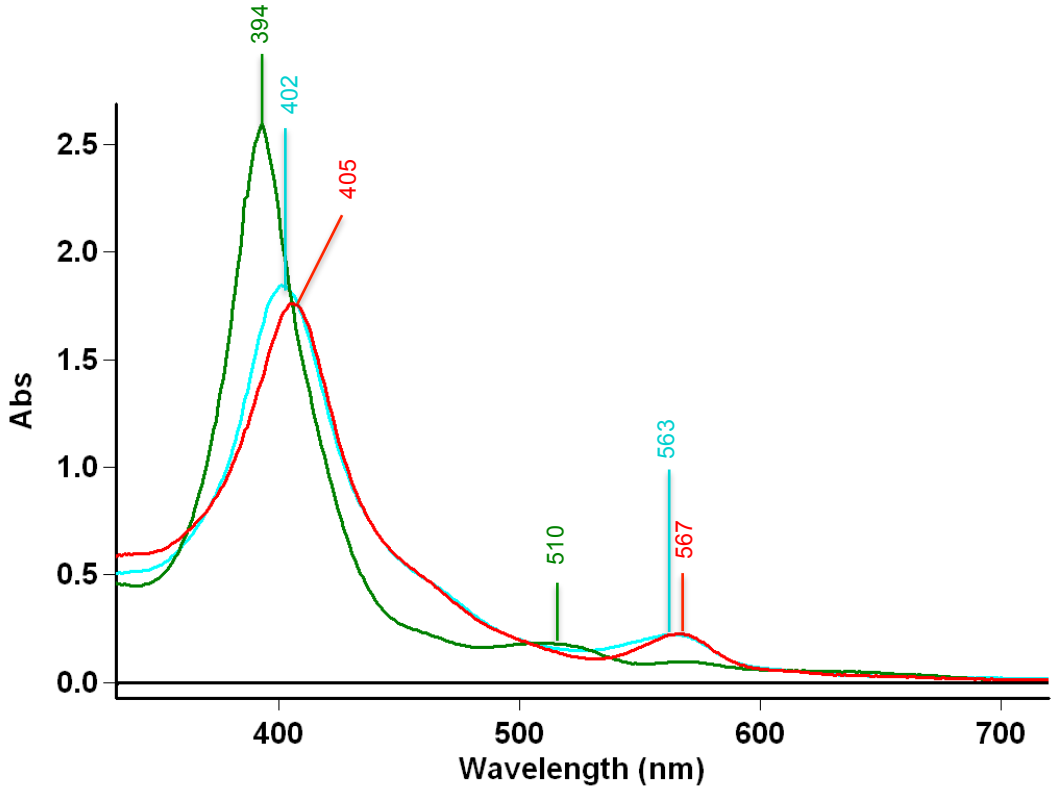

Figure S10. UV–vis spectra of $[(F_8)Fe^{III}(THF)_2](SbF_6)$ (green, λ_{max} = 394 (Soret), 510 nm) and $(F_8)Fe^{III}(NO_2)$ obtained by addition of 1 equiv $(Bu)_4N(NO_2)$ to solution of $[(F_8)Fe^{III}(THF)_2](SbF_6)$ (red, λ_{max} = 405 (Soret), 567 nm) followed by addition of 1 equiv $[(tmpa)Cu^{I}(MeCN)][B(C_6F_5)_4]$ (cyan, λ_{max} = 402 (Soret), 563 nm) 15 µM in acetone at RT.

5.5. Reaction of $(F_8)Fe^{II}$ with Nitrite

In the drybox, to a 25 mL acetone solution of $(F_8)Fe^{II}$ (10.0 mg, 0.012 mmol), $(Bu)_4N(NO_2)$ (3.6 mg, 0.012 mmol) was added. The mixture was stirred for several hours, without any significant color or UV–vis absorbance changes (Figure S11) indicating that nitrite reacts only very slowly with $(F_8)Fe^{II}$ in the absence of Cu^{II} as a Lewis Acid.

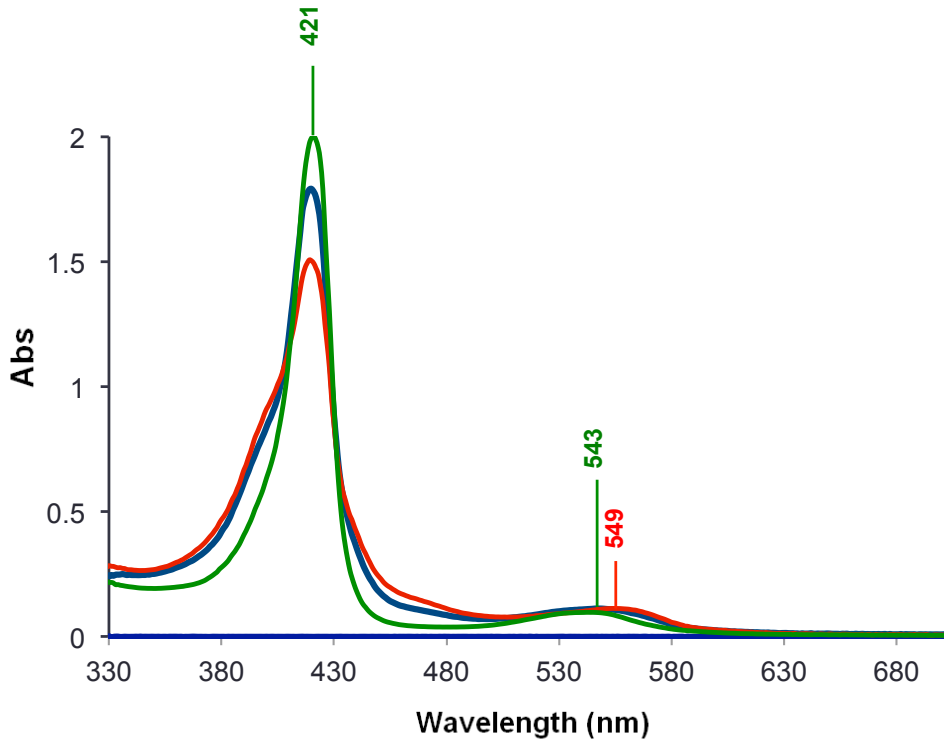

Figure S11. UV–vis spectra of $(F_8)Fe^{II}$ (green, λ_{max} = 421 (Soret), 543 nm) and the reaction solution of $(F_8)Fe^{II}$ and 1 equiv of $(Bu)_4N(NO_2)$ after stirring for 1 h (blue) for 5 h (red, λ_{max} = 421 (Soret), 549 nm) 10 μM in acetone at RT.

5.6. Reaction of $[(tmpa)Cu^{I}(MeCN)][B(C_6F_5)_4]$ with Nitrite

In the drybox, to a 25 mL acetone solution of $[(tmpa)Cu^{I}(MeCN)][B(C_6F_5)_4]$ (13.2 mg, 0.012 mmol), $(Bu)_4N(NO_2)$ (3.6 mg, 0.012 mmol) was added and the reaction

mixture was allowed to stir for 2 days, with the color turning from bright yellow to yellow probably caused by generation of *N*-bound nitro-Cu^{I} complex. UV–vis spectra showed no absorbance in the 500–1100 nm range (Figure S12), and along with an EPR silent spectrum (acetone, 20 K), no occurrence of a redox reaction is indicated.

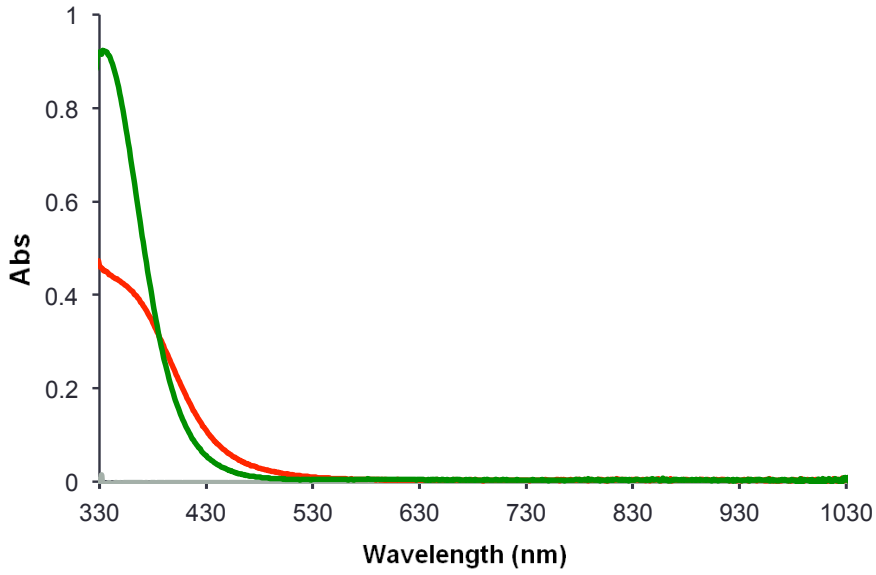

Figure S12. UV–vis spectra of [(tmpa)Cu^{I}(MeCN)][$B(C_6F_5)_4$] (green) and the reaction solution of [(tmpa)Cu^{I}(MeCN)][$B(C_6F_5)_4$] and 1 equiv of $(Bu)_4N(NO_2)$ after stirring for 2 days (red) in acetone at RT.

5.7. Reaction of $(F_8)Fe^{II}$ and [(tmpa)Cu^{I}(MeCN)][$B(C_6F_5)_4$] with Nitrite

To a 25 mL acetone solution of F8FeII (10.0 mg, 0.012 mmol), [(tmpa)Cu^{I}(MeCN)][$B(C_6F_5)_4$] (13.2 mg, 0.012 mmol) was added. The solution was stirred for 10 min, and then $(Bu)_4N(NO_2)$ (7.1 mg, 0.024 mmol) was introduced. A UV–vis spectrum was recorded after stirring for several hours and no significant absorbance change was observed (Figure S13). There was no detectable redox reaction occurring between nitrite and fully reduced complexes at RT under anaerobic conditions

even after several hours, based on the UV–vis spectroscopic monitoring.

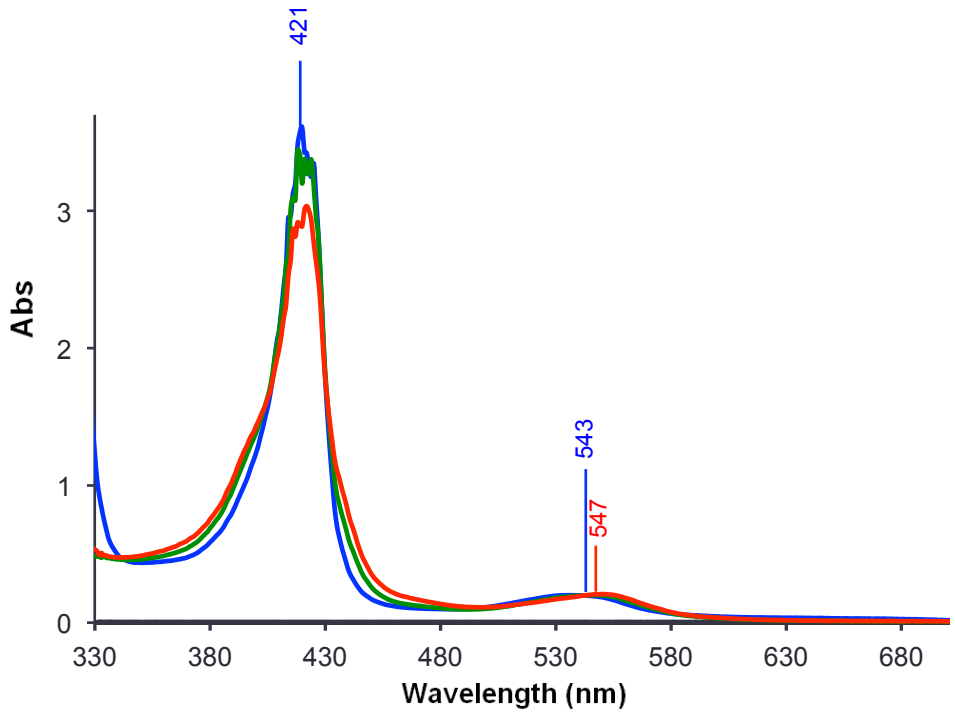

Figure S13. UV–vis spectra of $(F_8)Fe^{II}$ and $[(tmpa)Cu^{I}(MeCN)][B(C_6F_5)_4]$ (blue, λ_{max} = 421 (Soret), 543 nm) followed by addition of 1 equiv of $(Bu)_4N(NO_2)$ after stirring for 30 min (green) for 3 h (red, λ_{max} = 421 (Soret), 547 nm) (15 μM) in acetone at RT.

5.8. Reaction of $[(F_8)Fe^{III}–O–Cu^{II}(tmpa)][B(C_6F_5)_4]$ with $NO_{(g)}$

In a 25 mL-Schlenk flask equipped with a magnetic stir bar was added in the drybox $(F_8)Fe^{II}$ (12 mg, 0.015 mmol) and $[(tmpa)Cu^{I}(MeCN)][B(C_6F_5)_4]$ (16 mg, 0.015 mmol). Addition of 10 mL MeTHF resulted in the formation of an intense red solution, which was then bubbled with dry dioxygen to generate $[(F_8)Fe^{III}–O–Cu^{II}(tmpa)][B(C_6F_5)_4]$. The mixture was allowed to stir for 1 h and the solvent was removed under vacuum. The solid product was then redissolved in 10 mL deoxygenated acetone and 34 μL of the solution was diluted with acetone to 5.0 mL, and a UV–vis

spectrum was recorded. Then 2 mL of $NO_{(g)}$ was bubbled through this solution, and the UV–vis spectrum (Figure S14) showed the fast formation of $(F_8)Fe^{II}(NO)$ {λ_{max} = 399 (Soret), 540 nm}. Another UV–vis sample was prepared and only 1 mL of $NO_{(g)}$ was directly bubbled into the solution resulting in a slower disappearance of $[(F_8)Fe^{III}–O–Cu^{II}(tmpa)][B(C_6F_5)_4]$ {λ_{max} = 435 (Soret), 555 nm} followed by formation of $(F_8)Fe^{II}(NO)$ {λ_{max} = 399 (Soret), 540 nm} (Figure S15). The IR spectrum of the solid sample (ν_{NO} = 1688 cm^{-1}) directly indicates nitrosyl complex, $(F_8)Fe^{II}(NO)$ formation. An EPR spectrum (Figure S16) in acetone at 20 K revealed a mixture of Cu^{II} and heme-Fe-NO compounds. A sample (1 mM) of the reaction product of reaction of $[(F_8)Fe^{III}–O–Cu^{II}(tmpa)][B(C_6F_5)_4]$ and $NO_{(g)}$ in acetone at 20 K was identical in all regards to that of an authentic sample of a 1:1 mixture of $(F_8)Fe^{II}(NO)$ and $[(tmpa)Cu^{II}(NO_2)][B(C_6F_5)_4]$ (1 mM in acetone at 20 K), see Figure S16.

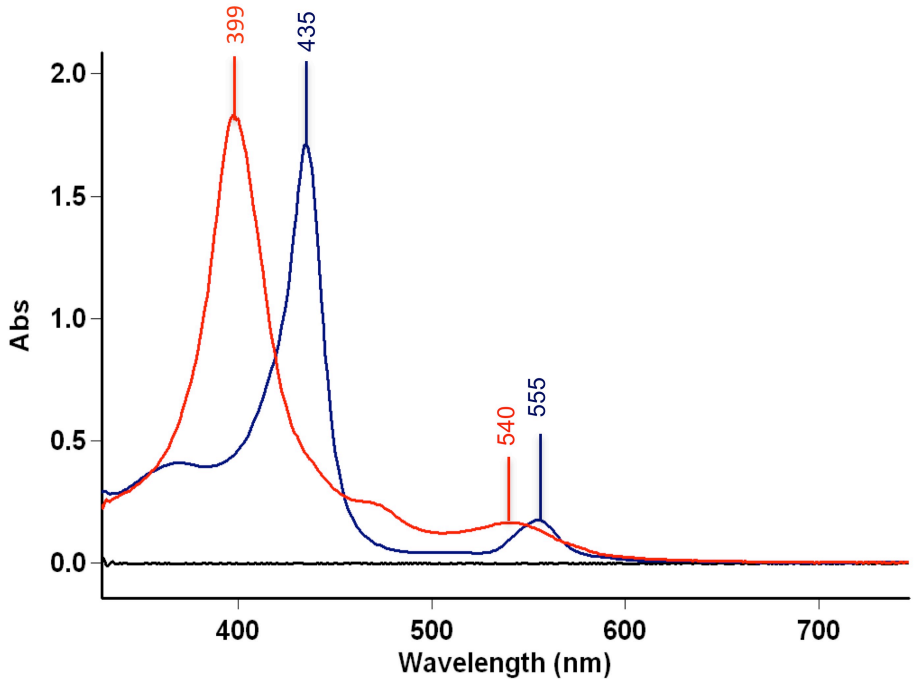

Figure S14. UV–vis spectra of $[(F_8)Fe^{III}–O–Cu^{II}(tmpa)][B(C_6F_5)_4]$ (1, blue), $(F_8)Fe^{II}(NO)$ (red) generated from 1 + 2 mL of $NO_{(g)}$ (12 μM) in acetone at RT.

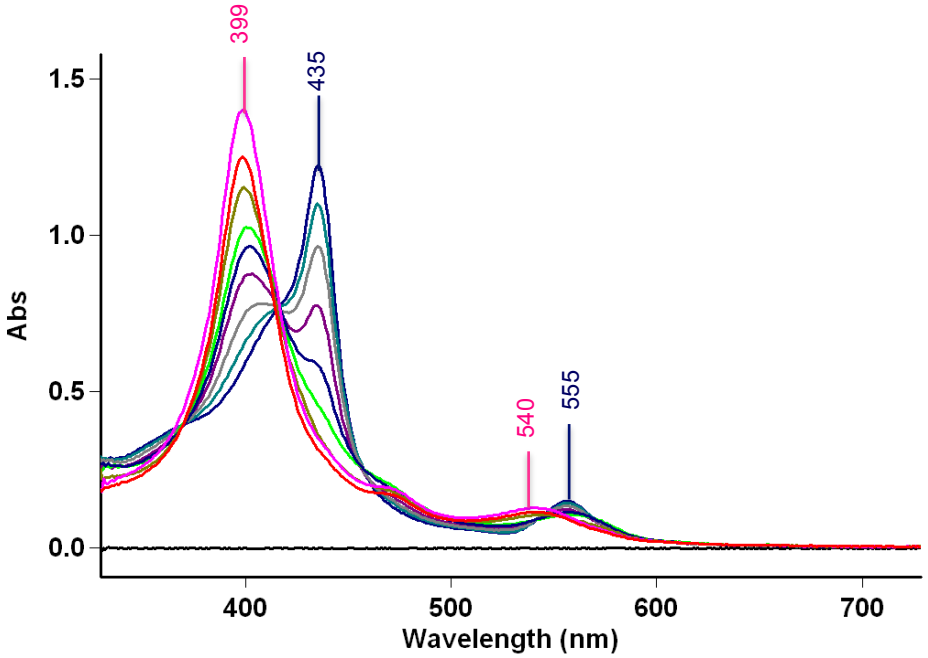

Figure S15. UV–vis spectra of $[(F_8)Fe^{III}–O–Cu^{II}(tmpa)][B(C_6F_5)_4]$ (1, blue), $(F_8)Fe^{II}(NO)$ (red) generated from 1 + 1 mL of $NO_{(g)}$ (the time intervals between two consecutive spectra (Δt) were approximately 1, 2, 1.5, 1.5, 2, 6, and 16 minutes respectively). Addition of a second mL of $NO_{(g)}$ to the solution resulted in completion of the reaction (purple) (10 μM) in acetone at RT.

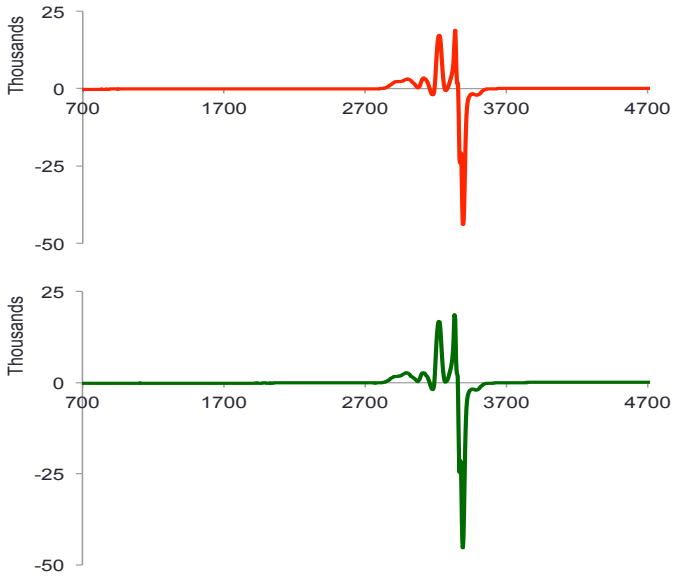

Figure S16. EPR spectrum comparison between the reaction product and an authentic sample: the products of the reaction between $[(F_8)Fe^{III}–O–Cu^{II}(tmpa)][B(C_6F_5)_4]$ and $NO_{(g)}$, giving signals of $(F_8)Fe^{II}(NO)$) and Cu^{II} (red); an authentic sample of a 1:1 mixture of $(F_8)Fe^{II}(NO)$ and $[(tmpa)Cu^{II}(NO_2)][B(C_6F_5)_4]$ (green) (1 mM) in MeTHF at 20 K.

5.9. Titration of the Product of Reaction of $[(F_8)Fe^{III}–O–Cu^{II}(tmpa)][B(C_6F_5)_4]$ with $NO_{(g)}$

The product mixture, $(F_8)Fe^{II}(NO)$ and $[(tmpa)Cu^{II}(NO_2)]^+$ (11.8 mg, 0.006 mmol), derived from reaction of $[(F_8)Fe^{III}–O–Cu^{II}(tmpa)][B(C_6F_5)_4]$ (11.4 mg, 0.006 mmol) with excess $NO_{(g)}$ (see above), was dissolved in 25 mL of deoxygenated acetone inside the drybox. To generate a 10 μM UV–vis sample, a 203 μL aliquot was withdrawn by syringe and diluted with acetone to 5.0 mL and UV–vis spectrum was recorded (λ_{max} = 399 (Soret), 540 nm). Then, $(F_8)Fe^{II}$ (10.0 mg, 0.012 mmol) was added to the product solution and the solution mixture was diluted with acetone to 50 mL and stirred for 30 min. A UV–vis spectrum (Figure S17) of the resulting solution revealed the presence of a nearly 2:1 mixture of $(F_8)Fe^{II}(NO)$ (λ_{max} = 399 nm) and $[(F_8)Fe^{III}–O–Cu^{II}(tmpa)]^+$ (435 nm, sh).

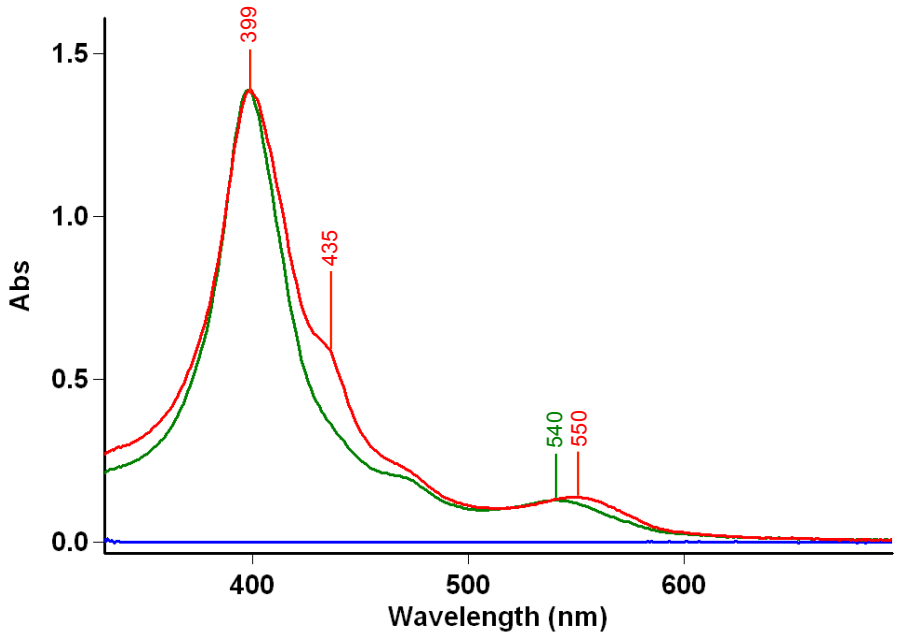

Figure S17. UV–vis spectra of $(F_8)Fe^{II}(NO)$ and $[(tmpa)Cu^{II}(NO_2)][B(C_6F_5)_4]$, derived from the reaction of $[(F_8)Fe^{III}–O–Cu^{II}(tmpa)][B(C_6F_5)_4]$ with excess $NO_{(g)}$ (10 μM) (green, λ_{max} = 399, 540 nm), followed by addition of 2 equiv of F_8Fe^{II} after stirring for 30 min (red, λ_{max} = 399, 435(sh) (Soret), 550 nm) (15 μM based on hemes present in the solution) in acetone at RT.

5.10. Reaction of $[(F_8)Fe^{III}\text{-}(OH)\text{-}Cu^{II}(tmpa)][B(C_6F_5)_4]_2$ with $NO_{(g)}$

In the drybox, to a 10 mL MeTHF solution of $[(F_8)Fe^{III}–O–Cu^{II}(tmpa)][B(C_6F_5)_4]$ (32.0 mg, 0.017 mmol), 1 equiv HBArF (14.3 mg, 0.017 mmol) was added. After stirring for 1 h, solvent was removed under re- duced pressure, and a brown solid was redissolved in acetone and a UV–vis spectrum revealed the formation of $[(F_8)Fe^{III}\text{-}(OH)\text{-}Cu^{II}(tmpa)][B(C_6F_5)_4]_2$. Then 3.5 mL of $NO_{(g)}$ was bubbled through this solution; no significant absorbance change was detected in UV–vis spectrum of the resulting solution, see Figure S18. After several hours of stirring formation of $(F_8)Fe^{II}(NO)$ was observed due to the well-known reductive nitrosylation reaction. Then, the solvent was removed and the solid product obtained was used for nitrite analysis, however, no nitrite ion was detected (see below for sample preparation for nitrite analysis).

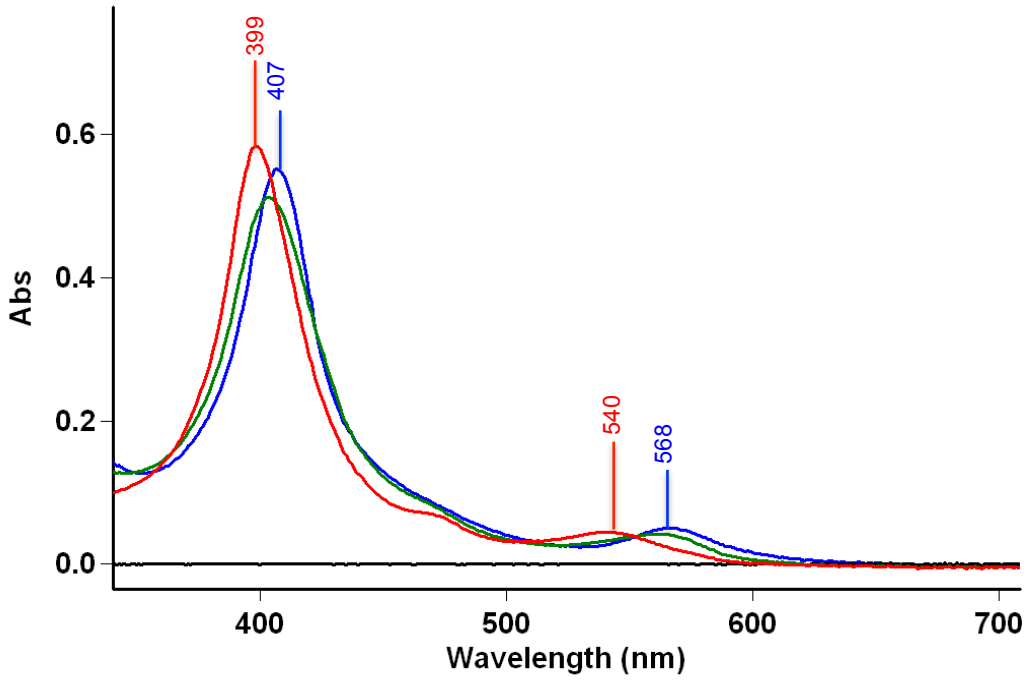

Figure S18. UV–vis spectra of $[(F_8)Fe^{III}\text{-}(OH)\text{-}Cu^{II}(tmpa)][B(C_6F_5)_4]_2$ (blue, λ_{max} = 407 (Soret), 568 nm) and after bubbling 5 mL $NO_{(g)}$ into the solution and stirring for 20 min (green, λ_{max} = 405 (Soret), 565 nm) after stirring for 5 h generating $(F_8)Fe^{III}(NO)$ (red, λ_{max} = 399 (Soret), 540 nm), 7 μM in acetone at RT.

5.11. Reaction of $(F_8)Fe^{III}(OH)$ with $NO_{(g)}$

In a 50 mL-Schlenk flask equipped with a magnetic stir bar, $(F_8)Fe^{III}(OH)$ (30 mg, 0.036 mmol) was dissolved in 25 mL acetone in the drybox. Then 5 mL $NO_{(g)}$ was bubbled through this solution using a three-way syringe. After stirring for several hours, the solvent was removed under reduced pressure and solid product was redissolved in 10 mL CH_2Cl_2 and nitrite analysis of an aqueous solution derived from the reaction mixture indicated no trace of nitrite was present. UV–vis monitoring of the reaction mixture indicated only a very slow (hours) reductive nitrosylation occurred where the heme present was converted to $(F_8)Fe^{II}(NO)$, see Figure S19.

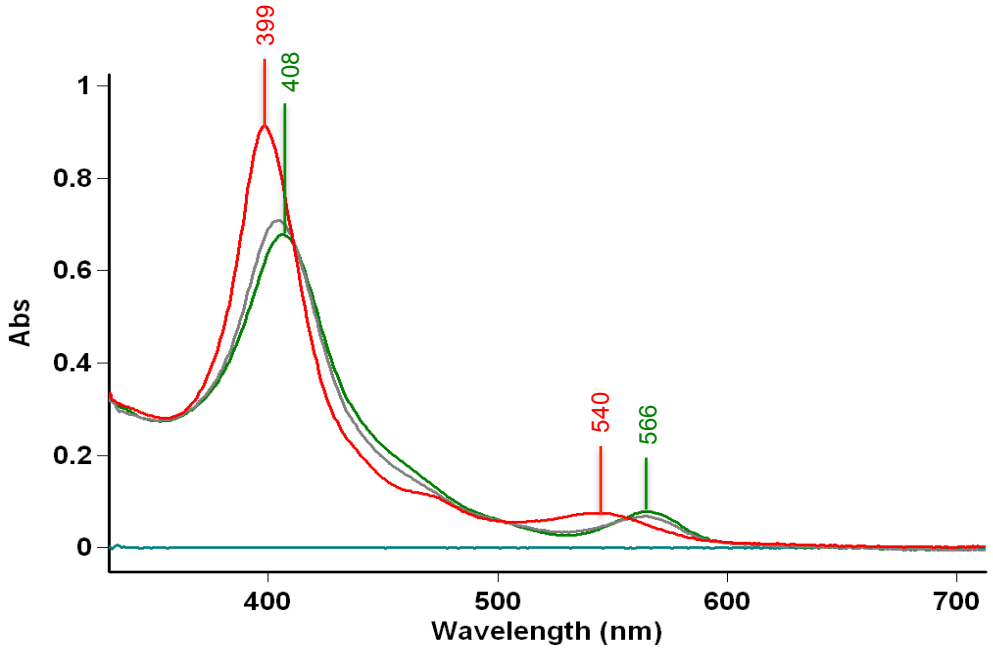

Figure S19. UV–vis spectra of $(F_8)Fe^{III}(OH)$ (green, λ_{max} = 408 (Soret), 566 nm; 8 μM in acetone at RT) and after bubbling 5 mL $NO_{(g)}$ into the solution and stirring for 20 min (gray, λ_{max} = 406 (Soret), 565 nm), after stirring for 5 h generating $(F_8)Fe^{II}(NO)$ (red, λ_{max} = 399 (Soret), 540 nm).

5.12. Rapid Electron Transfer from Cu^{I} to Fe^{III} and Redox Equilibrium

To a 100 mL Schlenk flask equipped with a magnetic stir bar was added $[(F_8)Fe^{III}(THF)_2](SbF_6)$ (14.7 mg, 0.012 mmol) in 50 mL deoxygenated acetone under a N_2 atmosphere. Complex $[(tmpa)Cu^{I}(MeCN)][B(C_6F_5)_4]$ (13.2 mg, 0.012 mmol) was added to the brown solution inducing an immediate color change to red owing to the formation reduced heme $(F_8)Fe^{II}$. A UV–vis spectrum of the solution mixture (Figure S20) right after addition of Cu^{I} complex revealed that the electron transfer from Cu^{I} to Fe^{III} readily occurs in acetone, resulting in complete formation of $(F_8)Fe^{II}$ as a major heme species in solution. After stirring for 1 h, a UV–vis spectrum of reaction mixture showed the presence of both $(F_8)Fe^{II}$ (λ_{max} = 419 (Soret)) and $[(F_8)Fe^{III}(THF)_2](SbF_6)$ (λ_{max} = 395(sh) (Soret)) as the equilibrium in acetone was reached.

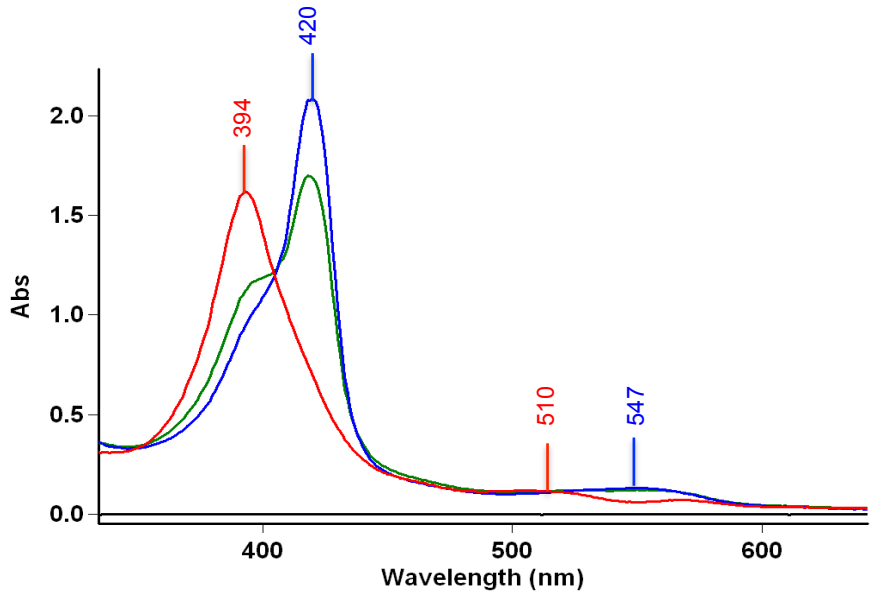

Figure S20. UV–vis spectra of $[(F_8)Fe^{III}(THF)_2](SbF_6)$ (red, λmax = 394 (Soret), 510 nm) and solution right after addition of $[(tmpa)Cu^{I}(MeCN)][B(C_6F_5)_4]$ (blue, λ_{max} = 420 (Soret), 547 nm) indicating electron transfer from Cu^{I} to Fe^{III} takes place generating $(F_8)Fe^{II}$. After stirring for 30 min, the green spectrum is observed (λ_{max} = 395 (sh), 419 (Soret), 547 nm), representative of an equilibrium state. The solutions for these experiments are 12 μM based on heme in acetone at RT.

This redox equilibrium, which is known to be dependent on solvent interaction, concentration, and temperature have already been reported for similar systems.[13] Since the Cu^{I}-to-Fe^{III} electron-transfer readily occurs in the present ligand-complexes, $[(tmpa)Cu^{I}(MeCN)]^{+}$ and $[(F_8)Fe^{III}(THF)_2](SbF_6)$, Cu^{I}-NO^{+} resulting from first nitric oxide molecule attack at the cupric center can be proposed as a possible reaction intermediate. Formation of Cu^{I}-NO^{+} can then be followed by a rapid Cu^{I}-to-Fe^{III} electron transfer generating a Cu^{II}-nitrito complex and ferrous heme, the latter is then trapped by a second $NO_{(g)}$ molecule.

5.13. Analysis of Nitrite Ion by Capillary Electrophoresis

In a 25 mL-Schlenk flask equipped with a magnetic stir bar was added in the drybox $(F_8)Fe^{II}$ (12 mg, 0.015 mmol) and $[(tmpa)Cu^{I}(MeCN)][B(C_6F_5)_4]$ (16 mg, 0.015 mmol). Addition of 10 mL MeTHF resulted in an intense red solution, which was bubbled with dry dioxygen to generate $[(F_8)Fe^{III}–O–Cu^{II}(tmpa)][B(C_6F_5)_4]$. The solvent was then removed under vacuum and solid was redissolved in 10 mL deoxygenated acetone followed by direct bubbling of excess $NO_{(g)}$ into the solution via a three-way long syringe needle and stirring for 1 h. Then the solvent was removed and solid product was dissolved in 10 mL CH_2Cl_2 and extracted with 25 mL of aqueous NaCl solution (6 mM). The presence of significant amounts of nitrite ion in the aqueous layer was confirmed by semiquantitative QUANTOFIX nitrite test strips as well as the UV–vis spectrum showing a band at 355 nm corresponding to nitrite $n \rightarrow \pi^*$ transitions.[14]

Afterwards, capillary electrophoresis (CE) was used for nitrite quantification in

the aqueous layer. A standard calibration curve was first constructed using sodium nitrite. By employing optimal conditions, the calibration curve was generated for a concentration range of 100–2000 μM. This nitrite analysis indicated nitrite (NO_2^-) was present in the product mixture with a yield of 95% (560 μM), according to eq 2.

5.14. Cyclic Voltammetry Measurements

The Cyclic voltammetry measurements were carried out on (F8)FeII, $[(tmpa)Cu^{I}(MeCN)][B(C_6F_5)_4]$, $[(F_8)Fe^{III}(THF)_2](SbF_6)$, and $[(tmpa)Cu^{II}(MeCN)](ClO_4)_2$ complexes under an argon atmosphere in acetone solutions, containing 100 mM $(Bu)_4N(PF_6)$ electrolyte, using 1 and 2 mM complex concentrations for the reduced and oxidized complexes, respectively. The cell consisted of a 50 mL four-necked round bottom flask equipped with rubber septa. Each neck possessed one of the following: a glassy carbon working electrode, an $Ag/AgNO_3$ reference electrode in MeCN, a platinum wire as the auxiliary electrode, and an adapter connected to an argon line. All voltammograms were classified as quasi-reversible having $i_{pc}/i_{pa} \approx 1$ with half-wave potentials in the range $E_{1/2} = -190$ to -425 mV versus Fc^+/Fc. The $E_{1/2}$ values obtained are listed in Table S1. We found that the $E_{1/2}$ values for the copper complexes are more negative than for the heme complexes (Table S1), suggesting that the former is a better reductant.

Table S1. Redox potentials of the heme and copper complexes recorded in acetone at RT.

Compound	$E_{1/2}$ [a] (mV vs Fc^+/Fc)	ΔE [a] (mV)	$E_{1/2}$ [b] (mV vs NHE)	Redox Couple
$(F_8)Fe^{II}$	–190	120	+360	Fe^{III}/Fe^{II}
$[(F_8)Fe^{III}(THF)_2](SbF_6)$	–205	110	+345	Fe^{III}/Fe^{II}
$[(tmpa)Cu^{I}(MeCN)][B(C_6F_5)_4]$	–410	130	+140	Cu^{II}/Cu^{I}
$[(tmpa)Cu^{II}(MeCN)](ClO_4)_2$	–425	130	+125	Cu^{II}/Cu^{I}

[a] Potentials are reported versus the Fc^+/Fc redox couple and are rounded to the nearest 5 mV.

[b] Potentials are converted to versus NHE by correcting for the expected Fc^+/Fc redox potential of +310 mV versus the KCl-saturated aqueous calomel electrode (SCE), where SCE is +241 mV versus NHE[15] and all values are rounded to the nearest 5 mV.

5.15. References for Supporting Information

(1) (a) Ford, P. C.; Lorkovic, I. *Chem. Rev*. **2002**, *102*, 993. (b) Wang, J.; Schopfer, M. P.; Sarjeant, A. A. N.; Karlin, K. D. *J. Am. Chem. Soc.* **2009**, *131*, 450. (c) Schopfer, M. P.; Mondal, B.; Lee, D.-H.; Sarjeant, A. A. N.; Karlin, K. D. *J. Am. Chem. Soc.* **2009**, *131*, 11304.

(2) Sheldrick, G.M. *Acta Cryst.* **2008**, *A64*, 112.

(3) Jacobson, R. R.; Tyeklar, Z.; Farooq, A.; Karlin, K. D.; Liu, S.; Zubieta, J. *J. Am. Chem. Soc.* **1988**, *110*, 3690.

(4) Wang, J.; Schopfer, M. P.; Puiu, S. C.; Sarjeant, A. A. N.; Karlin, K. D. *Inorg. Chem.* **2010**, *49*, 1404.

(5) Karlin, K. D.; Nanthakumar, A.; Fox, S.; Murthy, N. N.; Ravi, N.; Huynh, B. H.; Orosz, R. D.; Day, E. P. *J. Am. Chem. Soc*. **1994**, *116*, 4753.

(6) (a) Kopf, M.-A.; Neuhold, Y.-M.; Zuberbühler, A. D.; Karlin, K. D. *Inorg. Chem.* **1999**, *38*, 3093.

(b) Ghiladi, R. A.; Kretzer, R. M.; Guzei, I.; Rheingold, A. L.; Neuhold, Y. M.; Hatwell, K. R.; Zuberbühler, A. D.; Karlin, K. D. *Inorg. Chem.* **2001,** *40*, 5754.

(7) Jutzi, P.; Müller, C.; Stammler, A.; Stammler, H. *Organometallics* **2000**, *19*, 1442.

(8) Fox, S.; Nanthakumar, A.; Wikström, M.; Karlin, K. D.; Blackburn, N. J. *J. Am. Chem. Soc.* **1996**, *118*, 24.

(9) (a) Zubieta, J.; Karlin, K. D.; Hayes, J. C. "Structural Systematics of Cu(I) and Cu(II) Derivatives of Tripodal Ligands'," In *Copper Coordination Chemistry: Biochemical and Inorganic Perspectives*; K. D. Karlin and J. Zubieta, Ed.; Adenine Press: Albany, New York, 1983; pp 97. (b) Karlin, K. D.; Hayes, J. C.; Juen, S.; Hutchinson, J. P.; Zubieta, J. *Inorg. Chem.* **1982**, *21*, 4106.

(10) Addison, A. W.; Rao, T. N.; Reedijk, J.; Van Rijn, J.; Verschoor, G. C. *J. Chem. Soc., Dalton Trans.* **1984**, 1349.

(11) Lucas, H. R.; Meyer, G. J.; Karlin, K. D. *J. Am. Chem. Soc.* **2010**, *132*, 12927.

(12) Liang, H. C.; Kim, E.; Incarvito, C. D.; Rheingold, A. L.; Karlin, K. D. *Inorg. Chem.* **2002**, *41*, 2209.

(13) Fry, H. C.; Lucas, H. R.; Zakharov, L. N.; Rheingold, A. L.; Meyer,G. J.; Karlin, K. D. *Inorg. Chim. Acta* **2008**, *361*, 1100.

(14) Jankowski, J. J.; Kieber, D. J.; Mopper, K. *Photochem. Photobiol.* **1999**, *70*, 319.

(15) Brad, A. J.; Faulkner, L. R. *Electrochemical Methods: Fundamentals and applications*, 2nd Ed.; Wiley: New York, 2001.

Chapter 3:

Nitric Oxide Generation from Heme/Copper Assembly Mediated Nitrite Reductase Activity

This work was co-authored with the following authors and is published under the following citation:

Shabnam Hematian, Maxime A. Siegler, and Kenneth D. Karlin

J. Biol. Inorg. Chem. **2014**, *19*, 515−528

Abstract:

Nitric oxide (NO) as a cellular signaling molecule and vasodilator regulates a range of physiological and pathological processes. Nitrite (NO_2^-) is recycled in vivo to generate nitric oxide, particularly in physiologic hypoxia and ischemia. The cytochrome *c* oxidase binuclear heme-a_3/Cu_B active site is one entity known to be responsible for conversion of cellular nitrite to nitric oxide. We recently reported that a partially reduced heme/copper assembly reduces nitrite ion, producing nitric oxide; the heme serves as the reductant and the cupric ion provides a Lewis acid interaction with nitrite, facilitating nitrite (N–O) bond cleavage (Hematian et al., *J. Am. Chem. Soc.* 134:18912–18915, 2012). To further investigate this nitrite reductase chemistry, copper(II)–nitrito complexes with tridentate and tetradentate ligands were used in this study, where either *O*,*O'*-bidentate or *O*-unidentate modes of nitrite binding to the cupric center are present. To study the role of the reducing ability of the ferrous heme center, two different tetraarylporphyrinate-

iron(II) complexes, one with electron-donating *para*-methoxy peripheral substituents and the other with electron-withdrawing 2,6-difluorophenyl substituents, were used. The results show that differing modes of nitrite coordination to the copper(II) ion lead to differing kinetic behavior. Here, also, the ferrous heme is in all cases the source of the reducing equivalent required to convert nitrite to nitric oxide, but the reduction ability of the heme center does not play a key role in the observed overall reaction rate. On the basis of our observations, reaction mechanisms are proposed and discussed in terms of heme/copper heterobinuclear structures.

1. Introduction

The nitrite anion (NO_2^-) is biologically important, for example, in denitrifying bacteria, where it forms from nitrate (NO_3^-) reduction catalyzed by a molybdoenzyme. Then, either copper-containing or heme-containing enzymes reduce the nitrite to nitric oxide (NO), prior to its being reductively coupled to give nitrous oxide (N_2O) and eventually N_2.[1–4] However, in mammalian aerobic organisms, until relatively recently, nitrite was considered as a biologically inert one-electron-oxidative end product of endogenous $NO_{(g)}$ metabolism. In fact, this supposedly inert anion can be and is recycled in vivo to generate $NO_{(g)}$ and constitutes a biochemical circulating reservoir for this important signaling molecule, in particular under conditions of physiologic hypoxia and ischemia.[5–10]

The classic biological source of $NO_{(g)}$ is nitric oxide synthase (NOS) oxidation of L-arginine.[11,12] This nitrite reductase chemistry is an important alternative biological

source of $NO_{(g)}$.[1–4,13] Nitrite reduction to $NO_{(g)}$ involves both pH and oxygen sensor chemistry[13] because of its requirement for one electron and two protons:

$$NO_2^- + 2H^+ + e^- \rightarrow NO_{(g)} + H_2O$$

Remarkably, the L-arginine–NOS pathway is oxygen dependent, whereas the nitrite–$NO_{(g)}$ pathway is gradually activated as the oxygen tension falls. Therefore, nitrite derived $NO_{(g)}$ formation can be considered as a backup system to ensure that there is sufficient $NO_{(g)}$ production in hypoxic conditions where the $NO_{(g)}$ generation (for its signaling functions) in tissues is independent of NOS activity.[14]

Besides a nonenzymatic conversion of nitrite to $NO_{(g)}$ via acidic disproportionation,[5,15] nitrite as the major intravascular and tissue storage form of $NO_{(g)}$ is readily reduced to $NO_{(g)}$ along a physiological oxygen and pH gradient by a number of proteins/enzymes, such as hemoglobin,[16–18] myoglobin,[19,20] neuroglobin,[21] xanthine oxidoreductase,[8] aldehyde dehydrogenase,[8] cytochrome *c* oxidase (C*c*O; see below), cytochrome *c*,[22] and possibly cytochrome P-450[23–25] (Figure 1).

Cytochrome *c* oxidase, the terminal enzyme of the mitochondrial respiratory chain and known to catalyze the four-electron reduction of oxygen to water at a heme/copper heterobinuclear centered active site,[26–28] has recently been shown to have a novel enzymatic role catalyzing the reduction of nitrite to $NO_{(g)}$.[29,30] It is noteworthy that unlike the C*c*O oxidase reaction, which involves four electrons, only one electron is required for the C*c*O nitrite reductase reaction. This nitrite reductase activity is significantly elevated under hypoxic conditions and increases with the lower pH and higher nitrite concentrations that are found in hypoxia.[31–34]

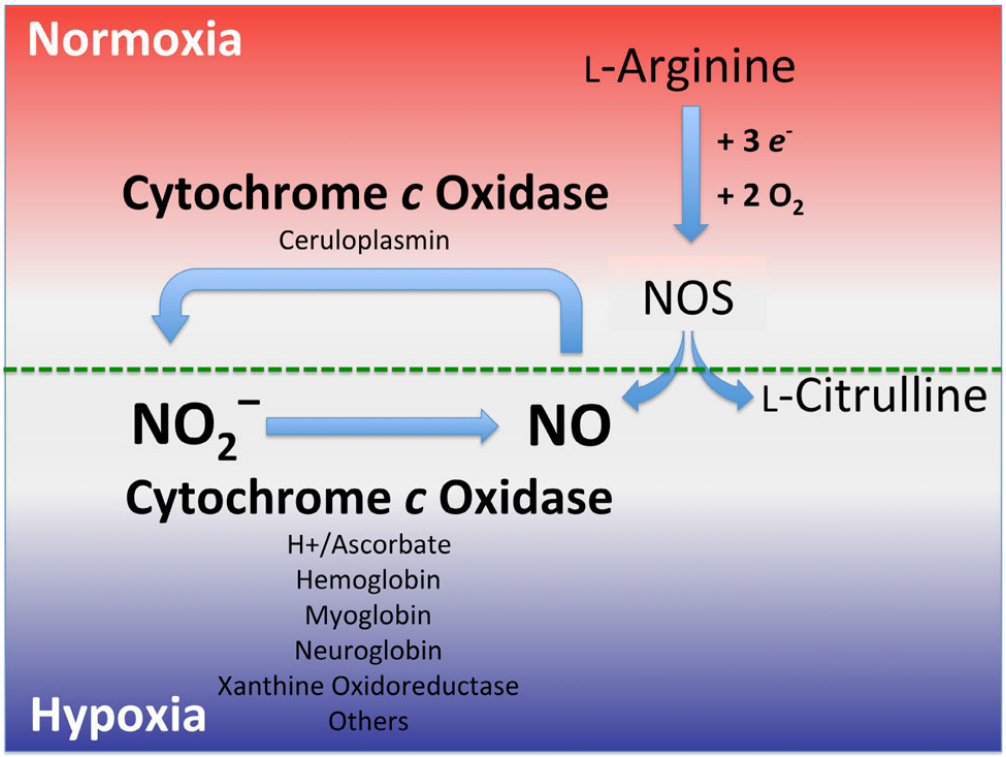

Figure 1. Nitrite is reduced to nitric oxide by a variety of metal containing enzymes along the physiological O_2 gradient. Under normal cellular O_2 tensions (normoxia), the critically important signaling molecule nitric oxide is predominantly produced by nitric oxide synthase (NOS). Under hypoxic (low O_2 concentrations) conditions, those associated with cellular stress, the nitrite anion can also serve as an alternative source of nitric oxide generation, via enzymatic reduction processes, including the process associated with cytochrome *c* oxidase.

These findings are consistent with the following reaction:

$$NO_2^- + C\textit{c}O\text{-}Cu^{II}\text{-}Fe^{II} + H^+ \rightarrow NO_{(g)} + C\textit{c}O\text{-}Cu^{II}\text{-}Fe^{III} + OH^-$$

However, more recent studies have revealed that the catalytic formation of $NO_{(g)}$ by C*c*O also occurs under normoxia and physiological nitrite concentrations and has been detected in a variety of eukaryotes, including yeast, rat liver, human endothelial cells, bovine heart, calf liver, plants, and algae.[29,31,35]

In this report, we describe several examples of heme/copper assembly coordination complexes which mediate nitrite reductase chemistry, the one-electron

reduction of nitrite to $NO_{(g)}$. This follows our initial report[36] on this type of chemistry showing a copper(II) complex with coordinated nitrite anion reacts with a ferrous heme, producing $NO_{(g)}$. Here, we provide additional examples of this newly discovered chemistry, where the exact nature of the heme and/or the copper chelating ligand is modified. For this reaction chemistry, this approach provides (1) differing modes of binding of nitrite to the cupric center, and (2) hemes with differing reducing abilities. For the former, we have examples of nitrite bound to the cupric center with either a tripodal tetradentate pyridyl-alkylamine ligand or a related tridentate alkylamine ligand. For the latter, we compare systems where the heme possesses electronwithdrawing peripheral substituents versus one that is electron-donating. The hope is that via such a systematic approach, we can learn details and fundamental concepts concerning how a heme/copper assembly may affect nitrite reduction chemistry.

Scheme 1 shows the structures of complexes used in this study. The copper complexes are $[(tmpa)Cu^{II}(NO_2)][B(C_6F_5)_4]$ (tmpa is tris(2-pyridylmethylamine))[36] and the new compound $[(AN)Cu^{II}(NO_2)](CF_3SO_3)$ (AN is 3,3'-iminobis(*N*,*N*-dimethylpropyl-amine)); an X-ray crystal structure reveals the binding of nitrite is different from that found for the tmpa-containing complex. The hemes used in this study include the iron(II) complex $(F_8)Fe^{II}$ (F_8 is tetrakis(2,6-difluorophenyl)porphyrinate(2–)][37,38] and a heme compound bearing an electron-rich porphyrinate, $(TMPP)Fe^{II}$ [TMPP is tetrakis(4-methoxyphenyl)porphyrinate(2–)]. As shown in Scheme 1, the reactivity observed by using pairwise combinations of the copper–nitrite complex and heme is that reaction of a 1:2 copper/iron complex mixture leads to highly efficient formation of $NO_{(g)}$, as trapped by the second reduced heme to give a stable ferrous heme–nitrosyl; the initially present

copper(II) combines with the ferric heme formed from the redox reaction where nitrite is reduced to $NO_{(g)}$, and a μ-oxo Fe^{III}–O–Cu^{II} complex is generated as the other product.

Scheme 1. Nitrite Reduction to Nitric Oxide Mediated by Heme/Copper Assemblies.

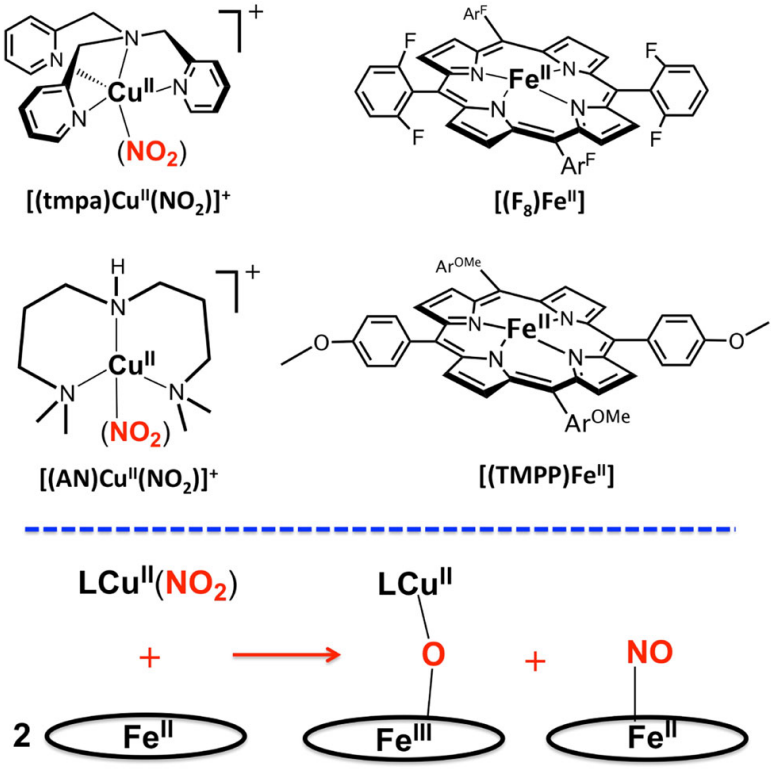

Top: Structures of copper and heme complexes used in this study. *Bottom*: Reaction equation representing the reductase chemistry. AN 3,3'-iminobis(*N,N*-dimethylpropylamine), F_8 tetrakis-(2,6-difluorophenyl)-porphyrinate(2–), tmpa tris(2-pyridylmethylamine), TMPP tetrakis(4-methoxyphenyl)porphyrinate(2–).

In fact, the heme/copper C*c*O active site is also responsible for the oxidation of $NO_{(g)}$ to nitrite,[36,39] when $NO_{(g)}$ is in excess and/or O_2 levels increase (recovery from hypoxia). Our research program in large part is concerned with the interplay between reductive or oxidative chemistry at a given heme/copper center, as modulated by metal ion center coordination and redox properties. Thus, as part of these efforts, obtaining an

in-depth understanding of the mechanism underlying heme/copper nitrite reductase activity is critical.

2. Materials and methods

All chemicals and solvents were purchased as commercially available analytical grade unless otherwise stated. Diethyl ether and methanol (MeOH) were used after they had been passed through a 60-cm-long column of activated alumina (Innovative Technologies) under argon. Acetonitrile (MeCN) and pentane were dried by distillation over calcium hydride, and acetone was freshly distilled from Drierite (anhydrous calcium sulfate) under argon prior to use. Tetrahydrofuran (THF) and 2-methyltetrahydrofuran (MeTHF) (Sigma, 673277, inhibitor free) were purified and dried by distillation from sodium/benzophenone ketyl under argon. Dioxygen was dried by passing it through a short column of supported P4O10 (Aquasorb, Mallinkrodt). NO gas was obtained from Matheson Gases and purified following methods previously described in the literature.[40–42] Addition of NO gas to metal complex solutions was effected by transfer via a three-way long syringe needle. Preparation and handling of air-sensitive compounds were performed under an argon atmosphere using standard Schlenk techniques or in an MBraun Labmaster 130 inert atmosphere (less than 1 ppm O_2, less than 1 ppm H_2O) drybox filled with nitrogen. Deoxygenation of solvents was effected by either repeated freeze/pump/thaw cycles or bubbling with argon for 45–60 min. Electrospray ionization mass spectrometry (ESI-MS) spectra were collected by the Mass Spectrometry Facility at Johns Hopkins University. Elemental analyses were performed by Columbia Analytical

Services (Tucson, AZ, USA). Infrared (IR) spectra were obtained using a Thermo Scientific Nicolet Nexus 670 Fourier transform IR (FT-IR) spectrophotometer. UV–vis spectra were recorded with a Cary-50 Bio spectrophotometer equipped with a fiber optic coupler (Varian). The spectrophotometer cells used were made by Quark Glass with a column and pressure/vacuum side stopcock and a 1-cm path length. ^{1}H-NMR spectra were acquired using a Bruker 400-MHz spectrometer. Chemical shifts were reported as d values relative to an internal standard (tetramethylsilane) and the residual solvent proton peak. Electron paramagnetic resonance (EPR) spectra were recorded with a Bruker EMX spectrometer controlled by a Bruker ER 041 X G microwave bridge operating at X-band (approximately 9.4 GHz).

The compounds $[(tmpa)Cu^{II}(NO_2)][B(C_6F_5)_4]$,[36] $[(tmpa)Cu^{I}(MeCN)][B(C_6F_5)_4]$,[36] $[(AN)Cu^{I}][B(C_6F_5)_4]$,[43] and $(F_8)Fe^{II}$ [37,38] were synthesized and characterized following methods previously described in the literature. $(TMPP)Fe^{III}(Cl)$ was purchased from TriPorTech (Germany).

2.1. Synthesis of Metal Complexes

$[(AN)Cu^{II}(Cl)](CF_3SO_3)$: Under an argon atmosphere using a Schlenk flask, a solution of AN (375 mg, 2.00 mmol) in 20 mL of freshly distilled MeCN was added to solid $Cu^{II}(CF_3SO_3)_2$ (362 mg, 1.00 mmol) and CuCl2 (134 mg, 1.00 mmol). The resulting blue solution was stirred for 30 min at room temperature. The solvent was removed in vacuo, and in the drybox the solid residue was dissolved in a minimal volume of THF. The solution was then filtered, and the filtrate was layered with pentane, affording

turquoise blue needles suitable for X-ray crystal structure analysis. After vacuum-drying, the crystals weighed 695 mg (80% yield). Anal. Calcd for $C_{11}H_{25}ClCuF_3N_3O_3S$: C, 30.34; H, 5.79; N, 9.65. Found: C, 3.54; H, 6.07; N, 9.52. UV–vis spectra [λ_{max}, nm (ε_{max}, $M^{-1}cm^{-1}$)]: 720 (250), 1,025 (227) in acetone (Figure S1); 722 (227), 1,000 (206) in MeOH (Figure S2). EPR spectra (X-band spectrometer, ν = 9.428 GHz): g_2 = 2.116, $g_3 \approx 2.040$ in acetone at 22 K (Figure S3); g_1 = 2.254, A_1 = 120 G, g_2 = 2.114, g_3 = 2.034 in THF–MeCN (4:1) at 15 K (Figure S4).

[(AN)Cu^{II}(NO$_2$)](CF$_3$SO$_3$): In the drybox, silver nitrite (77 mg, 0.50 mmol) was added to [(AN)Cu^{II}(Cl)](CF$_3$SO$_3$) (218 mg, 0.50 mmol) in 10 mL MeOH, resulting in a green solution. The reaction mixture was then sonicated for 3 h to ensure complete precipitation of AgCl, followed by filtration in the drybox. Slow addition of diethyl ether (30 mL) to the filtrate resulted in crystallization, and the green crystals were dried under a vacuum to afford 205 mg of product (92%). Anal. Calcd for $C_{11}H_{25}CuF_3N_4O_5S$: C, 29.63; H, 5.65; N, 12.56. Found: C, 30.13; H, 5.98; N, 12.26. UV–vis spectra [λ_{max}, nm (ε_{max}, $M^{-1}cm^{-1}$)]: 702 (327) in acetone (Figure S1); 702 (309) in MeOH (Figure S2). EPR spectrum (X-band spectrometer, ν = 9.428 GHz) in acetone at 22 K (Figure S5): g_2 = 2.108, $g_3 \approx 2.051$. FT-IR spectrum (solid) (Figure S6): $\nu_{as}(NO_2)$ 1,370 cm^{-1}, $\nu_s(NO_2)$ 1,110 cm^{-1}, $\delta(NO_2)$ 835 cm^{-1}. Analogous compounds have been previously described: [(AN)Cu^{II}(NO$_2$)](NO$_3$) (with the X-ray structure) and [(AN)Cu^{II}(NO$_2$)][B(C$_6$F$_5$)$_4$].[44]

(TMPP)Fe^{II}·1.5H$_2$O: Under an argon atmosphere, to a solution of (TMPP)Fe^{III}(Cl) (413 mg, 0.50 mmol) in deoxygenated dichloromethane (150 mL) was added 100 mL of deoxygenated saturated sodium hydrosulfite aqueous solution. The two solutions were vigorously mixed with argon bubbling for about 30 min, during which

time the color of the organic layer changed from dark brownish red to bright red. The reaction mixture was allowed to sit for ample time (approximately 20 min) to allow the separation of the two layers. Then the organic layer was allowed to slowly pass through a Schlenk filter tube (coarse porosity) and dried over a small plug of anhydrous sodium sulfate (approximately 6 g). The solvent was removed under a vacuum, yielding 298 mg of product (73%). Anal. Calcd for $C_{48}H_{39}FeN_4O_{5.5}$: C, 70.68; H, 4.82; N, 6.87. Found: C, 70.88; H, 4.83; N, 6.73. ^{1}H-NMR (pyridine-d_5, 400 MHz; d, ppm): 8.83 (s, 8H, pyrrole-H), 8.13 (d, 8H, *o*-phenyl-H), 7.29 (d, 8H, *m*-phenyl-H), 4.91 (s, 3H, H_2O), 3.88 (s, 12H, methoxy-H). UV–vis spectra [λ_{max}, nm (ε_{max}, $M^{-1}cm^{-1}$)]: 429 (243,000), 540 (11,400) in acetone (Figure S7); 430 (256,000), 542 (8,800) in THF (Figure S8).

[(TMPP)Fe^{III}–O–Cu^{II}(tmpa)][B(C$_6$F$_5$)$_4$]·3H$_2$O·2MeTHF: In a 50-mL Schlenk flask equipped with a stir bar, in the drybox, (TMPP)Fe^{II}·1.5H_2O (40 mg, 0.05 mmol) and [(tmpa)Cu^{I}(MeCN)][B(C_6F_5)$_4$] (53 mg, 0.05 mmol) were dissolved in 10 mL air-free freshly distilled MeTHF. Then dry dioxygen was bubbled through the solution for 2 min and this was accompanied by an immediate color change from dark red to dark green. The mixture was stirred for 20 min at room temperature. The solvent was then removed under a vacuum and solid was further dried under a vacuum for additional 6 h, yielding 86 mg of [(TMPP)Fe^{III}–O–Cu^{II}(tmpa)][B(C_6F_5)$_4$] (84%). Anal. Calcd for $C_{100}H_{80}$ $BCuF_{20}$ FeN_8O_{10}: C, 58.19; H, 3.91; N, 5.43. Found: C, 58.06; H, 3.86; N, 5.26. UV–vis spectra [λ_{max}, nm (ε_{max}, $M^{-1}cm^{-1}$)]: 443 (252,000), 564 (17,300), 605 (14,700) in acetone (Figure S8); 441 (189,000), 561 (14,800), 603 (12,100) in MeCN (Figure S8). ESI-MS spectrum in acetone (Figure S9): 1,157.3 (TMPP)Fe–O–Cu(tmpa), 788.2 (TMPP)Fe, 1,593.4 $[(TMPP)Fe]_2O$.

In Situ Generation of (TMPP)Fe^{II}(NO): The ferrous–nitrosyl complex (TMPP)Fe^{II}(NO) was generated in situ by bubbling excess NO gas through the solution of (TMPP)Fe^{II} under a nitrogen atmosphere at room temperature. UV–vis spectra [λ_{max}, nm (ε_{max}, $M^{-1}cm^{-1}$)]: 410 (142,000), 539 (11,900), 614 (4,800) in acetone (Figure S10); 410 (138,000), 535 (11,500), 610 (4,800) in MeCN (Figure S11). FT-IR spectrum in acetone: ν_{NO} 1,677 cm^{-1} (a published value obtained in dimethylformamide is 1,666 cm^{-1})[45].

2.2. Reaction of 2 equiv of $(F_8)Fe^{II}$ with $[(AN)Cu^{II}(NO_2)](CF_3SO_3)$

In the drybox, to a solution of (TMPP)Fe^{II}·1.5H_2O (20.0 mg, 0.024 mmol) in acetone (100 mL) was added $[(AN)Cu^{II}(NO_2)](CF_3SO_3)$ (5.4 mg, 0.012 mmol). After the mixture had been stirred for 3 h, the solvent was removed to yield a brown solid. During the reaction, 305-μL aliquots were withdrawn by syringe every 10 min, diluted with acetone to 5.0 mL, and a UV–vis spectrum was recorded (see "Results"). This procedure allowed quantitative determination of the $[(F_8)Fe^{III}–O–Cu^{II}(AN)]^+$ complex as one of the products and was necessary in order to avoid breakage (by hydrolysis) of the oxo bridge occurring at low concentrations. Formation of a one-to-one mixture of the heme–nitrosyl species $(F_8)Fe^{II}(NO)$ (λ_{max} = 399 nm) and the μ-oxo (λ_{max} = 439 nm) complex was observed. FT-IR spectrum (solid): ν_{NO} = 1,685 cm^{-1}.

2.3. Reaction of 2 equiv of (TMPP)Fe^{II} with [(tmpa)$Cu^{II}(NO_2)$][$B(C_6F_5)_4$]

In a drybox, to a solution of (TMPP)Fe^{II}·1.5H_2O (19.7 mg, 0.024 mmol) in acetone (100 mL) was added [(tmpa)$Cu^{II}(NO_2)$][$B(C_6F_5)_4$], (12.9 mg, 0.012 mmol), and after the mixture had been stirred for 3 h, the solvent was removed to yield a brown solid. The preparation of samples for UV–vis analysis during the reaction was done in a manner analogous to the procedure described in "Reaction of 2 equiv of (F_8)Fe^{II} with [(AN)$Cu^{II}(NO_2)$](CF_3SO_3)". UV–vis analysis directly indicated the formation of a one-to-one mixture of the heme–nitrosyl species (TMPP)Fe^{II}(NO) (λ_{max} = 410 nm) and the μ-oxo complex (λ_{max} = 443 nm) (see "Results"). FT-IR spectrum in acetone: ν_{NO} = 1,677 cm^{-1}.

2.4. Reaction of 2 equiv of (TMPP)Fe^{II} with [(AN)$Cu^{II}(NO_2)$](CF_3SO_3)

Addition of [(AN)$Cu^{II}(NO_2)$](CF_3SO_3) (5.4 mg, 0.012 mmol) to a solution of (TMPP)Fe^{II}·1.5H_2O (19.7 mg, 0.024 mmol) in acetone (100 mL) in a drybox was followed by stirring for 3 h. The solvent was then removed to yield a brown solid. The solid product was then dissolved in 10 mL CH2 Cl2 and was extracted with 25 mL of aqueous NaCl solution (6 mM). The absence of nitrite ion in the aqueous layer was determined by using QUANTOFIX semiquantitative nitrite test strips.[36] The preparation of samples for UV–vis analysis during the reaction was analogous to the procedure described "Reaction of 2 equiv of (F_8)Fe^{II} with [(AN)$Cu^{II}(NO_2)$](CF_3SO_3)". The UV–vis spectrum displays a Soret band at λ_{max} = 419 nm, indicating no μ-oxo complex formation (see "Results"). FT-IR spectrum in acetone: ν_{NO} = 1,677 cm^{-1}.

2.5. Reaction of $[(AN)Cu^{I}][B(C_6F_5)_4]$ with Nitrite

In the drybox, to a 25 mL acetone solution of $[(AN)Cu^{I}][B(C_6F_5)_4]$ (11.6 mg, 0.012 mmol), $(Bu)_4N(NO_2)$ (3.6 mg, 0.012 mmol) was added, followed by stirring overnight. The UV–vis spectra of the reaction mixture showed no absorbance in the 500–1,100-nm range (Figure S12), indicating that no redox reaction had occurred.

2.6. Reaction of $(TMPP)Fe^{II}$ with Nitrite

To a 25 mL acetone solution of $(TMPP)Fe^{II}\cdot 1.5H_2O$ (10.2 mg, 0.012 mmol), in the drybox, $(Bu)_4N(NO_2)$ (3.6 mg, 0.012 mmol) was added. The mixture was stirred for several hours, during which time no significant color or UV–vis absorbance changes were observed (Figure S13), confirming that nitrite reduction does not occur in the absence of Cu(II) as a Lewis acid.

2.7. X-ray Structure Determination

X-ray structure determination of $[(AN)Cu^{II}(Cl)](CF_3SO_3)$ and $[(AN)Cu^{II}(NO_2)](CF_3SO_3)$ was performed at the X-ray diffraction facility at Johns Hopkins University. CIF files have been deposited with the Cambridge Crystallographic Data Centre (CCDC). CCDC 961739 and 961740 contain the supplementary crystallographic data for this article. These data can be obtained free of charge from the CCDC via http://www.ccdc.cam.ac.uk/data_request/cif. All reflection intensities were measured at 110 (2) K using the Agilent Technologies KM4/Xcalibur (detector,

Sapphire3) with enhanced graphite-monochromated Mo Kα radiation (λ = 0.71073 Å) with use of the program CrysAlisPro (version 1.171.35.11, Agilent Technologies, 2011). CrysAlisPro (version 1.171.35.11, Agilent Technologies, 2011) was used to refine the cell dimensions. Data reduction was done using CrysAlisPro (version 1.171.35.11, Agilent Technologies, 2011). The structure was solved with the program SHELXS-97[46] and was refined on F^2 with SHELXL-97[46]. Analytical numeric absorption corrections based on a multifaceted crystal model were applied using CrysAlisPro (version 1.171.35.11, Agilent Technologies, 2011). The temperature of the data collection was controlled using a Cryojet system (manufactured by Oxford Instruments). The hydrogen atoms (unless otherwise specified) were placed at calculated positions using the instruction AFIX 23 or AFIX 137 with isotropic displacement parameters with values 1.2 or 1.5 times U_{eq} of the attached carbon atoms. For both complexes, the hydrogen atom attached to N2 was found from difference Fourier maps, and the N–H bond distance was restrained using the DFIX instruction.

The structure of $[(AN)Cu^{II}(Cl)](CF_3SO_3)$ is ordered. The absolute configuration was established by anomalous-dispersion effects in diffraction measurements on the crystal, and the Flack parameter refined to –0.017 (9). The structure of $[(AN)Cu^{II}(NO_2)](CF_3SO_3)$ is partly disordered. The trifluoromethanesulfonate counterion is disordered over two orientations [occupancy factor of the major component = 0.586 (4)]. The C4–C3–N1–C1–C2 fragment was also found to be disordered over two orientations [occupancy factor of the major component = 0.759 (4)].

$[(AN)Cu^{II}(Cl)](CF_3SO_3)$: For $[(AN)Cu^{II}(Cl)](CF_3SO_3)$, the following were found: formula weight 435.39, blue-green lath, 0.49 × 0.21 × 0.12 mm^3, orthorhombic, $P2_12_12_1$

(no. 19), a = 10.3160 (2), b = 10.9961 (2), c = 15.9762 (4) Å, V = 1812.27 (7) Å^3, Z = 4, D_x = 1.596 g cm^{-3}, l = 1.510 mm^{-1}, absorption correction range 0.75–0.863.Wemeasured 9,260 reflections up to a resolution of $(\sin \theta/\lambda)_{max}$ = 0.62 Å^{-1}. Of these, 3,665 reflections were unique (R_{int} = 0.0245), of which 3,421 were observed [$I > 2\sigma(I)$]. A total of 215 parameters were refined. R_1/wR_2 [$I > 2\sigma(I)$]: 0.0224/0.0548. R_1/wR_2 (all reflections): 0.0258/0.0561. S = 1.056. Residual electron density was found between –0.24 and 0.34 e^- Å^{-3}.

[(AN)Cu^{II}(NO$_2$)](CF$_3$SO$_3$): For [(AN)Cu^{II}(NO$_2$)](CF$_3$SO$_3$), the following were found: formula weight 445.95, blue-green irregular rod, 0.42 × 0.16 × 0.12 mm^3, monoclinic, $P2_1/n$ (no. 14), a = 10.1675 (2), b = 15.6928 (3), c = 11.7887 (2) Å, β = 90.9584 (16)°, V = 1,880.70 (6) Å^3, Z = 4, D_x = 1.575 g cm^{-3}, l = 1.329 mm^{-1}, absorption correction range 0.706–0.887. We measured 13,996 reflections up to a resolution of $(\sin \theta/\lambda)_{max}$ = 0.62 Å^{-1}. Of these, 3,802 reflections were unique (R_{int} = 0.0396), of which 3,154 were observed [$I > 2\sigma(I)$]. A total of 342 parameters were refined using 179 restraints. R_1/wR_2 [$I > 2\sigma(I)$]: 0.0354/0.0910. R_1/wR_2 (all reflections): 0.0452/0.0961. S = 1.053. Residual electron density was found between –0.42 and 0.53 e^- Å^{-3}.

3. Results

3.1. Copper Complex Syntheses and X-ray Structures

The nitrite complex, [(AN)Cu^{II}(NO$_2$)](CF$_3$SO$_3$), was synthesized by reacting silver nitrite with the chloride precursor [(AN)Cu^{II}(Cl)](CF$_3$SO$_3$), and X-ray structures of

both compounds were obtained (Figure 2). The chloride complex of copper(II) is tetracoordinated, with ligation from the three aliphatic nitrogen atoms of the ligand [N(1), N(2), and N(3)], along with the chloride ligand (Cl(1)). With use of the structural analysis criterion developed by Yang et al.,[47] the τ_4 value is 0.69, making the best description of this complex to be of the "seesaw" type. A three-coordinate copper(I) structure with AN has been previously described.[43] The cupric center in $[(AN)Cu^{II}(NO_2)](CF_3SO_3)$ is, however, pentacoordinated by the nitrogen donor atoms of the 3,3'-iminobis(*N*,*N*-dimethylpropylamine) ligand, and O(1) and O(2) of an anisobidentate nitrito ligand. The $Cu–O_{(nitrito)}$ bond distances are unequal, with O(1) of the nitrito ligand exhibiting a much weaker interaction with the cupric ion center: the Cu–O1 bond distance is 2.35 Å and the Cu–O2 bond distance is 2.00 Å (see Figure 2).

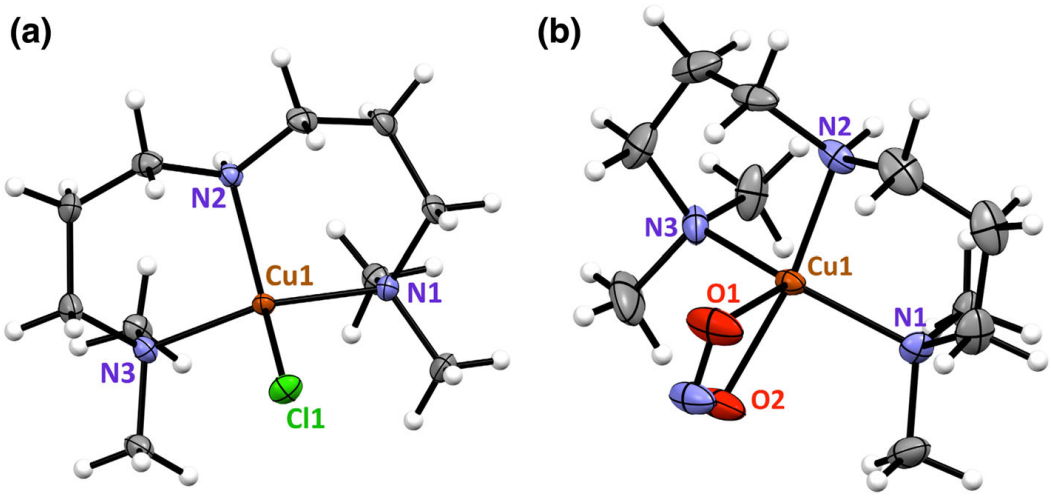

Figure 2. Displacement ellipsoid plot (50% probability level) of the copper complexes, showing the atom-labeling scheme. Relevant bond lengths (Å) and angles (deg) of $[(AN)Cu^{II}(Cl)]^+$ and $[(AN)Cu^{II}(NO_2)]^+$. **(a)** $[(AN)Cu^{II}(Cl)]^+$ Cu–N(1), 2.028 (2); Cu–N(2), 1.998 (2); Cu–N(3), 2.031 (2); Cu–Cl(1), 2.227 (6); N(1)–Cu–N(2), 96.5 (7); N(1)–Cu–N(3), 138.6 (4); N(2)–Cu–N(3), 95.7 (7); N(1)–Cu–C1(1), 102.6 (6); N(2)–Cu-Cl(1), 126.6 (8); N(3)–Cu–C1(1), 101.0 (8). **(b)** $[(AN)Cu^{II}(NO_2)]^+$ Cu–N(1), 2.011 (4); Cu–N(2), 1.993 (2); Cu–N(3), 2.043 (2); Cu–O(1), 2.347 (3); Cu–O(2), 2.002 (2); N(1)–Cu–N(2), 97.6 (1); N(1)–Cu–N(3), 136.8 (1); N(2)–Cu–N(3), 94.8 (9); N(1)–Cu–O(1), 109.0 (1); N(1)–Cu–O(2), 92.9 (1); N(2)–Cu–O(1), 95.7 (9); N(2)–Cu–O(2), 152.0 (6); N(3)–Cu–O(1), 110.6 (7); N(3)–Cu–O(2), 95.0 (1); O(1)–Cu–O(2), 56.2 (8).

By contrast, in our previously structurally characterized complex with the tetradentate TMPA ligand, $[(tmpa)Cu^{II}(NO_2)][B(C_6F_5)_4]$ (Scheme 1), the nitrito ligand is essentially unidentate, with highly different $Cu–O_{(nitrito)}$ bond distances, 1.93 and 2.93 Å.[36] Pentacoordination in this complex is completed via the four nitrogen donors of TMPA and the single oxygen atom of the nitrito ligand (Structure 1).

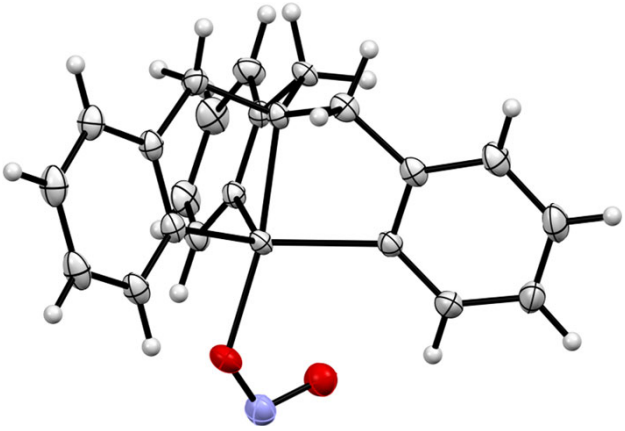

Structure 1 $[(tmpa)Cu^{II}(NO_2)]^{+}$ [36]

The IR spectrum (Figure S6) of solid $[(AN)Cu^{II}(NO_2)](CF_3SO_3)$ features nitrite ligand vibrations, further confirming the anisobidentate ONO^{-} binding ($\Delta\nu$ = 260 cm^{-1}).[48,49] Although nitrite vibrations can be assigned with certainty only by isotope labeling, they are tentatively attributed here through the differences in the spectra of the cupric–nitrite complex and its chloride precursor. Consistent with the X-ray structures observed, the EPR spectra of these complexes in frozen solution indicate either tetragonal or rhombically distorted structures, depending on the solvent (Figures S3, S4, S5).

3.2. Nitrite Reductase Reactivity; Cupric–Nitrite Complexes plus Ferrous Hemes

In our initial report on this topic,[36] we studied the reaction of $[(tmpa)Cu^{II}(NO_2)]^+$ with 2 equiv of the ferrous heme $(F_8)Fe^{II}$, under anaerobic conditions, in acetone at room temperature, and on the basis of spectroscopic analyses, a one-to-one mixture of the heme–nitrosyl species $(F_8)Fe^{II}(NO)$ and the μ-oxo complex $[(F_8)Fe^{III}–O–Cu^{II}(tmpa)]^+$ is produced (Scheme 2, top). On the basis of the results of control experiments, the reduced

Scheme 2. Reaction of 2 equiv of $(F_8)Fe^{II}$ with the Cupric Nitrite Complexes.

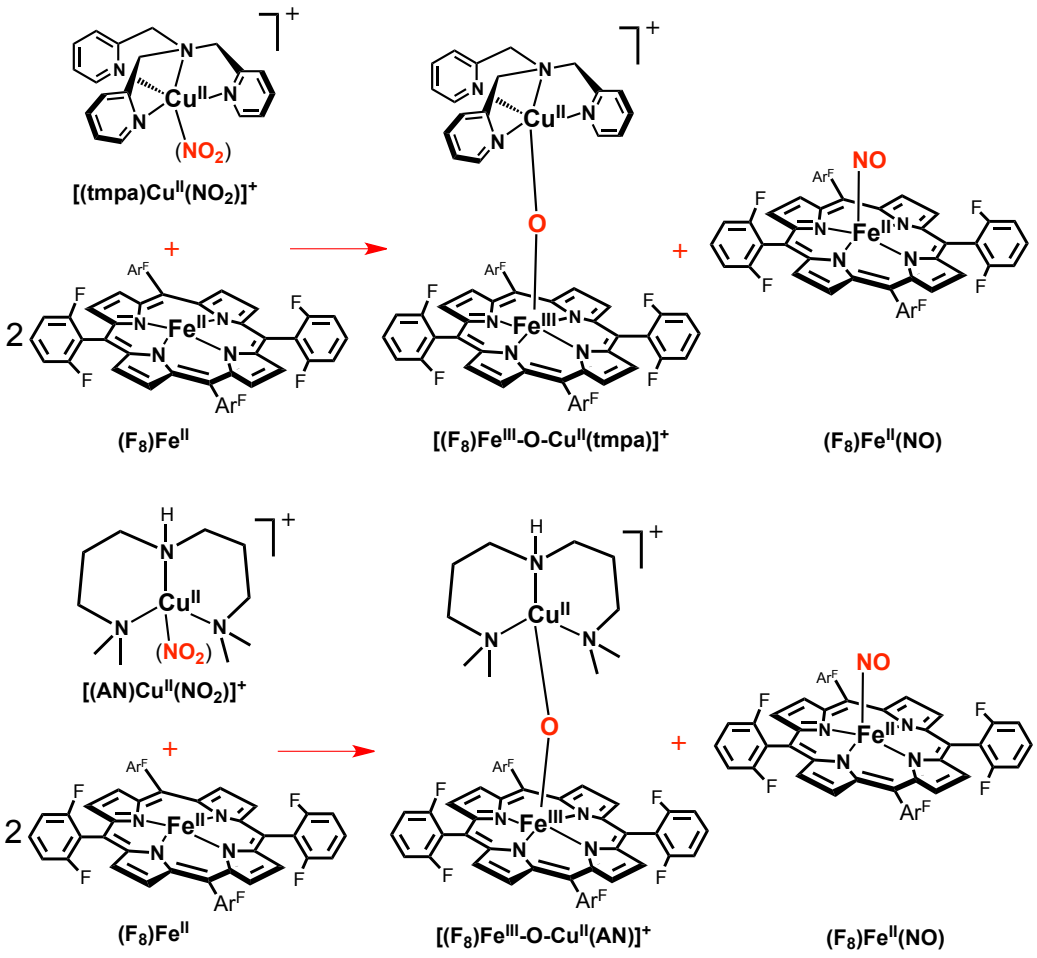

Top: Reaction with 1 equiv of $[(tmpa)Cu^{II}(NO_2)][B(C_6F_5)_4]$. *Bottom*: Reaction with 1 equiv of $[(AN)Cu^{II}(NO_2)](CF_3SO_3)$.

heme provides the one electron required for the reaction, where nitrite (formally NO^+) is reduced and one oxygen atom derived from the nitrite is trapped as an oxo-bridged Fe^{III}–O–Cu^{II} product. See below for further discussion on possible reaction mechanisms.

To expand on the initial study, we decided to compare and contrast the reactivity now using a copper(II)–nitrito complex with a tridentate ligand instead of a tetradentate ligand. We know from many years of study of dioxygen reduction chemistry using copper ion complexes that ligand denticity, along with other factors such as the exact nature of the donor (e.g., alkylamine vs pyridyl) and the chelate ring size (e.g., five-membered vs six-membered ring), governs the structures obtained, the redox properties of derived Cu^{II}/Cu^{I} complexes, and thus the overall reactivity.[50–55] When $[(AN)Cu^{II}(NO_2)]^+$ with a tridentate nitrogen chelate is reacted with 2 equiv of $(F_8)Fe^{II}$, the same overall reaction occurs (Scheme 2). The corresponding μ-oxo complex $[(F_8)Fe^{III}–O–Cu^{II}(AN)]^+$ (λ_{max} = 439 nm) forms in good yield (more than 80%), on the basis of the quantitative analyses of UV–vis and EPR spectra (Figure 3). $[(F_8)Fe^{III}–O–Cu^{II}(AN)]^+$ was previously structurally and spectroscopically characterized,[56] but this species is somewhat unstable with respect to hydrolysis owing to its very basic μ-oxo ligand, especially compared with its analogue $[(F_8)Fe^{III}–O–Cu^{II}(tmpa)]^+$).[57,58] Thus, some bridge protonation and bridge breaking occurs, leading to the mononuclear complex $(F_8)Fe^{III}(OH)$ and $(AN)Cu^{II}–X$ (X is solvent or hydroxide) species. Here, small amounts of these complexes are detected by a combination of UV–vis and EPR spectroscopies. The other product, $(F_8)Fe^{II}(NO)$, resulting from capture of $NO_{(g)}$ by one of the two ferrous hemes present in the reaction mixture is obtained in

essentially quantitative yield, on the basis of UV–vis spectroscopy (λ_{max} = 399 nm),[36,59] EPR spectroscopy (Figure 3), and IR spectroscopy (ν_{NO} = 1,685 cm^{-1}).

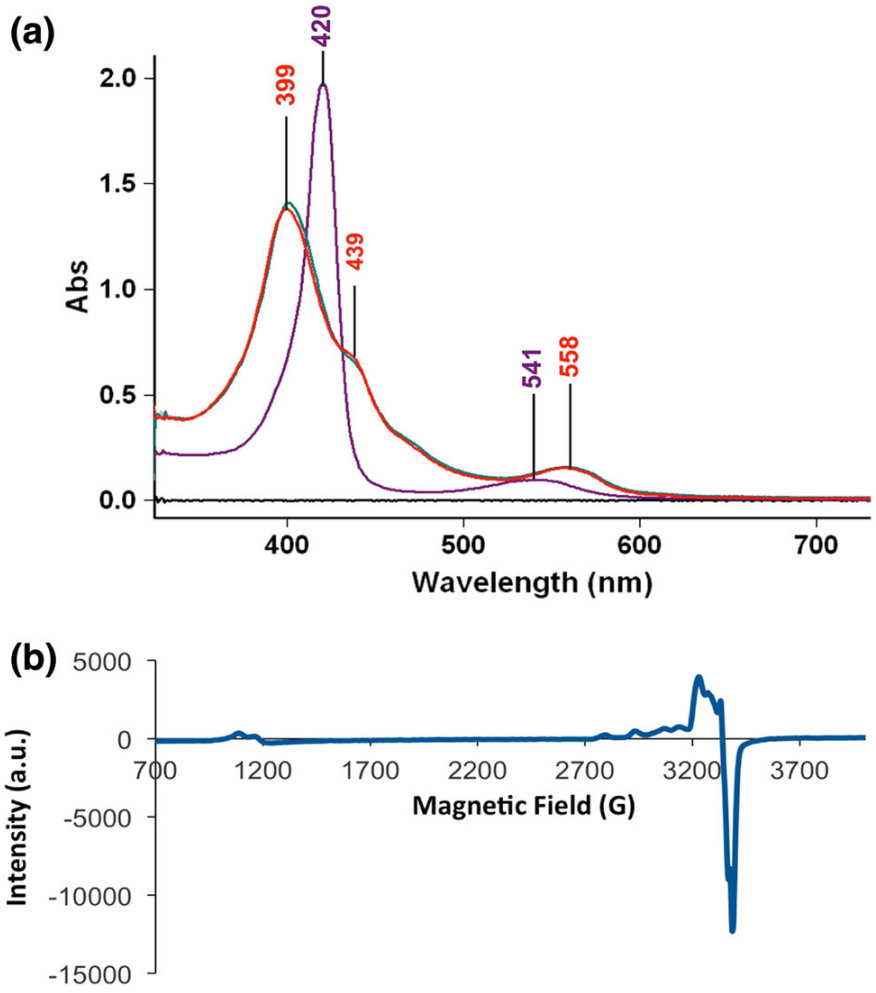

Figure 3. (a) UV–vis spectra of $(F_8)Fe^{II}$ (8 μM) [purple spectrum; λ_{max} = 420 nm (Soret), 541 nm] and the reaction solution of $(F_8)Fe^{II}$ and $[(AN)Cu^{II}(NO_2)](CF_3SO_3)$ after stirring for 10 min (15 μM) (green spectrum) and 1 h (15 μM) [red spectrum; λ_{max} = 399 nm (Soret), 439 nm (Soret), and 558 nm] in acetone at room temperature. **(b)** EPR spectrum of the products of the reaction of $(F_8)Fe^{II}$ and $[(AN)Cu^{II}(NO_2)](CF_3SO_3)$ in acetone at 20 K (2 mM).

When comparing this new system using the nitrite complex $[(AN)Cu^{II}(NO_2)]^+$ with that of the reaction using $[(tmpa)Cu^{II}(NO_2)]^+$, we observe the reaction is roughly

twice as fast for the former, on the basis of monitoring the disappearance of the UV–vis band for $(F_8)Fe^{II}$ (λ_{max} = 420 nm). This rate effect may be due to the differing nitrite coordination mode, bidentate versus unidentate in the AN versus the tmpa copper complexes (see "Discussion"). It is worth mentioning that a detailed kinetic analysis was not performed, owing to the exceptional instability of the product $[(F_8)Fe^{III}–O–Cu^{II}(AN)]^+$ when studied at concentrations used for UV–vis monitoring (see "Materials and methods").

In the second set of experiments, to study the role of the reducing ability of the ferrous heme center in nitrite reduction to $NO_{(g)}$, we used a different heme with strong electron donating peripheral substituents, $(TMPP)Fe^{II}$. This ferrous heme was generated by reduction of $(TMPP)Fe^{III}(Cl)$ under anaerobic conditions and was characterized by UV–vis spectroscopy, ^{1}H-NMR spectroscopy, and elemental analysis. Also, as one of the expected reaction products, the μ-oxo complex $[(TMPP)Fe^{III}–O–Cu^{II}(tmpa)]^+$ (Scheme 3) was synthesized by bubbling dry dioxygen through a one-to-one mixture of the reduced heme and copper mononuclear complexes, and it was characterized by UV–vis spectroscopy, ESI-MS, and elemental analysis. $[(TMPP)Fe^{III}–O–Cu^{II}(tmpa)][B(C_6F_5)_4]$ has a distinctive red-shifted Soret band ($\lambda_{max} \approx$ 443 nm; Figure S8),[57,60] which is quite different from other high-spin ferric hemes such as is observed for the μ-oxo porphyrin–iron(III) dimer, $[(TMPP)Fe^{III}]_2O$ [61] ($\lambda_{max} \approx$ 412 nm in acetone), and $(TMPP)Fe^{III}(OH)$ ($\lambda_{max} \approx$ 434 nm) (Figure S14). The authentic sample of $[(TMPP)Fe^{II}(NO)$ (ν_{NO} = 1,677 cm^{-1}), as the other expected product, was also generated in situ by bubbling excess NO gas into the solution of $[(TMPP)Fe^{II}$ in acetone under a nitrogen atmosphere, and it was characterized by UV–vis and IR spectroscopies.

Scheme 3. Reaction of 2 equiv of (TMPP)Fe^{II} with [(tmpa)$Cu^{II}(NO_2)$][$B(C_6F_5)_4$].

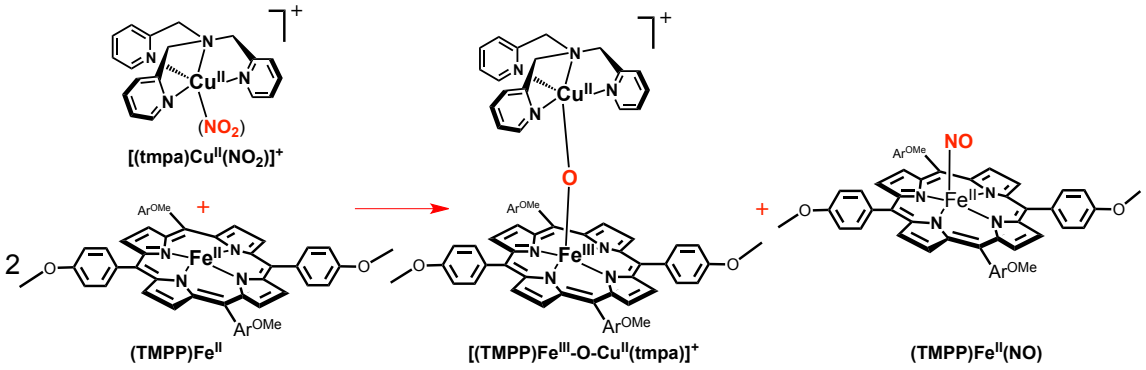

Reacting 1 equiv of the cupric–nitrite complex, [(tmpa)$Cu^{II}(NO_2)$]$^+$, with 2 equiv of the more electron rich porphyrin, (TMPP)Fe^{II}, results in same overall redox reaction, converting nitrite to $NO_{(g)}$ (Scheme 3). We observed the reaction proceeds with about the same rate as for the combination of (F_8)Fe^{II} and [(tmpa)$Cu^{II}(NO_2)$]$^+$, implying that the greater electron-donating ability of this ferrous heme does not accelerate the nitrite reduction reaction. The quantitative analyses of UV–vis and EPR spectra of the reaction products and authentic samples confirmed the generation of a one-to-one mixture of the ferrous heme–nitrosyl (TMPP)Fe^{II}(NO) (λ_{max} = 410 nm) and the corresponding μ-oxo complex [(TMPP)Fe^{III}–O–Cu^{II}(tmpa)]$^+$ (λ_{max} = 443 nm) in high yield (Figure 4).

In the final system investigated here, we used the copper(II)–nitrite complex with a tridentate (rather than a tetradentate) chelate, with the electron-rich ferrous heme. Reaction of [(AN)$Cu^{II}(NO_2)$]$^+$ with 2 equiv of (TMPP)Fe^{II} was studied (Scheme 4). IR spectroscopy (ν_{NO} = 1,677 cm^{-1}) directly indicated the production of the nitrosyl complex, (TMPP)Fe^{II}(NO). However, according to the UV–vis spectra, there was no formation of the μ-oxo complex [(TMPP)Fe^{III}–O–Cu^{II}(tmpa)]$^+$ (Figure 5). This may be due to its very

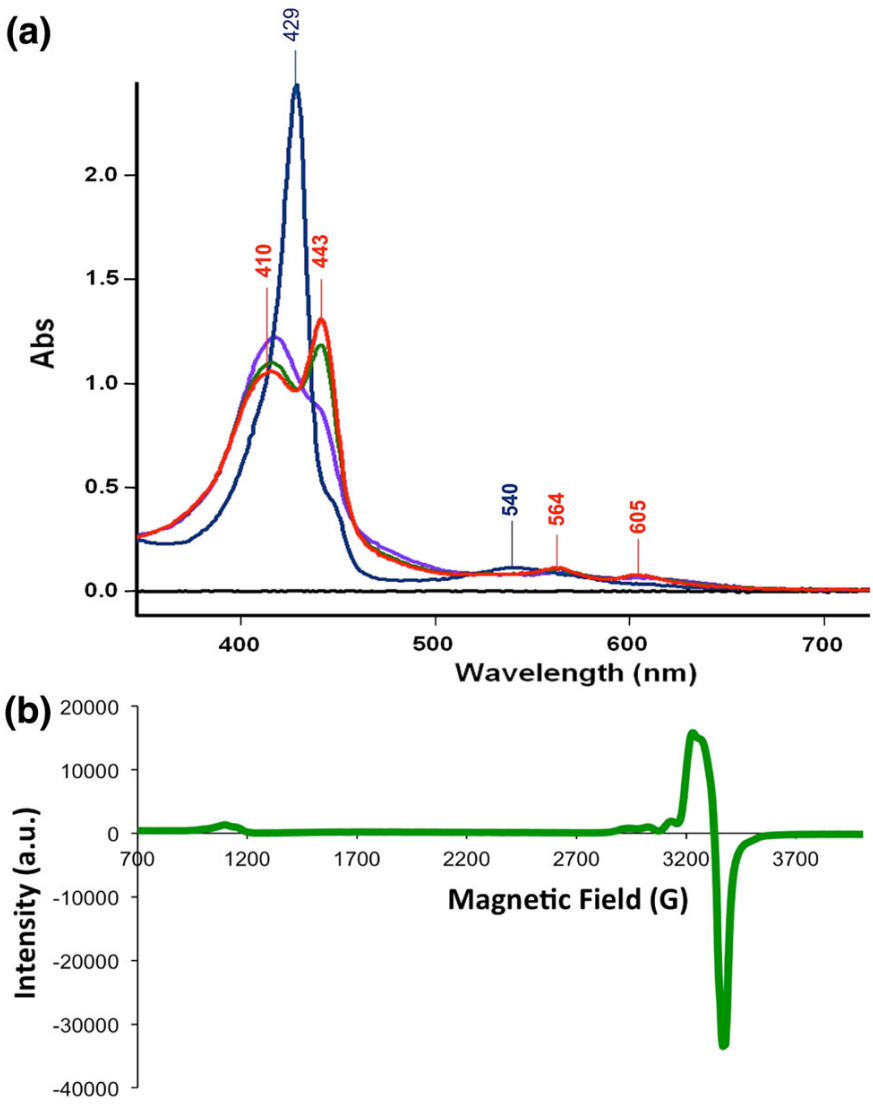

Figure 4. (a) UV–vis spectra of (TMPP)Fe^{II} (10 μM) [blue spectrum, λ_{max} = 429 nm (Soret), 540 nm] and the reaction solution of (TMPP)Fe^{II} and [(tmpa)$Cu^{II}(NO_2)$][$B(C_6F_5)_4$], after stirring for 10 min (10 μM) (purple spectrum) and 1 h (10 μM) [red spectrum; λ_{max} = 410 nm (Soret), 443 nm (Soret), 564 nm, and 605 nm) in acetone at room temperature. After the mixture had been stirred for 3 h, the green spectrum was recorded. **(b)** EPR spectrum of the products of the reaction of (TMPP)Fe^{II} and [(tmpa)$Cu^{II}(NO_2)$][$B(C_6F_5)_4$] in acetone at 20 K (2 mM).

basic μ-oxo ligand, resulting in instability toward protonation and hydrolysis. This was further validated when all attempts at the synthesis of the authentic μ-oxo complex by oxidation of reduced complexes (by O_2 bubbling, as described earlier) were unsuccessful,

even when using MeTHF as a "drier" solvent. The species which is instead generated is the μ-hydroxo complex $[(TMPP)Fe^{III}\text{-}(OH)\text{-}Cu^{II}(tmpa)]^{+}$ (λ_{max} = 417 nm), possessing a distinctive Soret band, different from that for the mononuclear complex, $(TMPP)Fe^{III}(OH)$ (λ_{max} = 434 nm). In spite of the difficulties in this system, comparison of the UV–vis spectra for the actual reaction with those of authentic compounds indicates the nitrite reduction reaction outlined in Scheme 4 occurs in very good yield. Nitrite analysis also confirmed the conversion of nitrite to $NO_{(g)}$ is nearly quantitative, as no trace of nitrite was detected following the reaction.

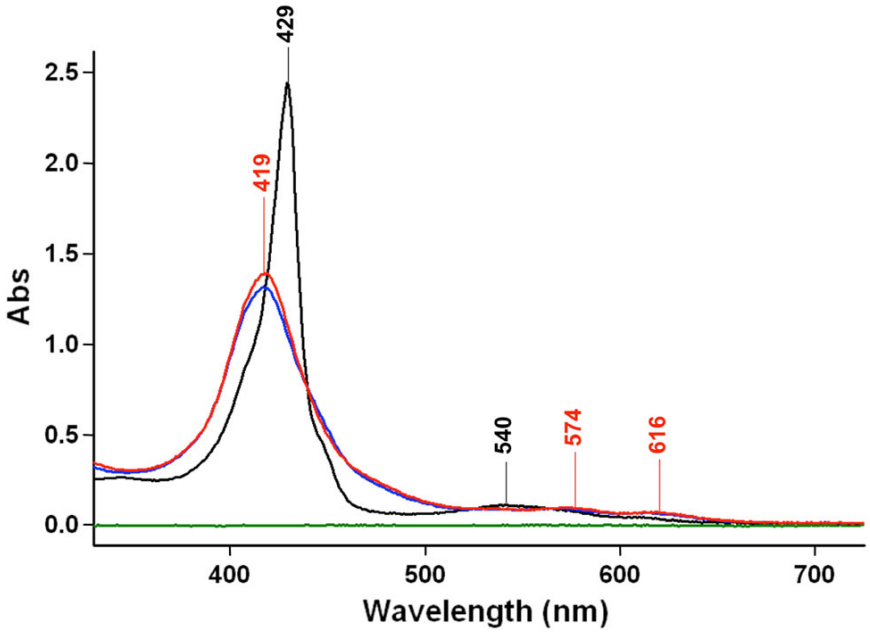

Figure 5. UV–vis spectra of $(TMPP)Fe^{II}$ (10 μM) [black spectrum; λ_{max} = 429 nm (Soret), 540 nm] and the reaction solution of $(TMPP)Fe^{II}$ and $[(AN)Cu^{II}(NO_2)](CF_3SO_3)$, after stirring for 10 min (10 μM) (blue spectrum) and 1 h (10 μM) [red spectrum; λ_{max} = 410 nm (Soret), 443 nm (Soret), 564 nm, and 605 nm] in acetone at room temperature. See also the text.

Scheme 4. Reaction of 2 equiv of (TMPP)Fe^{II} with [(AN)$Cu^{II}(NO_2)$](CF_3SO_3).

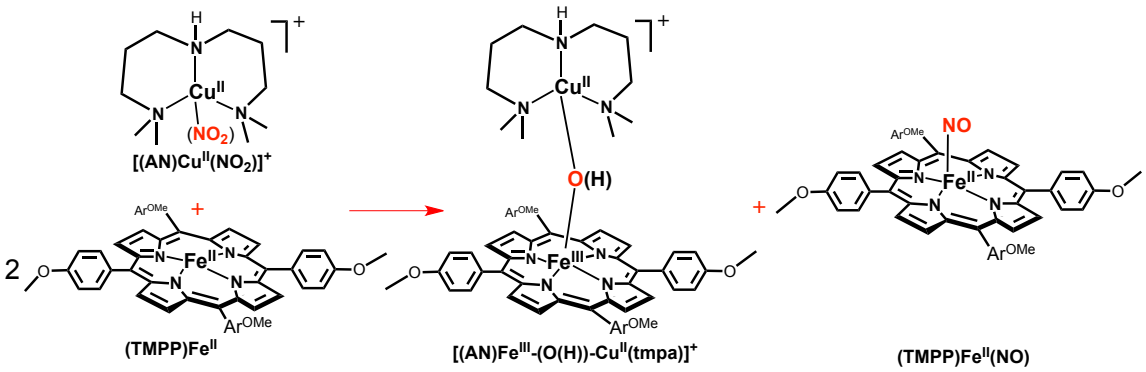

The rate of ferrous heme disappearance for this system (Scheme 4) could be semiquantitatively described as being a few times faster than for the reaction of the same heme with the [(tmpa)$Cu^{II}(NO_2)$]$^+$ analogue (Scheme 3). This observation is the same as that for the reaction of the more electron poor heme, (F_8)Fe^{II}, where the reaction of the nitrito complex with the tridentate chelate AN, [(AN)$Cu^{II}(NO_2)$]$^+$, is again faster than with [(tmpa)$Cu^{II}(NO_2)$]$^+$ (bearing a tetradentate chelate). Thus, in both cases, faster reduction of nitrite to $NO_{(g)}$ was observed when the ligation of nitrite is bidentate versus unidentate.

4. Discussion

In "Results", we demonstrated the heme/copper assembly mediated reduction of nitrite to $NO_{(g)}$, using two different ferrous hemes reacting with either of two cupric–nitrite complexes, one having tetradentate N_4 (TMPA) chelation and the other using a

tridentate N_3 (AN) ligand. Very clean and high-yielding reactions occur giving $NO_{(g)}$, as trapped by our ferrous heme, and an oxo-bridged heme/copper product is also produced. The reaction stoichiometry is indicated in Scheme 1, bottom. Control experiments previously reported for $(F_8)Fe^{II}$ and $[(tmpa)Cu^{I}(MeCN)]^{+}$ [36] showed that neither of these reduced complexes, nor the combination of the two, is capable of reducing nitrite to NO. $[(AN)Cu^{I}]^{+}$ and $(TMPP)Fe^{II}$ by themselves are also unreactive to nitrite ion (Figs. S12, S13).*

We believe that these reactions to a significant extent relate to what happens in C*c*O nitrite reductase biochemistry. In our synthetic coordination chemistry system, a second heme equivalent is present in order to trap the $NO_{(g)}$ produced, allowing 100% conversion. If less than two molar equivalents of ferrous heme are added, the reaction occurs only partially, because the $NO_{(g)}$ produced reacts very rapidly with any ferrous heme that has not reacted with the cupric–nitrite complex. In the enzyme, of course this does not occur, but since only oxidized metal ions are present in the active site following nitrite reduction, i.e., iron(III) and copper(II), the $NO_{(g)}$ produced escapes since $NO_{(g)}$ binds at best weakly to these oxidized metal ions (Scheme 1, bottom). As concerns possible reaction mechanisms, we can start by drawing two significant conclusions from the results presented. The first is that the reducing ability of the heme does not seem to matter in determining the course of the overall reaction, and more importantly it does not affect the observed reaction rate (but, of, course in the absence of detailed kinetics). Yet, we can deduce that the electron required for nitrite (formally NO^{+}) reduction comes from

* In further control experiments, combinations of reduced complexes, $(F_8)Fe^{II}/[(AN)Cu^{I}]^{+}$, $(TMPP)Fe^{II}/[(tmpa)Cu^{I}(MeCN)]^{+}$, and $(TMPP)Fe^{II}/[(AN)Cu^{I}]^{+}$, were studied. We observed slow reactivity toward nitrite ion, hours compared with minutes for the Fe^{II}/Cu^{II}–nitrite "parent" reactions, and the final solutions appeared to be a mixtures of the complexes.

the heme iron(II). We know this because control experiments related to these systems reported earlier[36] showed that a ferric heme with added nitrite does not react with either ligand–copper(I) complex (see Figure 6).

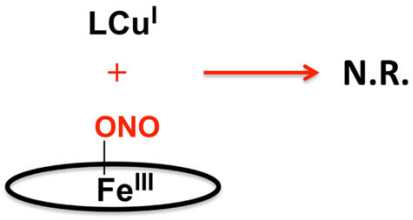

Figure 6. Reaction of ferric heme nitrite with cuprous complex (N.R. is no reaction)

In fact, from electrochemical measurements,[36] we know that for the case of ferrous heme $(F_8)Fe^{II}$, the ligand–copper(I) complexes are chemically stronger reductants. So, the ferrous heme supplies the one electron required in the reaction, but when a stronger reductant is used, $(TMPP)Fe^{II}$, as compared with $(F_8)Fe^{II}$, the ferrous heme reduction of nitrite bound to copper(II) does not proceed at an observably greater overall reaction rate. Thus, the electron-transfer reduction apparently does not occur in the rate-determining step.

A second, perhaps key observation is that in a relative sense, the reactions of $[(AN)Cu^{II}(NO_2)]^+$ with ferrous hemes are faster than those of $[(tmpa)Cu^{II}(NO_2)]^+$. We believe that this is an effect of the differing coordination of nitrite in the two cupric complexes. This quite likely leads to differing approaches of the cupric–nitrite complex to form a ferrous heme–(nitrite)–cupric assembly (Scheme 5). As precedent for this supposition, it has been proposed that enzymatic nitrite reduction in heme enzymes

occurs either by nitrite nitrogen coordination or by oxygen ligation to the iron and that these lead to alternative courses of reaction with accompanying differing kinetic behavior.[62–65]

With $[(AN)Cu^{II}(NO_2)]^+$, *O,O'*-bidentate nitrite coordination (vide supra) allows easier approach of a nitrogen atom to the ferrous heme, i.e., favoring nitrogen (nitro) coordination to the iron(II) ion (Scheme 5a), quite likely in the rate-determining step. Then, electron transfer from iron(II) to the bridged nitrite moiety could readily lead to an $[(AN)Cu^{II}(oxo)]$ (formally oxo is O^{2-}) species and ashort-lived ferric–nitrosyl complex; the latter would readily lose $NO_{(g)}$ as a gas, especially in the presence of an exogenous (the second equivalent) ferrous heme, and the ferric ion can easily couple to the cupric–oxo species, giving very kinetically stable μ-oxo compounds $[(porphyrinate)Fe^{III}–O–Cu^{II}(AN)]^+$ (porphyrinate is F_8 or TMPP) (Scheme 5a).

As observed in studies on nitrite reduction by heme protein bacterial nitrite reductases and/or myoglobin,[62–65] the approach of the nitrite to the ferrous heme, either via the nitrogen atom or the oxygen atom, is controlled by factors related to the binding pocket, especially nitrite oxygen atom hydrogen bonding from nearby protein amino acid residues. In essence, the cupric ion in the present heme/copper assemblies plays an analogous role, as a Lewis acid surrogate of a proton which (1) orients/directs the nitrite anion to favor iron nitrogen binding [for the $(AN)Cu^{II}$ complex] or oxygen binding [in the case of $(tmpa)Cu^{II}$] and (2) acts as a strong oxo acceptor [note that copper(II) is very oxophilic], which facilitates nitrite (N–O) bond cleavage, leading to subsequent formation of $NO_{(g)}$ along with a μ-oxo heme/copper complex. We cannot, however, rule out a mechanism (not shown) in which the exogenous ferrous heme reduces (by electron

transfer) the intermediate ferric–nitrosyl complex (just mentioned) followed by coupling of the Cu^{II}–oxo moiety to the newly produced ferric ion.

Scheme 5. Proposed reaction mechanisms for nitrite reductase chemistry mediated by the heme/copper assembly. Also, see text.

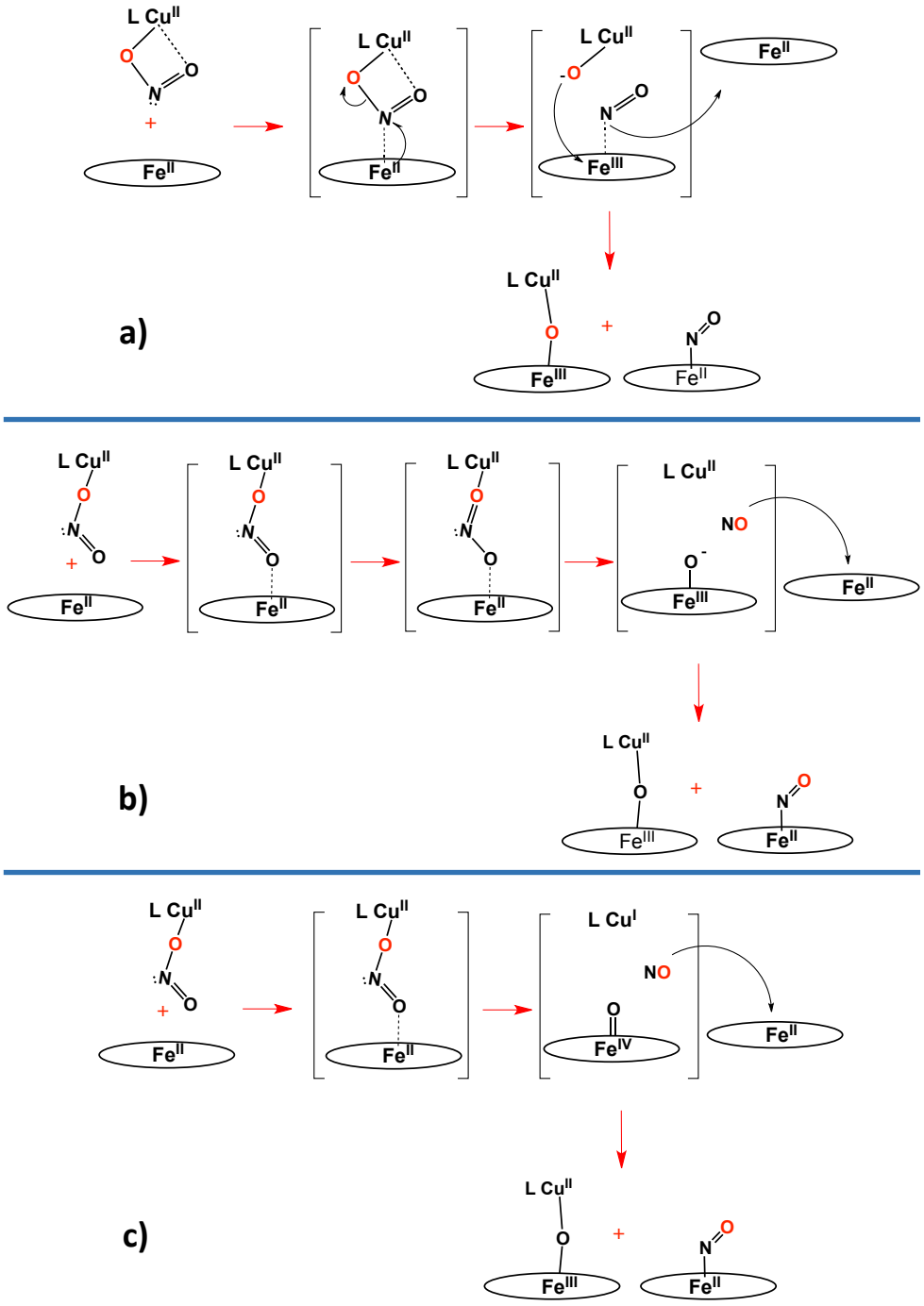

For reaction of $[(tmpa)Cu^{II}(NO_2)]^+$ with either ferrous heme, we envision that the oxygen unidentate nitrite copper(II) coordination could very well lead to different reaction mechanisms, as outlined in Scheme 5 b and c. Now, the nitrito oxygen atom far from and not coordinated to the cupric center approaches the iron(II) ion, whereupon (1) electron transfer occurs, leading to a short-lived ferric–oxo species, (2) $NO_{(g)}$ forms, escapes, and is trapped by the second ferrous heme, and (3) a cupric complex is generated. The $Fe^{III}–O^-$ couples to the ligand–copper(II) complex, giving $[(porphyrinate)Fe^{III}–O–Cu^{II}(tmpa)]^+$ (Scheme 5b). An alternative but interesting mechanistic proposal would be something like that depicted in Scheme 5c, where the nitrito oxygen atom furthest from copper approaches the iron(II) ion and formally two-electron oxygen-atom transfer occurs, giving a high-valence Fe(IV)=O species, $NO_{(g)}$, and a corresponding cuprous complex; $NO_{(g)}$ is again trapped by a second ferrous heme and the Fe(IV)=O and copper(I) moieties couple to give the product $[(porphyrinate)Fe^{III}–O–Cu^{II}(tmpa)]^+$. A precedent for such a mechanism exists. For instance, oxo transfer to an active-site iron has been previously suggested as a mechanistic alternative in nitric oxide reductase biochemistry.[66,67] Also, we have previously demonstrated that ligand–copper(I) complexes do react with (porphyrinate) Fe(IV)=O species to generate the corresponding μ-oxo heme/copper complex.[56]

In addition to the courses of the reaction depicted in Scheme 5 b and c, we suggest one other possibility, which is that in all cases, with either $[(tmpa)Cu^{II}(NO_2)]^+$ or $[(AN)Cu^{II}(NO_2)]^+$, nitrite ion nitrogen-atom coordination to the ferrous heme is what leads to a productive reaction, with nitrite (N–O) bond cleavage and NO gas formation. Such coordination is favored on the basis of known (bio)chemistry and expectations from

"hard–soft" acid–base considerations. So, even for the chemistry with $[(tmpa)Cu^{II}(NO_2)]^+$, a successful reaction may require dissociation of nitrite from the cupric ion and/or isomerization or rearrangement so the nitrite nitrogen atom can reach and bind the reduced heme. Perhaps this accounts for the generally slower kinetics observed for the reactions of $[(tmpa)Cu^{II}(NO_2)]^+$ with either ferrous heme complex. Further studies will be required to address these mechanistic considerations.

5. Conclusion

Our interest in small-molecule activation at heme/copper centers, such as O_2 reduction,[68] $NO_{(g)}$ reductive coupling,[41,59] $NO_{(g)}$ oxidation by an oxidized heme/copper center to give nitrite, and nitrite reduction by a partially reduced heme/copper assembly to $NO_{(g)}$,[36] has led us to expand on our previous initial report for the latter, nitrite reductase chemistry with heme/copper assemblies. Such chemistry occurs in the mitochondria of cells, generating additional $NO_{(g)}$, as needed by cellular demands, such as in hypoxia. Here, with combinations of ferrous or cupric–nitrite complexes, we have shown that NO_2^- can be readily reduced to $NO_{(g)}$, with the electron coming from the ferrous heme. Clean, stoichiometric, and high-yielding examples of such reactions were presented and were accompanied by detailed chemical and spectroscopic characterization. Although detailed kinetic analyses could not be performed, qualitative but clear trends in reaction rates and results as a function of heme or copper ligation tendencies and/or redox properties were observed. On these bases, possible reaction mechanisms were proposed and discussed, highlighting how the details of particular

coordination chemistry situations may influence the course of reactions. Of particular note is that the cupric ion binding mode of nitrite is controlled by the denticity of the chelate on copper, leading to how the coordination of nitrite to the ferrous heme occurs, via either nitrogen-atom or oxygen-atom binding. Such discrimination in enzymes with nitrite reductase activity occurs via heme pocket features, especially hydrogen bonding involving the nitrite anion. In C*c*O, the copper ion may serve exactly such a role, (1) orienting the nitrite for subsequent binding to the reduced heme and (2) acting as an oxo acceptor, as shown by the findings in the present synthetic chemistry study.

6. References

(1) Schopfer, M. P.; Wang, J.; Karlin, K. D. *Inorg. Chem.* **2010**, *49*, 6267.

(2) Tavares, P.; Pereira, A. S.; Moura, J. J. G.; Moura, I. *J. Inorg. Biochem.* **2006**, *100*, 2087.

(3) Zumft, W. G. *Microbiol. Mol. Biol. Rev*. **1997**, *61*, 533.

(4) Poole, R. K. *Biochem. Soc. Trans.* **2005**, *33*,176.

(5) Samouilov, A.; Kuppusamy, P.; Zweier, J. L. *Arch. Biochem. Biophys.* **1998**, *357*, 1.

(6) Dezfulian, C.; Raat, N.; Shiva, S.; Gladwin, M. T. *Cardiovasc. Res.* **2007**, *75*, 327.

(7) Lundberg, J. O.; Gladwin, M. T.; Ahluwalia, A.; Benjamin, N.; Bryan, N. S.; Butler, A.; Cabrales, P.; Fago, A.; Feelisch, M.; Ford, P. C.; Freeman, B. A.; Frenneaux, M.; Friedman, J.; Kelm, M.; Kevil, C. G.; Kim-Shapiro, D. B.; Kozlov, A. V.; Lancaster, J. R.; Lefer, D.J.; McColl, K.; McCurry, K.; Patel, R. P.; Petersson, J.; Rassaf, T.; Reutov, V. P.; Richter-Addo, G. B.; Schechter, A.; Shiva, S.; Tsuchiya, K.; van Faassen, E.E.; Webb, A. J.; Zuckerbraun, B. S.; Zweier, J. L.; Weitzberg, E. *Nat. Chem. Biol.* **2009**, *5*, 865.

(8) van Faassen, E. E.; Bahrami, S.; Feelisch, M.; Hogg, N.; Kelm, M.; Kim-Shapiro, D. B.; Kozlov, A. V.; Li, H.; Lundberg, J. O.; Mason, R.; Nohl, H.; Rassaf, T.; Samouilov, A.; Slama-Schwok, A.; Shiva, S.; Vanin, A. F.; Weitzberg, E.; Zweier, J.; Gladwin, M. T. *Med. Res. Rev.* **2009**, *29*, 683.

(9) Fukuto, J. M.; Carrington, S. J.; Tantillo, D. J.; Harrison, J. G.; Ignarro, L. J.; Freeman, B. A.; Chen, A.; Wink, D. A. *Chem. Res. Toxicol.* **2012**, *25*, 769.

(10) Kozlov, A. V.; Staniek, K.; Nohl, H. *FEBS Lett.* **1999**, *454*, 127.

(11) Crane, B. R. *Biochem. Soc. Trans.* **2008**, *036*, 1149.

(12) Zhu, Y.; Silverman, R. B. *Biochemistry* **2008**, *47*, 2231.

(13) Gladwin, M. T.; Schechter, A. N.; Kim-Shapiro, D. B.; Patel, R. P.; Hogg, N.; Shiva, S.; Cannon, R. O.; Kelm, M.; Wink, D. A.; Espey, M. G.; Oldfield, E. H.; Pluta, R. M.; Freeman, B.A.; Lancaster, J. R.; Feelisch, M.; Lundberg, J. O. *Nat. Chem. Biol.* **2005**, *1*, 308.

(14) Gladwin, M. T.; Shiva, S. *Circ. Res.* **2009**, *104*, 1136.

(15) Zweier, J. L.; Samouilov, A.; Kuppusamy, P. *Biochim. Biophys. Acta* **1999**, *1411*, 250.

(16) Cosby, K.; Partovi, K. S.; Crawford, J. H.; Patel, R. P.; Reiter, C. D.; Martyr, S.; Yang, B. K.; Waclawiw, M. A.; Zalos, G.; Xu, X. L.; Huang, K. T.; Shields, H.; Kim-Shapiro, D. B.; Schechter, A. N.; Cannon, R. O.; Gladwin, M. T. *Nat. Med.* **2003**, *9*,1498.

(17) Shiva, S.; Huang, Z.; Grubina, R.; Sun, J. H.; Ringwood, L. A.; MacArthur, P. H.; Xu, X. L.; Murphy, E.; Darley-Usmar, V. M.; Gladwin, M. T. *Circ. Res.* **2007**, *100*, 654.

(18) Shiva, S.; Rassaf, T.; Patel, R. P.; Gladwin, M. T. *Cardiovasc. Res.* **2011**, *89*, 566.

(19) Rassaf, T.; Flogel, U.; Drexhage, C.; Hendgen-Cotta, U.; Kelm, M.; Schrader, J. *Circ. Res.* **2007**, *100*, 1749.

(20) Totzeck, M.; Hendgen-Cotta, U. B.; Luedike, P.; Berenbrink, M.; Klare, J. P.; Steinhoff, H. J.; Semmler, D.; Shiva, S.; Williams, D.; Kipar, A.; Gladwin, M. T.; Schrader, J.; Kelm, M.; Cossins, A. R.; Rassaf, T. *Circulation* **2012**, *126*, 325.

(21) Tiso, M.; Tejero, J.; Basu, S.; Azarov, I.; Wang, X.; Simplaceanu, V.; Frizzell, S.; Jayaraman, T.; Geary, L.; Shapiro, C.; Ho, C.; Shiva, S.; Kim-Shapiro, D. B.; Gladwin, M. T. *J. Biol. Chem.* **2011**, *286*, 18277.

(22) Basu, S.; Azarova, N. A.; Font, M. D.; King, S. B.; Hogg, N.; Gladwin, M. T.; Shiva, S.; Kim-Shapiro, D. B. *J. Biol. Chem*. **2008**, *283*, 32590.

(23) Gladwin, M. T. *Nat. Chem. Biol.* **2005**, *1*, 245.

(24) Lundberg, J. O.; Weitzberg, E.; Gladwin, M. T. *Nat. Rev. Drug. Discov.* **2008**, *7*, 156.

(25) de Mel, A.; Murad, F.; Seifalian, A. M. *Chem. Rev.* **2011**, *111*, 5742.

(26) Babcock, G. T.; Wikström, M. *Nature* **1992**, *356*, 301.

(27) Ferguson-Miller, S.; Babcock, G. T. *Chem. Rev.* **1996**, *96*, 2889.

(28) Kim, E.; Chufán, E. E.; Kamaraj, K.; Karlin, K. D. *Chem. Rev.* **2004**, *104*, 1077.

(29) Poyton, R. O.; Ball, K. A. *Discov. Med.* **2011**, *57*, 154.

(30) Shiva, S. *Redox. Biol.* **2013**, *1*, 40.

(31) Castello, P. R.; David, P. S.; McClure, T.; Crook, Z.; Poyton, R. O. *Cell Metab.* **2006**, *3*, 277.

(32) Gupta, K. J.; Stoimenova, M.; Kaiser, W. M. *J. Exp. Bot.* **2005**, *56*, 2601.

(33) Castello, P. R.; Woo, D. K.; Ball, K.; Wojcik, J.; Liu, L.; Poyton, R. O. *Proc. Natl. Acad. Sci. U.S.A.* **2008**, *105*, 8203.

(34) Poyton, R. O.; Castello, P. R.; Ball, K. A.; Woo, D. K.; Pan, N. *Ann. N.Y. Acad. Sci.* **2009**, *1177*, 48.

(35) Gupta, K. J.; Igamberdiev, A. U. *Mitochondrion* **2011**, *11*, 537.

(36) Hematian, S.; Siegler, M. A.; Karlin, K. D. *J. Am. Chem. Soc.* **2012**, *134*, 18912.

(37) Kopf, M.-A.; Neuhold, Y.-M.; Zuberbühler, A. D.; Karlin, K. D. *Inorg. Chem.* **1999**, *38*, 3093.

(38) Ghiladi, R. A.; Kretzer, R. M.; Guzei, I.; Rheingold, A. L.; Neuhold, Y.-M.; Hatwell, K. R.; Zuberbühler, A. D.; Karlin, K. D. *Inorg. Chem.* **2001**, *40*, 5754.

(39) Torres, J.; Sharpe, M. A.; Rosquist, A.; Cooper C. E.; Wilson, M. T. *FEBS Lett.* **2000**, *475*, 263.

(40) Ford, P. C.; Lorkovic, I. M. *Chem. Rev.* **2002**, *102*, 993.

(41) Wang, J.; Schopfer, M. P.; Sarjeant, A. A. N.; Karlin, K. D. *J. Am. Chem. Soc.* **2009**, *131*, 450.

(42) Schopfer, M. P.; Mondal, B.; Lee, D.-H.; Sarjeant, A. A. N.; Karlin, K. D. *J. Am. Chem. Soc*. **2009**, *131*, 11304.

(43) Liang, H.-C.; Zhang, C. X.; Henson, M. J.; Sommer, R. D.; Hatwell, K. R.; Kaderli, S.; Zuberbuehler, A. D.; Rheingold, A. L.; Solomon, E. I.; Karlin, K. D. *J. Am. Chem. Soc.* **2002**, *124*, 4170.

(44) Park, G. Y.; Deepalatha, S.; Puiu, S. C.; Lee, D.-H.; Mondal, B.; Narducci, Sarjeant, A. A.; del Rio, D.; Pau, M. Y. M.; Solomon, E. I.; Karlin, K. D. *J. Biol. Inorg. Chem.* **2009**, *14*, 1301.

(45) Vogel, K. M.; Kozlowski, P. M.; Zgierski, M. Z.; Spiro, T. G. *J. Am. Chem. Soc.* **1999**, *121*, 9915.

(46) Sheldrick, G. M. *Acta Crystallogr. Sect. A* **2008**, *64*, 112.

(47) Yang, L.; Powell, D. R.; Houser, R. P. *Dalton. Trans.* **2007**, 955.

(48) Mukhopadhyay, U.; Bernal, I.; Massoud, S. S.; Mautner, F. A. *Inorg. Chim. Acta* **2004**, *357*, 3673.

(49) Nakamoto, K. *Infrared and Raman Spectra of Inorganic and Coordination Compounds*; 5th Ed.; Wiley Interscience: New York, 1997; pp 48–53.

(50) Hatcher, L. Q.; Karlin, K. D. *J. Biol. Inorg. Chem.* **2004**, *9*, 669.

(51) Hatcher, L. Q.; Karlin, K. D. Adv. *Inorg. Chem.* **2006**, *58*, 131.

(52) Chufán, E. E.; Mondal, B.; Gandhi, T.; Kim, E.; Rubie, N. D.; Moënne-Loccoz, P.; Karlin, K. D. *Inorg. Chem.* **2007**, *46*, 6382.

(53) Kakuda, S.; Peterson, R. L.; Ohkubo, K.; Karlin, K. D.; Fukuzumi, S. *J. Am. Chem. Soc.* **2013**, *135*, 6513.

(54) Das, D.; Lee, Y.-M.; Ohkubo, K.; Nam, W.; Karlin, K. D.; Fukuzumi, S. *J. Am. Chem. Soc.* **2013**, *135*, 2825.

(55) Itoh, S. *Copper-Oxygen Chemistry*; Itoh, S., Karlin, K. D. Eds.; Wiley: Hoboken, 2011; pp 225–282.

(56) Halime, Z.; Kieber-Emmons, M. T.; Qayyum, M. F.; Mondal, B.; Gandhi, T.; Puiu, S. C.; Chufán, E. E.; Sarjeant, A. A. N.; Hodgson, K. O.; Hedman, B.; Solomon, E. I.; Karlin, K. D. *Inorg. Chem.* **2010**, *49*, 3629.

(57) Fox, S.; Nanthakumar, A.; Wikström, M.; Karlin, K. D.; Blackburn, N. J. *J. Am. Chem. Soc.* **1996**, *118*, 24.

(58) Obias, H. V.; van Strijdonck, G. P. F.; Lee, D.-H.; Ralle, M.; Blackburn, N. J.; Karlin, K. D. *J. Am. Chem. Soc.* **1998**, *120*, 9696.

(59) Wang, J.; Schopfer, M. P.; Puiu, S. C.; Sarjeant, A. A. N.; Karlin, K. D. *Inorg. Chem.* **2010**, *49*, 1404.

(60) Karlin, K. D.; Nanthakumar, A.; Fox, S; Murthy, N. N.; Ravi, N.; Huynh B. H.; Orosz, R. D.; Day, E. P. *J. Am. Chem. Soc.* **1994**, *116*, 4753.

(61) Helms, J. H.; Terhaar, L. W.; Hatfield, W. E.; Harris, D. L.; Jayaraj, K.; Toney, G. E.; Gold, A.; Mewborn, T. D.; Pemberton, J. R. *Inorg. Chem.* **1986**, *25*, 2334.

(62) Yi, J.; Heinecke, J.; Tan, H.; Ford, P. C.; Richter-Addo, G. B. *J. Am. Chem. Soc.* **2009**, *131*, 18119.

(63) Silaghi-Dumitrescu, R. *Inorg. Chem.* **2004**, *43*, 3715.

(64) Williams, P. A.; Fulop, V.; Garman, E. F.; Saunders, N. F. W.; Ferguson, S. J.; Hajdu, J. *Nature* **1997**, *389*, 406.

(65) Perissinotti, L. L.; Marti, M. A.; Doctorovich, F.; Luque, F. J.; Estrin, D. A. *Biochemistry* **2008**, *47*, 9793.

(66) Blomberg, L. M.; Blomberg, M. R. A.; Siegbahn, P. E. M. *Biochim. Biophys. Acta* **2006**, *1757*, 240.

(67) Blomberg, L. M.; Blomberg, M. R. A.; Siegbahn, P. E. M. *J. Biol. Inorg. Chem.* **2007**, *12*, 79.

(68) Halime, Z.; Kotani, H.; Li, Y.; Fukuzumi, S.; Karlin, K. D. *Proc. Natl. Acad. Sci. U.S.A.* **2011**, *108*, 13990.

7. Supporting Information

7.1. Characterization of Copper and Heme Complexes

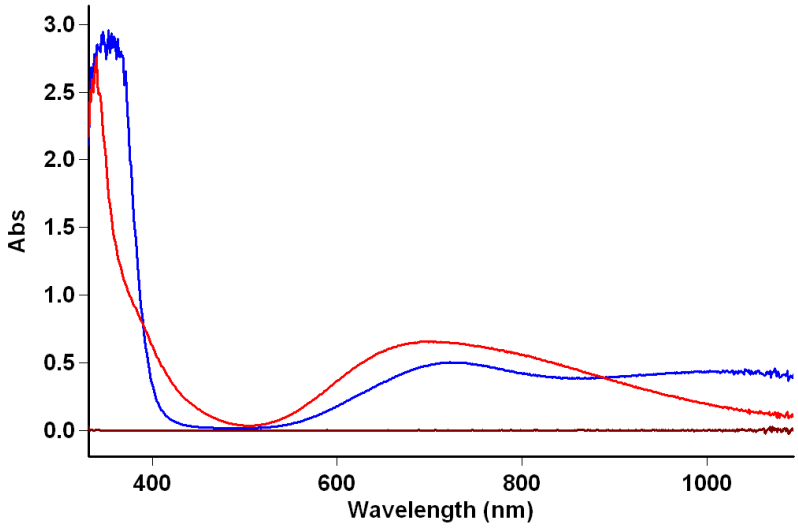

Figure S1. UV–vis spectra of $[(AN)Cu^{II}(Cl)](CF_3SO_3)$ (blue, λ_{max} = 720 and 1025 nm) and $[(AN)Cu^{II}(NO_2)](CF_3SO_3)$ (red, λ_{max} = 702 nm) 2mM in acetone.

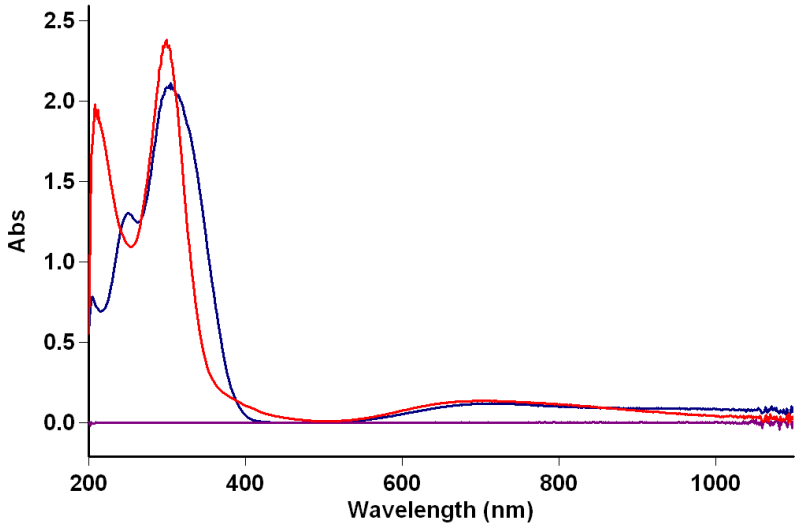

Figure S2. UV–vis spectra of $[(AN)Cu^{II}(Cl)](CF_3SO_3)$ (blue, λ_{max} = 722 and 1000 nm) and $[(AN)Cu^{II}(NO_2)](CF_3SO_3)$ (red, λ_{max} = 702 nm) 2mM in MeOH.

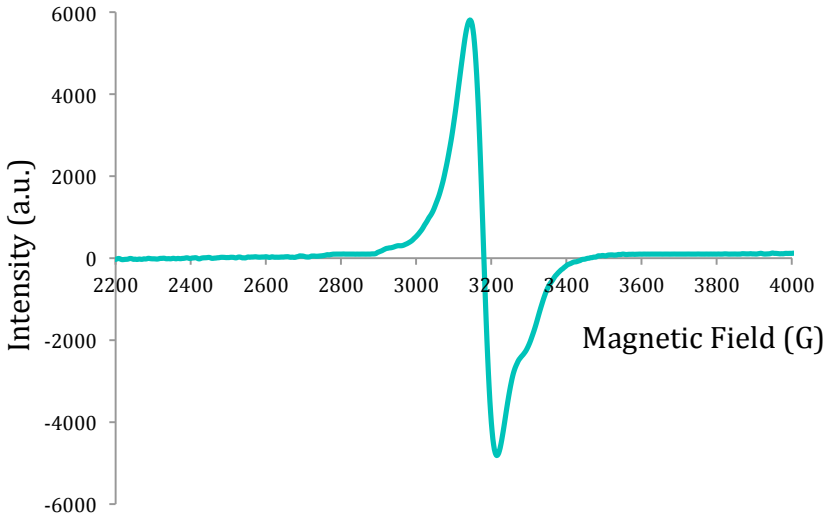

Figure S3. EPR spectrum of $[(AN)Cu^{II}(Cl)](CF_3SO_3)$ (2mM) in acetone at 22 K.

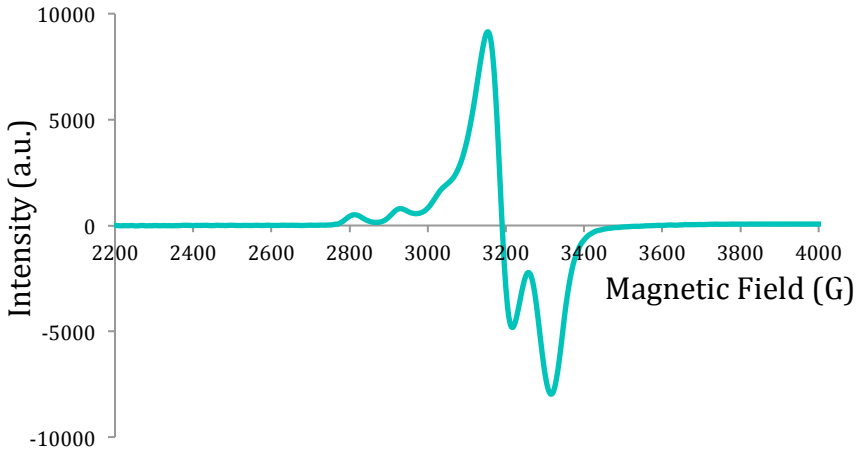

Figure S4. EPR spectrum of $[(AN)Cu^{II}(Cl)](CF_3SO_3)$ (2mM) in THF:MeCN (4:1) at 15 K.

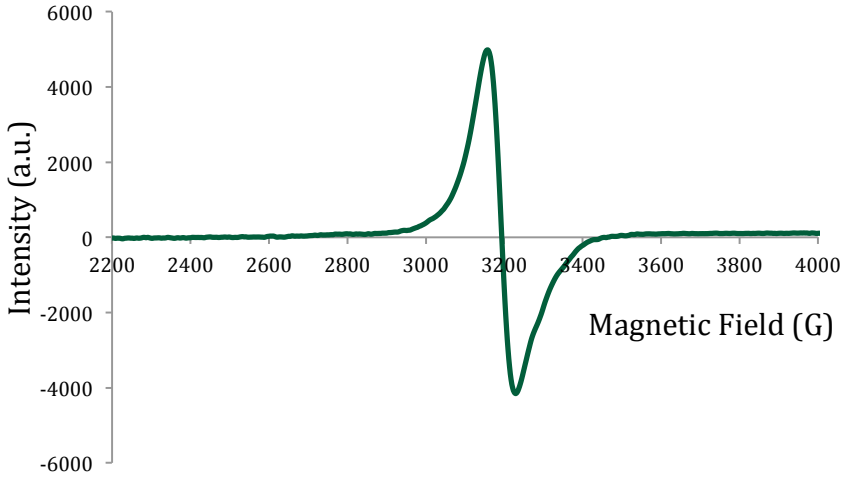

Figure S5. EPR spectrum of $[(AN)Cu^{II}(NO_2)](CF_3SO_3)$ (2mM) in acetone at 22 K.

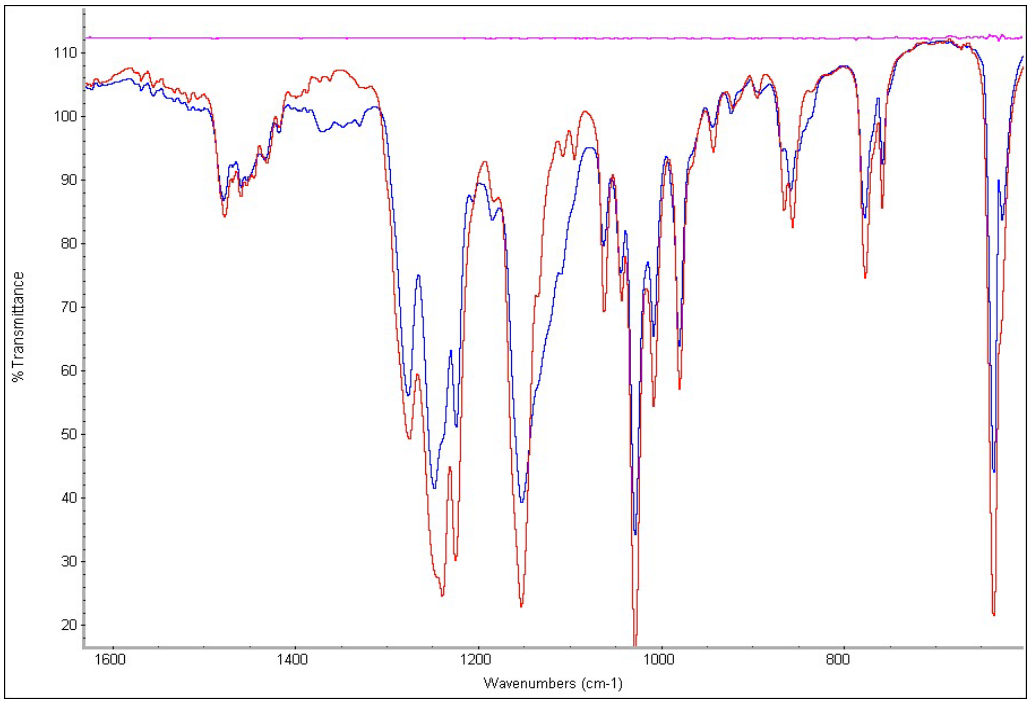

Figure S6. IR spectra (solid) comparison between the two cupric complexes: $[(AN)Cu^{II}(Cl)](CF_3SO_3)$ (red) $[(AN)Cu^{II}(NO_2)](CF_3SO_3)$ (blue); $\nu_{as(NO2)}$ = 1370 cm^{-1}, $\nu_{s(NO2)}$ = 1110 cm^{-1}, and $\delta_{(NO2)}$ = 835 cm^{-1}.

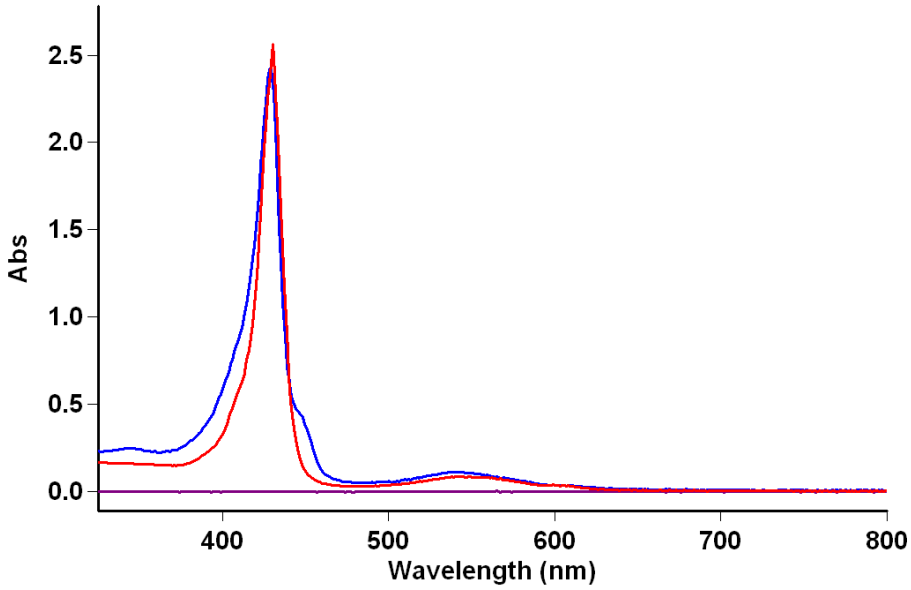

Figure S7. UV–vis spectra of (TMPP)Fe^{II} (10 μM) in acetone (blue, λ_{max} = 429 and 540 nm) and THF (red, λ_{max} = 430 and 542 nm).

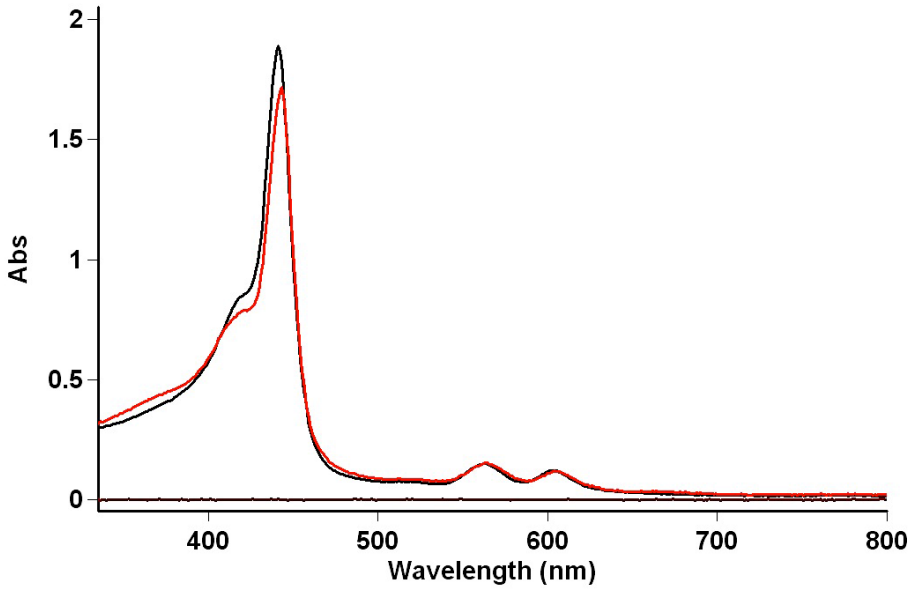

Figure S8. UV–vis spectra of (TMPP)Fe^{III}–O–Cu^{II}(tmpa)][$B(C_6F_5)_4$] in acetone (7 μM) (red, λ_{max} = 443, 564 and 605 nm) and MeCN (10 μM) (black, λ_{max} = 441, 561 and 603 nm).

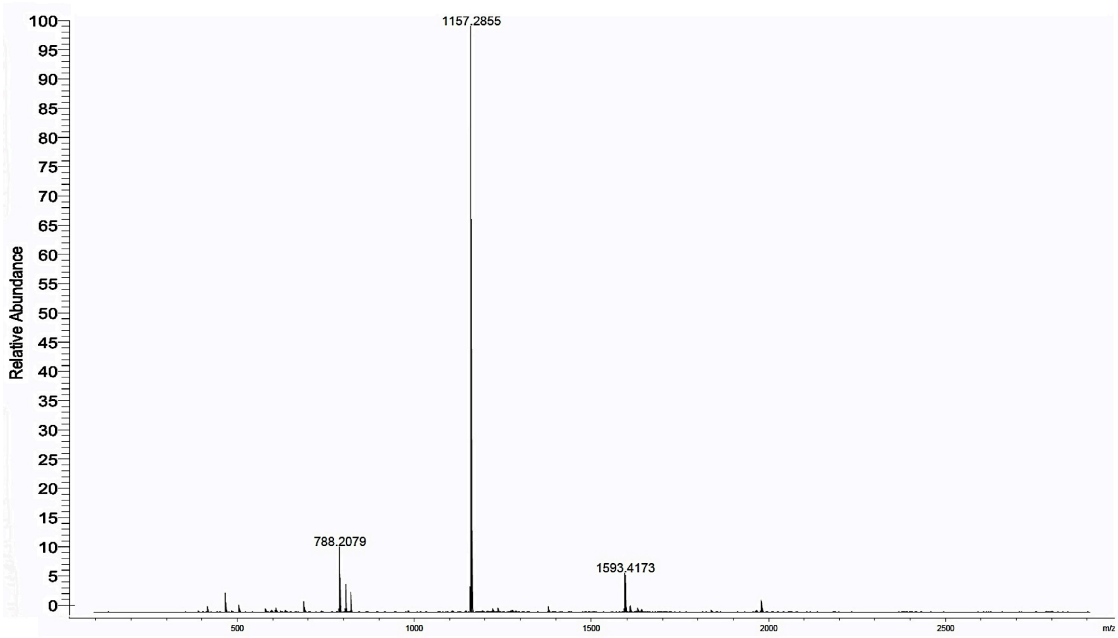

Figure S9. ESI-MS of (TMPP)Fe^{III}–O–Cu^{II}(tmpa)][$B(C_6F_5)_4$] in acetone: 1157.3 (TMPP)Fe–O–Cu(tmpa); 788.2 (TMPP)Fe; 1593.4 $[(TMPP)Fe]_2O$.

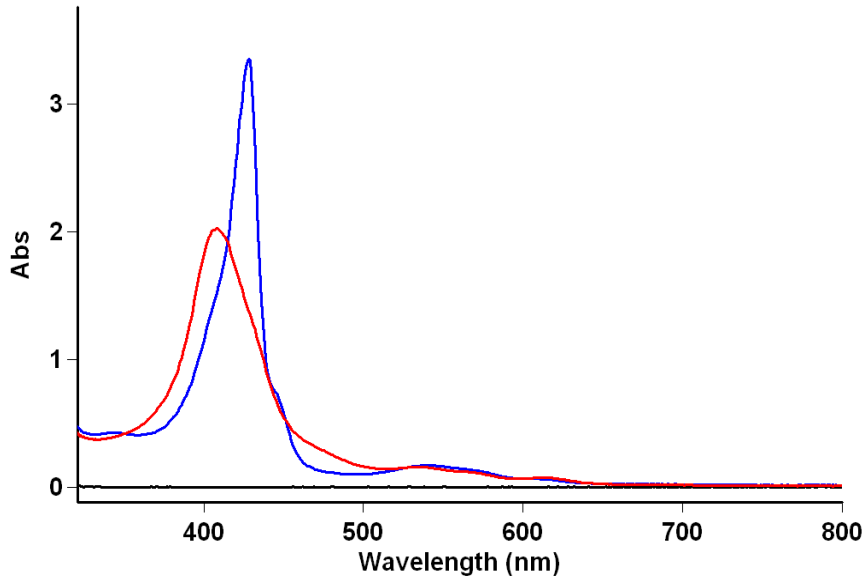

Figure S10. UV–vis spectra of (TMPP)Fe^{II} in acetone (14 μM) (blue, λ_{max} = 429 and 540 nm) and after bubbling excess $NO_{(g)}$ through the solution to form (TMPP)Fe^{II}(NO) (red, λ_{max} = 410, 539 and 614 nm).

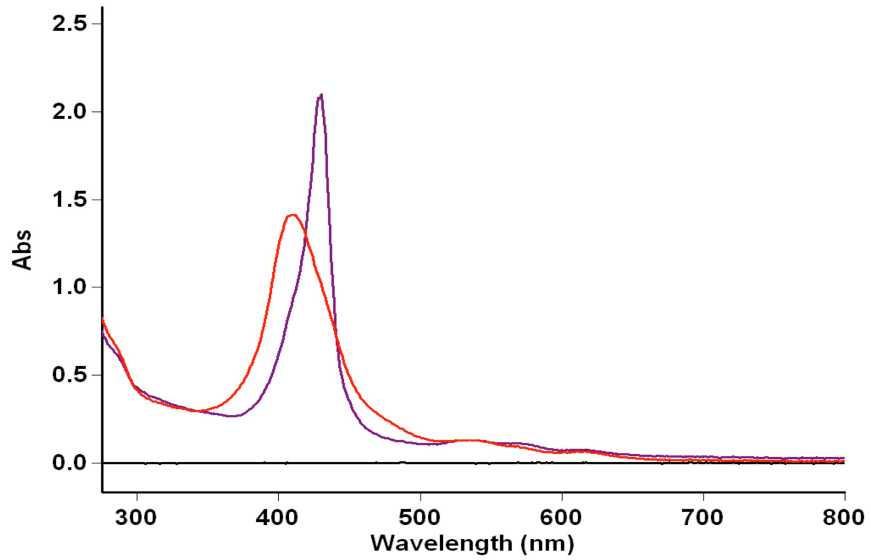

Figure S11. UV–vis spectra of (TMPP)Fe^{II} in MeCN (10 μM) (purple, λ_{max} = 430 and 533 nm) and after bubbling excess $NO_{(g)}$ through the solution to form (TMPP)Fe^{II}(NO) (red, λ_{max} = 410 and 535nm).

7.2. Control Reactions of Nitrite with Reduced Copper or Heme complexes

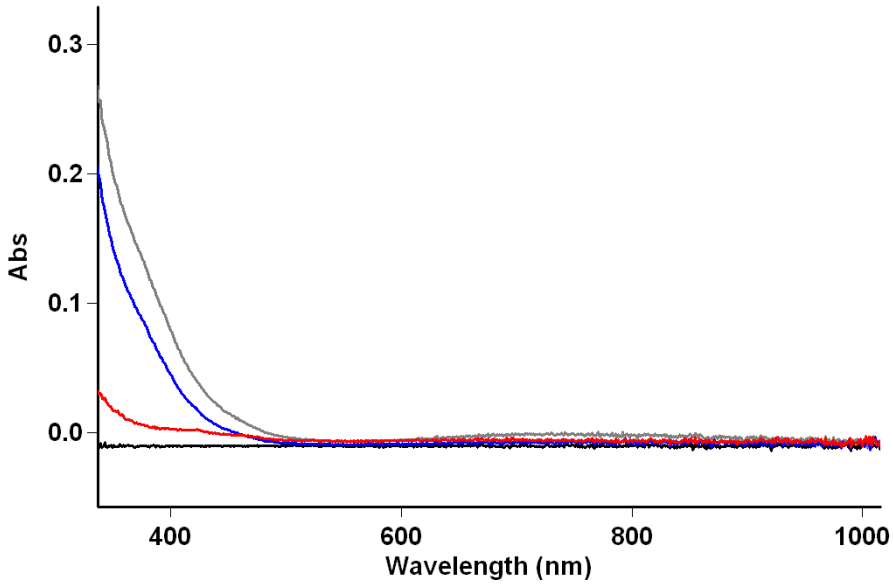

Figure S12. UV–vis spectra of [(AN)Cu^{I}][$B(C_6F_5)_4$] in acetone (100 μM) (red), after addition of 1 equiv of $(Bu)_4N(NO_2)$ (blue) and after stirring overnight (gray).

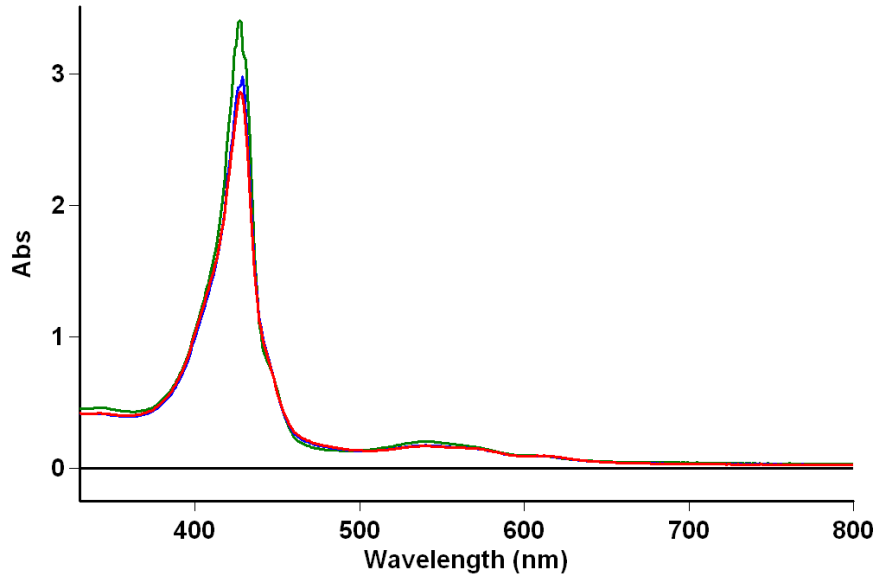

Figure S13. UV–vis spectra of (TMPP)Fe^{II} in acetone (14 μM) (green, λ_{max} = 429 and 540 nm), after addition of 1 equiv of $(Bu)_4N(NO_2)$ (blue) and after stirring for 5 h (red).

7.3. Absorption Spectra of $[(TMPP)Fe^{III}]_2O$ and $(TMPP)Fe^{III}(OH)$

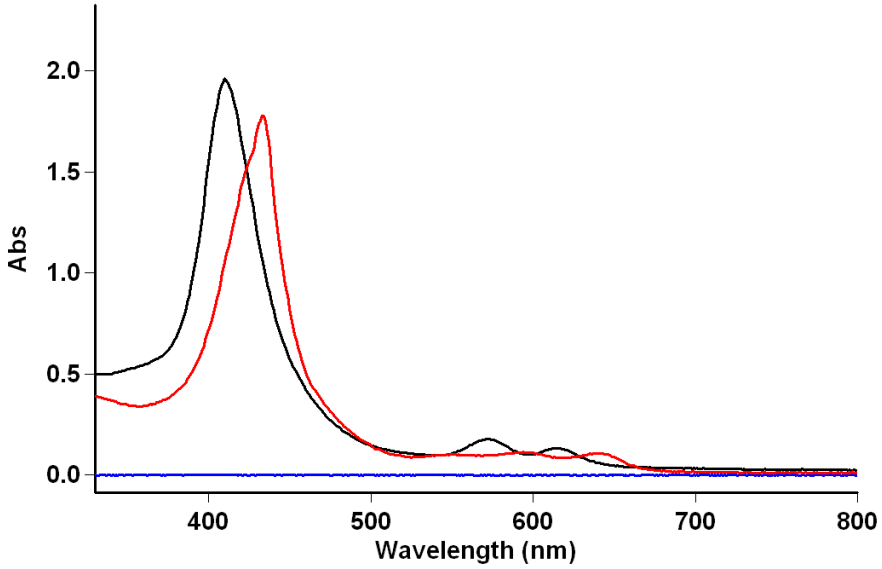

Figure S14. UV–vis spectra of $[(TMPP)Fe^{III}]_2O$ in acetone (15 μM) (black, λ_{max} = 412, 572 and 614 nm) and $(TMPP)Fe^{III}(OH)$ in MeCN (10 μM) (red, λ_{max} = 434, 594 and 640 nm). *Note*: To obtain the spectrum of $(TMPP)Fe^{III}(OH)$, we first synthesized $[(TMPP)Fe^{III}(THF)_2](SbF_6)$ via $AgSbF_6$ addition to $(TMPP)Fe^{III}(Cl)$ in THF solvent, for which full experimental details will be presented elsewhere. Then, to a MeCN solution of $[(TMPP)Fe^{III}(THF)_2](SbF_6)$ was added a small excess of tetraethylammonium hydroxide.

Chapter 4:

Nitrogen Oxide Atom-Transfer Redox Chemistry; Mechanism of $NO_{(g)}$ to Nitrite Conversion Utilizing μ-oxo Heme-Fe^{III}–O–Cu^{II}(L) Constructs

---

This work was co-authored with the following authors and is published under the following citation:

Shabnam Hematian, Isabell Kenkel, Tatyana E. Shubina, Maximilian Dürr, Jeffrey J. Liu, Maxime A. Siegler, Ivana Ivanovic-Burmazovic, and Kenneth D. Karlin

J. Am. Chem. Soc. **2015**, *137*, 6602−6615

Abstract:

While nitric oxide (NO, nitrogen monoxide) is a critically important signaling agent, its cellular concentrations must be tightly controlled, generally through its oxidative conversion to nitrite (NO_2^-) where it is held in reserve to be reconverted as needed. In part, this reaction is mediated by the binuclear heme-a_3/Cu_B active site of cytochrome *c* oxidase. In this report, the oxidation of $NO_{(g)}$ to nitrite is shown to occur efficiently in new synthetic μ-oxo heme-Fe^{III}–O–Cu^{II}(L) constructs (L being a tridentate or tetradentate pyridyl/alkylamino ligand), and spectroscopic and kinetic investigations provide detailed mechanistic insights. Two new X-ray structures of μ-oxo complexes have been determined and compared to literature analogs. All μ-oxo complexes react with 2 mol equiv $NO_{(g)}$ to give 1:1 mixtures of discrete $[(L)Cu^{II}(NO_2^-)]^+$ plus ferrous heme-nitrosyl compounds; when the first $NO_{(g)}$ equiv reduces the heme center and itself is oxidized to

nitrite, the second equiv of NO(g) traps the ferrous heme thus formed. For one μ-oxo heme-Fe^{III}–O–Cu^{II}(L) compound, the reaction with $NO_{(g)}$ reveals an intermediate species ("intermediate"), formally a *bis*-NO adduct, [(NO)(porphyrinate)Fe^{II}–(NO_2^-)–Cu^{II}(L)]$^+$ (λ_{max} = 433 nm), confirmed by cryo-spray ionization mass spectrometry and EPR spectroscopy, along with the observation that cooling a 1:1 mixture of [(L)Cu^{II}(NO_2^-)]$^+$ and heme-Fe^{II}(NO) to −125 °C leads to association and generation of the key 433 nm UV−vis feature. Kinetic-thermodynamic parameters obtained from low-temperature stopped-flow measurements are in excellent agreement with DFT calculations carried out which describe the sequential addition of $NO_{(g)}$ to the μ-oxo complex.

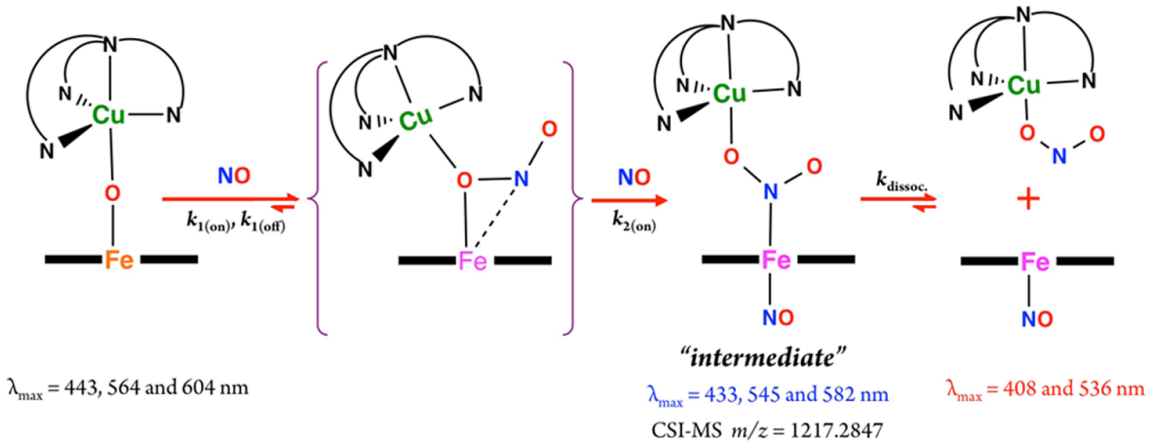

1. Introduction

Nitric oxide (NO) is a multitasking signaling molecule of great importance in living systems, which is now widely regarded as a muscle relaxant, vasodilator, neurotransmitter, etc.[1,2] This versatile second messenger has a short half-life and can be produced by either oxidative or reductive pathways.[3] Under conditions of having a normal level of oxygen (normoxia), when the oxidative pathway dominates, $NO_{(g)}$ is produced through an oxygen-dependent L-arginine-NO synthase (NOS) pathway,[4] while in hypoxic conditions, as oxygen tensions fall, enzymatic one-electron reduction of nitrite (NO_2^-) is gradually activated, serving as a back-up system to ensure that there is sufficient $NO_{(g)}$ production.[3,5] It is believed that cytochrome *c* oxidase (C*c*O) is the major mitochondrial site of $NO_{(g)}$ production in hypoxic cells.[6]

Cytochrome *c* oxidase is the terminal enzyme of the respiratory chain that is traditionally known to catalyze the four-electron reduction of molecular oxygen (O_2) to water (H_2O) in all eukaryotes. The active site of C*c*O contains a binuclear center comprising an iron porphyrin heme-a_3 and a tris-histidine-coordinated copper (Cu_B) ion, to which O_2 binds, acting as the terminal electron acceptor in the respiratory chain.[7] When the O_2 concentration is low, the $NO_{(g)}$ thus generated by C*c*O nitrite reduction reversibly inhibits the oxygen consumption at the same center, resulting in cellular O_2 accumulation (Figure 1).[8] At this stage, the mitochondrially produced $NO_{(g)}$ is also known to participate in hypoxic signaling and induction of nuclear hypoxic genes.[9]

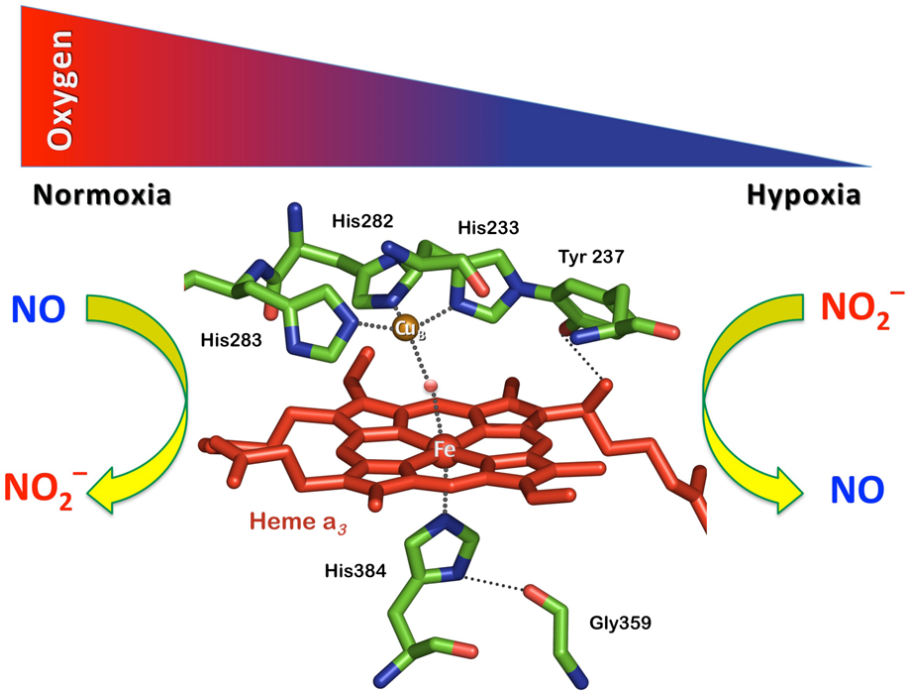

Figure 1. Endogenous nitrite (NO_2^-) and nitric oxide (NO) modulate cell respiration in an oxygen-dependent manner through interaction with the heme-a_3/Cu_B active site of cytochrome *c* oxidase (C*c*O). The structural features of the binuclear center of C*c*O are based on PDB code 1XME.

In turn, at mitochondrial sites recovering from hypoxia, an increase in the local O_2 availability stimulates one-electron oxidation of $NO_{(g)}$ back to NO_2^-. This redox reaction also occurs at the C*c*O binuclear center as an adaptive way to remove $NO_{(g)}$ from the system, which is critical for retrieving normal cell function. Thus, C*c*O is involved in both endogenous generation and metabolism of nitric oxide, i.e., the heme-a_3/Cu_B active site is both a source of and target for this redox-active signaling molecule (Figure 1).[10]

The roles that metal centers may play in this redox interplay between nitrite and nitric oxide have inspired us to generate a synthetic heme/Cu assembly that in its partially reduced form could reduce nitrite to $NO_{(g)}$, while its fully oxidized form, a different μ-oxo heme-Fe^{III}–O–Cu^{II}(L) complex (L = *N*-donor chelating ligand), oxidizes $NO_{(g)}$

back to nitrite.[11] Our findings showed that in the nitrite reductase chemistry, the cupric center serves as a Lewis acid, while the heme is the redox active center and provides the electron. We also further studied some synthetic variation of both heme and copper centers, and based on our observations, we found that the reaction rate was independent of the heme reducing ability.[12] Also, differing modes of nitrite coordination to the cupric center, monodentate vs *O,O′*-bidentate, lead to different kinetic behavior in nitrite reduction.[12] This suggests that the binding mode of nitrite to the cupric ion may dictate in what fashion nitrite approaches and coordinates to the ferrous heme and binding of nitrite to the iron center either via a *N*- or *O*-atom influences the overall kinetics. Here, the cupric center also acts as a strong oxo-acceptor facilitating nitrite (N−O) bond cleavage.

In this report, we focus on nitric oxide oxidase chemistry and describe different μ-oxo heme-Fe^{III}−O−Cu^{II}(L) complexes mediating the one-electron oxidation of $NO_{(g)}$ to nitrite. New insights are provided by detailed studies where modifications of the heme or copper chelating ligand are utilized. Thus, the copper coordination environment contains either a tripodal tetradentate pyridyl-alkylamine ligand or a related tridentate alkylamine ligand. Two different tetraarylporphyrinates are employed in the present work, one with electron-withdrawing peripheral substituents versus one with strong electrondonating groups.

Scheme 1 shows the structures of μ-oxo heme-Fe^{III}−O−Cu^{II}(L) complexes used in this study. As indicated, the reactivity observed by using [$(F_8)Fe^{III}$−O−Cu^{II}(tmpa)]-[$B(C_6F_5)_4$], [$(F_8)Fe^{III}$−O−Cu^{II} (AN)][$B(C_6F_5)_4$], [$(F_8)Fe^{III}$−O−Cu^{II}(MePY2)][$B(C_6F_5)_4$], or [(TMPP)Fe^{III}−O−Cu^{II}(tmpa)][$B(C_6F_5)_4$] (see Experimental Section) with $NO_{(g)}$ results in highly efficient production of nitrite forming the corresponding cupric-nitrite complex;

the reduced heme is trapped by a second equiv of $NO_{(g)}$ giving a stable ferrous heme-nitrosyl. Through a combination of kinetic investigations, spectroscopic interrogation, application of cryo-spray ionization (CSI) mass spectrometry, and DFT calculations, we reveal intimated details of the course and mechanism of reaction, including the discovery of a novel metastable intermediate which reveals a new kind of $NO_{(g)}$ reactivity and following oxo-transfer chemistry.

Scheme 1. Structures of μ-oxo Heme-Fe^{III}–O–Cu^{II}(L) Complexes Used in This Study.

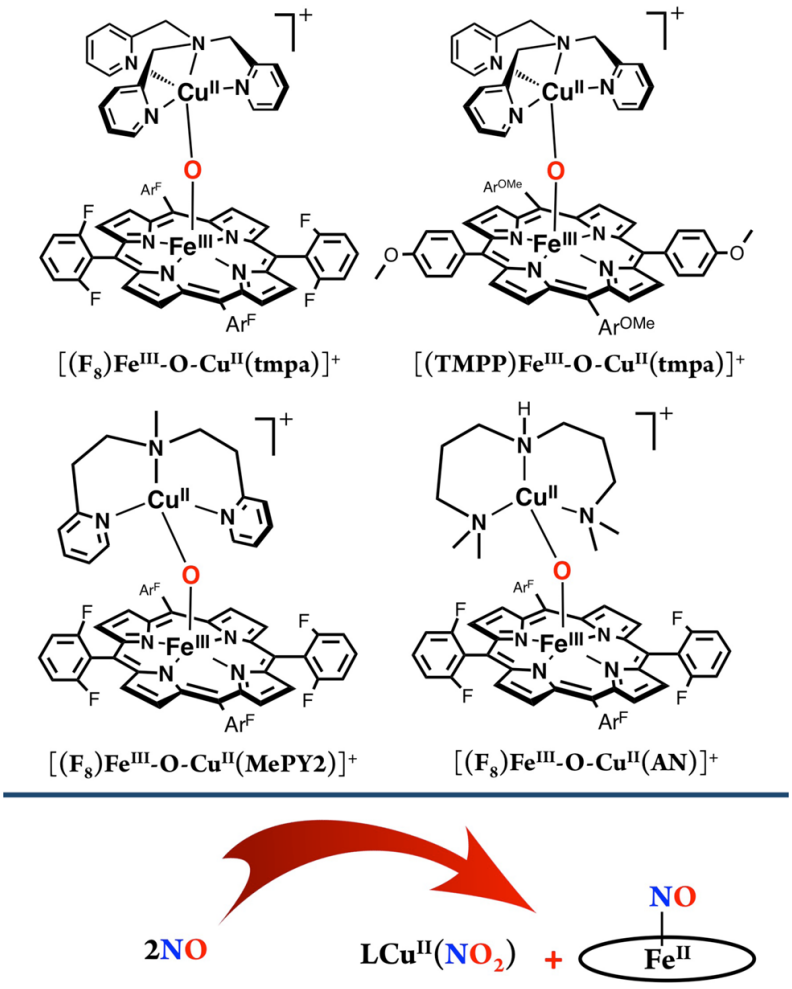

F_8: tetrakis(2,6-difluorophenyl)porphyrinate(2−); TMPP: tetrakis(4-methoxyphenyl)porphyrinate(2−); tmpa: tris(2-pyridylmethylamine); AN: 3,3′-imino-bis(*N*,*N*-dimethylpropylamine); MePY2: bis(2-pyridylethyl)methylamine.

2. Results and Discussion

2.1. The μ-oxo Heme-Fe^{III}−O−Cu^{II}(L) Compounds

Two of the complexes used here to carry out the nitric oxide oxidation to nitrite have been previously structurally characterized, $[(F_8)Fe^{III}–O–Cu^{II}(tmpa)]^{+}$ and $[(F_8)Fe^{III}–O–Cu^{II}(AN)]^{+\cdot}$ Such species are themselves rather novel, as (i) they can be synthesized via metal-dioxygen chemistry; (ii) they possess interesting magnetic-electronic properties (i.e., having S = 2 ground states, which leads to EPR silence), and the high-spin iron(III) ion, well above (~0.5 Å, see Table 1) the porphyrinate plane, is antiferromagnetically coupled to the S = 1/2 d^9 cupric ion; (iii) the bridging oxo atom is very basic, and in some cases the protonated acid−base partner, the μ-hydroxo complexes heme-Fe^{III}-(OH)-Cu^{II}(L), have been characterized and pK_a values measured;[13] (iv) with L being a tetradentate chelate, the Fe−O−Cu moiety is near linear (170−180°), but for L = a tridentate ligand, ∠Fe−O−Cu = 140−150° (Table 1); and (v) the Soret bands of these μ-oxo complexes are considerably red-shifted (λ_{max} = 430−450 nm) relative to those of classical high-spin ferric hemes, and this distinctive feature of the μ-oxo heme-Fe^{III}−O−Cu^{II}(L) compounds may be due to the higher degree of π charge donation onto the available Fe^{III} ion by the bridging oxo group.

Table 1. Structural Comparison of μ-oxo Heme-Fe^{III}–O–Cu^{II}(L) Complexes.

Compound	∠Fe–O–Cu (deg)	Cu–O (Å)	Fe–O (Å)	Fe…Cu (Å)	Fe out of N_4 plane (Å)	Ref
$[(F_8)Fe^{III}–O–Cu^{II}(tmpa)]^+$	178.1(4)	1.856(6)	1.740(6)	3.596	0.554	14-15
$[(F_8)Fe^{III}–O–Cu^{II}(MePY2)]^+$	142.48(8)	1.8452(13)	1.7563(14)	3.410	0.553	This work
$[(F_8)Fe^{III}–O–Cu^{II}(AN)]^+$	149.5(1)	1.816(2)	1.746(2)	3.437	0.507	16
$[(TMPP)Fe^{III}–O–Cu^{II}(tmpa)]^+$	173.6(15)	1.824(7)	1.720(7)	3.539	0.548	This work
$[(F_8)Fe^{III}–O–Cu^{II}(L^{Me_2N})]^+$	143.4(1)	1.852(2)	1.747(2)	3.417	0.550	17
$[(OEP)Fe^{III}–O–Cu^{II}(Me_6tren)]^+$	175.3(3)	1.828(6)	1.746(6)	3.575	0.581	18
$[(^6L)Fe^{III}–O–Cu^{II}]^+$	171.1(3)	1.848(4)	1.749(4)	3.586	0.579	19
$[(TMP)Fe^{III}–O–Cu^{II}(5MeTPA)]^+$	172.8(2)	1.854(3)	1.760(3)	3.607	0.601	20

L^{Me_2N} *N,N*-bis{2-[2-(*N′,N′*-4-dimethylamino)pyridyl]ethyl}methylamine; OEP octaethylporphyrinate(2–); Me_6tren tris[(*N,N*-dimethylamino)ethyl]amine; ^{6}L 5-(*o-O*-[(*N,N*-bis(2-pyridylmethyl)-2-(6-methoxyl)pyridinemethanamine)phenyl] 10,15,20-tris(2,6-difluorophenyl)porphyrinate(2–); TMP-5MeTPA 10,15,20-tris(2,4,6-trimethylphenyl)-5-(2′-bis((5″-methyl-2″-pyridylmethyl)aminomethyl)pyridine-5′-carboxy-amidophenyl) porphyrinate(2–).

For the present studies, two new crystal structures have been determined via single crystal X-ray crystallography, $[(F_8)Fe^{III}–O–Cu^{II}(MePY2)]^+$ and $[(TMPP)Fe^{III}–O–Cu^{II}(tmpa)]^+$ (Figures 2 and 3). Relevant bond distances and angles are given in the figure captions, while we also provide additional core structure parameters for all known (and published) μ-oxo heme-Fe^{III}–O–Cu^{II}(L) compounds of this type (Table 1). Our new complexes conform to the previously observed findings in that the Fe–O–Cu core in the structure with MePY2 is bent (Figure 2), while in the complex bearing the tmpa ligand, the core is near linear (Figure 3). $[(TMPP)Fe^{III}–O–Cu^{II}(tmpa)]^+$ is the first μ-oxo complex of the Fe–O–Cu class which contains the strongly donating TMPP porphyrinate. We infer that the donating ability of TMPP as compared to F_8 will make the oxo atom more electron rich, which could be responsible for the small shortening of both the Cu–O and Fe–O bond distances in $[(TMPP)Fe^{III}–O–Cu^{II}(tmpa)]^+$ as compared to $[(F_8)Fe^{III}–O–Cu^{II}(tmpa)]^+$ (Table 1).

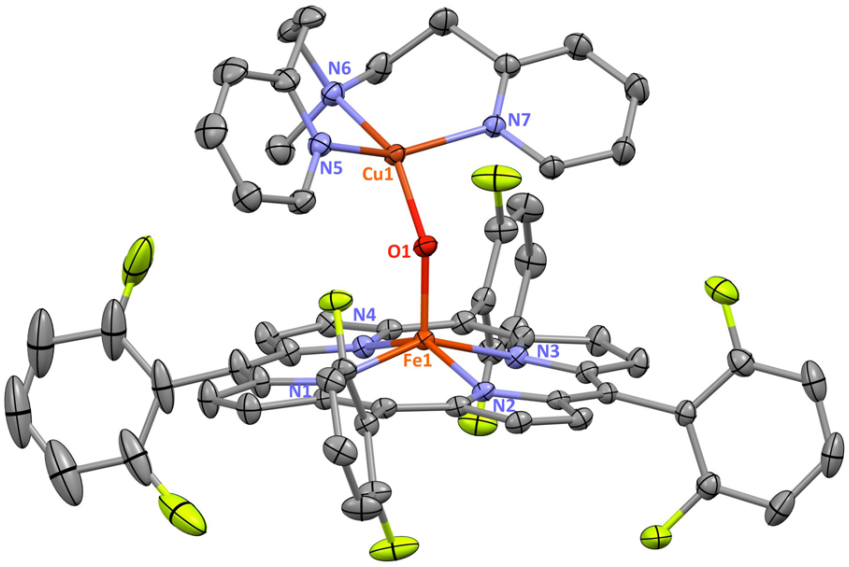

Figure 2. Displacement ellipsoid plot (50% probability level) of the cationic portion of $[(F_8)Fe^{III}–O–Cu^{II}(MePY2)][B(C_6F_5)_4]$ at 100(2) K. Counteranion and hydrogen atoms have been omitted for clarity. Selected bond lengths (Å) and angles (deg): Cu1−N5, 1.9997(17); Cu1−N6, 2.0557(17); Cu1−N7, 2.0150(17); Cu1−O1, 1.8452(13); Fe1−$N_{p(average)}$, 2.0940(8); Fe1−O1, 1.7563(14); Cu1−O1−Fe1, 142.48(8); N5−Cu1−N6, 91.97(7); N5−Cu1−N7, 148.46(7); N5−Cu1−O1, 93.44(7); N6−Cu1−N7, 96.94(7); N6−Cu1−O1, 148.15(7); N7−Cu1−O1, 94.67(7); N_p−Fe1−$O1_{(average)}$, 105.32(7). See Table 1 and Supporting Information for further structural details.

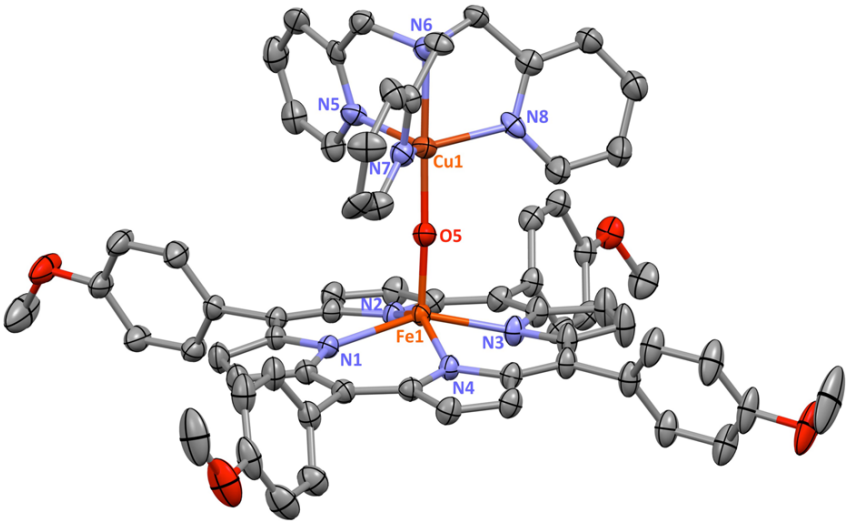

Figure 3. Displacement ellipsoid plot (50% probability level) showing the cationic portion of $[(TMPP)Fe^{III}–O–Cu^{II}(tmpa)][B(C_6F_5)_4]$ at 100(2) K. Counteranion, solvent molecules, and hydrogen atoms have been omitted for clarity. Selected bond lengths (Å) and angles (deg): Cu1−N5, 2.086(8); Cu1−N6, 2.086(6); Cu1−N7, 2.046(5); Cu1−N8, 2.045(6); Cu1−O5, 1.824(7); Fe1−$N_{p(average)}$, 2.1022(6); Fe1−O5, 1.720(7); Cu1−O5−Fe1, 173.6(15); N5−Cu1−N6, 81.0(3); N5−Cu1−N7, 118.0(2); N5−Cu1−N8, 110.9(3); N5−Cu1−O5, 101.6(7); N6−Cu1−N7, 81.0(2); N6−Cu1−N8, 81.1(2); N6−Cu1−O5, 177.3(8); N7−Cu1−N8, 123.9(3); N7−Cu1−O5, 97.0(7); N8−Cu1−O5, 98.6(6); N_p−Fe1−$O5_{(average)}$, 105.1(6). See Table 1 and Supporting Information for further structural details.

The cupric centers of both $[(F_8)Fe^{III}–O–Cu^{II}(tmpa)]^+$ and $[(TMPP)Fe^{III}–O–Cu^{II}(tmpa)]^+$ complexes are pentacoordinated and bearing the same TMPA ligand, with three pyridyl nitrogens and one amino nitrogen and a bridging oxo ligand that occupies the fifth site. Interestingly, coordination geometry analysis of these two compounds reveals that the Cu(II) adopts very different geometries (Figure S1). We propose that the steric constraints imposed by the peripheral substituents on the attached porphyrin ring dictate the structural properties of the cupric center. In the former structure, steric hindrance of the fluorine groups of the F_8 ligand cause the copper center to adjust to a distorted square pyramidal coordination geometry ($\tau = 0.3$). All three pyridyl groups on the copper ligand are placed above and between the difluorophenyl *meso*-substituents of the heme.[14] In contrast, in the latter μ-oxo complex, absence of steric hindrance allows the cupric center to adopt a nearly perfect trigonal bipyramidal (TBP) structure ($\tau = 0.9$); the amine nitrogen N(6) and bridging oxo ion occupying the axial positions and the pyridyl nitrogens N(5), N(7), and N(8) in the trigonal plane. TBP structures are favored and very well-known for the TMPA framework, as found for many examples of structurally characterized $[(tmpa)Cu^{II}(X)]^{n+}$ ($X = H_2O$, MeCN, Cl^-, NO_2^-) compounds.

2.2. Copper Fragment Coordination Environment Variants in $NO_{(g)}$ Oxidase Chemistry

As mentioned, one set of alterations we carried out was to vary the chelating ligand on the copper ion for the μ-oxo heme-$Fe^{III}–O–Cu^{II}(L)$ compounds employed for $NO_{(g)}$ oxidation (Schemes 1 and 2).

Scheme 2. Reactions of $[(F_8)Fe^{III}–O–Cu^{II}(L)]^+$ Complexes with $NO_{(g)}$.

$$[(F_8)Fe^{III}\text{-}O\text{-}Cu^{II}(tmpa)]^+ \xrightarrow{2NO} [(tmpa)Cu^{II}(NO_2)]^+ + (F_8)Fe^{II}(NO)$$

$$[(F_8)Fe^{III}\text{-}O\text{-}Cu^{II}(AN)]^+ \xrightarrow{2NO} [(AN)Cu^{II}(NO_2)]^+ + (F_8)Fe^{II}(NO)$$

$$[(F_8)Fe^{III}\text{-}O\text{-}Cu^{II}(MePY2)]^+ \xrightarrow{2NO} [(MePY2)Cu^{II}(NO_2)]^+ + (F_8)Fe^{II}(NO)$$

Such changes in coordination environment, tridentate vs tetradentate ligands, pyridyl vs alkylamino donors or 5- vs 6-membered chelate rings, are well-known to dramatically influence both compound physical properties and reactivity patterns. In this section, we discuss how changes in L affect $NO_{(g)}$ oxidase chemistry using a series of $[(F_8)Fe^{III}–O–Cu^{II}(L)]^+$ complexes, Scheme 1.

As previously reported for the case using the tetradentate TMPA ligand (Scheme 1), exposure of $[(F_8)Fe^{III}–O–Cu^{II}(tmpa)]^+$ to $NO_{(g)}$ at RT resulted in a relatively slow conversion to the final cupric-nitrite and heme-nitrosyl products $[(tmpa)Cu^{II}(NO_2)]^+$ and $(F_8)Fe^{II}(NO)$.[11] From UV−vis monitoring of the reaction, no intermediate was observed. Further, even when we repeated the chemistry at –40 °C, where the reaction was of course slower, still no intermediate could be detected (Figure 4a).[21]

In the present study, we have also employed the tridentate chelates, L = AN and MePY2, for the $NO_{(g)}$ oxidase reaction; under the same conditions as for L = TMPA for $NO_{(g)}$ oxidation, these transformations are considerably faster. For $NO_{(g)}$ oxidation by $[(F_8)Fe^{III}–O–Cu^{II}(AN)]^+$, the benchtop reaction at RT is over within the mixing time (Figure S2 (right)). The generation of a one-to-one mixture of $(F_8)Fe^{II}(NO)$ and $[(AN)Cu^{II}(NO_2)]^+$ in high yields was further confirmed by semiquantitative nitrite ion

analysis and EPR spectroscopy (Figure S3). Similar results were obtained for the $[(F_8)Fe^{III}–O–Cu^{II}(MePY2)]^+ + NO_{(g)}$ reaction and even at −40 °C monitoring reveals an essentially instantaneous conversion to the Cu(II)-nitrite plus ferrous heme-nitrosyl products (Scheme 2, Figures 4b and S4).

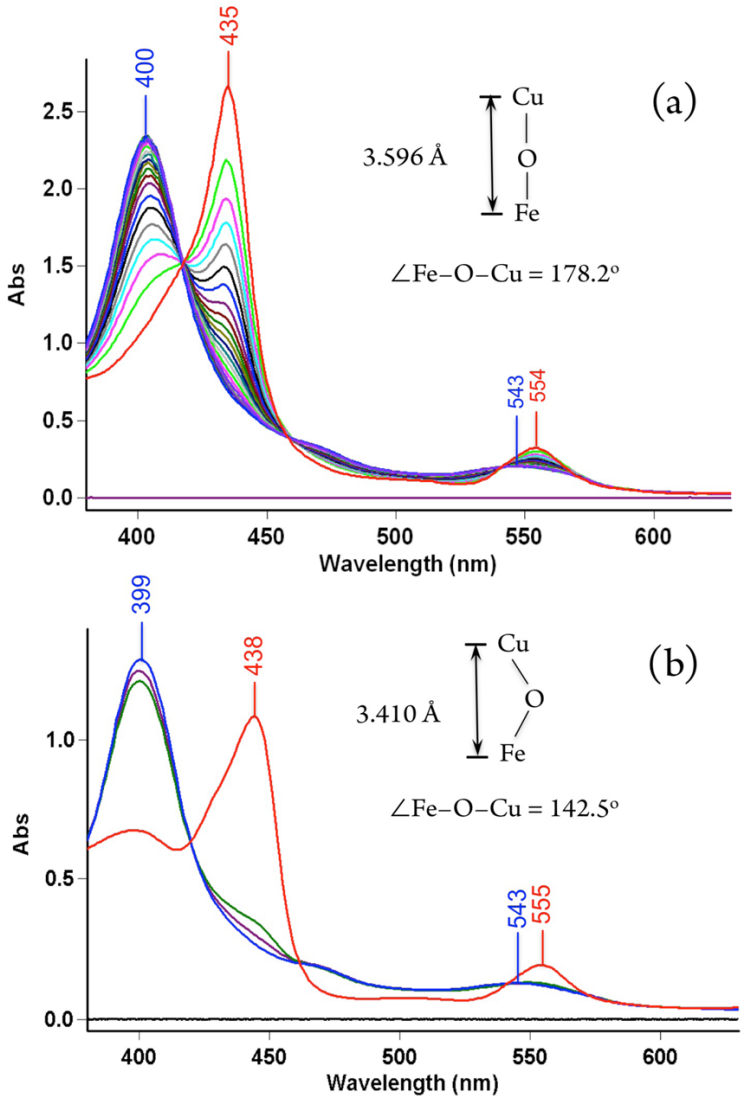

Figure 4. UV−vis spectra of **(a)** $[(F_8)Fe^{III}–O–Cu^{II}(tmpa)][B(C_6F_5)_4]$ (red), $(F_8)Fe^{II}(NO)$ (blue) generated from addition of 1 mL of $NO_{(g)}$ to the solution 75 μM in acetone in a 2 mm cuvette at −40 °C, after 30 min and **(b)** $[(F_8)Fe^{III}–O–Cu^{II}(MePY2)][B(C_6F_5)_4]$ (red) and $(F_8)Fe^{II}(NO)$ (blue) promptly generated after addition of 1 mL $NO_{(g)}$ into the μ-oxo complex solution 50 μM in acetone in a 2 mm cuvette at −40 °C.

These observations point to the importance of cupric ligation and influence of electronic and steric eff ects around the copper center on $NO_{(g)}$ oxidase chemistry. Based on our previous studies on μ-oxo heme-Fe^{III}–O–Cu^{II}(L) complexes where L is the tridentate ligand AN or MePY2, the basicity of the bridging oxo ion is elevated compared to the complex containing TMPA. This then may be responsible for a faster reaction with $NO_{(g)}$. Another possible factor explaining the acceleration of the reaction with $NO_{(g)}$ can be linked to a lack of steric hindrance. This may facilitate the approach of $NO_{(g)}$ molecule to the more exposed bridging oxo atom where (i) the Fe^{III}–O–Cu^{II} is relatively bent and (ii) the tetracoordination environment around the copper ion is indeed less crowded than for pentacoordination (with TMPA).

2.3. $NO_{(g)}$ Oxidase Reactivity with [(TMPP)Fe^{III}–O–Cu^{II}(tmpa)]$^+$; Mechanistic Insights via Observation of Intermediates

As described in the Introduction, hoping to obtain some detailed mechanistic insights regarding this $NO_{(g)}$ oxidase chemistry, we also altered the nature of the porphyrin ligand in the μ-oxo heme-Fe^{III}–O–Cu^{II}(L) compound. Here, we kept the copper chelate TMPA constant and employed a different porphyrin ring with electron-donating *para* methoxy peripheral substituents, TMPP (Scheme 1). This new μ-oxo complex [(TMPP)Fe^{III}–O–Cu^{II}(tmpa)]$^+$ was synthesized, characterized, and studied for its $NO_{(g)}$ oxidation chemistry. Upon addition of $NO_{(g)}$, UV−vis monitoring (Figure S5) of the reaction progress at RT showed an instant change from starting μ-oxo complex to a mixture of species followed by formation of the expected final products (Scheme 1). IR

spectroscopy (ν_{NO} = 1677 cm^{-1}) directly indicated the production of the ferrous heme nitrosyl (TMPP)Fe^{II}(NO). The quantitative analyses of UV−vis and EPR spectra of the reaction products (Figure S6) along with semiquantitative nitrite ion analysis confirmed the generation of a one-to-one mixture of (TMPP)Fe^{II}(NO) (λ_{max} = 410 nm) and the cupric-nitrite complex, $[(tmpa)Cu^{II}(NO_2)]^+$, in high yields.

Scheme 3. Proposed Reaction Steps for Nitric Oxide Oxidase Chemistry Mediated by μ-oxo Heme-Fe^{III}–O–Cu^{II}(L) Complexes Leading to Observed Products.

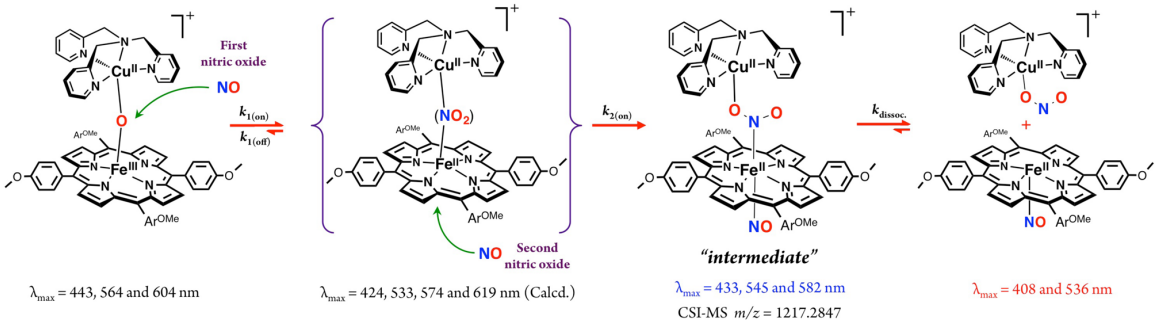

We repeated the reaction at −20 ° C, where we were able to detect a new species, now to be referred to as the "intermediate" (Scheme 3) forming right after $NO_{(g)}$ addition to the solution of μ-oxo complex, as monitored by UV−vis spectroscopy (Figure 5). This "intermediate" (λ_{max} = 433 nm)[22] then isosbestically converts to the final products $[(tmpa)Cu^{II}(NO_2)]^+$ and (TMPP)Fe^{II}(NO) in a first-order process with rate constant $k_{dissoc.}$ = 6.7 × 10^{-3} s^{-1} at −20 °C (Figure 5), while $\Delta H^{\ddagger}$ and $\Delta S^{\ddagger}$ are 41.1 ± 0.1 kJ mol^{-1} and −123 ± 2 J mol^{-1} K^{-1}, respectively (Figure S8). The possible origin of the large and negative $\Delta S^{\ddagger}$ is discussed below.

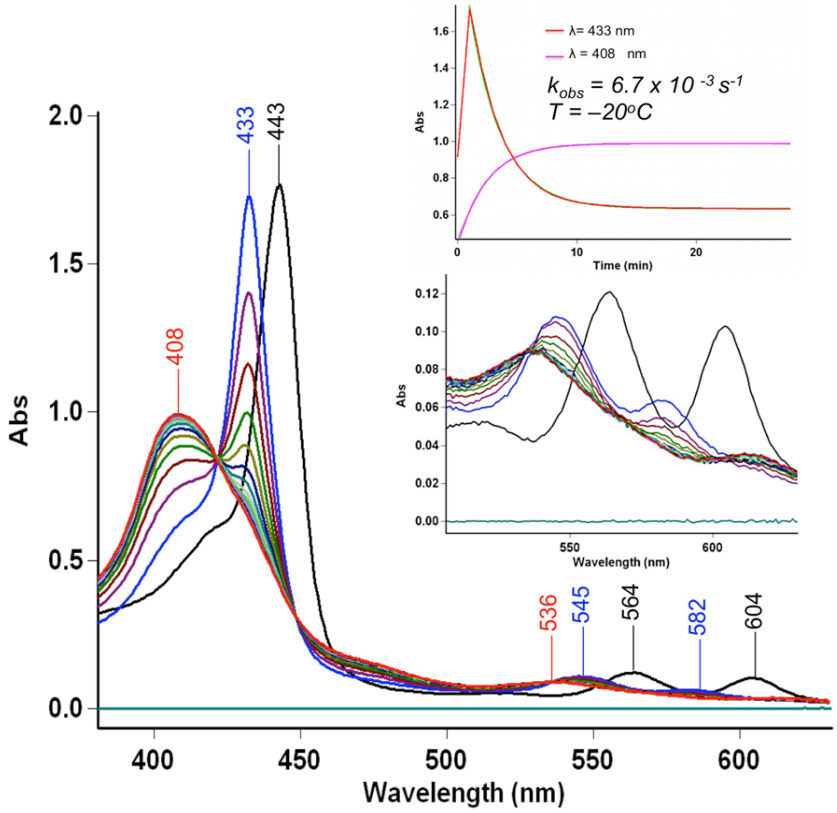

Figure 5. UV−vis spectra of [(TMPP)Fe^{III}−O−Cu^{II}(tmpa)][$B(C_6F_5)_4$] (black) 35 μM in acetone in a 2 mm cuvette at −20 °C, the "intermediate" (blue) generated upon addition of 1 mL of $NO_{(g)}$ into the solution. Slow conversion of the "intermediate" to the final product (TMPP)Fe^{II}(NO) (red) was monitored.

Our further analyses using DFT calculations (see further below) indicates that the λ_{max} = 433 nm "intermediate" is a ferrous species. An experiment to support this supposition was to see if nitrite anion, as bound to a cupric center, could bind to a ferrous-nitrosyl complex. Cooling of a mixture of [(tmpa)$Cu^{II}(NO_2)]^+$ and (TMPP)Fe^{II}(NO) to −125 °C (in MeTHF) resulted in a new UV−vis spectrum identical to that of the "intermediate" (Figure S9). In fact, this adduct formation is reversible (see diagram), as warming the "intermediate" releases the two mononuclear units, as already indicated by the kinetic study described above. Thus, together, these experimental

observations (along with stopped-flow spectroscopy and CSIMS results; see below) support the hypothesis that the "intermediate" comprises a six-coordinate ferrous heme-nitrosyl species joined to a cupric-nitrite entity (Scheme 3).

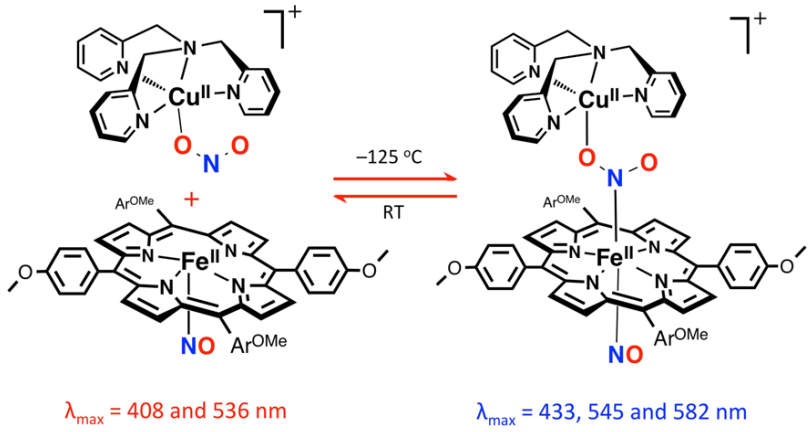

The nature of this intermediate was further examined using EPR spectroscopy. $[(TMPP)Fe^{III}–O–Cu^{II}(tmpa)]^{+}$ is EPR silent as known for other μ-oxo heme-$Fe^{III}–O–Cu^{II}(L)$ compounds. An EPR spectrum of the "intermediate" (Figure S10) is dominated by a signal typical for $[(tmpa)Cu^{II}(NO_2^{-})]^{+}$ in a trigonal bipyramidal geometry, on top of an additional signal interpreted to be a six-coordinated ferrous-nitrosyl absorption, modified some from the signal most typical of $\{FeNO\}^{7}$ complexes. EPR spectra of both the "intermediate" and products were simulated as a mixture of two one-electron systems, cupric and ferrous heme nitrosyl components (Figure S11). Successful modeling of the "intermediate" required consideration of the hyperfine coupling to both the nitrogen nucleus of the $NO_{(g)}$ ligand ($A_{2,NO}$ = 18.9 G) and the trans axial nitrogenous donor, the bridging nitrite ($a_{2,Nitrite}$ = 7.74 G). These hyperfi ne coupling

constants are consistent with reported values for six-coordinated ferrous heme nitrosyl complexes bearing trans nitrogen bases.[23] Conversion of the "intermediate" to the product species (TMPP)Fe^{II}(NO) results in a slightly enhanced coupling to the nitrosyl ligand; the $A_{2,NO}$ value is now increased to 22.8 G. This suggests that the unpaired electron has considerable interaction with the axial bridging nitrite ($a_{2,Nitrite}$ = 7.74 G) in the "intermediate", thus, the coupling to the $NO_{(g)}$ ligand is somewhat decreased, relative to that in the final product, (TMPP)Fe^{II}(NO).[24]

We posit that the overall reaction of $NO_{(g)}$ with [(TMPP)Fe^{III}−O−Cu^{II}(tmpa)]$^+$ involves an initial an electrophilic attack of $NO_{(g)}$ on the bridging oxo group, possible transient formation of a hydronitrite radical anion (i.e., NO_2^{2-}),[25] followed by rapid electron transfer and formation of the nitrite bridged ferrous heme moiety; this is then attacked by a second $NO_{(g)}$ molecule on the open face of the heme (Scheme 3). These proposals are further supported via detailed kinetic studies and DFT calculations, as described and discussed below.

2.4. Stopped-Flow Kinetics of Sequential $NO_{(g)}$ Binding to [(TMPP)Fe^{III}−O−Cu^{II}(tmpa)]$^+$

Thus, as described above, −20 °C benchtop UV−vis spectroscopic monitoring revealed the presence of a rather stable intermediate. As it decays to isolable nitrito-Cu plus ferrous heme-nitrosyl complexes and can independently be generated from these moieties (i.e., from [(tmpa)$Cu^{II}(NO_2)$]$^+$ and (TMPP)Fe^{II}(NO)) in a reverse manner, it can be assigned as a [(NO)(TMPP)Fe^{II}−NO_2−Cu^{II}(tmpa)]$^+$ complex. As outlined in Scheme 3,

the initial step is very fast $NO_{(g)}$ electrophilic attack on the bridging nucleophilic oxo ion, and this is followed by reaction of a second $NO_{(g)}$ molecule, on the open face of the heme. This resulting *bis*-NO adduct, is in fact the 433 nm intermediate observed even at −20 °C by UV−vis spectroscopy (vide supra) and could be detected by CSI-MS at −60 °C (vide infra). By employing low-temperature stopped-flow kinetic methods, we have also been able to characterize the kinetics-thermodynamics for formation of the intermediate formed from addition of the first $NO_{(g)}$ molecule, along with analogous data for the second $NO_{(g)}$ addition reaction.

The kinetic measurements were carried out using 10 μM complex solutions (see Experimental Section) for a range of low-temperatures, down to −83 °C while $NO_{(g)}$ concentrations ranged between 0.28 and 2.3 mM. At all temperatures, the reaction proceeded in two consecutive steps that were both dependent on $NO_{(g)}$ concentration; this finding is in agreement with our supposition concerning the binding of two NO's and generation of the *bis*-NO adduct as the intermediate stable at low temperatures. The analysis of the overall spectral changes (Figure 6a) gave rise to the predicted (i.e., calculated) spectra of the species formed over the course of the reaction (Figure 6b), namely that the first $NO_{(g)}$ molecule very rapidly adds to $[(TMPP)Fe^{III}–O–Cu^{II}(tmpa)]^{+}$ (λ_{max} = 443 nm), and this is followed by slightly slower (also see below) addition of the second $NO_{(g)}$. From the two exponential fits of the two-phase kinetic traces (Figure 7), the corresponding observed rate constants for the first (k_1) and the second (k_2) reaction steps were obtained (Table S1)

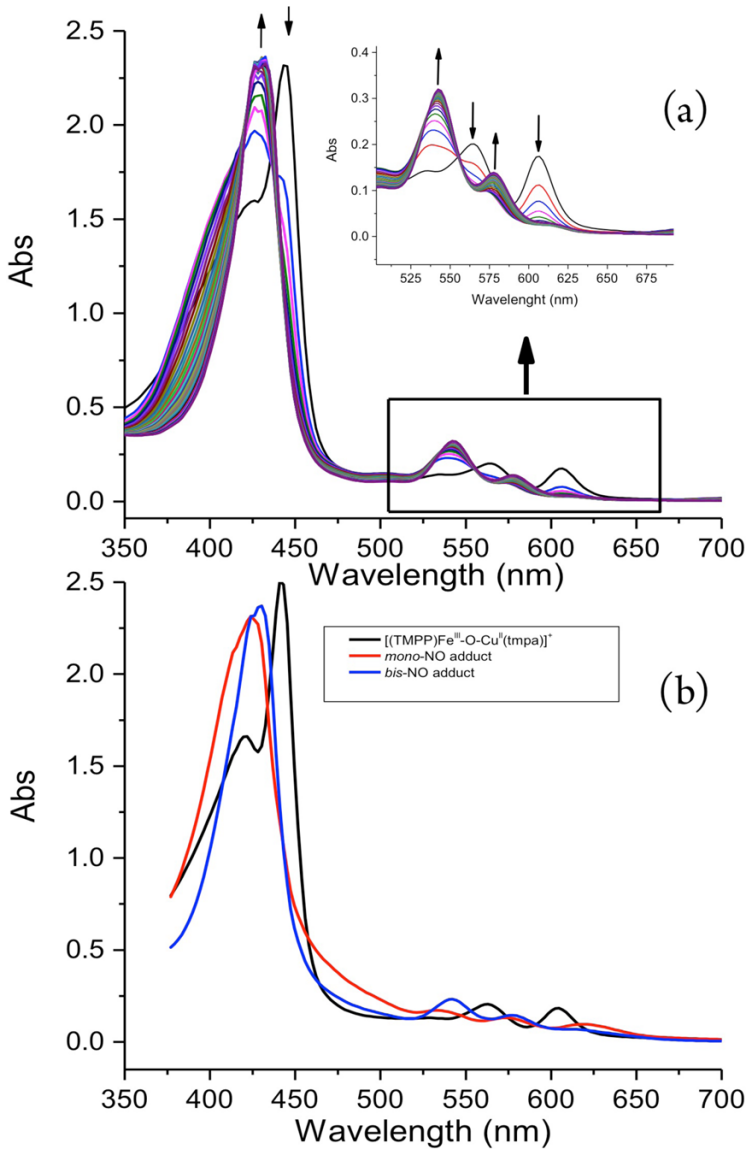

Figure 6. (a) Time resolved spectra for the reaction between $[(TMPP)Fe^{III}–O–Cu^{II}(tmpa)]$-$[B(C_6F_5)_4]$ (λ_{max} = 443, 564 an 604 nm, 10 μM) and $NO_{(g)}$ (2.3 mM) in a 10 mm cuvette in acetone at −60 °C (monitoring time 1.2 s; spectrum shown every 40 ms). **(b)** Spectra of the species involved in the two-step reaction ($[(TMPP)Fe^{III}–O–Cu^{II}(tmpa)][B(C_6F_5)_4]$ (black), *mono*-NO adduct (red, λ_{max} = 424, 533, 574, and 619 nm) and *bis*-NO adduct (blue, λ_{max} = 433, 545 and 582 nm).

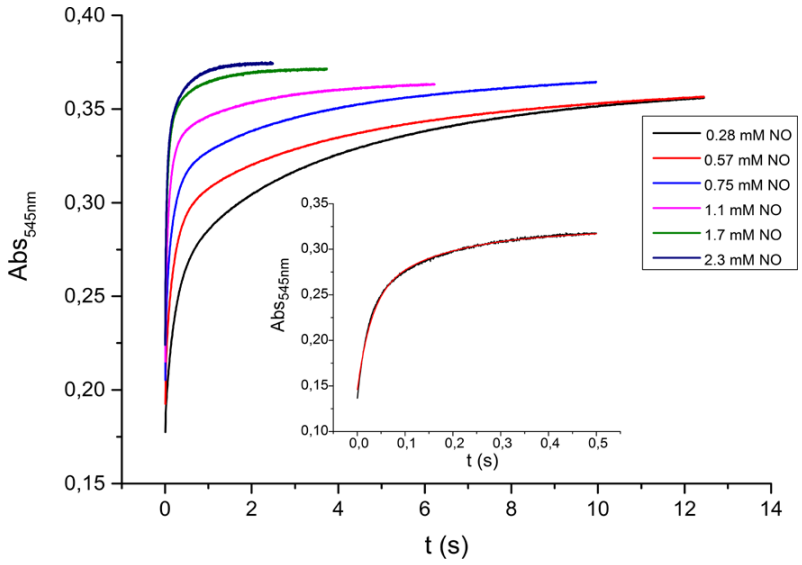

Figure 7. Traces at 545 nm for different $NO_{(g)}$ concentrations were obtained for the reaction between $[(TMPP)Fe^{III}–O–Cu^{II}(tmpa)][B(C_6F_5)_4]$ and $NO_{(g)}$ in acetone at −60 °C. Inset: Kinetic trace with a two-exponential fit (red curve) for 0.28 mM $NO_{(g)}$; for examples of such traces at other wavelengths, see Figure S12.

At all temperatures, linear dependencies ($k_{(obs)} = k_{(on)}$ [NO] + $k_{(off)}$) of the observed rate constants ($k_{1(obs)}$ and $k_{2(obs)}$) on concentration were obtained (Figure 8) with a slope corresponding to the second-order rate constants $k_{1(on)}$ and $k_{2(on)}$ for the forward reaction (Table 2). An intercept corresponding to the rate constant for the back reaction ($k_{1(off)}$) was observed only for the first reaction step (Table 2), whereas the intercept in the case of the second reaction step was close to zero (within the error limits), suggesting an irreversible nature for the binding of the second $NO_{(g)}$.

Table 2. Temperature Dependence of $k_{1(on)}$, $k_{1(off)}$ and $k_{2(on)}$.

T (°C)	$k_{1(on)}$ (M^{-1} s^{-1})	$k_{1(off)}$ (s^{-1})	$k_{2(on)}$ (M^{-1} s^{-1})
–60	6,053 ± 186	2.61 ± 0.24	706 ± 20
–67	5,061 ± 244	1.47 ± 0.32	637 ± 40
–74	2,356 ± 69	1.07 ± 0.09	504 ± 40
–83*	1,184 ± 12	0.50 ± 0.01	

* The second step at –83 °C was very slow and $k_{2(obs)}$ and thus $k_{2(on)}$, could not be accurately determined.

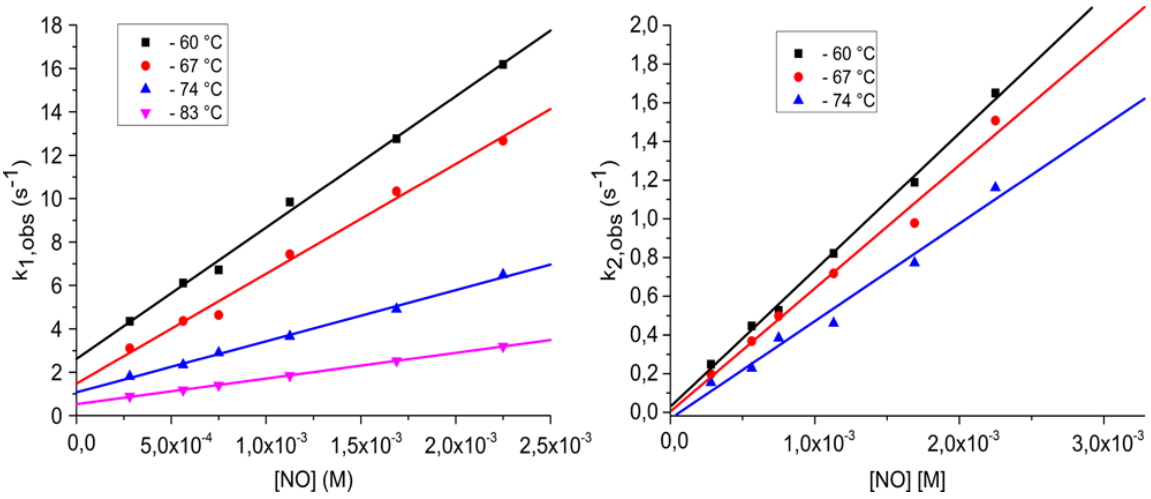

Figure 8. *Left*: Linear dependence of $k_{1(obs)}$ on concentration at different temperatures for the reaction between [(TMPP)Fe^{III}–O–Cu^{II}(tmpa)][B(C_6F_5)$_4$] and $NO_{(g)}$ in acetone. *Right*: Linear dependence of $k_{2(obs)}$ on concentration at different temperatures for the reaction between the μ-oxo complex and $NO_{(g)}$ in acetone.

From the corresponding Eyring plots (Figures S13 and S14), activation parameters for the forward ($\Delta H^{\ddagger}_{(on)}$ and $\Delta S^{\ddagger}_{(on)}$) for the first ($k_1$) and second ($k_2$) step and for the reverse reaction ($\Delta H^{\ddagger}_{(off)}$ and $\Delta S^{\ddagger}_{(off)}$) for the first step ($k_1$) were determined (Table 3).

Table 3. Activation and Reaction Parameters for Binding of the First and Second $NO_{(g)}$.

Reaction	$\Delta H^{\ddagger}_{(on)}$ (kJ mol^{-1})	$\Delta S^{\ddagger}_{(on)}$ (J mol^{-1} K^{-1})	$\Delta H^{\ddagger}_{(off)}$ (kJ mol^{-1})	$\Delta S^{\ddagger}_{(off)}$ (J mol^{-1} K^{-1})	$\Delta H°$ (kJ mol^{-1})	$\Delta S°$ (J mol^{-1} K^{-1})
first $NO_{(g)}$	24 ± 3	–64 ± 10	22 ± 2	–131 ± 9	2.0 ± 0.4	67 ± 15
second $NO_{(g)}$	7 ± 2	–155 ± 8				

We note that the first $NO_{(g)}$ molecule binds to $[(TMPP)Fe^{III}–O–Cu^{II}(tmpa)]^{+}$ at rates which are about 1 order of magnitude greater than for the second $NO_{(g)}$ molecule (Scheme 3; Table 2), which allowed us to obtain kinetic parameters for both steps. The low values of the $\Delta H^{\ddagger}_{(on)}$ and strong negative values for $\Delta S^{\ddagger}_{(on)}$ are consistent with the associative character of both reaction steps, confi rming that they are related to the binding of $NO_{(g)}$. The negligible activation enthalpy (7 ± 2 kJ mol^{-1}, i.e., 1.7 ± 0.5 kcal mol^{-1}) for the binding of the second $NO_{(g)}$ suggests an almost activation-less character for this reaction step. This, together with the very negative $\Delta S^{\ddagger}_{(on)}$ value, reveals that in the rate-determining step bond breaking does not play a role and that bond making predominates. These data are in agreement with the DFT studies (vide infra).

Having activation parameters for both the forward and reverse reaction, it is possible to calculate the reaction thermodynamic parameters for the binding of the first $NO_{(g)}$ molecule, i.e., reaction enthalpy $\Delta H°$ and reaction entropy $\Delta S°$ (Table 3). It is notable that the overall reaction entropy is positive (Table 3), pointing to the important role of solvation/electrostriction effects in the overall entropy changes for addition of the first $NO_{(g)}$.[26]

For the binding of the first $NO_{(g)}$ molecule, the reaction free energy $\Delta G°$ and equilibrium constant K at a certain temperature can also be calculated. At −60 °C (213.15 K) the reaction free energy for the binding of the first $NO_{(g)}$ is $\Delta G° = -12 \pm 3$ kJ mol^{-1}, while the kinetically determined equilibrium constant has a value of $K_1 = k_{1(on)}/k_{1(off)} = 2319 \pm 284$ M^{-1}.[27]

To corroborate this value of the equilibrium constant obtained based on the

kinetic data that corresponds to the first $NO_{(g)}$ binding, we have also analyzed the spectral changes at 545 nm (Figure 9) related to this step as a function of $NO_{(g)}$ concentration according to eq 1,

$$A_x = A_0 + \left[(A_\infty - A_0) \times \frac{K \times [NO]}{1 + K \times [NO]}\right] \quad (1)$$

where Ax is the absorption of the *mono*-NO adduct at a certain $NO_{(g)}$ concentration, A_0 is the initial absorption, A_∞ is the final absorption, and K is the binding constant.

The K_1 values at −60 °C obtained from kinetics (2319 ± 284 M^{-1}) and then thermodynamics (3506 ± 240 M^{-1}, Figure 9) are in reasonable agreement,[28] confirming the reversible nature of the process that results in the *mono*-NO adduct. By way of comparison, the value for K_1 at −74 °C obtained by the analysis of the spectral changes

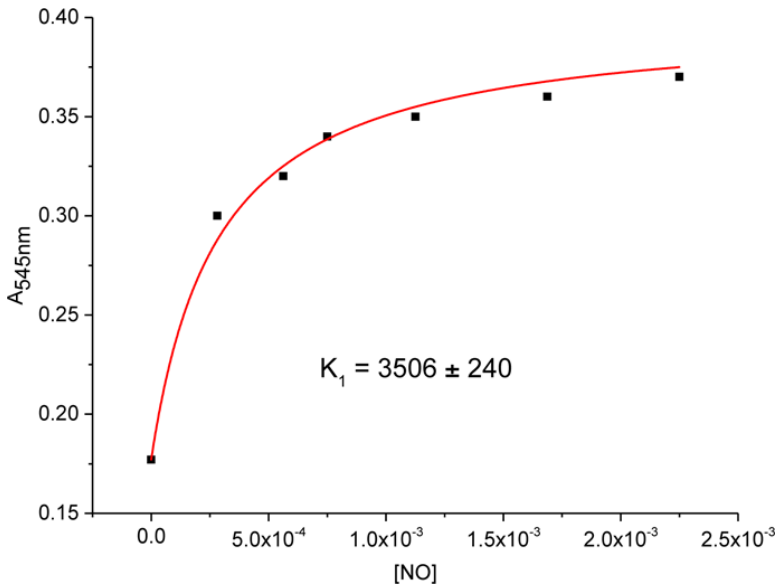

Figure 9. Absorbance at 545 nm (at the end of the first reaction step at −60 °C) as a function of $NO_{(g)}$ concentration (data fitted in eq 1).

as a function of $NO_{(g)}$ concentration is 3044 ± 144 M^{-1} (Figure S15), with corresponding $K_1 = k_{1(on)}/k_{1(off)}$ = 2202 ± 250 M^{-1}.[27] A rather small eff ect of temperature on this equilibrium is in an accord with the negligible reaction enthalpy, which is also confi rmed by experimentally obtained kinetic parameters (Table 3) as well as by DFT calculations (vide infra).

2.5. Cryo-Spray Ionization Mass Spectrometry (CSI-MS)

CSI-MS proved to be very useful for the study and characterization of the "intermediate" described herein. A manifold of intense peaks (with maximum at *m /z* = 1217.2847) corresponds to this *bis*-NO adduct which is moderately stable at −60 ° C; the isotope pattern is in agreement with theory (Figure 10). Mass spectra obtained before addition of $NO_{(g)}$ showed the intact starting μ-oxo complex, $[(TMPP)Fe^{III}–O–Cu^{II}(tmpa)]^+$, as the main species observed (Figure S16), whereas the mass spectrum of the product solution confirmed the cleavage of the "intermediate" into $[(tmpa)Cu^{II}(NO_2)]^+$ and $(TMPP)Fe^{II}(NO)$ (Figure S17).

To try to provide further insight, titration of $[(TMPP)Fe^{III}–O–Cu^{II}(tmpa)]^+$ with small amounts of a $NO_{(g)}$ solution did not lead to the mass spectrometric detection of a *mono*-NO adduct. Mass spectra always resulted in the presence of the *bis*-NO adduct, the "intermediate" (Scheme 3) independent of the volume of $NO_{(g)}$ solution added. This is in agreement with our kinetic studies (vide supra), where we observed that the *mono*-NO adduct is prone to irreversibly bind the second $NO_{(g)}$ molecule.

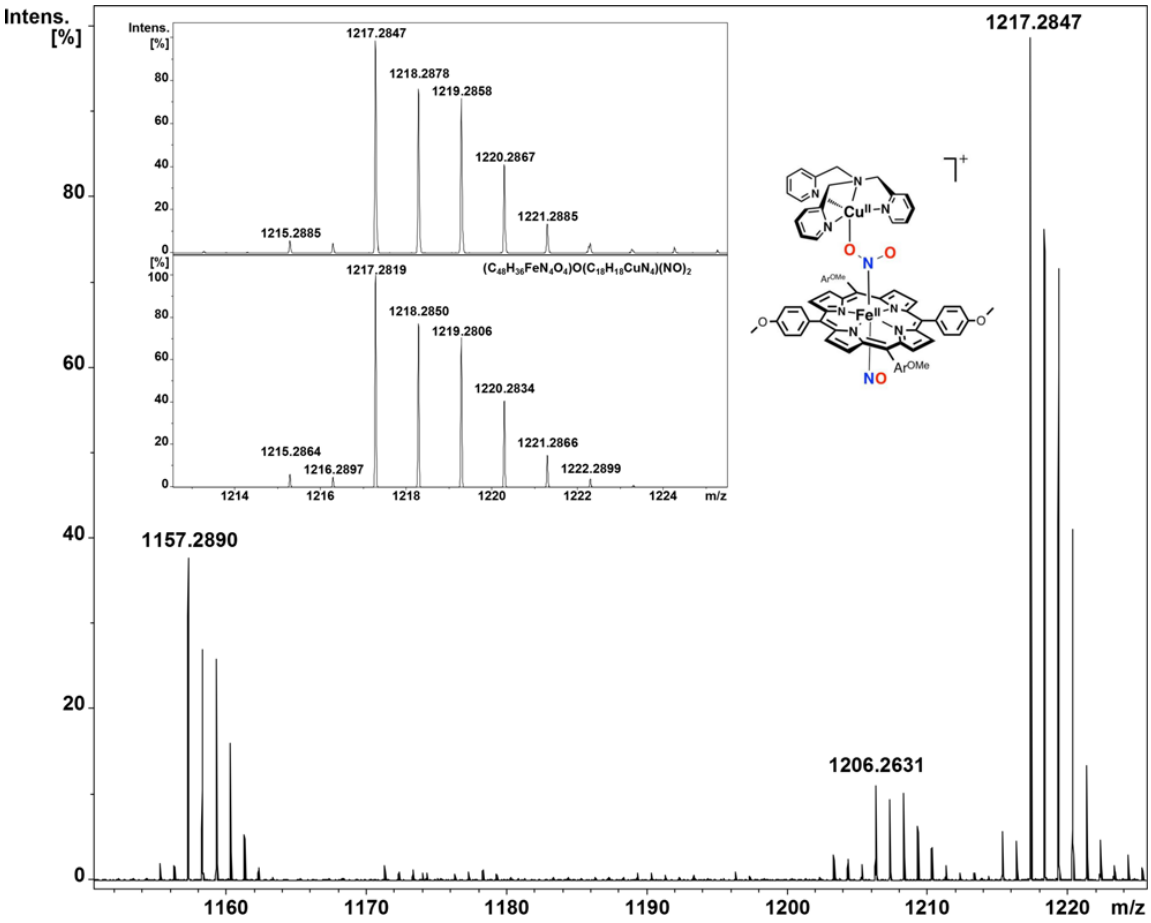

Figure 10. Mass spectrum of $[(TMPP)Fe^{III}–O–Cu^{II}(tmpa)]^{+}$ in acetone immediately after bubbling with $NO_{(g)}$ (spray gas temperature −60 °C, dry gas temperature −55 °C; main species *m/z* = 1217.2847).

2.6. Theory

DFT calculations confirm the proposed nature of the observed intermediates and are in agreement with the kinetic and thermodynamic parameters experimentally obtained for the first and second reaction steps (Scheme 3). The corresponding DFT derived reaction mechanism that takes place on multiple-spin potential energy surfaces is visualized in Scheme 4. We should note that BP86/6-31G(d) incorrectly predicts intermediate spin state (IS) for $[(TMPP)Fe^{III}–O–Cu^{II}(tmpa)]^{+}$ as the ground state,

whereas OLYP/6-311+G(d,p) results in the correct high-spin state (HS) for the starting complex (Scheme 4). Nevertheless, both methods give a similar trend for the entire reaction pathway.

Scheme 4. Schematic Calculated Energy Profile for $[(TMPP)Fe^{III}–O–Cu^{II}(tmpa)]^{+}$ Reaction with $NO_{(g)}$.

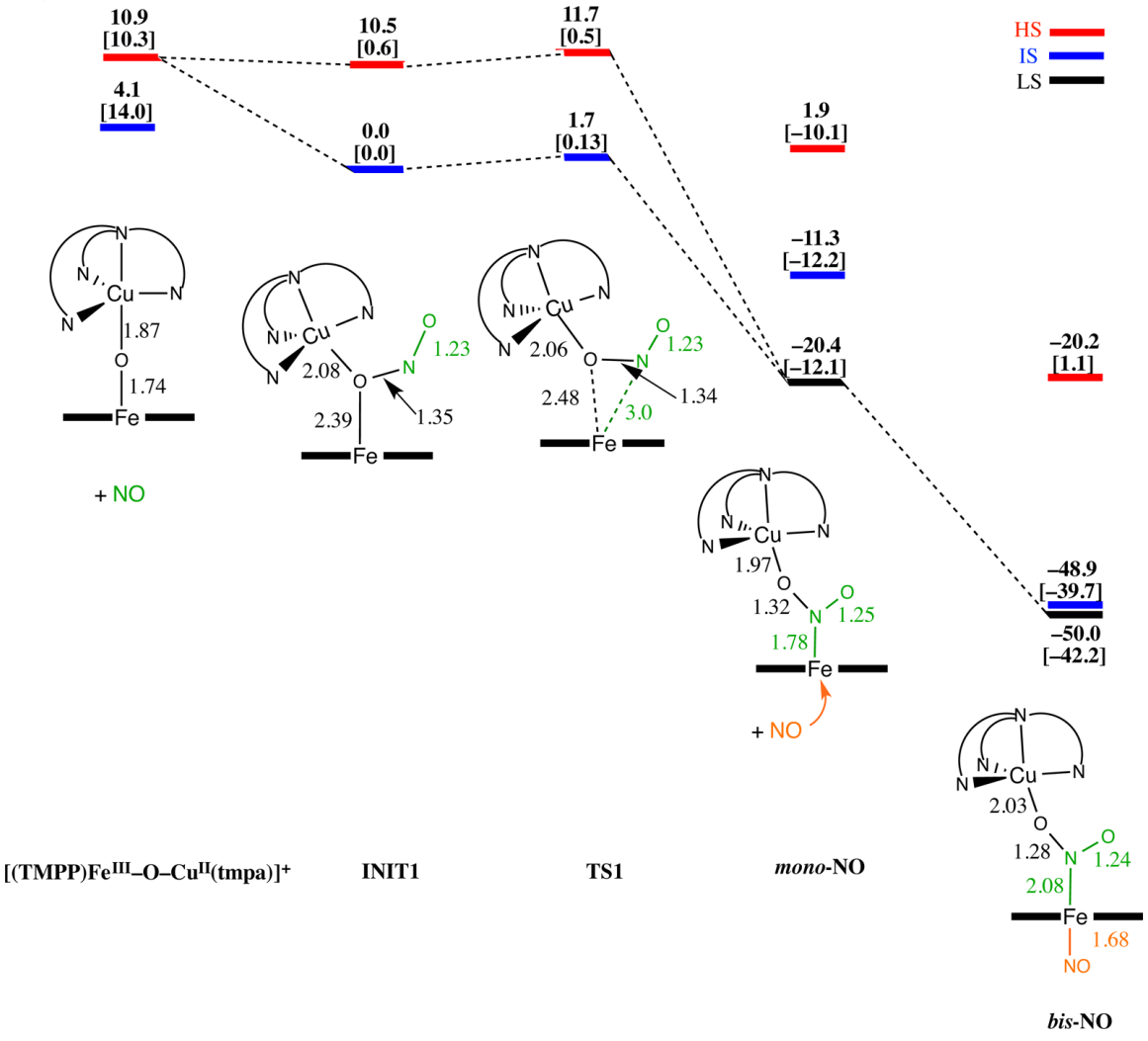

{ΔE + ZPE in kcal mol^{-1} including solvent correction at both the BP86/6-31G(d) level and OLYP/6-311+G(d,p) level (given in brackets)}. Selected bond lengths are in Å; red is high spin (HS), blue is intermediate spin (IS), and black is low spin (LS) state potential energy surfaces.

The results suggest that generation of the *mono*-NO adduct requires the formation of a three-membered O−Fe−N chelate ring in a corresponding transition state (TS1 in Scheme 4). This predominantly requires bond formation between Fe and the nitrogen atom from $NO_{(g)}$, accompanied to a smaller extent by weakening of the Fe−O bond in the oxo bridge (bond elongation from 2.39 to 2.48 Å). This explains the low activation enthalpy (24 ± 3 kJ/mol) and negative activation entropy experimentally obtained for the fi rst reaction step (Table 3). After the formation of TS1, the Fe−O−Cu bridge breaks completely giving the *mono*-NO adduct. Based on the fact that the SOMO of this species is predominantly localized on the Fe-porphyrin moiety (Figure S18), we can suggest that binding of the first $NO_{(g)}$ is accompanied by electron transfer from $NO_{(g)}$ to the heme-iron center. Thus, the *mono*-NO adduct probably already has a character of the Fe(II)-nitrite species bridged to Cu(II). As expected, based on the principle of the microscopic reversibility, the back reaction characterized by a negative activation entropy (Table 3), because on going from the *mono*-NO adduct to TS1 (Scheme 4) bond formation between Fe and the bridging *O*-atom is required. Importantly, this *mono*-NO adduct resembles the structure of an *N*-bound nitrite ferrous species characterized by resonance Raman spectroscopy in the binuclear heme-a_3/Cu_B active site of ba_3-C*c*O.[35]

After formation of the *mono*-NO adduct, the reaction proceeds virtually without any barrier, since there is no significant bond breaking required for the formation of *bis*-NO adduct. Namely, directly from the *mono*-NO adduct, the *bis*-NO adduct, "intermediate", is generated as a thermodynamic sink (Scheme 4). This is again perfectly in agreement with the experimental data that demonstrate the irreversible character of this reaction step (Scheme 3 and Figure 8 (right)) and negligible activation barrier (Table 3).

A strong $NO_{(g)}$ binding affinity by the *mono*-NO adduct (here, actually the ferrous *N*-bound nitrite species) for the incoming second $NO_{(g)}$ molecule can be explained by its five-coordinate ferrous character. Both in *mono*- and *bis*-NO adducts, the N−O bond lengths within the NO_2-moiety are typical for a bridging nitrite coordination,[29] further supporting the view that electron transfer, i.e., $NO_{(g)}$ oxidation, proceeded during the course of the first reaction step. The calculated $Fe{-}N_{(nitrite)}$ bond length in this "intermediate", the *bis*-NO adduct (Scheme 4 and Figure S19), is longer than reported for $[(TMPP)Fe^{III}(NO_2)(NO)]$,[30] and the $Fe{-}N_{(NO)}$ bond length is similar to that in $(TPP)Fe^{II}(NO)$,[31] which is indicative of the ferrous character of the Fe center in the "intermediate". The computed spin densities on the iron center (δ = 1.2) and NO (δ = −0.19) are in agreement with those generally predicted by previous calculations[32] for low-spin six-coordinate ferrous-nitrosyl species. Also, both DFT methods applied here indicate that *bis*-NO adduct has low-spin ground state.

The elongated $N_{(nitrite)}$ bond facilitates the final reaction step, which results in the dissociation of the binuclear adduct to give mononuclear complexes, $[(tmpa)Cu^{II}(NO_2)]^+$ and $(TMPP)Fe^{II}(NO)$ (Figures S20 and S21). However, a corresponding transition state to describe this process could not be located, and therefore this step was not analyzed. To do so likely would require explicit inclusion of solvent molecules, which suggests a solvent-assisted mechanism is involved in this $Fe{-}N_{(nitrite)}$ bond cleavage step.

Further investigations will include our probing of the mechanisms of the reactions described in this report. For nitrite reduction, critical mechanistic components will certainly include the heme reductive capability and the nitrite−Cu binding mode (e.g., *O*- vs *O*,*O*′- vs *N*-bound). As our heme and Cu centers have switched redox capabilities

compared with C*c*O, we also wish to change the heme or the Cu ligand to make the Cu center a better oxidant than the heme. For our heme/Cu $NO_{(g)}$ oxidation chemistry, we are uncertain about which metal is the real oxidant,[18] so further investigations are required; as is often the case, "the devil is in the details".

3. Concluding Remarks and Summary

The one-electron oxidation of nitric oxide is a vital component of biological control of cellular $NO_{(g)}$ concentrations, this molecule being a critical signaling agent. The product, nitrite ion, resides as a cellular storage pool for regeneration of $NO_{(g)}$ as needed, via NO_2^- binding to heme centers and subsequent reduction. The active site of C*c*O is where $NO_{(g)}$ and nitrite redox interconversion occurs. This study addresses such critical reactivity at the molecular level by detailed structural and mechanistic studies on synthetic models mediating $NO_{(g)}$ oxidase reaction. The following are the major findings, conclusions, or comments related to this work:

(1) Heme/Cu compounds, which are μ-oxo heme-Fe^{III}–O–Cu^{II}(L) constructs, with metal ions in their typical higher oxidation states serve as excellent starting points for the study of $NO_{(g)}$ oxidation. Here, two new X-ray structures are added to library of such compounds, and they are compared to previous members. $[(F_8)Fe^{III}–O–Cu^{II}(MePY2)]^+$ with its tridentate chelate for copper(II) has a very bent μ-oxo moiety ($\angle$Fe–O–Cu = 142.48°), while for $[(TMPP)Fe^{III}–O–Cu^{II}(tmpa)]^+$, this fragment is near-linear ($\angle$Fe–O–Cu = 173.6°).

(2) A notable structural feature, for such compounds where only the porphyrinate identity varies, is that $[(F_8)Fe^{III}–O–Cu^{II}(tmpa)]^+$ exhibits a square pyramidal Cu^{II}-coordination, while for $[(TMPP)Fe^{III}–O–Cu^{II}(tmpa)]^+$, the tmpa-Cu N_4O-ligation occurs within a trigonal bipyramidal geometry. Porphryinate *o*-fluorine substituents of *meso*-phenyl groups for F_8 are seen to be responsible for this deviation from the normal TBP geometry generally seen for $[(tmpa)Cu^{II}(X)]^{n+}$ complexes.

(3) In the overall reaction where a μ-oxo heme-$Fe^{III}–O–Cu^{II}L$) complex reacts with two $NO_{(g)}$ molecules (but only one is accountable for the redox chemistry), forming cupric nitrite plus ferrous-heme nitrosyl complexes, the first $NO_{(g)}$ molecule (reversibly) attacks the bridging oxo atom, in a very fast reaction ($k_{1(on)} = 6053 \pm 186\ M^{-1}\ s^{-1}$ (−60 °C). This study was carried out for the chemistry with $[(TMPP)Fe^{III}–O–Cu^{II}(tmpa)]^+$, which was amenable to our interrogation by various spectroscopies, low-temperature stopped-flow kinetics, and DFT calculations and analysis.

(4) This $NO_{(g)}$ attack is accompanied by electron transfer (formally from $NO_{(g)}$ to the heme), and based on our DFT calculations, a “triangular” structure at iron develops wherein both the original μ-oxo atom and the $NO_{(g)}$-derived *N*-atom bind iron in one of the transition states (cf. Scheme 4, TS1).

(5) In a downhill process, the NO_2^- ligates to Fe(II) as a nitro ligand, i.e., *N*-bound, with one of its O atoms (that derived from the μ-oxo atom) coordinated and thus bridged to the cupric center; this is the *mono*-NO adduct, Scheme 4. As

mentioned in the discussion, strong credence is given to our conclusion about the structure of the *mono*-NO adduct; such a *N*-bound nitrite to iron(II) structure was just recently detected for the ba_3-C*c*O.[33] This is the first description of a nitrite ion binding to this enzyme center, where the importance of this finding relates to the C*c*O nitrite reductase function. We note that in our previously published C*c*O nitrite reductase model system,[12] we also proposed that nitrite *N*-binding to the reduced heme was key to reaction progress. So, for both chemical and biochemical heme/Cu-mediated nitrite reductase and $NO_{(g)}$ oxidase chemistry (the latter as in this report; Scheme 4), *N*-atom binding to a ferrous heme along with O atom coordination to the cupric ion are key.

(6) Then, the second $NO_{(g)}$ molecule irreversibly attacks ($k_{2(on)}$ = 706 ± 20 at −60 °C) the open face of the heme in the *mono*-NO adduct to give the *bis*-NO adduct, which was observed by UV−vis spectroscopy (even at −20 °C; λ_{max} = 433 nm) and confirmed by using CSI-MS at −60 °C.

(7) This *bis*-NO adduct "intermediate" then undergoes dissociation in a first-order process ($k_{dissoc.}$ = 6.7 × 10^{-3} s^{-1}; −20 °C) to release the finally observed mononuclear adducts, the cupric-nitrite and ferrous heme nitrosyl complexes.

(8) Strong evidence for our conclusion that the last step is a dissociation and that our formulation and DFT structural characterization of the "intermediate" is correct comes from the fact that cooling the products, consisting of a 1:1 mixture of $(TMPP)Fe^{II}(NO)$ plus $[(tmpa)Cu^{II}(NO_2)]^+$, results in reformation of the "intermediate", where the nitrite bound to copper ion coordinates and thus forms a

bridge to the ferrous heme-nitrosyl complex (vide supra). Another piece of evidence supporting the formulation of the "intermediate" is its EPR spectrum, the analysis of which indicates the presence of a six-coordinated ferrous-heme nitrosyl linked to an EPR active cupric species in a TBP coordination environment.

(9) Aside from our proposed mechanism (Schemes 3 and 4), we also considered other possible/alternative pathways for reaction of the first $NO_{(g)}$ molecule with $[(TMPP)Fe^{III}–O–Cu^{II}(tmpa)]^{+}$, involving initial binding of the $NO_{(g)}$ to either the cupric center or the open face of the ferric heme (i.e., trans to the bridging oxo moiety). Both of these possibilities fail to satisfactorily describe and match our spectroscopic data and DFT calculations. The former event is a nonproductive pathway as it requires breakage of the newly formed Cu(II)−NO bond in order to generate an *O*-bound nitrite to the cupric center in the *mono*-NO adduct. In the latter alternative, binding of the first $NO_{(g)}$ to the five-coordinate high-spin heme would result in a dramatic spin change, which therefore would be a quite slow reaction when forming a six-coordinate low-spin heme; this goes against the observed kinetics which reveal a fast process. In addition, based on our experimental data and DFT calculations, the second step (involving the addition of second $NO_{(g)}$) is an activation- less process; if the first $NO_{(g)}$ goes to the heme open face, the second $NO_{(g)}$ would now involve its attack on the oxo group followed by an $Fe–O_{(nitrite)}$ bond breaking, which is unlikely to be activation-less.

(10) Another point of discussion is the relevance of the present study to the process of reductive nitrosylation of heme-Fe^{III} complexes, a widely known and utilized

method to generate either synthetic or biological ferrous heme-nitrosyl compounds (i.e., $\{FeNO\}^7$), wherein $NO_{(g)}$ oxidation to nitrite is involved.[34] The most common pathway known for reductive nitrosylation is thought to function via initial coordination of $NO_{(g)}$ to a ferric site forming a heme-Fe^{III}(NO) species, perhaps better formulated as a heme $Fe^{II}(NO^+)$ complex. This is followed by nucleophilic attack of OH^- or H_2O at the coordinated nitrosyl and then dissociation of the nitrosylated nucleophile, NO_2^-, from the metal center resulting in formation of reduced metal center which further reacts with a second molecule of $NO_{(g)}$ to form a stable ferrous heme-Fe^{II}(NO) product.35 However, as Ford describes,[34b] an alternative pathway could involve attack of $NO_{(g)}$ at "a nucleophile coordinated to the oxidizing metal center", here the μ-oxo moiety of the heme-Fe^{III}–O–Cu^{II}(L) framework. The μ-oxo group acts as an inner-sphere nucleophile assisting formation of the first reaction intermediate, which bears the heme- Fe–(NO_2)–Cu component. Coordination to the neighboring cupric center would provide further stability for the bridged nitrite species toward addition of the second $NO_{(g)}$ (at low temperatures, below −20 °C) generating the bis-NO adduct, aka the "intermediate". A temperature increase results in the final cleavage of the nitrite bridge. Thus, this study provides evidence for formation of a six-coordinate ferrous heme nitrosyl compound during a reductive nitrosylation process.

(11) It may be viewed that the family of μ-oxo heme-Fe^{III}–O–Cu^{II}(L) complexes studied here for their NO oxidase chemistry are not species which are present in C*c*O turnover intermediates or resting-state structures. However, these μ-oxo

compounds should be thought of as representatives of heme-Fe^{III}–OH···Cu^{II} enzyme species, i.e., just different by one proton from our synthetic complexes. New computational studies[36] in fact suggest that a heme-Fe^{III}–OH···Cu^{II} or heme-Fe^{III}–(μ-OH)–Cu^{II} complex can or does form during CcO enzymatic function. We suggest that such an entity can be responsible for $NO_{(g)}$ oxidase chemistry when in its protein environment. $NO_{(g)}$ attacks the hydroxo-group, giving a six-coordinate nitro ferrous heme (i.e., with *N*-ligated nitrite and proximal His ligand), which may be stabilized by nitrite interaction with the neighboring cupric ion, as in our synthetic compound.

In conclusion, the present report provides many molecular level details pertaining to metal/nitrogen-oxide chemistries, in particular showing how nitric oxide and/or nitrite can undergo atom-transfer redox chemistry, when binding to hemes (and copper) during $NO_{(g)}$ oxidation and/or nitrite reductive processes.

4. Experimental Section

4.1. General Methods

All reagents and solvents were of commercially available grade, unless otherwise noted. Acetone was distilled over Drierite under argon atmosphere and kept over 3 Å molecular sieves prior to use. Tetrahydrofuran (THF), 2-methyltetrahydrofuran (MeTHF) (inhibitor free, 673277), and hexanes were purchased from Sigma-Aldrich and dried by distillation under argon from sodium/benzophenone. Pentane and acetonitrile (MeCN)

were distilled over calcium hydride under argon. Toluene was used after passing through a 60 cm-long column of activated alumina (Innovative Technologies) under argon. Air- and moisture-sensitive compounds were prepared and handled under an argon atmosphere using standard Schlenk techniques or in a Vacuum Atmospheres OMNI-Lab inert atmosphere (<1 ppm of O_2 and H_2O) glovebox filled with nitrogen. O_2 gas was dried by passing through a short column of supported P4O10 (Aquasorb, Mallinckrodt). NO gas was obtained from Matheson Gases and purified following methods previously described in the literature.37 This purified $NO_{(g)}$ was transferred and stored in a 50 mL Schlenk flask capped with a rubber septum. Addition of NO gas to metal complex solutions was effected by transfer via a three-way long syringe needle. Deoxygenation of solvents was effected by either repeated freeze/pump/thaw cycles or bubbling with argon for 45−60 min.

Infrared (IR) spectra were obtained using a Thermo Scientific Nicolet Nexus 670 Fourier transform IR (FT-IR) spectrophotometer. Bench-top low-temperature UV−vis spectra were recorded with a Cary-50 Bio spectrophotometer equipped with a Unisoku USP-203A cryostat using a 2 mm modified Schlenk cuvette. Electron paramagnetic resonance (EPR) measurements were performed on an X- band Bruker EMX CW EPR spectrometer (~9.4 GHz) controlled with a Bruker ER 041 XG microwave bridge, using 5 mm quartz EPR tubes. EPR spectral simulations were carried out using EasySpin v. 4.5.5 on a Mac (running OS X). Elemental analysis was accomplished at Columbia Analytical Services (Tucson, AZ). Single-crystal X-ray data were collected using either an Xcalibur3 or a SuperNova (Agilent Technologies) diffractometer at the X-ray diffraction facility of the Johns Hopkins University. Cryo-spray ionization mass spectrometry

(CSI-MS) spectra were collected by a Bruker maXis 4G coupled with a Bruker cryospray unit. Low-temperature stopped-flow experiments were performed with a Biologic cryo SFM-4000 4-syringe stopped- flow, combined with a 150 W xenon lamp and a J&M TIDAS diode array detector (200−724 nm, integration time 0.5 ms). All reactions were performed in acetone unless specified otherwise.

The compounds $(F_8)Fe^{II}$,[13b,38] $(TMPP)Fe^{II}$,[12] $[(tmpa)Cu^{I}(MeCN)][B(C_6F_5)_4]$,[11,39] $[(MePY2)Cu^{I}(MeCN)][B(C_6F_5)_4]$,[13b] $[(AN)Cu^{I}][B(C_6F_5)_4]$,[40] $[(AN)Cu^{II}(NO_2)](SO_3CF_3)$,[12] and $(F_8)Fe^{II}(NO)$[37b,41] were synthesized and characterized following literature methods. $(TMPP)Fe^{III}(Cl)$ was purchased from TriPorTech (Germany). The μ-oxo complexes, $[(F_8)Fe^{III}–O–Cu^{II}(tmpa)][B(C_6F_5)_4]$,[11] $[(F_8)Fe^{III}–O–Cu^{II}(AN)][B(C_6F_5)_4]$,[16] $[(F_8)Fe^{III}–O–Cu^{II}(MePY2)][B(C_6F_5)_4]$,[13b] and $[(TMPP)Fe^{III}–O–Cu^{II}(tmpa)][B(C_6F_5)_4]$[12] were synthesized by bubbling dry dioxygen through a one-to-one mixture of the corresponding reduced heme and copper mononuclear complexes as we previously reported. All these μ-oxo compounds are very moisture sensitive, but otherwise stable, and are soluble in a variety of solvents.

4.2. Synthesis of $[(TMPP)Fe^{III}(THF)_2](SbF_6)\cdot THF$

The current synthesis method is a slightly modified version of our method reported earlier for the synthesis of $[(F_8)Fe^{III}(THF)_2](SbF_6)$.[41] In the glovebox, to a solution of $(TMPP)Fe^{III}(Cl)$ (292 mg, 0.354 mmol) in THF (50 mL) was added $AgSbF_6$ (128 mg, 0.373 mmol). The reaction mixture was allowed to stir for 2 h under reduced

light at RT. The solution was then filtered to remove AgCl, and addition of deoxygenated pentane (100 mL) resulted in precipitation. The supernatant was decanted, and the compound obtained was recrystallized twice from THF/pentane affording very dark-red crystals suitable for X-ray structure determination (Figure S22). After vacuum drying, the crystals weighted 340 mg (78% yield). Anal. calcd for $C_{60}H_{60}F_6FeN_4O_7Sb$: C, 58.08; H, 4.87; N, 4.52. Found: C, 57.98; H, 4.85; N, 4.56. UV−vis [λ_{max}, nm (ε_{max}, $M^{-1}cm^{-1}$)]: 401 (162,100), 533 (17,300) and 679 (3300) in acetone and 404 (161,200), 532 (16,100) and 698 (4600) in MeCN (Figure S23). FT-IR (solid): $\nu_{(SbF6)}$ = 655 cm−1. EPR: $g_{\perp}$ = 5.56, $g_{\parallel}$ = 1.99 in THF/MeTHF (1:4) at 12 K (Figure S24).

4.3. Reactions of *μ*-oxo Complexes with $NO_{(g)}$

Reaction of [(F8)Fe^{III}−O−Cu^{II}(AN)][B(C6F5)4] with $NO_{(g)}$: In a 10 mL Schlenk flask, $(F_8)Fe^{II}\cdot H_2O$ (16.6 mg, 0.020 mmol) and $[(AN)Cu^{I}][B(C_6F_5)_4]$ (18.6 mg, 0.020 mmol) were dissolved in MeTHF (4 mL). Dry dioxygen was then bubbled through the solution for 2 min with the color turning from dark red to dark orange. The solvent was removed under vacuum. The resulting solid product was then dissolved in 10 mL deoxygenated acetone. UV−vis: [λ_{max}, nm (ε_{max}, $M^{-1}cm^{-1}$)]: 439 (141,200) and 555 (19,700) in acetone. Samples for UV−vis monitoring were prepared by diluting 25 μL of the stock solution with acetone to 5 mL that was then transferred to a 10 mm modified Schlenk cuvette. The spectra were recorded upon bubbling of 1 mL of $NO_{(g)}$ directly into the solution at RT (Figure S2). Formation of $(F_8)Fe^{II}(NO)$ was confirmed by examination

of the IR spectrum of the solid product (ν_{NO} = 1688 cm^{-1}). An EPR spectrum of the reaction mixture was recorded in MeCN/toluene (1:1) at 20 K revealing a mixture of a cupric and ferrous heme nitrosyl compounds. An EPR spectrum of an authentic sample of a 1:1 mixture of $(F_8)Fe^{II}(NO)$ and $[(AN)Cu^{II}(NO_2)](CF_3SO_3)$ was also recorded for comparison (Figure S3). The production of significant amount of nitrite ion (50−100%) was detected by semiquantitative QUANTOFIX nitrite test strips as previously described.[11]

Reaction of $[(F_8)Fe^{III}-O-Cu^{II}(tmpa)][B(C_6F_5)_4]$ with $NO_{(g)}$: In the glovebox, $(F_8)Fe^{II}\cdot H_2O$ (16.6 mg, 0.020 mmol) and $[(tmpa)Cu^{I}(MeCN)][B(C_6F_5)_4]$ (21.5 mg, 0.020 mmol) were dissolved in MeTHF (4 mL) in a 10 mL Schlenk flask. Dry dioxygen was bubbled through this solution affording a color change from dark red to dark orange. After removal of the solvent under vacuum, the product was dissolved in 10 mL deoxygenated acetone. UV−vis samples for low- temperature studies were prepared by diluting 38 μL of the stock solution with acetone to 1 mL that was then transferred to a 2 mm modified Schlenk cuvette. The spectra were recorded upon bubbling of 1 mL of NO(g) directly into the solution at −40 °C(Figure 4a).

Reaction of $[(F_8)Fe^{III}-O-Cu^{II}(MePY2)][B(C_6F_5)_4]$ with $NO_{(g)}$: In the glovebox, solution of $(F_8)Fe^{II}\cdot H_2O$ (16.6 mg, 0.020 mmol) and $[(MePY2)Cu^{I}(MeCN)][B(C_6F_5)_4]$ (20.5 mg, 0.020 mmol) in MeTHF (4 mL) was prepared in a 10 mL Schlenk flask. Bubbling of dry dioxygen through the solution for 2 min resulted in the color turning from dark red to dark orange. The solvent was removed under vacuum, and the solid product was then dissolved in 10 mL deoxygenated acetone. UV−vis: [λ_{max}, nm (ε_{max}, $M^{-1}cm^{-1}$)]: 438 (114,300) and 555 (18,600) in acetone. Samples for UV−vis

monitoring were prepared by diluting 25 μL of the stock solution with acetone to 1 mL that was then transferred to a 2 mm modified Schlenk cuvette. The spectra were recorded upon bubbling of 1 mL of $NO_{(g)}$ directly into the solution at −40 °C (Figure 4b). The IR spectrum of the solid product (ν_{NO} = 1688 cm^{-1}) directly indicated formation of $(F_8)Fe^{II}(NO)$. An EPR spectrum of the reaction mixture prepared at RT and redissolved in acetone was recorded at 12 K indicating a mixture of a cupric and ferrous heme nitrosyl compounds (Figure S4). The presence of significant amount of nitrite ion (50−100%) was confirmed by semiquantitative QUANTOFIX nitrite test strips as previously described.[11]

Reaction of [(TMPP)Fe^{III}−O−Cu^{II}(tmpa)][$B(C_6F_5)_4$] with $NO_{(g)}$: To a 4 mL MeTHF solution of $(TMPP)Fe^{II}\cdot 1.5H_2O$ (16.3 mg, 0.020 mmol) in a 10 mL Schlenk flask, $[(tmpa)Cu^{I}(MeCN)][B(C_6F_5)_4]$ (21.5 mg, 0.020 mmol) was added. The solution was then bubbled with dry dioxygen for 2 min resulting an immediate color change from dark red to dark green. The solvent was removed under vacuum. The resulting solid product was then dissolved in 10 mL deoxygenated acetone. UV−vis: [λ_{max}, nm (ε_{max}, $M^{-1}cm^{-1}$)]: 443 (252,000), 564 (17,300) and 605 (14,700) in acetone. Samples for UV−vis monitoring were prepared by diluting 25 μL of the stock solution with acetone to 1 mL that was then transferred to a 2 mm modified Schlenk cuvette. Spectra were recorded upon bubbling of 1 mL of $NO_{(g)}$ directly into the solution at RT (Figure S5). The reaction was also followed at −20 °C, and upon addition of 1 mL of $NO_{(g)}$ to the cold solution, immediate formation of a new intermediate was detected. UV−vis: [λmax, nm (εmax, $M^{-1}cm^{-1}$)]: 433 (246,000), 545 (15,400) and 582 (9,100) in acetone at −20 °C (Figure 5). Clean isosbestic conversion of this intermediate to the final products $(TMPP)Fe^{II}(NO)$ and $[(tmpa)Cu^{II}(NO_2)]^+$ (not detectable due to the small extinction

coefficient relative to the heme) was obtained within 12 min as monitored by UV−vis spectroscopy. The reaction was repeated at different temperatures, 0, −10, −15, −20, −25, −30, and −40 °C. First-order rate constants for conversion of the intermediate to the final products were obtained by observing the disappearance of the Soret band at 433 nm and/or appearance of the 408 nm bands, and a linear Eyring plot was then derived from the data (Figure S8). The IR spectrum of the solid product (ν_{NO} = 1677 cm^{-1}) directly indicates formation of (TMPP)Fe^{II}(NO). EPR samples were prepared by dissolving of the solid products of the reaction at RT in acetone or MeTHF. The spectra were recorded at 12 K revealing a mixture of a cupric and ferrous heme nitrosyl compounds (Figure S6). An EPR sample of [(TMPP)Fe^{III}−O−Cu^{II}(tmpa)][$B(C_6F_5)_4$] in MeTHF was also prepared and cooled to −80 °C (dry ice-acetone bath). Then 1 mL of $NO_{(g)}$ was directly bubbled into this cold solution, and the sample was frozen in liquid nitrogen. The EPR spectrum was recorded at 12 K again suggesting the presence of a cupric compound and a ferrous heme nitrosyl species (Figures S10 and S11b) but with a different hyperfine coupling than the one observed in the spectrum of the products mixture (Figures S6 and S11a). The generation of significant amount of nitrite ion (50−100%) as a final product was also confirmed by utilization of semiquantitative QUANTOFIX nitrite test strips, as previously described.[11] (*Note:* When extracting nitrite ion from reaction products to the aqueous layer, (TMPP)Fe^{II}(NO) also generates 1 equiv of additional nitrite ion. This was also taken into account in the semiquantitative nitrite analysis).

In Situ Generation of [(TMPP)Fe^{III}(NO)(NO_2)]: A 1 mL acetone solution of [(TMPP)$Fe^{III}$$(THF)_2$]($SbF_6$) (50 μM) was placed in a 2 mm Schlenk cuvette under nitrogen. The sample was cooled to −20 °C, and an initial spectrum was recorded. One

mL of $NO_{(g)}$ was directly bubbled into the cold solution resulting in a large UV−vis change assigned to the formation of $[(TMPP)Fe^{III}(NO)](SbF_6)$. Then 10 equiv of tetrabutylammonium nitrite, $(n\text{Bu})_4N(NO_2)$, were added forming a new species formulated as $[(TMPP)Fe^{III}(NO_2)(NO)]$.[30] UV−vis: [$\lambda_{max}$, nm ($\varepsilon_{max}$, $M^{-1}cm^{-1}$)]: 433 (281,000), 545 (19,200), and 581 (9500) in acetone at −20 °C (Figure S7). For comparison, we also prepared $[(TMPP)Fe^{III}(NO_2)_{1\text{ or }2}]$ in situ by reaction of 10 equiv $(n\text{Bu})_4N(NO_2)$ with $[(TMPP)Fe^{III}(THF)_2](SbF_6)$ at −20 °C; the result led to a species with a UV−vis spectrum (λ_{max} = 423 nm) which is very different from $[(TMPP)Fe^{III}(NO)(NO_2)]$ (λ_{max} = 433 nm), so the excess nitrite does not replace the bound nitrosyl.

In situ Generation of $[(NO)(TMPP)Fe^{II}-(NO_2)-Cu^{II}(tmpa)][B(C_6F_5)_4]$: In the glovebox, a 1 mL MeTHF solution of $[(TMPP)Fe^{III}-O-Cu^{II}(tmpa)][B(C_6F_5)_4]$ (50 μM) was placed in a 2 mm Schlenk cuvette, and an initial spectrum was recorded at RT. Then, 1 mL of $NO_{(g)}$ was directly bubbled into the solution resulting in the formation of final products, the ferrous heme nitrosyl, $(TMPP)Fe^{II}(NO)$, and cupric nitrite, $[(tmpa)Cu^{II}(NO_2)][B(C_6F_5)_4]$. The excess $NO_{(g)}$ was removed from the reaction solution by application of vacuum/argon purge cycles. This sample was then cooled to −125 °C, and UV−vis spectrum of this cold solution reveals generation of a new species formulated as $[(NO)(TMPP)Fe^{II}-(NO_2)-Cu^{II}(tmpa)][B(C_6F_5)_4]$ (λ_{max} = 434, 545, and 582 in MeTHF at −125 °C, Figure S9). Warming up to RT resulted the reformation of initial spectrum of the final products. Note: If excess NO(g) is not removed from the reaction solution, then upon cooling, the heme ferrous nitrosyl $(TMPP)Fe^{II}(NO)$ reversibly reacts with an additional $NO_{(g)}$ to form a dinitrosyl species (λ_{max} = 423, 544, and 582 in MeTHF

at −125 °C), as previously described for related complexes.[41,42] Generation of the dinitrosyl complex was also confirmed through bubbling excess $NO_{(g)}$ into the ferrous heme (TMPP)Fe^{II} solution in MeTHF at RT followed by cooling the sample to −125 °C.

4.4. Crystallographic Studies

Crystallization of μ-oxo Complexes: [$(F_8)Fe^{III}$−O−Cu^{II}(MePY2)][$B(C_6F_5)_4$] was prepared as described earlier by bubbling dry dioxygen through a 1:1 mixture of $(F_8)Fe^{II}$ and [(MePY2)Cu^{I}(MeCN)][$B(C_6F_5)_4$]. Diffraction quality crystals of the complex were grown by slow liquid diffusion in 5 mm glass tubes using MeTHF and pentane at RT in the glovebox.

[(TMPP)Fe^{III}−O−Cu^{II}(tmpa)][$B(C_6F_5)_4$] was prepared as we previously reported.[12] In the glovebox, suitable X-ray-quality crystals were obtained by layering hexanes onto a solution of the μ-oxo complex in toluene in 5 mm glass tubes at RT.

X-ray Structure Determinations: For crystals of [(TMPP)$Fe^{III}(THF)_2$](SbF_6) and [(TMPP)Fe^{III}−O−Cu^{II}(tmpa)][$B(C_6F_5)_4$], all reflection intensities were measured at 100(2) K using a SuperNova diffractometer (equipped with Atlas detector) with Cu Kα radiation (mirror optics, λ = 1.54178 Å), while all reflection data for [$(F_8)Fe^{III}$−O−Cu^{II}(MePY2)][$B(C_6F_5)_4$] were collected at 110(2) K using a KM4/Xcalibur (detector: Sapphire3) with enhance graphite-mono-chromated Mo Kα radiation (λ = 0.71073 Å) under the program CrysAlisPro (Version 1.171.36.24, Agilent Technologies, 2012). The structures were solved with the program SHELXS-97, SHELXS-2013, or SHELXS-

2014[43] and were refined on F^2 with SHELXL-97, SHELXL-2013, or SHELXL-2014.[43] Analytical numeric absorption correction based on a multifaceted crystal model was applied using CrysAlisPro. The temperature of the data collection was controlled using the system Cryojet (manufactured by Oxford Instruments). The H atoms were placed at calculated positions using the instructions AFIX 23, AFIX 43, or AFIX 137 with isotropic displacement parameters having values 1.2 or 1.5 times U_{eq} of the attached C atoms.

The structure of $[(TMPP)Fe^{III}(THF)_2](SbF_6)$ is mostly ordered. The SbF_6^- counterion is disordered over two orientations, and the occupancy factor of the major component refines to 0.9303(18). The crystal that was mounted on the diffractometer was racemically twinned, and the BASF refines to 0.246(3). The structure of $[(F_8)Fe^{III}{-}O{-}Cu^{II}(MePY2)][B(C_6F_5)_4]$ is also mostly ordered. One of the four difluorophenyl groups is found to be disordered over two orientations. The occupancy factor of the major component of the disorder refines to 0.576(3). The crystal lattice also includes some very disordered and/or not fully occupied solvent molecule (most likely MeTHF). Their contribution has been taken out in the final refinement (SQUEEZE details are provided in the CIF file).

The structure of $[(TMPP)Fe^{III}{-}O{-}Cu^{II}(tmpa)][B(C_6F_5)_4]$ is partly disordered. The Cu^{II}(tmpa) is disordered over two orientations, and the occupancy factor of the major component refines to 0.505(2). The crystal lattice also contains a significant amount of lattice disordered toluene molecules. The disorder has been resolved for two solvent molecules (found in the asymmetric unit). One solvent molecule is found at sites of inversion symmetry and thus must be disordered over two orientations, and each

component of the disorder must have the occupancy of 0.5. The disorder of the other solvent molecule is not constrained by any symmetry operations, and this molecule is disordered over two orientations. The occupancy factor of the major component refines to 0.789(11). The crystal lattice also contains some other very disordered toluene molecules, for which their contributions had been taken out using the program SQUEEZE for the final refinement. All details of the SQUEEZE refinement are provided in the final CIF file.

[(TMPP)Fe^{III}(THF)$_2$](SbF$_6$): Moiety formula: $C_{56}H_{52}FeN_4O_6$, SbF_6, C_4H_8O, formula weight 1240.72, dark-red irregular block, 0.28 × 0.23 × 0.17 mm^3, triclinic, *P*1 (no. 1), a = 11.0724(3), b = 11.5867(3), c = 12.3676(4) Å, α = 110.731(3), β = 105.499(3), γ = 99.599(2)°, V = 1,368.53(7) Å3, Z = 1, D_x = 1.505 g cm^{-3}, μ = 6.704 mm^{-1}, T_{min} − T_{max}: 0.298−0.487. 16,389 reflections up to a resolution of (sin $\theta/\lambda)_{max}$ = 0.62 Å^{-1}. 8,891 reflections were unique (R_{int} = 0.0175), of which 8854 were observed [$I > 2\sigma(I)$]. 740 parameters were refined using 24 restraints. $R1/wR2$ [$I > 2\sigma(I)$]: 0.0212/0.0556. $R1/wR2$ [all refl.]: 0.0213/0.0556. S = 1.029. Residual electron density was found between −0.43 and 0.61 e^- Å^{-3}.

[(F$_8$)Fe^{III}−O−Cu^{II}(MePY2)][B(C$_6$F$_5$)$_4$]: Moiety formula: $C_{59}H_{39}Cu_{F8}FeN_7O$, $C_{24}BF_{20}$, formula weight 1812.41, dark-purple block, 0.43 × 0.27 × 0.17 mm^3, triclinic, *P*1 (no. 2), a = 9.7091(2), b = 19.3628(3), c = 21.9984(4) Å, α = 71.8792(17), β = 82.6473(17), γ = 83.5370(17)°, V = 3,886.53(13) Å3, Z = 2, D_x = 1.549 g cm^{-3}, μ = 0.580 mm^{-1}, T_{min} − T_{max}: 0.831−0.918. 54,873 reflections up to a resolution of (sin $\theta/\lambda)_{max}$ = 0.65 Å^{-1}, 17,874 reflections were unique (R_{int} = 0.0605), of which 14,985 were observed [$I > 2\sigma(I)$]. 1167 parameters were refined using 334 restraints. $R1/wR2$ [$I >$

$2\sigma(I)$]: 0.0443/0.1200. $R1/wR2$ [all refl.]: 0.0536/0.1260. S = 1.049. Residual electron density was found between −0.64 and 0.73 e^- Å^{-3}.

[(TMPP)Fe^{III}−O−Cu^{II}(tmpa)][B(C$_6$F$_5$)$_4$]: Moiety formula: 2-($C_{66}H_{54}CuFeN_8O_5$), 2($C_{24}BF_{20}$), 3(C_7H_8), formula weight 3951.63, dark-purple block, 0.39 × 0.32 × 0.26 mm^3, triclinic, $P1$ (no. 2), a = 13.4443(2), b = 16.3732(2), c = 25.7041(4) Å, α = 91.5300(12), β = 97.5727(14), γ = 112.0953(15)°, V = 5,178.93(13) Å^3, Z = 1, D_x = 1.267 g cm^{-3}, μ = 2.142 mm^{-1}, $T_{min} - T_{max}$: 0.552−0.680. 61,250 reflections up to a resolution of (sin θ/λ)max = 0.62 Å^{-1}. Of these, 20,331 reflections were unique (R_{int} = 0.0162), of which 19,196 were observed [$I > 2\sigma(I)$]. 1544 parameters were refined using 1057 restraints. $R1/wR2$ [$I > 2\sigma(I)$]: 0.0361/0.1047. $R1/wR2$ [all refl.]: 0.0377/0.1064. S = 1.046. Residual electron density was found between −0.35 and 0.40 e^- Å^{-3}.

4.5. Cryo-Spray Ionization Mass Spectrometry Measurements (CSI-MS)

CSI-MS measurements were performed on a UHR-TOF Bruker Daltonik (Bremen, Germany) maXis 4G, an ESI-TOF MS capable of resolution of at least 40,000 fwhm, which was coupled to a Bruker Daltonik Cryo-spray unit. Detection was in positive-ion mode, and the source voltage was 4.5 kV. The flow rates were 250 μL/hour. The drying gas (N_2), to aid solvent removal, was held at −55 °C, and the spray gas was held at −60 °C.

CSI-MS samples were prepared in a glovebox by dissolving [(TMPP)Fe^{III}–O–Cu^{II}(tmpa)][$B(C_6F_5)_4$] in dry acetone. The complex solution was taken out in a Schlenk tube equipped with a rubber septum. Samples for measurement were taken out directly from this Schlenk tube. The intermediate observed at 433 nm, at −20 °C or below, with two $NO_{(g)}$ molecules added to the μ-oxo complex (thus, a *bis*-NO adduct) was prepared by bubbling $NO_{(g)}$ directly through the cooled (−60 °C) complex solution. NO gas was purified as described for the stopped-flow measurements (vide infra).

The machine was calibrated prior to every experiment via direct infusion of the Agilent ESI-TOF low concentration tuning mixture, which provided an *m/z* range of singly charged peaks up to 2700 Da in both ion modes.

4.6. Low-Temperature Stopped-Flow Measurements

All measurements were performed in dry acetone as solvent. $NO_{(g)}$ solutions were prepared by bubbling pure NO gas through acetone (from drybox, Schlenk tube equipped with septum). Usually 15 mL of acetone was bubbled for 30 min. NO gas was purified along to literature known procedures (saturated potassium hydroxide, column of Ascarite, column of P2O5).44 Complex solutions were prepared in the drybox and brought outside by using Hamilton gastight syringes equipped with 3-way valves. The concentration of the saturated $NO_{(g)}$ solution in acetone was determined by a $NO_{(g)}$-sensitive electrode (4.5 mM).

Prior to use, the stopped-flow system was flushed two times with nitrogen and one time with dry solvent. For the measurements only two syringes were used. The complex and $NO_{(g)}$ solutions were mixed in a 1:1 ratio with a total flow rate of 6.00 mL/s, resulting in a total volume of 202 μL. For cooling a Huber C-905 cryostat filled with silicon oil was used.

Kinetic measurements were performed at four different temperatures and with at least four different $NO_{(g)}$ concentrations. For the different $NO_{(g)}$ concentrations, dilutions were performed by using a Hamilton gastight syringe equipped with a 3-way valve. $NO_{(g)}$ solution and dry acetone were kept in Schlenk flasks equipped with septa, and the required amounts of $NO_{(g)}$ and acetone were taken out from the flasks with the Hamilton gastight syringe. Spectra collected were analyzed by SpecFit.

4.7. Computational Methods

Geometries of all compounds were fully optimized at the BP86 level of theory with a 6-31G(d) basis set using the Gaussian 09 program package. Stationary points were confirmed to be minima or transition states by calculating the normal vibrations within the harmonic approximation. All relative energies are corrected for zero-point vibrational energies (ZPVE). The effect of the solvent (acetone) was included via a PCM model. In order to evaluate values of spin density and relative energies, additional single point calculations were performed at the PCM-OLYP/6-311+G(d,p) level. (For further details and references see Supporting Information).

5. References

(1) (a) Ignarro, L. J. Nitric Oxide as a Communication Signal in Vascular and Neuronal Cells. In *Nitric Oxide: Principles and Actions*; Lancaster, J., Ed.; Academic Press: New York, 1996; p 111. (b) Pfeiffer, S.; Mayer, B.; Hemmens, B. *Angew. Chem., Int. Ed.* **1999**, *38*, 1715. (c) Nitric Oxide, Biology and Pathobiology; Ignarro, L. J., Ed.; Academic Press: San Diego, 2000. (d) Miranda, K. M.; Espey, M. G.; Jourd'heuil, D.; Grisham, M. B.; Fukuto, J. M.; Feelisch, M.; Wink, D. A. *Nitric Oxide* **2000**, 41. (e) Feelisch, M.; Olson, K. R. *Nitric Oxide* **2013**, *35*, 2.

(2) Lehnert, N.; Berto, T. C.; Galinato, M. G. I.; Goodrich, L. E. The Role of Heme-Nitrosyls in the Biosynthesis, Transport, Sensing, and Detoxification of Nitric Oxide (NO) in Biological Systems: Enzymes and Model Complexes. In *The Handbook of Porphyrin Science*; Kadish, K. M., Smith, K., Guilard, R., Eds.; World Scientific: Singapore, 2011; *Vol. 14*; p 1−247.

(3) Maia, L. B.; Moura, J. J. G. *Chem. Rev.* **2014**, *114*, 5273.

(4) (a) Marletta, M. A. *J. Biol. Chem.* **1993**, *268*, 12231. (b) Stuehr, D. J. *Biochim. Biophys. Acta* **1999**, *1411*, 217. (c) Alderton, W. K.; Cooper, C. E.; Knowles, R. G. *Biochem. J.* **200**1, *357*, 593. (d) Zhu, Y.; Silverman, R. B. *Biochemistry* **2008**, *47*, 2231. (e) Crane, B. R. *Biochem. Soc. Trans.* **2008**, *036*, 1149.

(5) (a) Dezfulian, C.; Raat, N.; Shiva, S.; Gladwin, M. T. *Cardiovasc. Res.* **2007**, *75*, 327. (b) Samouilov, A.; Kuppusamy, P.; Zweier, J. L. *Arch. Biochem. Biophys.* **1998**, *357*, 1. (c) Gladwin, M. T.; Grubina, R.; Doyle, M. P. *Acc. Chem. Res.* **2009**, *42*, 157. (d) van Faassen, E. E.; Bahrami, S.; Feelisch, M.; Hogg, N.; Kelm, M.; Kim-Shapiro, D. B.; Kozlov, A. V.; Li, H.; Lundberg, J. O.; Mason, R.; Nohl, H.; Rassaf, T.; Samouilov, A.; Slama-Schwok, A.; Shiva, S.; Vanin, A. F.; Weitzberg, E.; Zweier, J.; Gladwin, M. T. *Med. Res. Rev.* **2009**, *29*, 683. (e) Kim-Shapiro, D. B.; Gladwin, M. T. *Nitric Oxide* **2014**, *38*, 58.

(6) (a) Castello, P. R.; David, P. S.; McClure, T.; Crook, Z.; Poyton, R. O. *Cell Metab.* **2006**, *3*, 277.

(b) Feelisch, M.; Fernandez, B. O.; Bryan, N. S.; Garcia-Saura, M. F.; Bauer, S.; Whitlock, D. R.; Ford, P. C.; Janero, D. R.; Rodriguez, J.; Ashrafian, H. *J. Biol. Chem.* **2008**, *283*, 33927. (c) Poyton, R. O.; Castello, P. R.; Ball, K. A.; Woo, D. K.; Pan, N. *Ann. N.Y. Acad. Sci.* **2009**, *1177*, 48. (d) Gupta, K. J.; Igamberdiev, A. U. *Mitochondrion* **2011**, *11*, 537.

(7) (a) Kim, E.; Chufán, E. E.; Kamaraj, K.; Karlin, K. D. Chem. Rev.

2004, 104, 1077−1133. (b) Yoshikawa, S.; Shinzawa-Itoh, K.; Nakashima, R.; Yaono, R.; Yamashita, E.; Inoue, N.; Yao, M.; Jei-Fei, M.; Libeu, C. P.; Mizushima, T.; Yamaguchi, H.; Tomizaki, T.; Tsukihara, T. *Science* **1998**, *280*, 1723.

(8) (a) Torres, J.; Cooper, C. E.; Wilson, M. T. *J. Biol. Chem.* **1998**, *273*, 8756. (b) Sarti, P.; Giuffre, A.; Barone, M. C.; Forte, E.; Mastronicola, D.; Brunori, M. *Free Radic. Biol. Med.* **2003**, *34*, 509. (c) Mason, M. G.; Nicholls, P.; Wilson, M. T.; Cooper, C. E. *Proc. Natl. Acad. Sci. U.S.A.* **2006**, *103*, 708. (d) Sarti, P.; Forte, E.; Mastronicola, D.; Giuffre , A.; Arese, M. *Biochim. Biophys. Acta* **2012**, *1817*, 610.

(9) (a) Castello, P. R.; Woo, D. K.; Ball, K.; Wojcik, J.; Liu, L.; Poyton, R. O. *Proc. Natl. Acad. Sci. U.S.A.* **2008**, *105*, 8203. (b) Benamar, A.; Rolletschek, H.; Borisjuk, L.; Avelange-Macherel, M.-H.; Curien, G.; Mostefai, H. A.; Andriantsitohaina, R.; Macherel, D. *Biochim. Biophys. Acta* **2008**, *1777*, 1268. (c) Gladwin, M. T.; Shiva, S. *Circ. Res.* **2009**, *104*, 1136.

(10) (a) Nicholls, P.; Sharpe, M.; Torres, J.; Wilson, M. T.; Cooper, C. E. *Biochem. Soc. Trans.* **1998**, *26*, S323. (b) Torres, J.; Sharpe, M. A.; Rosquist, A.; Cooper, C. E.; Wilson, M. T. *FEBS Lett.* **2000**, *475*, 263. (c) Igamberdiev, A. U.; Ratcliffe, R. G.; Gupta, K. J. *Mitochondrion* **2014**, *19*, 329.

(11) Hematian, S.; Siegler, M. A.; Karlin, K. D. *J. Am. Chem. Soc.* **2012**, *134*, 18912.

(12) Hematian, S.; Siegler, M. A.; Karlin, K. D. *J. Biol. Inorg. Chem.* **2014**, *19*, 515.

(13) (a) Fox, S.; Nanthakumar, A.; Wikström, M.; Karlin, K. D.; Blackburn, N. J. *J. Am. Chem. Soc.* **1996**, *118*, 24. (b) Kopf, M.-A.; Neuhold, Y.-M.; Zuberbühler, A. D.; Karlin, K. D. *Inorg. Chem.*

1999, *38*, 3093.

(14) Karlin, K. D.; Nanthakumar, A.; Fox, S.; Murthy, N. N.; Ravi, N.; Huynh, B. H.; Orosz, R. D.; Day, E. P. *J. Am. Chem. Soc.* **1994**, *116*, 4753.

(15) Nanthakumar, A.; Fox, S.; Murthy, N. N.; Karlin, K. D.; Ravi, N.; Huynh, B. H.; Orosz, R. D.; Day, E. P.; Hagen, K. S.; Blackburn, N. J. *J. Am. Chem. Soc.* **1993**, *115*, 8513.

(16) Halime, Z.; Kieber-Emmons, M. T.; Qayyum, M. F.; Mondal, B.; Gandhi, T.; Puiu, S. C.; Chufán, E. E.; Sarjeant, A. A. N.; Hodgson, K. O.; Hedman, B.; Solomon, E. I.; Karlin, K. D. *Inorg. Chem.* **2010**, *49*, 3629.

(17) Kim, E.; Helton, M. E.; Wasser, I. M.; Karlin, K. D.; Lu, S.; Huang, H.-w.; Moënne-Loccoz, P.; Incarvito, C. D.; Rheingold, A. L.; Honecker, M.; Kaderli, S.; Zuberbühler, A. D. *Proc. Natl. Acad. Sci. U.S.A.* **2003**, *100*, 3623.

(18) Lee, S. C.; Holm, R. H. *J. Am. Chem. Soc.* **1993**, *115*, 5833.

(19) Ju, T. D.; Ghiladi, R. A.; Lee, D.-H.; van Strijdonck, G. P. F.; Woods, A. S.; Cotter, R. J.; Young, V. G., J.; Karlin, K. D. *Inorg. Chem*. **1999**, *38*, 2244.

(20) Chishiro, T.; Shimazaki, Y.; Tani, F.; Naruta, Y. *Chem. Comm.* **2005**, 1079.

(21) We note, however, that kinetic and CSI-MS measurements below −60 °C, from data that are not presented here, revealed the existence of a *bis*-NO intermediate for $[(F_8)Fe^{III}–O–Cu^{II}(tmpa)]^+$, similar to that for the case of $[(TMPP)Fe^{III}–O–Cu^{II}(tmpa)]^+$, which is described later in the text in detail.

(22) Interestingly, the spectral features of this intermediate resemble those of the previously known and structurally characterized complex ferric heme−nitrosyl nitrite complex $[(TMPP)Fe^{III}(NO)(NO_2)]$ (Figure S7). However, a detailed examination of the spectra revealed differences in relative extinction coefficients of the Soret and Q-bands.

(23) Yoshimura, T. *Bull. Chem. Soc. Jpn.* **1991**, *64*, 2819.

(24) (a) Morse, R. H.; Chan, S. I. *J. Biol. Chem.* **1980**, *255*, 7876. (b) Cheng, L.; Richter-Addo, G. B. Binding and Activation of Nitric Oxide by Metalloporphyrins and Heme. In *Porphyrin Handbook*; Kadish, K. M., Simith, K. M., Guilard, R., Eds.; Academic Press: San Diego, CA, 2000; *Vol. 4*, Chapter 33, p 219−291.

(25) (a) Lymar, S. V.; Schwarz, H. A.; Czapski, G. *J. Phys. Chem. A* **2002**, *106*, 7245. (b) Yamamoto, Y.; Moribe, S.; Ikoma, T.; Akiyama, K.; Zhang, Q.; Saito, F.; Tero-Kubota, S. *Mol. Phys.* **2006**, *104*, 1733. (c) Kudrik, E. V.; Makarov, S. V.; Zahl, A.; van Eldik, R. *Inorg. Chem.* **2003**, *42*, 618.

(26) This can be explained by higher local charges (+3 on Fe and −2 on the bridging *O*-atom) in the starting μ-oxo $[(TMPP)Fe^{III}-O-Cu^{II}(tmpa)]^{+}$ complex that thus require a larger number of solvent molecules in the solvation sphere and the fact that as the reaction progresses forming the *mono*-NO adduct, a decrease in charge localization (or perhaps better described as increase in charge delocalization, +2 on Fe and −1 on the bridging NO_2 moiety that is larger than the *O*-atom) results in the interaction with fewer solvent molecules. This causes the release of a number of solvent molecules

from the solvation sphere escaping to the bulk, which leads to the positive entropy change, the value of which is dependent on solvent polarity.

(27) The equilibrium constant can also be calculated using $K = e^{-\Delta G/RT} = e^{-(\Delta H - T\Delta S)/RT}$ employing the parameters given in Table 3, resulting in $K_1 = 1023 \pm 300\ M^{-1}$ at −60 °C and $K_1 = 920 \pm 300\ M^{-1}$ at −74 °C.

(28) (a) Wanat, A.; Schneppensieper, T.; Stochel, G.; van Eldik, R.; Bill, E.; Wieghardt, K. *Inorg. Chem.* **2002**, *41*, 4. (b) Schneppensieper, T.; Wanat, A.; Stochel, G.; van Eldik, R. *Inorg. Chem.* **2002**, *41*, 2565. (c) Deviation from the thermodynamically determined binding constant is most probably related to errors involved in the determination of k_{off} via extrapolation of the kinetic data obtained in the stopped-flow experiments..

(29) (a) Greenwood, N. N.; Earnshaw, A. *Chemistry of the Elements*; Pergamon Press: Oxford, 1993.

(b) Heinecke, J.; Ford, P. C. *Coord. Chem. Rev.* **2010**, *254*, 235.

(30) Ellison, M. K.; Schulz, C. E.; Scheidt, W. R. *Inorg. Chem.* **1999**, *38*, 100.

(31) Scheidt, W. R.; Frisse, M. E. *J. Am. Chem. Soc.* **1975**, *97*, 17.

(32) Shubina, T. E. Adv. *Inorg. Chem.* **2010**, *62*, 261.

(33) Loullis, A.; Noor, M. R.; Soulimane, T.; Pinakoulaki, E. *Chem. Comm.* **2015**, *51*, 286−289.

(34) (a) Hoshino, M.; Maeda, M.; Konishi, R.; Seki, H.; Ford, P. C. *J. Am. Chem. Soc.* **1996**, *118*, 5702. (b) Ford, P. C.; Fernandez, B. O.; Lim, M. D. *Chem. Rev.* **2005**, *105*, 2439. (c) Fernandez, B. O.; Lorkovic, I. M.; Ford, P. C. *Inorg. Chem.* **2003**, *42*, 2.

(35) Ford, P. C. *Inorg. Chem.* **2010**, *49*, 6226.

(36) Sharma, V.; Karlin, K. D.; Wikström, M. *Proc. Natl. Acad. Sci. U.S.A.* **2013**, *110*, 16844.

(37) (a) Ford, P. C.; Lorkovic, I. M. *Chem. Rev.* **2002**, *102*, 993. (b) Wang, J.; Schopfer, M. P.; Sarjeant, A. A. N.; Karlin, K. D. *J. Am. Chem. Soc.* **2009**, *131*, 450. (c) Schopfer, M. P.; Mondal, B.; Lee, D.-H.; Sarjeant, A. A. N.; Karlin, K. D. *J. Am. Chem. Soc.* **2009**, *131*, 11304.

(38) Ghiladi, R. A.; Kretzer, R. M.; Guzei, I.; Rheingold, A. L.; Neuhold, Y.-M.; Hatwell, K. R.; Zuberbühler, A. D.; Karlin, K. D. *Inorg. Chem.* **2001**, *40*, 5754.

(39) Lucas, H. R.; Meyer, G. J.; Karlin, K. D. *J. Am. Chem. Soc.* **2010**, *132*, 12927.

(40) Liang, H.-C.; Zhang, C. X.; Henson, M. J.; Sommer, R. D.; Hatwell, K. R.; Kaderli, S.; Zuberbuehler, A. D.; Rheingold, A. L.; Solomon, E. I.; Karlin, K. D. *J. Am. Chem. Soc.* **2002**, *124*, 4170.

(41) Wang, J.; Schopfer, M. P.; Puiu, S. C.; Sarjeant, A. A. N.; Karlin, K. D. *Inorg. Chem*. **2010**, *49*, 1404.

(42) Lorkovic, I.; Ford, P. C. *J. Am. Chem. Soc.* **2000**, *122*, 6516.

(43) Sheldrick, G. M. *Acta Crystallogr., Sect. A* **2008**, *64*, 112.

(44) Jee, J. E.; Eigler, S.; Hampel, F.; Jux, N.; Wolak, M.; Zahl, A.; Stochel, G.; van Eldik, R. *Inorg. Chem.* **2005**, *44*, 7717.

6. Supporting Information

6.1. Reaction of $[(F_8)Fe^{III}–O–Cu^{II}(L)][B(C_6F_5)_4]$ (L = TMPA, AN or MePY2) with $NO_{(g)}$

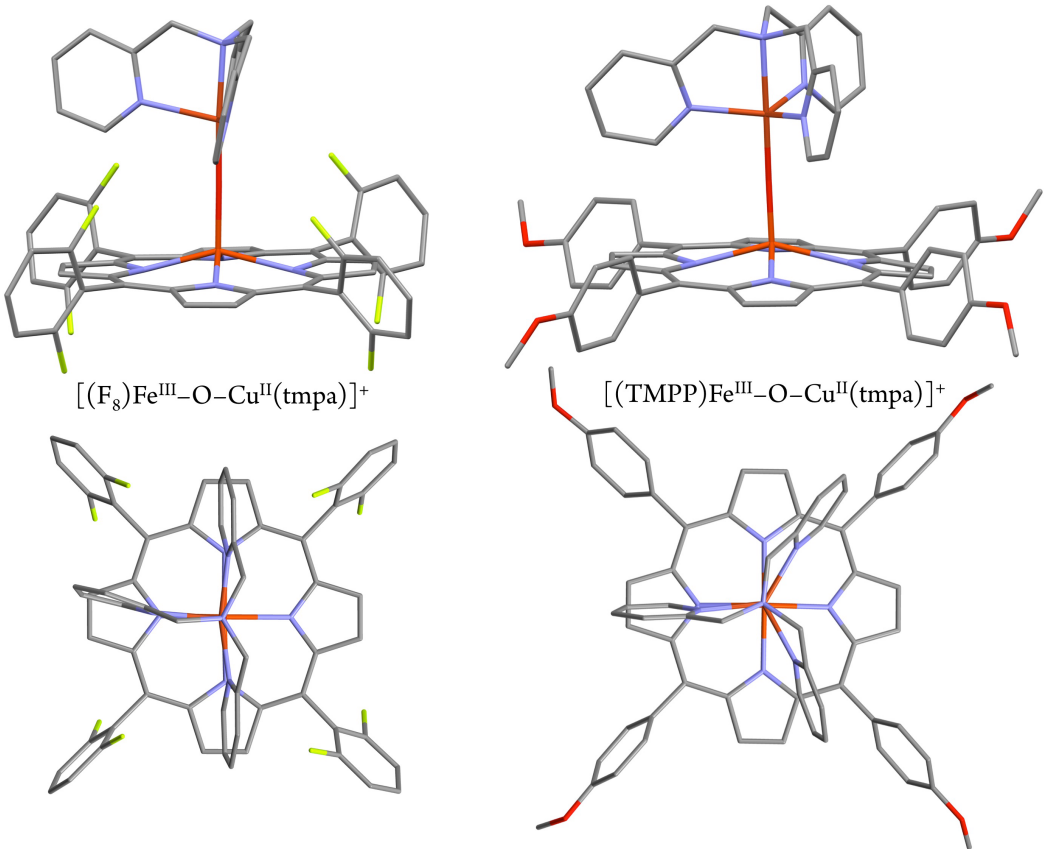

Figure S1. Molecular structures (side and top views) of the oxo-bridged heteronuclear cations $[(F_8)Fe^{III}–O–Cu^{II}(tmpa)]^+$ (adapted from text reference 14) and $[(TMPP)Fe^{III}–O–Cu^{II}(tmpa)]^+$ showing that the cupric center adapted different geometries; in the former compound Cu(II) adjusts to a distorted square pyramidal geometry (τ = 0.3) while in the latter it is present in a trigonal bipyramidal arrangement (τ = 0.9). All the hydrogen atoms are omitted for clarity.

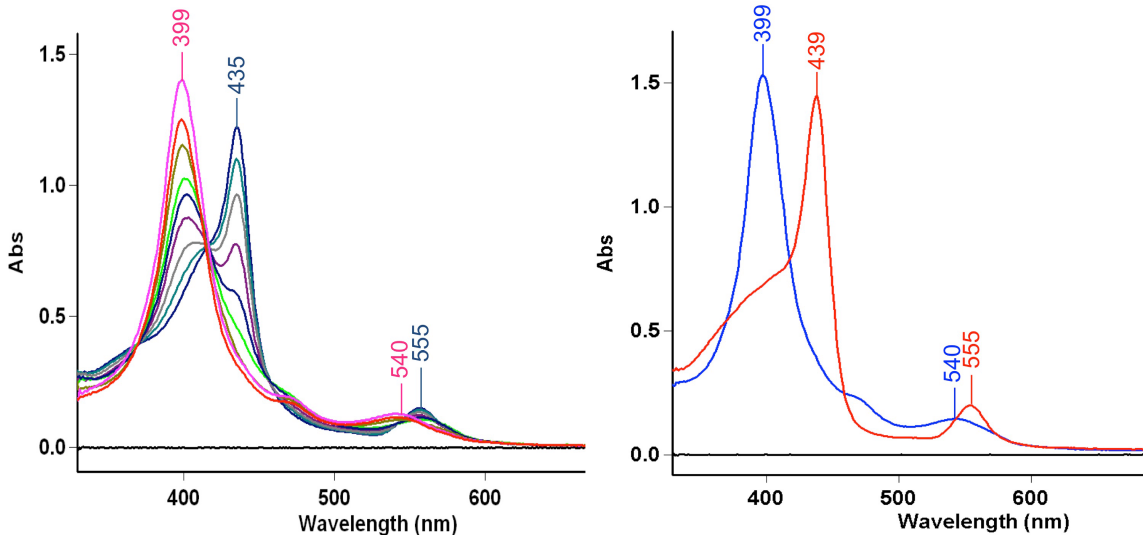

Figure S2. UV−vis spectra of: *Left*: (adapted from text reference 11) $[(F_8)Fe^{III}–O–Cu^{II}(tmpa)][B(C_6F_5)_4]$ (blue), $(F_8)Fe^{II}(NO)$ (red) generated from addition of 1 mL of $NO_{(g)}$. Addition of second mL of $NO_{(g)}$ to the solution resulted in completion of the reaction (purple) 10 μM in acetone at RT. *Right*: $[(F_8)Fe^{III}–O–Cu^{II}(AN)][B(C_6F_5)_4]$ (red) and $(F_8)Fe^{II}(NO)$ (blue) immediately generated after addition of 1 mL $NO_{(g)}$ into the μ-oxo complex solution 10 μM in acetone at RT.

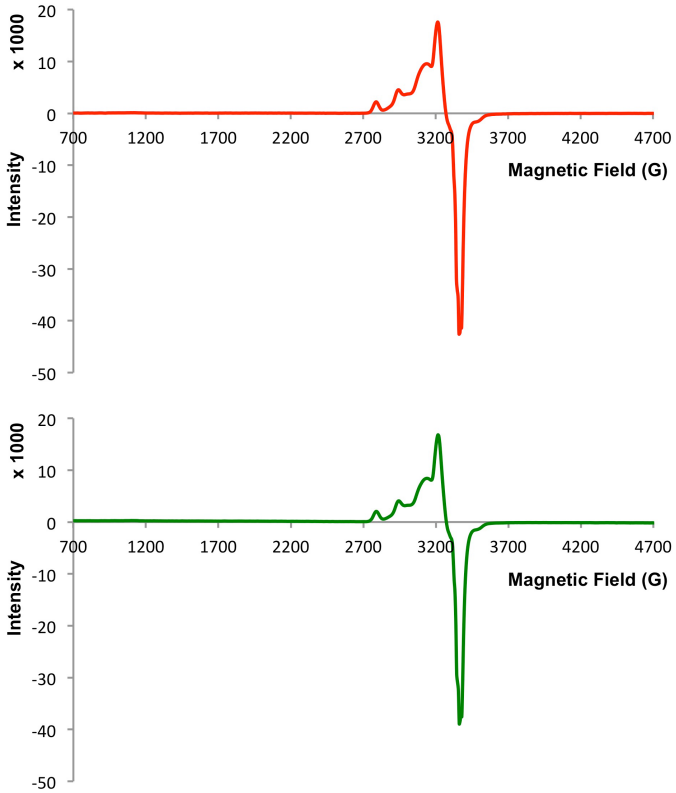

Figure S3. EPR spectrum comparison between the reaction mixture and an authentic sample: the products of the reaction of $NO_{(g)}$ and $[(F_8)Fe^{III}–O–Cu^{II}(AN)][B(C_6F_5)_4]$, giving signals of $(F_8)Fe^{II}(NO)$ and Cu(II) (red); an authentic sample of a 1:1 mixture of $(F_8)Fe^{II}(NO)$ and $[(AN)Cu^{II}(NO_2)](CF_3SO_3)$ (green) 1 mM in MeCN/toluene (1:1) at 20 K.

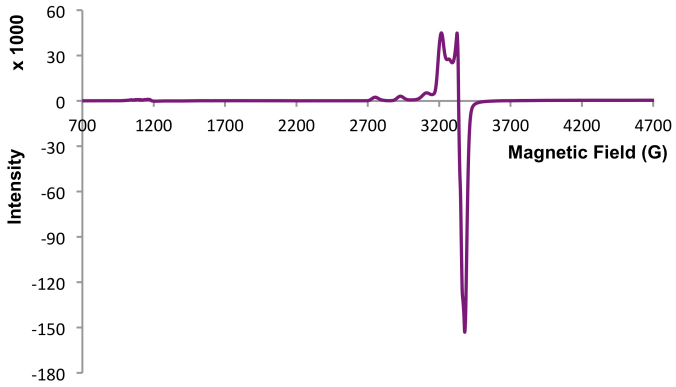

Figure S4. EPR spectrum of the products of the reaction of $NO_{(g)}$ and $[(F_8)Fe^{III}–O–Cu^{II}(MePY2)][B(C_6F_5)_4]$ (purple), giving signals of $(F_8)Fe^{II}(NO)$ and Cu(II) in acetone 2 mM at 12 K.

6.2. Reaction of $[(TMPP)Fe^{III}–O–Cu^{II}(tmpa)][B(C_6F_5)_4]$ with $NO_{(g)}$

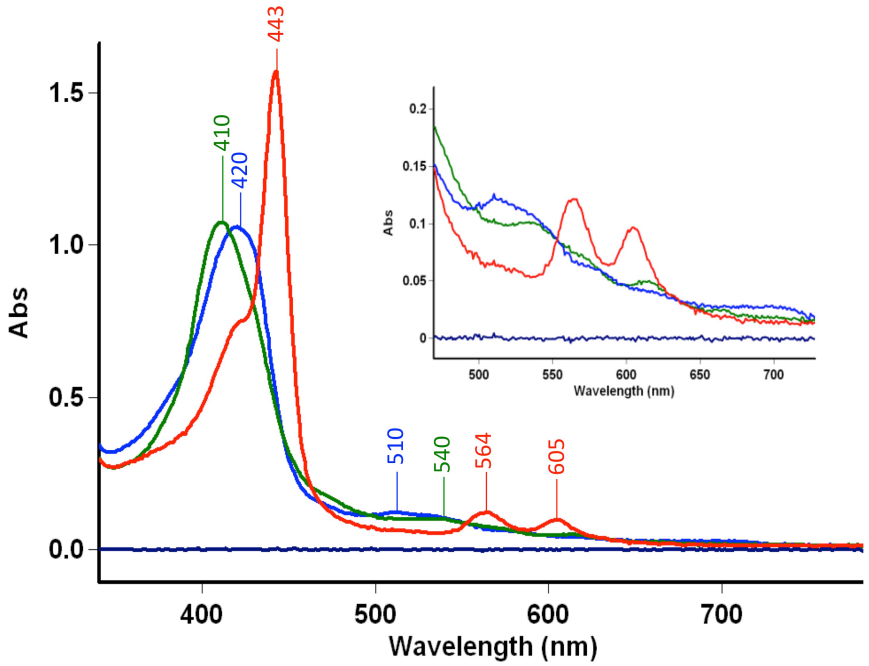

Figure S5. UV−vis spectra of $[(TMPP)Fe^{III}–O–Cu^{II}(tmpa)][B(C_6F_5)_4]$ (red) 35 μM in acetone in a 2-mm cuvette at RT, right after addition of 1 mL of $NO_{(g)}$ into the solution(blue), after stirring for 4 min forming $(TMPP)Fe^{II}(NO)$ (green).

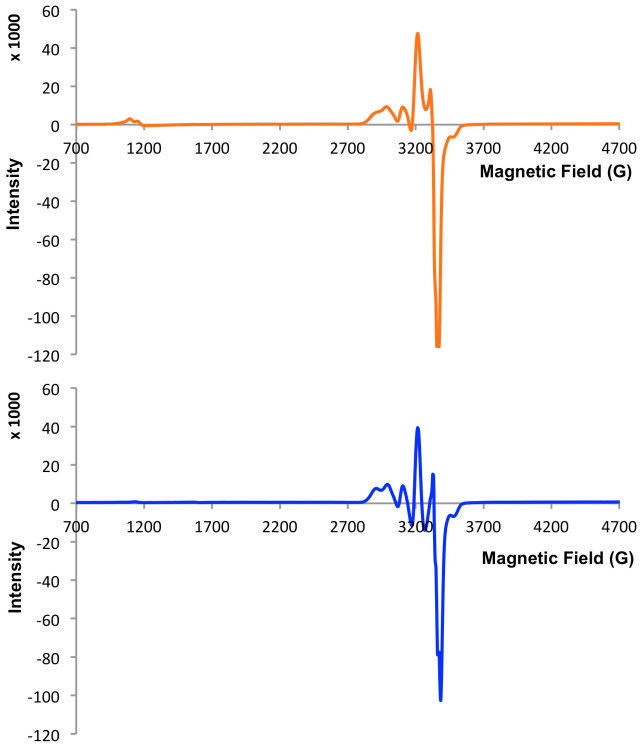

Figure S6. EPR spectra of the products of the reaction of $NO_{(g)}$ and [(TMPP)Fe^{III}–O–Cu^{II}(tmpa)][$B(C_6F_5)_4$], giving signals of (TMPP)Fe^{II}(NO) and Cu(II) in acetone (orange) and in MeTHF (blue) 2 mM at 12 K.

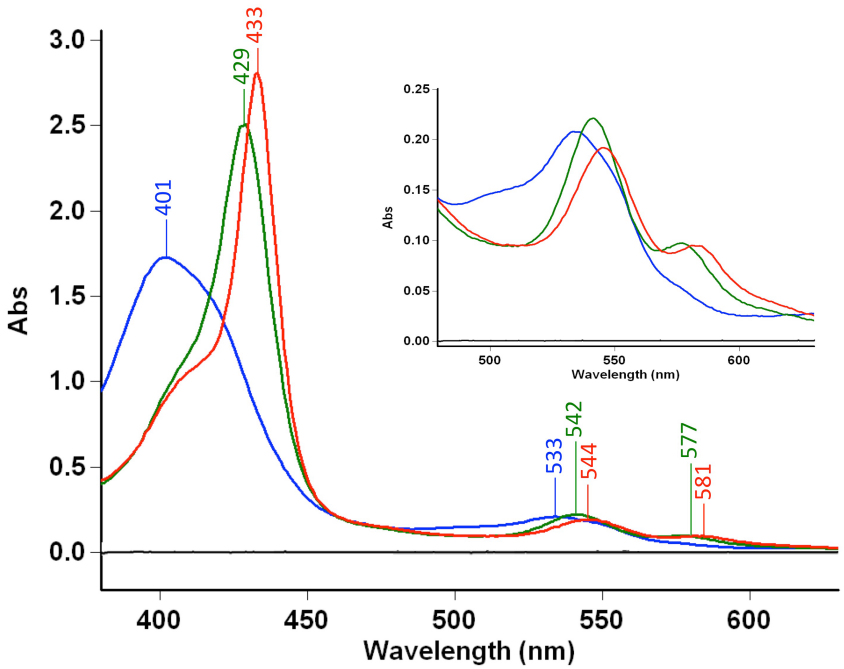

Figure S7. UV−vis spectra of [(TMPP)$Fe^{III}$$(THF)_2$]$(SbF_6)$ (blue) 50 μM in acetone in a 2-mm cuvette at –20 °C, right after addition of 1 mL of $NO_{(g)}$ into the solution generating (TMPP)Fe^{III}(NO) (green), after addition of 10 equiv $(n\text{Bu})_4N(NO_2)$ forming (TMPP)Fe^{III}(NO)(NO_2) (red).

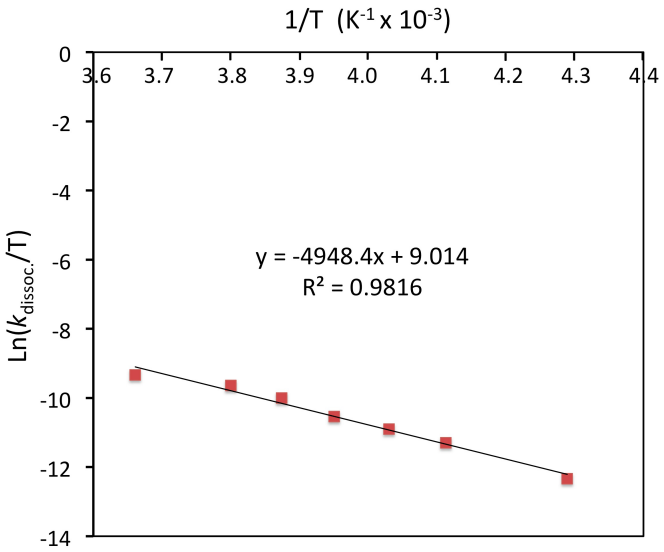

Figure S8. Eyring plot, $\ln(k_{obs}/T)$ vs 1/T, for the final step, slow dissociation of the "intermediate", $[(NO)(TMPP)Fe^{II}–(NO_2)–Cu^{II}(tmpa)][B(C_6F_5)_4]$, generated from reaction of $[(TMPP)Fe^{III}–O–Cu^{II}(tmpa)][B(C_6F_5)_4]$ with $NO_{(g)}$ to the two final Cu-nitrite and heme-$Fe^{II}(NO)$ products. The rate constants ($k_{dissoc.}$) were obtained from monitoring of the decay of the 433 nm intermediate in acetone at 0, –10, –15, –20, –25, –30, –40 °C. From the plot, activation parameters for the final step were obtained, $\Delta S^{\ddagger}_{dissoc.}$ = R(intercept – $\ln k_B/h$) = –123 ± 2 J mole^{-1} K^{-1} and $\Delta H^{\ddagger}_{dissoc.}$ = –R(slope) = +41,141 ± 100 J mol^{-1}.

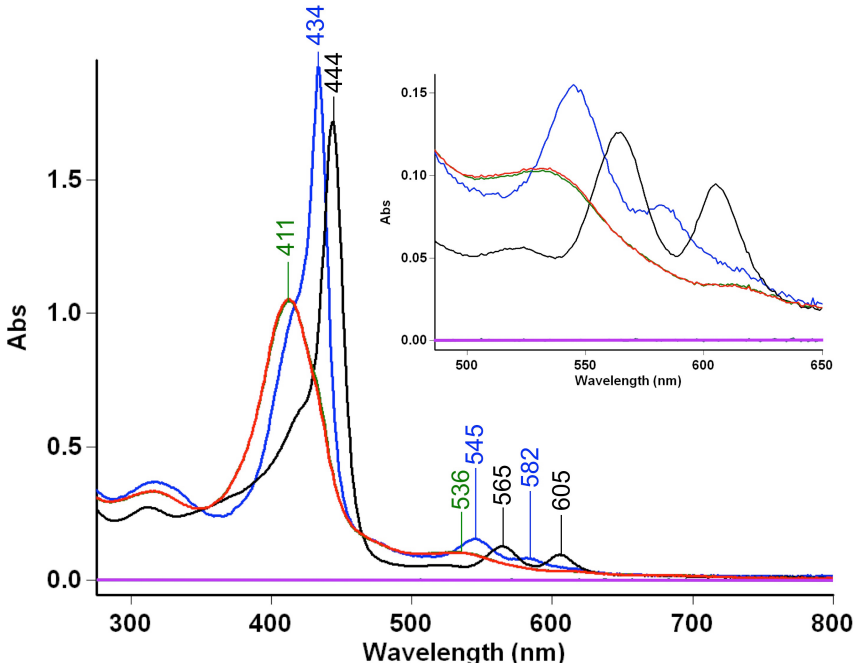

Figure S9. UV−vis spectra of $[(TMPP)Fe^{III}–O–Cu^{II}(tmpa)][B(C_6F_5)_4]$ (black) 35 μM in MeTHF in a 2-mm cuvette at RT, after addition of 1 mL of $NO_{(g)}$ into the solution forming final products, $(TMPP)Fe^{II}(NO)$ and $[(tmpa)Cu^{II}(NO_2)][B(C_6F_5)_4]$ (green). The excess $NO_{(g)}$ was then removed and the sample was cooled to –125 °C generating a new species formulated as $[(NO)(TMPP)Fe^{II}–(NO_2)–Cu^{II}(tmpa)][B(C_6F_5)_4]$ (blue). Warming up to RT resulted the reformation of initial spectrum of the final products (red).

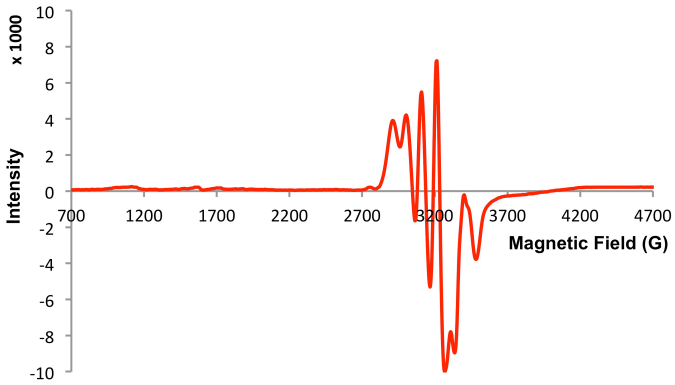

Figure S10. EPR spectrum of the "intermediate" for the reaction of $NO_{(g)}$ and $[(TMPP)Fe^{III}–O–Cu^{II}(tmpa)][B(C_6F_5)_4]$ at 12 K giving signals of Cu(II) and ferrous heme nitrosyl species, but with a different hyperfine coupling observed in the spectrum of products mixture (Figure S9). Sample was prepared by addition of 1 mL $NO_{(g)}$ into the 1 mM solution of $[(TMPP)Fe^{III}–O–Cu^{II}(tmpa)][B(C_6F_5)_4]$ in MeTHF at –80 ^{o}C (dry ice-acetone bath). Then excess $NO_{(g)}$ was removed via vacuum/Ar-purge cycles and the EPR sample was frozen in liquid nitrogen prior to measurement.

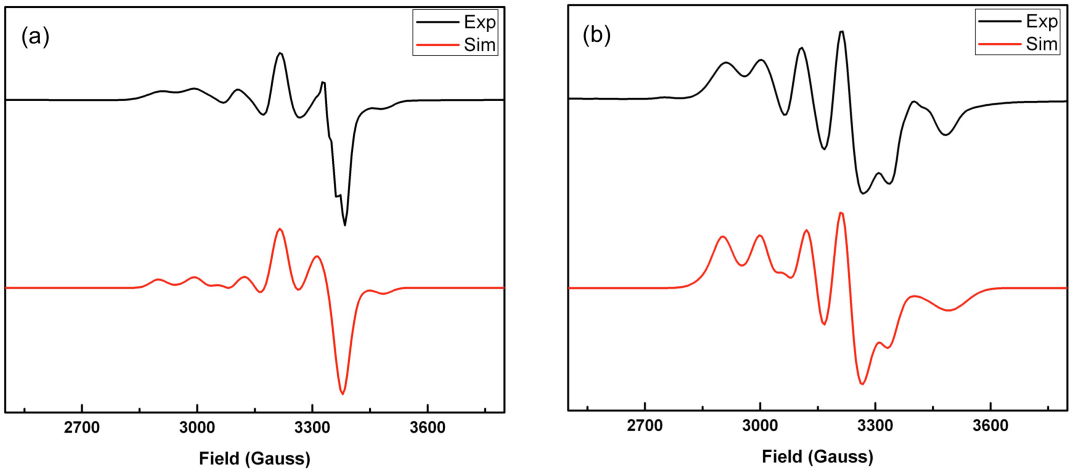

Figure S11. Experimental (black) and simulated (red) spectra (for the reaction of $NO_{(g)}$ with $[(TMPP)Fe^{III}–O–Cu^{II}(tmpa)][B(C_6F_5)_4]$) of the product species **(a)** $g_{1,Cu}$ = 2.153, $g_{2,Cu}$ = 2.195, $g_{3,Cu}$ = 1.987, $A_{1,Cu}$ = 82.1 G, $A_{2,Cu}$ = 115 G, $A_{3,Cu}$ = 69.2 G, $g_{1,FeNO}$ = 2.094, $g_{2,FeNO}$ = 2.009, $g_{3,FeNO}$ = 1.993, $A_{1,FeNO}$ = 10.3 G, $A_{2,FeNO}$ = 22.8 G, $A_{3,FeNO}$ = 7.1 G and the "intermediate" species **(b)** $g_{1,Cu}$ = 2.161, $g_{2,Cu}$ = 2.187 $g_{3,Cu}$ = 2.056, $A_{1,Cu}$ = 73.1 G, $A_{2,Cu}$ = 110 G, $A_{3,Cu}$ = 51.2 G, $g_{1,FeNO}$ = 2.340, $g_{2,FeNO}$ = 1.920, $g_{3,FeNO}$ = 2.066, $A_{2,NO}$ = 18.9 G, $A_{2,Nitrite}$ = 7.74 G. EPR conditions: microwave frequency, 9.41 GHz; microwave power, 0.2 mW; modulation frequency, 100 kHz; modulation amplitude, 10 G; temperature, 12 K. EPR simulations were performed using EasySpin v. 4.5.5 (Stoll, S.; Schweiger, A. J. Magn. Reson. 2006, 178, 42; http://www.easyspin.org).

Table S1. Observed Rate Constants for the First Reaction Step ($k_{1(obs)}$, Binding of 1st $NO_{(g)}$) and Second Reaction Step ($k_{2(obs)}$, Binding of 2nd $NO_{(g)}$) as a Function of Temperature and Concentration.

[NO] mM	Temperature						
	–60 °C		–67 °C		–74 °C		–83 °C*
	$k_{1(obs)}$	$k_{2(obs)}$	$k_{1(obs)}$	$k_{2(obs)}$	$k_{1(obs)}$	$k_{2(obs)}$	$k_{1(obs)}$
0.281	4.35 ± 0.15	0.25 ± 0.02	3.11 ± 0.26	0.20 ± 0.04	1.81 ± 0.26	0.16 ± 0.03	0.92 ± 0.04
0.563	6.11 ± 0.66	0.45 ± 0.06	4.36 ± 0.23	0.37 ± 0.03	2.34 ± 0.03	0.23 ± 0.01	1.16 ± 0.03
0.750	6.72 ± 0.06	0.53 ± 0.04	4.64 ± 0.26	0.50 ± 0.04	2.90 ± 0.03	0.38 ± 0.02	1.38 ± 0.05
1.13	9.84 ± 0.86	0.82± 0.11	7.43 ± 0.18	0.72 ± 0.05	3.66 ± 0.06	0.46 ± 0.02	1.88 ± 0.10
1.69	12.76 ± 0.19	1.19 ± 0.03	10.33 ± 0.36	0.98 ± 0.08	4.91 ± 0.13	0.77 ± 0.06	2.52 ± 0.08
2.25	16.19 ± 0.37	1.65 ± 0.11	12.67 ± 1.47	1.51 ± 0.10	6.49 ± 0.09	1.16 ± 0.15	3.22 ± 0.11

* The second step at –83 °C was very slow and $k_{2(obs)}$ could not be accurately determined.

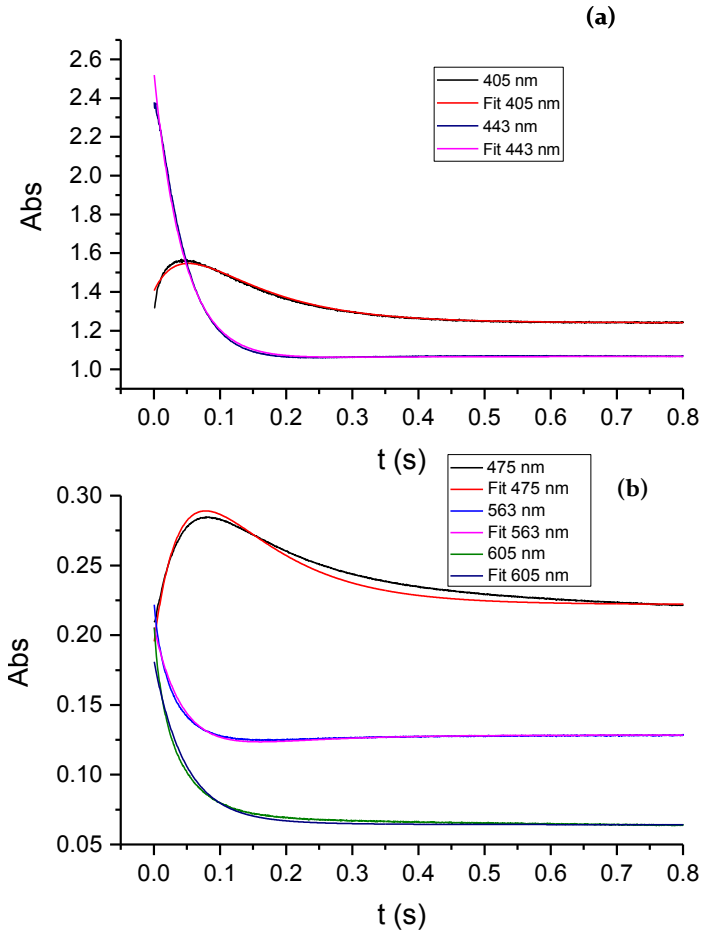

Figure S12. Kinetic traces with a two-exponential fit for the reaction of [(TMPP)Fe^{III}–O–Cu^{II}(tmpa)][$B(C_6F_5)_4$] with 2.3 mM $NO_{(g)}$ at –60 °C in acetone monitored **(a)** at 405 and 443 nm, as well as **(b)** at 475, 563 and 605 nm.

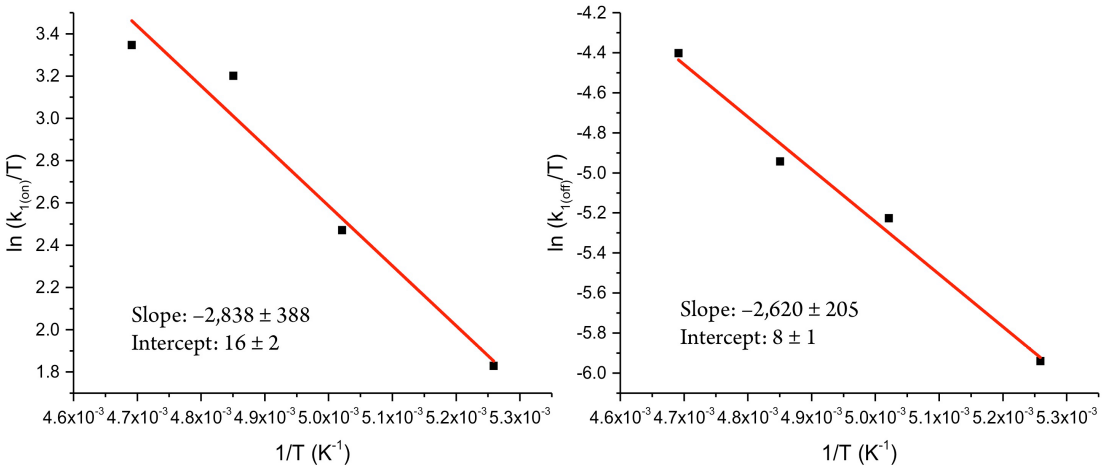

Figure S13. Eyring plots ($\ln(k/T) = -(\Delta H^{\ddagger}/R)(1/T) + \Delta S^{\ddagger}/R + \ln(k_b/h)$; $k = k_{1(on)}$ or $k_{1(off)}$) for the forward and reverse reactions for the first reaction step, reaction of $[(TMPP)Fe^{III}–O–Cu^{II}(tmpa)]^{+}$ with the first $NO_{(g)}$.

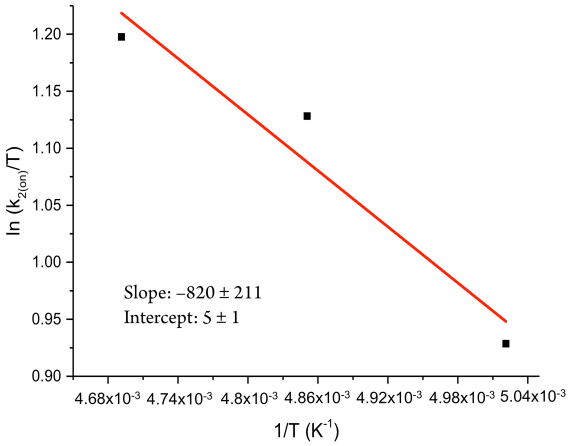

Figure S14. Eyring plot ($\ln(k/T) = -(\Delta H^{\ddagger}/R)(1/T) + \Delta S^{\ddagger}/R + \ln(k_b/h)$; $k = k_{2(on)}$) for the forward reaction for the second reaction step, binding of the second $NO_{(g)}$.

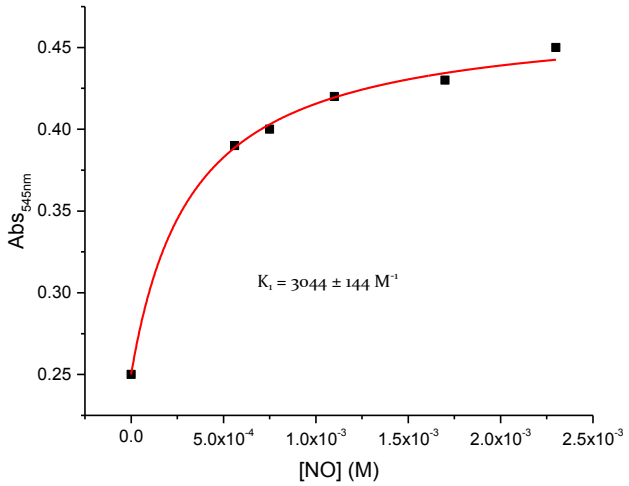

Figure S15. Absorbance at 545 nm (at the end of the first reaction step at –74 °C) as a function of $NO_{(g)}$ concentration (data fitted by eq 1 given in the main text).

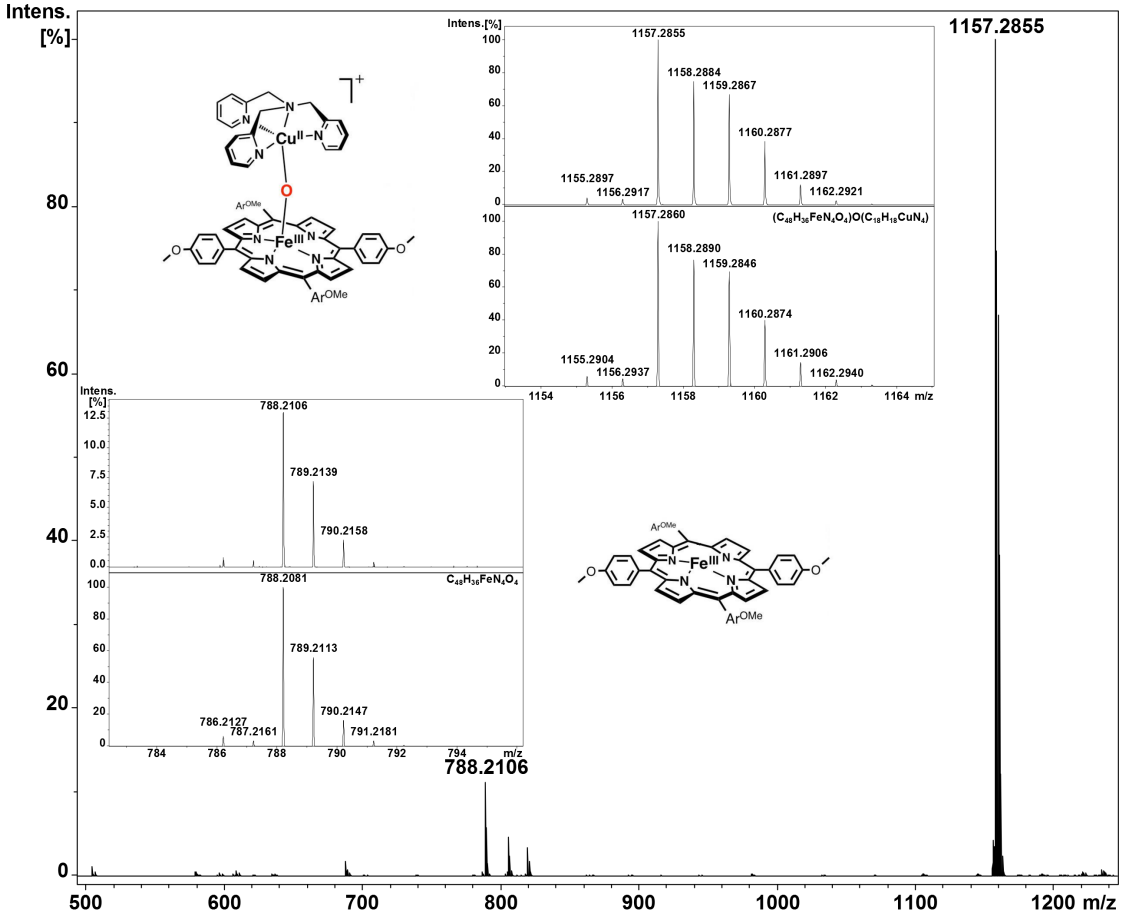

Figure S16. Mass spectrum of $[(TMPP)Fe^{III}–O–Cu^{II}(tmpa)]^+$ in acetone before bubbling with $NO_{(g)}$, spray gas temperature –60 °C, dry gas temperature –55 °C; main species *m/z* = 1157.2855, which is assigned to the μ-oxo compound.

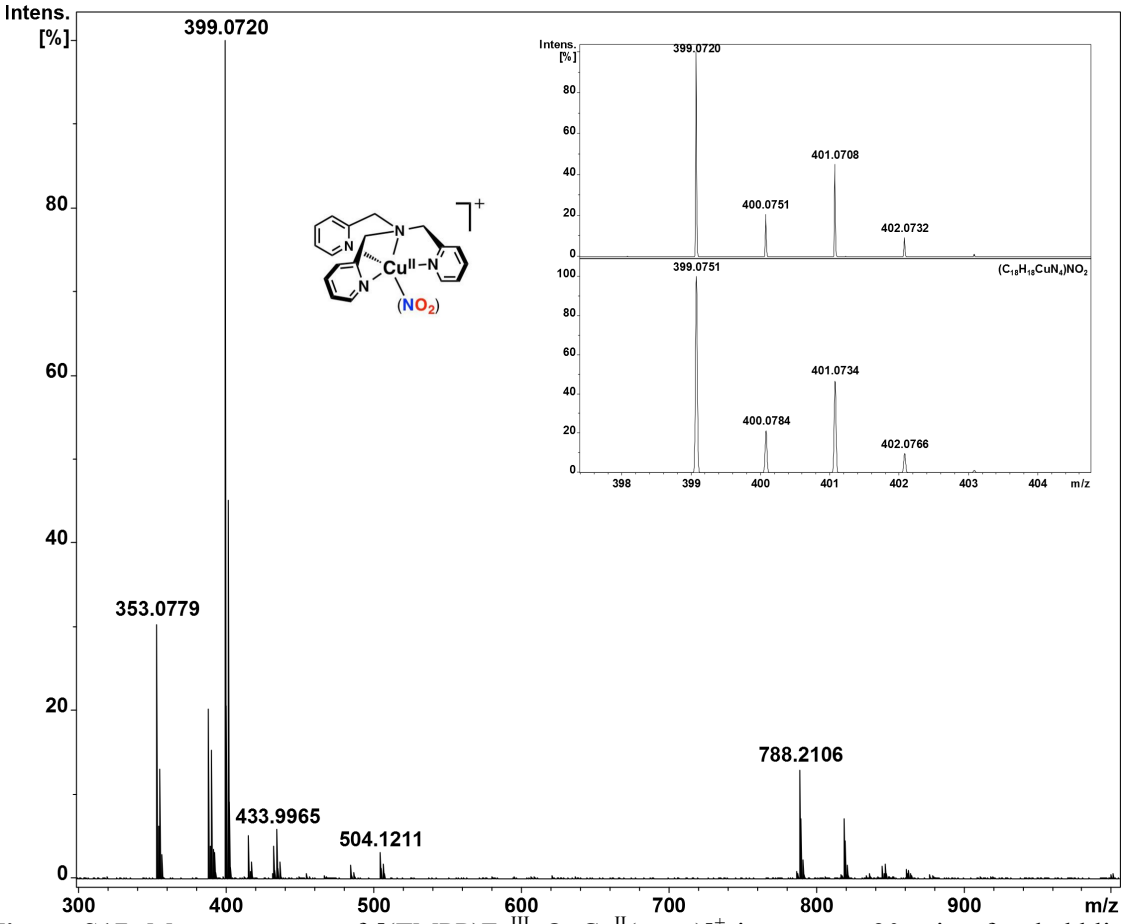

Figure S17. Mass spectrum of $[(TMPP)Fe^{III}–O–Cu^{II}(tmpa)]^+$ in acetone 20 min after bubbling with $NO_{(g)}$. Experimental conditions: spray gas temperature –60 °C; dry gas temperature –55 °C. (Main species *m/z* = 399.0720, which can be assigned to the $[(tmpa)Cu^{II}(NO_2)]^+$ complex; the ferrous heme nitrosyl $(TMPP)Fe^{II}(NO)$ compound cannot be observed because it is not charged.)

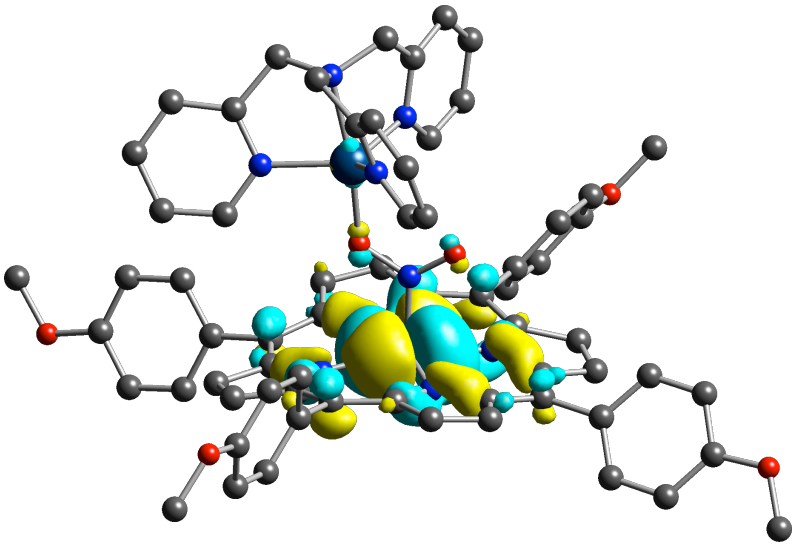

Figure S18. SOMO of the *mono*-NO adduct (BP86/6–31G(d)). Isodensity value α = 0.02.

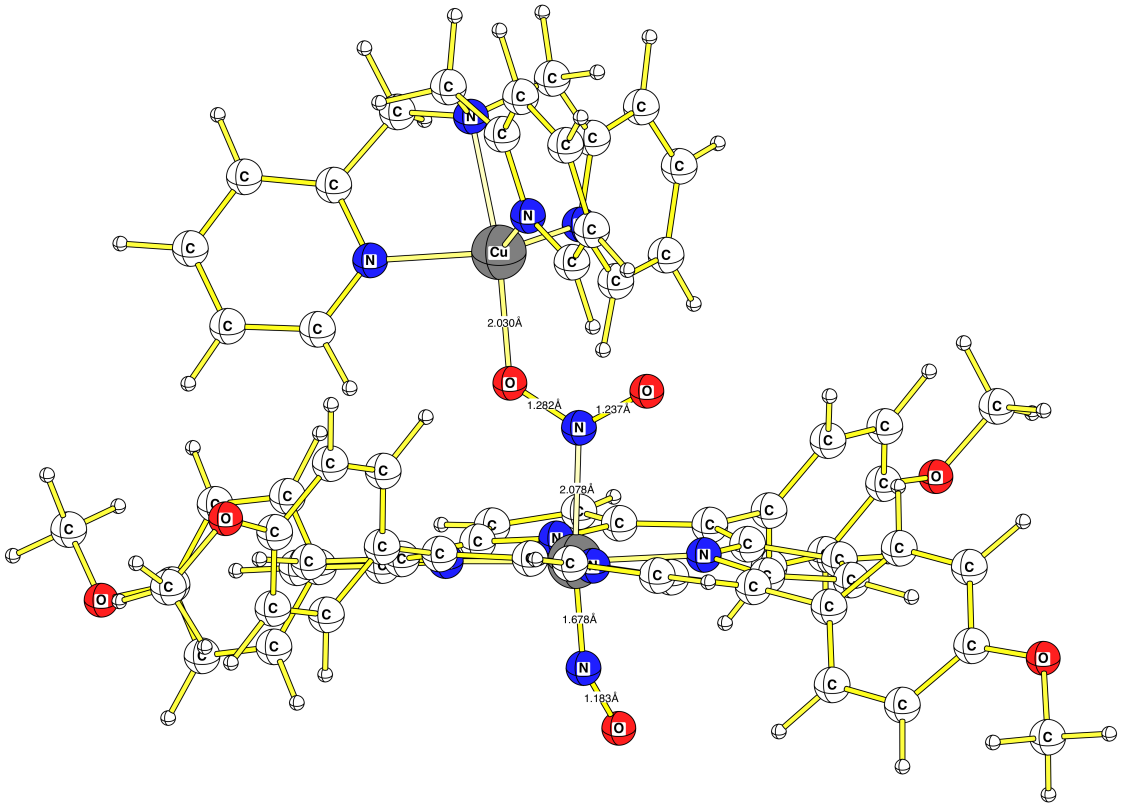

Figure S19. Optimized geometry of the *bis*-NO complex, BP86/6–31G(d).

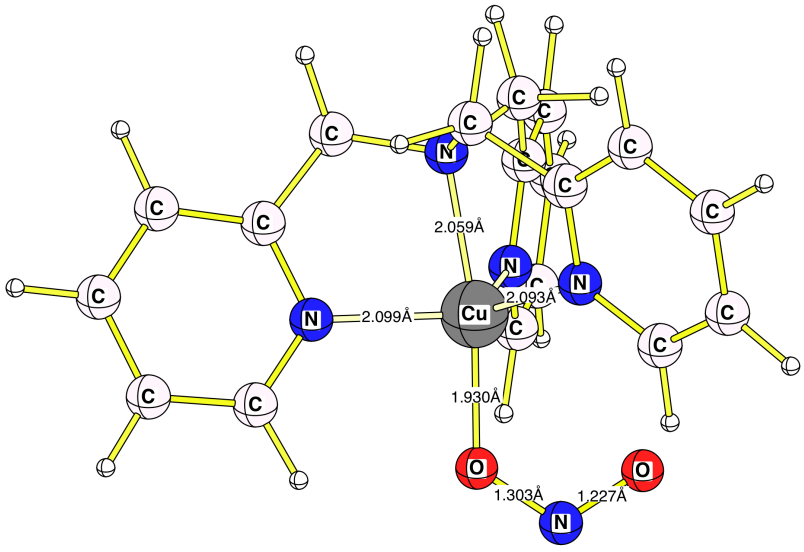

Figure S20. Optimized geometry of $[(tmpa)Cu^{II}(NO_2)]^+$ complex, BP86/6–31G(d).

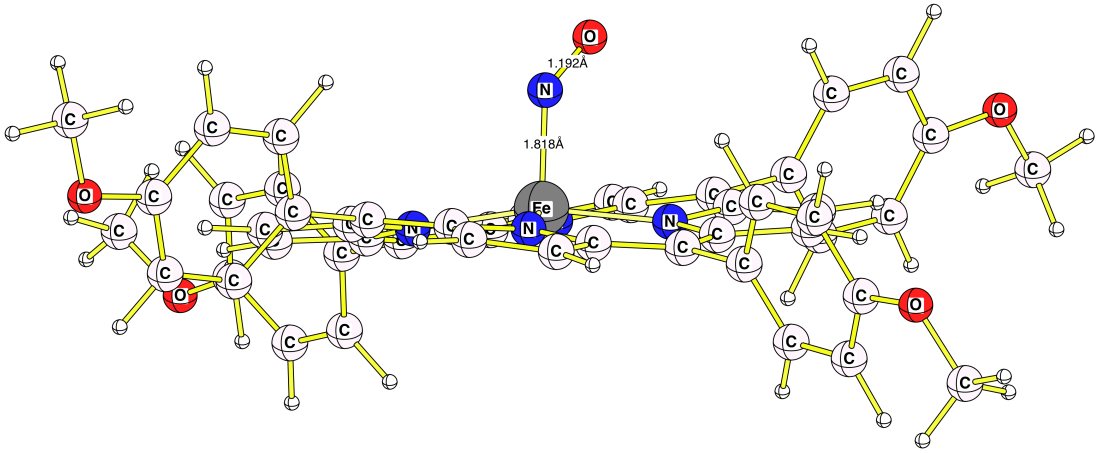

Figure S21. Optimized geometry of (TMPP)Fe^{II}(NO) complex, BP86/6–31G(d).

6.3. [(TMPP)$Fe^{III}$$(THF)_2$]$(SbF_6)$

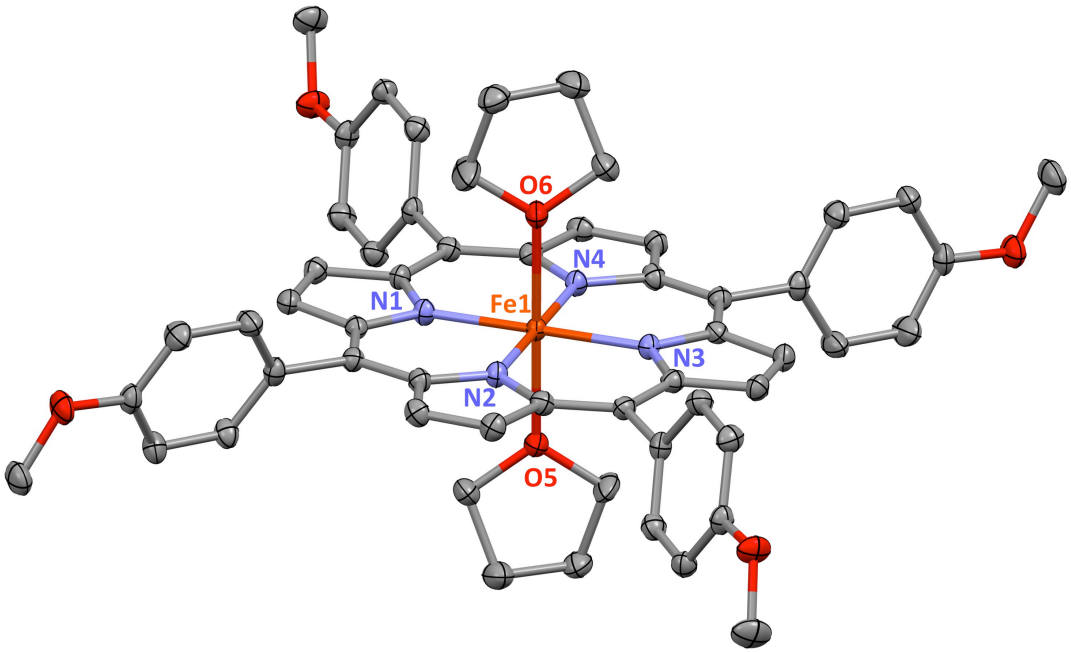

Figure S22. Displacement ellipsoid plot (50% probability level) of [(TMPP)$Fe^{III}$$(THF)_2$]$^+$, showing the atom-labeling scheme. Lattice solvent molecules and hydrogen atoms have been omitted for the sake of clarity. Selected bond lengths (Å) and angles (deg): Fe1–O6, 2.156(2); Fe1–O5, 2.154(2); Fe1–N1, 2.015(3); Fe1–N2, 2.025(3); Fe1–N3, 2.032(3); Fe1–N4, 2.014(3); O5–Fe1–O6, 179.68(10); N1–Fe1–N2, 89.40(10); N1–Fe1–N3, 179.70(11); N1–Fe1–N4, 90.98(10); N1–Fe1–O5, 90.58(9); N1–Fe1–O6, 89.67(9); N2–Fe1–N3, 90.30(10); N2–Fe1–N4, 179.26(10); N2–Fe1–O5, 90.68(9); N2–Fe1–O6, 89.13(9); N3–Fe1–N4, 89.32(10); N3–Fe1–O5, 89.38(9); N3–Fe1–O6, 90.37(9); N4–Fe1–O5, 89.96(9); N4–Fe1–O6, 90.24(9).

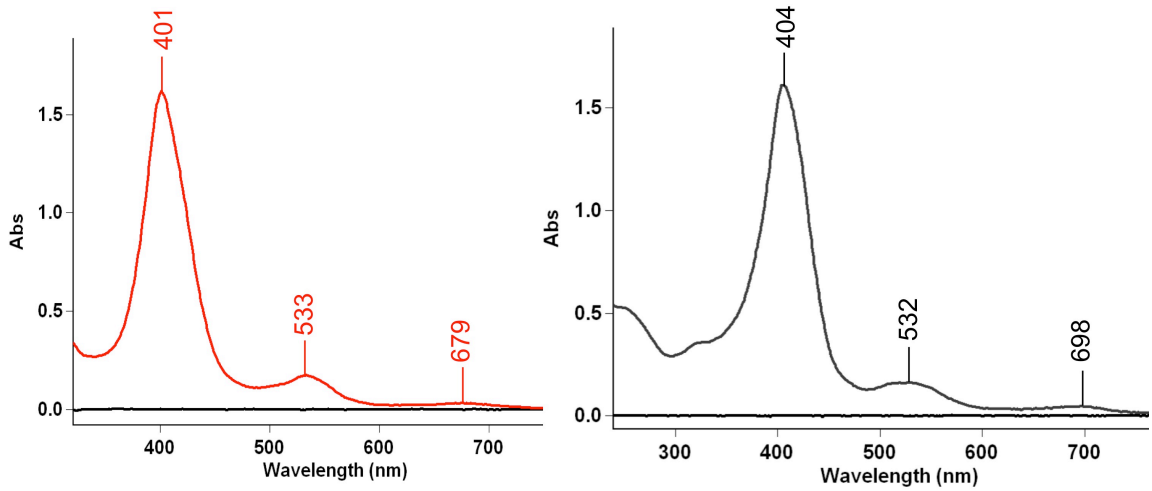

Figure S23. UV−vis spectra of $[(TMPP)Fe^{III}(THF)_2](SbF_6)$ in acetone (*left,* red) and MeCN (*right,* black) 50 μM in a 2-mm cuvette at RT.

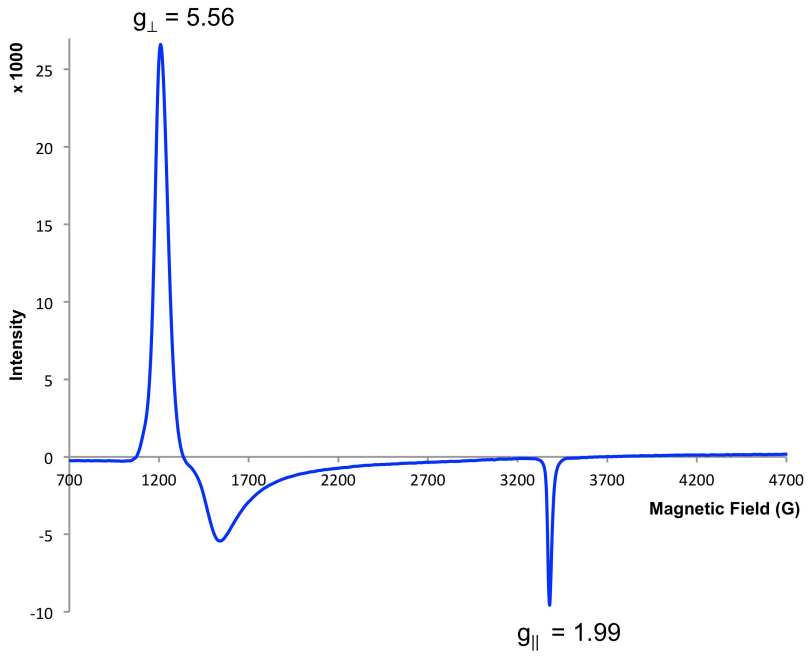

Figure S24. EPR spectrum of $[(TMPP)Fe^{III}(THF)_2](SbF_6)$ (1 mM) in THF/MeTHF (1:4) at 12 K.

6.4. Computational Details

All structures were fully optimized in the presence of solvent (acetone, PCM model) within Gaussian 09 program.[1] The BP86[2,3] functional with the 6–31G(d)[4-18] basis sets for all the atoms were used. In all case the nature of stationary points were checked (full optimization, NIMag= 0 for minima and NIMag=1 – for transition state).

Various spin states of the complexes were considered in our calculations (high spin (HS), intermediate spin (IS) and low spin (LS)). Single-point energy evaluation was performed at the OLYP[19–22]/6–311+G(d,p) level of theory, including solvent correction via PCM model.

Table S2. Absolute energies (E, Hartree) of studied compounds at the OLYP/6-311+G(d,p) level, for different (HS–high spin, IS–intermediate spin, LS–low spin) states in the presence of solvent (acetone).

Compounds	HS	IS	LS
	E	E	E
[(TMPP)Fe^{III}–O–Cu^{II}(tmpa)]$^{+}$	-6266.15854	-6266.15260	–
INIT1	-6396.06924	-6396.07014	–
TS1	-6396.06936	-6396.06993	–
***mono*-NO**	-6396.08632	-6396.08955	-6396.08947
***bis*-NO**	-6525.96359	-6526.02858	-6526.03250
NO	–	–	-129.895151

Table S3. Absolute energies (E, Hartree) and zero-point correction energy (ZPE, kcal/mol) of studied compounds at the BP86/6-31G(d) level, for different (HS–high spin, IS–intermediate spin, LS–low spin) states in the presence of solvent (acetone).

Compounds	HS		IS		LS	
	E	ZPE	E	ZPE	E	ZPE
[(TMPP)Fe^{III}–O–Cu^{II}(tmpa)]$^{+}$	-6266.00970	648.85	-6266.021454	649.37	–	–
INIT1	-6395.90702	652.47	-6395.925409	653.50	–	–
TS1	-6395.90517	652.52	*-6395.923805*	*653*	–	–
***mono*-NO**	-6395.92571	655.67	-6395.94428	654.00	-6395.96122	655.55
***bis*-NO**	-6525.85606	658.31	-6525.90377	659.56	-6525.90605	659.87
NO	–	–	–	–	-129.895151	2.70

6.5. XYZ Coordinates

NO

2

N	-0.62483	-0.00000	0.00000
O	0.54711	0.00000	0.00000

[(TMPP)Fe^{III}–O–Cu^{II}(tmpa)]$^{+}$

135

Fe	-0.05373	-1.86193	0.08131
C	2.61924	-2.22350	-1.55535
C	4.04803	-2.39887	-1.38933
H	4.77127	-2.46632	-2.20086
C	4.28455	-2.51253	-0.04429
H	5.23772	-2.69142	0.45137
C	3.00175	-2.40947	0.62202
C	2.82882	-2.55675	2.02081
C	1.56911	-2.64379	2.66265
C	1.38831	-2.82795	4.08915
H	2.18986	-2.89372	4.82354
C	0.03886	-2.92076	4.31330
H	-0.46858	-3.09267	5.26165
C	-0.61637	-2.76179	3.03117
C	-2.01830	-2.81947	2.84496
C	-2.66140	-2.72701	1.58709
C	-4.09966	-2.73301	1.40812
H	-4.83292	-2.82589	2.20826
C	-4.33768	-2.58422	0.06521
H	-5.30241	-2.53262	-0.43774
C	-3.04741	-2.49163	-0.58701
C	-2.87259	-2.31388	-1.98098
C	-1.61301	-2.19795	-2.61638
C	-1.43287	-2.10925	-4.05086
H	-2.23537	-2.10702	-4.78725
C	-0.08275	-2.05000	-4.28383
H	0.42414	-1.97490	-5.24488
C	0.57355	-2.12880	-2.99450
C	1.97837	-2.13560	-2.81458
N	1.99153	-2.23690	-0.31583
N	0.33267	-2.59287	2.03064
N	-2.03011	-2.57881	0.35683
N	-0.37605	-2.20875	-1.98219
C	1.62965	1.00128	2.68957
H	1.62106	0.03262	2.18152
C	2.43973	1.25559	3.80188
H	3.09366	0.46864	4.18804
N	-0.43510	3.82910	0.68812
C	0.66336	4.38774	-0.14022
C	0.81960	3.57900	-1.41423
C	1.28110	4.12826	-2.61678
H	1.49448	5.19964	-2.68137
C	1.46509	3.28350	-3.72224
H	1.82509	3.68896	-4.67302
C	1.17504	1.91760	-3.58900
H	1.30448	1.22152	-4.42225
C	0.70354	1.44568	-2.35870
H	0.45308	0.39396	-2.19248
N	0.52584	2.25627	-1.29098
O	-0.20015	-0.14262	0.28478
Cu	-0.31088	1.71869	0.47822
N	0.80028	1.93255	2.16715
C	2.39907	2.52877	4.38921
H	3.02718	2.76630	5.25353
C	1.54345	3.50000	3.84746
H	1.48601	4.50539	4.27597
C	0.75119	3.16441	2.74228
C	-0.26241	4.11597	2.13440
C	-1.77903	4.21294	0.18707
C	-2.80515	3.17404	0.59865
C	-4.15202	3.48038	0.82859
H	-4.49584	4.51734	0.76334
C	-4.55160	1.12769	1.21246
H	-5.20504	0.28370	1.44911
C	-3.18962	0.90271	0.98231
H	-2.74535	-0.09527	1.03358
N	-2.32958	1.90200	0.68167
C	-5.04156	2.43964	1.13735
H	-6.09916	2.65355	1.32089
H	0.51098	5.46249	-0.35695
H	1.59497	4.30344	0.44995
H	-2.06911	5.22724	0.52238
H	-1.72207	4.23881	-0.91726
H	0.01385	5.17276	2.31368
H	-1.24114	3.94997	2.62196
C	-4.09755	-2.26097	-2.84040
C	4.06345	-2.66088	2.86087
C	4.34691	-3.81502	3.62137
H	3.65253	-4.66192	3.59171
C	5.51019	-3.91852	4.40115
H	5.69481	-4.83573	4.96662
C	6.42580	-2.84642	4.43403
C	6.16136	-1.68396	3.67561
H	6.87836	-0.85718	3.70938
C	5.00199	-1.59966	2.90144
H	4.81138	-0.69205	2.31825
C	7.89699	-3.99533	5.94114
H	7.12141	-4.18138	6.70708
H	8.85446	-3.77373	6.43411
H	8.00862	-4.89238	5.30425
C	-4.42162	-1.10380	-3.57930
H	-3.76962	-0.22545	-3.51455
C	-5.56952	-1.03993	-4.38588
H	-5.78761	-0.11977	-4.93446
C	-6.42515	-2.15763	-4.46923
C	-6.11376	-3.32714	-3.73998
H	-6.78010	-4.19221	-3.82057
C	-4.96983	-3.37265	-2.94003
H	-4.73642	-4.29046	-2.38927
C	-7.91981	-1.04510	-5.97978
H	-8.08954	-0.17202	-5.32243
H	-8.85446	-1.30020	-6.49967
H	-7.13880	-0.79959	-6.72321
O	7.58867	-2.83206	5.15677
O	-7.56979	-2.21221	-5.21975
C	-2.87794	-2.99311	4.05924
C	-3.66324	-4.15095	4.23870
H	-3.63432	-4.94204	3.48110
C	-4.47113	-4.32632	5.37409
H	-5.05654	-5.24352	5.47835
C	-4.50893	-3.32261	6.36363
C	-3.73015	-2.15507	6.19947
H	-3.77291	-1.37976	6.97148
C	-2.92803	-1.99899	5.06678
H	-2.33539	-1.08488	4.94994
C	-6.06709	-4.54870	7.71505
H	-6.81833	-4.66564	6.91187
H	-6.57815	-4.38874	8.67537
H	-5.44705	-5.46249	7.77458
C	2.84484	-2.08464	-4.03427
C	2.79552	-3.10805	-5.01287
H	2.11767	-3.95668	-4.86999
C	3.60844	-3.06602	-6.14746
H	3.57335	-3.86450	-6.89581
C	4.50254	-1.98919	-6.34232
C	4.57031	-0.96122	-5.37956
H	5.24971	-0.11397	-5.50497
C	3.74862	-1.02115	-4.24209
H	3.80397	-0.21276	-3.50462
C	6.17917	-0.96714	-7.71968
H	5.65841	0.00513	-7.80115
H	6.66937	-1.20219	-8.67537
H	6.93919	-0.91167	-6.91836
O	-5.25810	-3.37998	7.50903
O	5.25216	-2.03916	-7.48739

INIT1_IS

137

Initial complex in acetone

Fe	0.22176	-1.83067	-0.27991
C	2.67357	-1.84956	-2.06462
C	4.05870	-2.25149	-2.07368
H	4.70494	-2.23912	-2.95031
C	4.36444	-2.66594	-0.80356
H	5.31202	-3.05397	-0.43283
C	3.17451	-2.48862	-0.00788
C	3.13883	-2.65632	1.38732
C	1.96248	-2.45224	2.12964
C	1.90603	-2.48718	3.57092
H	2.76494	-2.62844	4.22527
C	0.59044	-2.32964	3.92257
H	0.15650	-2.33268	4.92171
C	-0.16162	-2.19868	2.69760
C	-1.56546	-2.21970	2.64349
C	-2.26302	-2.25610	1.42284
C	-3.68714	-2.45676	1.31837
H	-4.35952	-2.59497	2.16395
C	-4.00160	-2.43476	-0.01636
H	-4.98102	-2.54574	-0.47949
C	-2.77626	-2.17596	-0.73161
C	-2.73412	-1.87679	-2.10353
C	-1.54313	-1.49902	-2.74723
C	-1.47186	-1.06769	-4.12052
H	-2.32775	-0.94958	-4.78318
C	-0.14767	-0.85098	-4.40242
H	0.29027	-0.51387	-5.34084
C	0.59977	-1.21251	-3.22273
C	1.99941	-1.35909	-3.19745
N	2.11446	-2.04277	-0.80089
N	0.69369	-2.22941	1.59298
N	-1.69609	-2.09045	0.15521
N	-0.26660	-1.54937	-2.17920
C	0.25199	1.56896	3.22825
H	0.45143	0.59479	2.77320
C	0.54026	1.81449	4.57418
H	0.97396	1.02021	5.18794
N	-1.03590	4.39381	0.58581
C	0.16418	5.09025	0.07001
C	0.65182	4.39552	-1.18562
C	1.29839	5.07160	-2.22723
H	1.44267	6.15472	-2.16601
C	1.75046	4.34037	-3.33565
H	2.25978	4.84589	-4.16201
C	1.52858	2.95603	-3.36808
H	1.85832	2.34337	-4.21173
C	0.86910	2.35293	-2.29160
H	0.67736	1.27680	-2.26793
N	0.44045	3.05076	-1.21390
O	0.45322	0.48554	0.24469
Cu	-0.50620	2.31943	0.40437
N	-0.28702	2.50309	2.40819

C	0.27463	3.08782	5.09949
H	0.50439	3.32378	6.14323
C	-0.29341	4.05635	4.26085
H	-0.52361	5.05994	4.63227
C	-0.57773	3.72583	2.92845
C	-1.31315	4.68535	2.01010
C	-2.22645	4.57470	-0.27816
C	-3.17935	3.40888	-0.09230
C	-4.57037	3.56371	-0.14764
H	-5.00135	4.55717	-0.30652
C	-4.78330	1.18911	0.22113
H	-5.37399	0.27951	0.35784
C	-3.38500	1.11907	0.26856
H	-2.87194	0.16944	0.44185
N	-2.58600	2.20046	0.11426
C	-5.38853	2.43454	0.00645
H	-6.47827	2.53046	-0.03021
H	-0.02484	6.16634	-0.11424
H	0.94403	5.02026	0.85190
H	-2.73306	5.54081	-0.08899
H	-1.87686	4.59087	-1.32661
H	-1.08478	5.73805	2.26511
H	-2.39808	4.54861	2.17452
N	1.77261	0.60500	0.51265
O	2.13738	1.74441	0.79433
C	-4.00195	-1.95298	-2.89830
C	4.38951	-3.04248	2.10992
C	4.46364	-4.25300	2.83076
H	3.59502	-4.92068	2.84965
C	5.62954	-4.63631	3.51261
H	5.64621	-5.58797	4.05019
C	6.75976	-3.79348	3.48769
C	6.70150	-2.57368	2.77661
H	7.58169	-1.92237	2.77345
C	5.53552	-2.20993	2.09921
H	5.50237	-1.25637	1.56098
C	8.04773	-5.28880	4.85188
H	7.31270	-5.32379	5.67741
H	9.06608	-5.30263	5.26631
H	7.90500	-6.16634	4.19425
C	-4.62231	-0.79822	-3.41582
H	-4.17779	0.18421	-3.22201
C	-5.80651	-0.87219	-4.16854
H	-6.25754	0.04833	-4.54831
C	-6.39727	-2.12823	-4.41584
C	-5.79180	-3.29500	-3.89807
H	-6.25823	-4.26505	-4.09896
C	-4.61384	-3.20397	-3.15262
H	-4.15012	-4.11842	-2.76621
C	-8.18489	-1.16669	-5.69487
H	-8.50913	-0.46458	-4.90421
H	-9.06608	-1.54552	-6.23247
H	-7.51818	-0.64044	-6.40326
O	7.94810	-4.06040	4.11422
O	-7.54544	-2.32510	-5.13732
C	-2.33459	-2.29485	3.92775
C	-3.00611	-3.47425	4.30979
H	-2.96200	-4.35328	3.65703
C	-3.72165	-3.55801	5.51578
H	-4.22348	-4.49357	5.77638
C	-3.77345	-2.44017	6.37356
C	-3.10325	-1.25177	6.00717
H	-3.15293	-0.38945	6.68018
C	-2.39617	-1.18544	4.80385
H	-1.88498	-0.25507	4.53288
C	-5.12647	-3.59277	7.98515
H	-5.92065	-3.86837	7.26648
H	-5.57949	-3.34947	8.95705
H	-4.42848	-4.44212	8.10544
C	2.79442	-1.06268	-4.42853
C	2.57756	-1.76846	-5.63811
H	1.81558	-2.55450	-5.67364
C	3.33301	-1.49732	-6.78047
H	3.16908	-2.05325	-7.70939
C	4.33544	-0.50158	-6.75135
C	4.57167	0.21005	-5.55705
H	5.34018	0.98570	-5.50523
C	3.80756	-0.08002	-4.41478
H	3.99764	0.47970	-3.49236
C	6.05009	0.68623	-7.93697
H	5.64462	1.69092	-7.71509
H	6.46010	0.67286	-8.95705
H	6.85081	0.44419	-7.21369
O	-4.43658	-2.40295	7.57204
O	5.01510	-0.30974	-7.92416

TS1_IS

137

Fe	-0.645382	0.077981	-1.339409
C	-3.525808	-0.912272	-1.482112
C	-4.878476	-0.413685	-1.510218
H	-5.761994	-1.019227	-1.705228
C	-4.811111	0.926968	-1.232023
H	-5.627915	1.643666	-1.158440
C	-3.415492	1.257223	-1.086668
C	-2.953549	2.551626	-0.781396
C	-1.600979	2.902717	-0.925737
C	-1.104081	4.253361	-0.829248
H	-1.689236	5.107905	-0.492259
C	0.180868	4.242118	-1.309906
H	0.856763	5.085240	-1.447024
C	0.499602	2.873207	-1.630180
C	1.723568	2.456912	-2.179837
C	2.037349	1.095527	-2.346226
C	3.329625	0.627061	-2.776588
H	4.133152	1.269699	-3.134568
C	3.341880	-0.735299	-2.604409
H	4.158842	-1.430252	-2.794031
C	2.045856	-1.110701	-2.103094
C	1.684123	-2.426101	-1.762245
C	0.357776	-2.767544	-1.441250
C	-0.096436	-4.126019	-1.278357
H	0.554352	-4.998740	-1.247452
C	-1.467993	-4.088885	-1.246679
H	-2.163222	-4.923735	-1.169163
C	-1.855962	-2.708007	-1.383272
C	-3.191201	-2.277090	-1.493901
N	-2.622456	0.135855	-1.298356
N	-0.588142	2.042669	-1.357083
N	1.232381	0.018847	-1.960741
N	-0.727490	-1.887795	-1.444225
C	0.351262	2.798922	2.741260
H	-0.063161	2.571103	1.755343
C	0.164438	4.051543	3.334128
H	-0.402079	4.821280	2.802394
N	2.135594	-0.386491	4.600700
C	1.068796	-1.055127	5.364262
C	0.395058	-2.117859	4.512876
C	-0.130347	-3.297713	5.052887
H	-0.029348	-3.499554	6.124801
C	-0.786552	-4.203265	4.204713
H	-1.207356	-5.131956	4.603647
C	-0.885426	-3.894884	2.840787
H	-1.380355	-4.566500	2.133414
C	-0.329274	-2.697948	2.375893
H	-0.389424	-2.409701	1.322445
N	0.302076	-1.817525	3.188794
O	-0.106554	0.130104	1.002243
Cu	1.164187	-0.094768	2.606744
N	1.044312	1.796817	3.334981
C	0.698366	4.282273	4.609530
H	0.553783	5.242331	5.115622
C	1.425651	3.254728	5.226826
H	1.866962	3.394522	6.219889
C	1.596132	2.037673	4.553916
C	2.496239	0.943812	5.114721
C	3.296711	-1.240568	4.294700
C	3.967223	-0.774860	3.010864
C	5.355160	-0.813376	2.834264
H	5.998601	-1.161951	3.649453
C	5.031990	0.037447	0.601112
H	5.400279	0.367731	-0.373727
C	3.654711	0.052581	0.856268
H	2.941497	0.389824	0.098490
N	3.118464	-0.338835	2.036634
C	5.900891	-0.402441	1.607517
H	6.983768	-0.421820	1.447046
H	1.431622	-1.487938	6.321585
H	0.321583	-0.278028	5.617235
H	4.029821	-1.284350	5.127729
H	2.917248	-2.269026	4.146084
H	2.508070	0.977732	6.224450
H	3.531256	1.156180	4.785493
N	-1.385153	0.359075	1.408083
O	-1.535664	0.408816	2.623738
C	2.708560	-3.514474	-1.837697
C	-3.950081	3.574188	-0.343221
C	-4.225615	4.731302	-1.100311
H	-3.707484	4.886135	-2.053303
C	-5.173530	5.676719	-0.677549
H	-5.369516	6.553376	-1.300899
C	-5.868281	5.475201	0.532984
C	-5.604828	4.319541	1.302151
H	-6.151820	4.179741	2.239930
C	-4.666185	3.384752	0.865106
H	-4.463056	2.494981	1.471220
C	-7.124529	7.500993	0.294378
H	-6.240616	8.157278	0.179031
H	-7.895892	8.025666	0.876644
H	-7.526753	7.247153	-0.704935
C	3.122574	-4.202635	-0.679976
H	2.697763	-3.920296	0.290340
C	4.070381	-5.237841	-0.736659
H	4.368445	-5.744656	0.185341
C	4.625923	-5.606427	-1.978746
C	4.218821	-4.929156	-3.149597
H	4.648678	-5.236776	-4.108039
C	3.274728	-3.904102	-3.076186
H	2.951964	-3.402807	-3.995353
C	5.978611	-7.328937	-1.008976
H	6.473414	-6.670419	-0.268923
H	6.702348	-8.069149	-1.379945
H	5.131483	-7.852786	-0.525779
O	-6.809309	6.323826	1.046277
O	5.552524	-6.595810	-2.161299
C	2.739899	3.483894	-2.572404
C	3.052827	3.703679	-3.928790
H	2.531355	3.124702	-4.699342
C	4.007042	4.657260	-4.318633
H	4.214459	4.803303	-5.382080
C	4.674569	5.417592	-3.336910
C	4.373887	5.207469	-1.972621
H	4.906100	5.801870	-1.223097
C	3.422368	4.255495	-1.601705
H	3.205701	4.096138	-0.539128
C	5.954108	6.626880	-4.961505
H	6.371232	5.726465	-5.451857
H	6.718727	7.416854	-4.936757

H 5.075488 6.982932 -5.532544
C -4.271381 -3.303081 -1.596477
C -4.296963 -4.212762 -2.683280
H -3.524380 -4.145367 -3.457045
C -5.300416 -5.174448 -2.798585
H -5.328844 -5.866636 -3.645906
C -6.315343 -5.263292 -1.819498
C -6.304855 -4.372151 -0.726530
H -7.072102 -4.424751 0.050750
C -5.291654 -3.405785 -0.627901
H -5.284710 -2.726023 0.231459
C -8.310489 -6.357416 -1.071147
H -7.924123 -6.602606 -0.063161
H -8.941132 -7.183043 -1.431486
H -8.912138 -5.429942 -1.018889
O 5.620455 6.371536 -3.592291
O -7.249091 -6.239771 -2.024829

NORMALMODES 405
Fe -0.04 0.00 -0.09
C -0.05 0.00 -0.09
C -0.07 0.00 -0.06
H -0.07 0.00 -0.05
C -0.06 0.00 -0.06
H -0.05 0.00 -0.05
C -0.04 -0.01 -0.07
C -0.03 -0.02 -0.05
C -0.03 -0.02 -0.02
C -0.02 -0.03 0.02
H -0.02 -0.04 0.06
C -0.01 -0.01 0.03
H -0.01 -0.01 0.07
C -0.02 0.00 -0.03
C -0.02 0.00 -0.02
C -0.02 0.01 -0.01
C -0.02 0.00 -0.02
H -0.03 -0.01 -0.04
C -0.03 0.00 0.00
H -0.04 0.00 0.00
C -0.03 0.01 0.02
C -0.04 0.02 0.02
C -0.05 0.02 0.00
C -0.05 0.02 0.01
H -0.05 0.03 0.04
C -0.06 0.01 -0.02
H -0.05 0.00 -0.03
C -0.06 0.00 -0.05
C -0.06 0.01 -0.07
N -0.05 0.00 -0.11
N -0.03 0.00 -0.07
N -0.03 0.01 0.01
N -0.06 0.01 -0.05
C -0.03 0.00 0.09
H -0.02 0.00 0.09
C -0.04 0.00 0.10
H -0.05 -0.01 0.10
N 0.04 0.02 0.04
C 0.05 0.01 0.05
C 0.05 0.01 0.05
C 0.05 0.00 0.04
H 0.05 -0.01 0.03
C 0.04 0.02 0.03
H 0.04 0.01 0.01
C 0.03 0.04 0.03
H 0.03 0.05 0.02
C 0.03 0.04 0.04
H 0.03 0.06 0.05
N 0.03 0.03 0.06
O 0.36 0.02 0.04
Cu 0.09 0.02 0.12
N 0.00 0.01 0.09
C -0.03 0.00 0.09
H -0.03 0.00 0.09
C 0.00 0.01 0.09
H 0.00 0.02 0.08
C 0.01 0.02 0.08
C 0.03 0.02 0.06
C 0.07 0.03 0.07
C 0.08 0.01 0.06
C 0.07 -0.01 0.05
H 0.08 -0.01 0.05
C 0.06 -0.05 0.03
H 0.05 -0.08 0.02
C 0.06 -0.02 0.05
H 0.05 -0.03 0.05
N 0.08 0.01 0.06
C 0.06 -0.04 0.03
H 0.06 -0.06 0.02
H 0.07 0.01 0.04
H 0.05 0.00 0.07
H 0.05 0.06 0.08
H 0.08 0.02 0.09
H 0.05 0.00 0.05
H 0.02 0.04 0.04
N 0.28 -0.15 -0.30
O -0.08 -0.04 -0.35
C -0.04 0.01 0.02
C -0.02 -0.02 -0.03
C -0.01 -0.01 -0.01
H -0.01 0.00 -0.01
C 0.00 0.00 0.00
H 0.01 0.01 0.01
C 0.00 -0.01 0.00
C -0.01 -0.02 -0.01
H -0.01 -0.03 -0.01
C -0.02 -0.03 -0.03
H -0.03 -0.04 -0.04
C 0.01 0.00 0.02
H 0.01 0.00 0.02
H 0.01 0.00 0.02
H 0.01 0.01 0.02
C -0.03 0.02 0.01
H -0.02 0.02 0.02
C -0.03 0.02 0.01
H -0.02 0.02 0.01
C -0.04 0.02 0.01
C -0.05 0.01 0.01
H -0.05 0.01 0.01
C -0.05 0.01 0.01
H -0.06 0.00 0.01
C -0.02 0.02 0.00
H -0.02 0.02 0.00
H -0.02 0.02 0.00
H -0.02 0.02 0.01
O 0.01 -0.01 0.01
O -0.03 0.02 0.00
C -0.01 0.00 -0.02
C -0.02 0.02 -0.02
H -0.03 0.04 -0.02
C -0.01 0.02 -0.01
H -0.02 0.03 -0.01
C 0.00 0.00 0.00
C 0.00 -0.02 0.00
H 0.01 -0.03 0.00
C 0.00 -0.01 -0.01
H 0.00 -0.03 -0.01
C 0.00 0.01 0.00
H -0.01 0.01 -0.01
H 0.01 0.00 0.01
H 0.00 0.02 0.01
C -0.05 0.00 -0.05
C -0.06 -0.01 -0.04
H -0.06 -0.01 -0.05
C -0.05 -0.02 -0.02
H -0.05 -0.03 -0.02
C -0.04 -0.02 -0.01
C -0.03 -0.01 -0.02
H -0.03 -0.01 -0.01
C -0.04 0.00 -0.04
H -0.04 0.01 -0.05
C -0.02 -0.02 0.01
H -0.02 -0.01 0.01
H -0.02 -0.03 0.03
H -0.03 -0.03 0.01
O 0.00 0.00 0.00
O -0.03 -0.03 0.01
-49.5795

TS1_HS

137

Fe -0.638549 0.168130 -1.105222
C -3.018175 -1.870703 -1.436591
C -4.463211 -1.941471 -1.354220
H -5.060000 -2.838697 -1.513321
C -4.909277 -0.677823 -1.059778
H -5.939785 -0.345385 -0.940141
C -3.741475 0.176475 -0.983571
C -3.800069 1.572643 -0.750197
C -2.705425 2.456584 -0.907148
C -2.793210 3.897209 -0.787399
H -3.682154 4.452621 -0.491308
C -1.569789 4.405457 -1.146927
H -1.276596 5.452928 -1.206764
C -0.710057 3.276918 -1.436975
C 0.646688 3.381360 -1.827301
C 1.492248 2.269223 -2.055297
C 2.899458 2.370698 -2.382272
H 3.446746 3.301643 -2.524957
C 3.390076 1.090354 -2.449150
H 4.413076 0.780350 -2.658666
C 2.284992 0.196040 -2.172637
C 2.394539 -1.215343 -2.141070
C 1.304552 -2.098010 -1.943430
C 1.392234 -3.535747 -2.074566
H 2.308188 -4.096518 -2.255960
C 0.115916 -4.029579 -1.959890
H -0.200332 -5.070615 -2.013274
C -0.762798 -2.895835 -1.769198
C -2.172452 -2.984212 -1.659497
N -2.595076 -0.563656 -1.237149
N -1.416101 2.091051 -1.280220
N 1.128936 0.932115 -1.928720
N -0.017269 -1.720094 -1.726541
C 0.064480 2.425563 3.565224
H -0.388749 2.401720 2.571856
C -0.198961 3.476885 4.448330
H -0.866207 4.287703 4.142905
N 2.261338 -0.890594 4.507090
C 1.323911 -1.840437 5.145027
C 0.682940 -2.722596 4.091600
C 0.286338 -4.040174 4.350347
H 0.466961 -4.477153 5.337317
C -0.337305 -4.777279 3.332825
H -0.657974 -5.808306 3.511409
C -0.526917 -4.171171 2.082444
H -0.996043 -4.705996 1.251796
C -0.094816 -2.853832 1.898509
H -0.209902 -2.346658 0.936390

N	0.492422	-2.128265	2.880759
O	0.071523	0.153899	1.053222
Cu	1.239332	-0.260897	2.727948
N	0.881775	1.387093	3.870289
C	0.396283	3.455756	5.717931
H	0.199549	4.250546	6.444162
C	1.255306	2.395964	6.038453
H	1.750766	2.345870	7.013221
C	1.491230	1.393100	5.088238
C	2.524682	0.306239	5.332636
C	3.497638	-1.527540	3.996778
C	4.087892	-0.677126	2.885622
C	5.467561	-0.522938	2.705107
H	6.164704	-1.015654	3.390053
C	4.997271	0.890389	0.805846
H	5.307172	1.524740	-0.028736
C	3.633489	0.688831	1.052102
H	2.870515	1.154888	0.421921
N	3.174586	-0.078339	2.068701
C	5.932829	0.271428	1.645722
H	7.006856	0.410592	1.487754
H	1.813713	-2.448390	5.931501
H	0.537784	-1.237990	5.638634
H	4.239025	-1.705636	4.799966
H	3.216439	-2.515891	3.588421
H	2.594902	0.057268	6.409116
H	3.512480	0.706451	5.037768
N	-1.256870	0.279553	1.270520
O	-1.636941	0.125159	2.421967
C	3.740154	-1.825504	-2.391135
C	-5.122320	2.140686	-0.337028
C	-5.829941	3.057481	-1.142000
H	-5.410865	3.360975	-2.107822
C	-7.073185	3.578250	-0.746792
H	-7.594115	4.278102	-1.405401
C	-7.634460	3.183914	0.485244
C	-6.939779	2.265297	1.303885
H	-7.383549	1.970163	2.260388
C	-5.707895	1.751962	0.893013
H	-5.174842	1.046359	1.539711
C	-9.576103	4.558673	0.173355
H	-9.006884	5.493104	0.012552
H	-10.489475	4.778775	0.744573
H	-9.848857	4.120837	-0.804859
C	4.399086	-2.562397	-1.385706
H	3.924648	-2.673233	-0.404235
C	5.656401	-3.149401	-1.604173
H	6.135401	-3.706177	-0.794563
C	6.282578	-3.006046	-2.859265
C	5.634559	-2.274771	-3.879895
H	6.125999	-2.179339	-4.853695
C	4.385043	-1.695979	-3.645302
H	3.889339	-1.143349	-4.451016
C	8.191701	-4.292432	-2.183925
H	8.413944	-3.676010	-1.292917
H	9.133443	-4.615421	-2.650607
H	7.606757	-5.180561	-1.880352
O	-8.834877	3.625771	0.975234
O	7.504085	-3.531494	-3.188943
C	1.229346	4.750952	-1.997859
C	1.652936	5.205278	-3.264131
H	1.542126	4.548927	-4.134575
C	2.200869	6.486007	-3.443789
H	2.508594	6.801051	-4.444288
C	2.337602	7.346451	-2.335307
C	1.921788	6.906571	-1.058601
H	2.041007	7.580438	-0.203834
C	1.376656	5.630453	-0.897919
H	1.068949	5.300323	0.100423
C	3.293082	9.098243	-3.666931
H	4.107400	8.472770	-4.077610
H	3.667769	10.115872	-3.485235
H	2.457459	9.136114	-4.390326
C	-2.804216	-4.334606	-1.791687
C	-2.684794	-5.081053	-2.990040
H	-2.132075	-4.655983	-3.834918
C	-3.274249	-6.339980	-3.122103
H	-3.188162	-6.907631	-4.054399
C	-4.004291	-6.899803	-2.049382
C	-4.135268	-6.175076	-0.847142
H	-4.689025	-6.584925	0.001512
C	-3.540937	-4.907509	-0.732931
H	-3.645303	-4.356762	0.208572
C	-5.300314	-8.740270	-1.218658
H	-4.677340	-8.904798	-0.319811
H	-5.640014	-9.709229	-1.611889
H	-6.177344	-8.122209	-0.950938
O	2.855997	8.613578	-2.387569
O	-4.540620	-8.138683	-2.278892

NORMALMODES 405

Fe	0.05	0.00	0.04
C	0.03	0.00	0.02
C	0.03	0.00	0.00
H	0.03	0.01	-0.02
C	0.03	0.00	0.00
H	0.03	0.01	-0.01
C	0.03	0.00	0.02
C	0.02	0.00	0.02
C	0.02	0.00	0.02
C	0.02	0.00	0.00
H	0.01	0.00	-0.02
C	0.02	0.00	0.00
H	0.01	0.00	-0.02
C	0.02	0.00	0.03
C	0.02	-0.01	0.02
C	0.02	-0.01	0.01
C	0.01	0.00	0.00
H	0.01	0.00	0.01
C	0.02	0.00	-0.01
H	0.02	0.00	-0.02
C	0.03	-0.01	-0.01
C	0.03	-0.01	-0.02
C	0.02	0.00	-0.03
C	0.02	-0.01	-0.02
H	0.02	-0.01	-0.01
C	0.02	0.00	-0.01
H	0.02	0.00	0.01
C	0.03	0.00	-0.02
C	0.03	0.00	0.00
N	0.04	0.00	0.04
N	0.03	-0.01	0.05
N	0.03	-0.01	0.01
N	0.03	0.00	-0.04
C	0.06	0.05	-0.08
H	0.11	0.08	-0.11
C	0.03	0.03	-0.07
H	0.05	0.04	-0.07
N	-0.02	0.00	-0.04
C	-0.02	0.00	-0.04
C	-0.01	0.00	-0.04
C	-0.01	0.00	-0.03
H	-0.02	0.01	-0.02
C	-0.01	0.00	-0.02
H	-0.01	0.00	-0.02
C	-0.01	-0.01	-0.03
H	-0.02	-0.01	-0.02
C	-0.01	-0.01	-0.03
H	-0.03	0.00	-0.03
N	0.00	0.00	-0.04
O	-0.40	-0.03	-0.06
Cu	-0.05	0.00	-0.06
N	0.04	0.03	-0.08
C	-0.02	0.00	-0.05
H	-0.04	-0.02	-0.03
C	-0.03	-0.01	-0.04
H	-0.06	-0.03	-0.03
C	0.00	0.01	-0.06
C	-0.02	0.00	-0.04
C	-0.03	0.00	-0.05
C	-0.04	0.00	-0.04
C	-0.03	0.01	-0.03
H	-0.04	0.01	-0.02
C	-0.02	0.02	-0.02
H	-0.02	0.03	-0.01
C	-0.03	0.01	-0.04
H	-0.02	0.01	-0.04
N	-0.04	0.00	-0.05
C	-0.03	0.02	-0.02
H	-0.03	0.03	-0.01
H	-0.02	0.01	-0.03
H	-0.02	0.00	-0.04
H	-0.03	-0.01	-0.05
H	-0.04	0.00	-0.05
H	-0.03	0.00	-0.04
H	-0.01	-0.01	-0.03
N	-0.36	0.05	0.42
O	0.11	-0.06	0.55
C	0.03	0.00	-0.01
C	0.02	0.00	0.00
C	0.02	0.00	0.00
H	0.02	0.00	0.00
C	0.02	0.00	-0.01
H	0.02	-0.01	-0.01
C	0.01	0.00	-0.01
C	0.01	0.00	-0.01
H	0.00	0.00	-0.01
C	0.01	0.00	0.00
H	0.00	0.00	0.00
C	0.01	0.00	-0.01
H	0.01	0.00	-0.01
H	0.01	0.00	-0.02
H	0.01	0.00	-0.02
C	0.02	0.00	-0.01
H	0.02	0.00	-0.01
C	0.02	0.00	0.00
H	0.02	0.00	0.00
C	0.02	-0.01	0.00
C	0.03	-0.01	-0.01
H	0.03	-0.01	-0.01
C	0.03	-0.01	-0.01
H	0.03	-0.01	-0.01
C	0.02	-0.01	0.00
H	0.02	-0.01	0.00
H	0.02	-0.01	0.01
H	0.02	-0.01	0.00
O	0.01	0.00	-0.01
O	0.02	-0.01	0.00
C	0.02	-0.01	0.01
C	0.01	-0.01	0.01
H	0.01	-0.01	0.01
C	0.00	-0.01	0.00
H	0.00	-0.01	0.00
C	0.00	0.00	0.00
C	0.00	0.00	0.00
H	0.00	0.01	0.00
C	0.01	0.00	0.00
H	0.01	0.00	0.01
C	0.00	0.00	-0.01
H	0.00	0.00	0.00

H	0.00	0.00	-0.01
H	0.00	-0.01	-0.01
C	0.02	0.00	0.00
C	0.02	0.00	0.00
H	0.02	0.00	0.00
C	0.01	0.00	0.00
H	0.01	0.00	0.00
C	0.01	0.01	0.00
C	0.01	0.01	0.00
H	0.01	0.01	0.00
C	0.01	0.01	0.00
H	0.01	0.01	0.00
C	0.00	0.01	0.00
H	0.00	0.01	0.00
H	0.00	0.01	0.00
H	0.00	0.01	0.00
O	0.00	0.00	-0.01
O	0.00	0.01	0.00

-82.9500

***mono*-NO LS**

137

Final complex in acetone

Fe	0.17437	-2.30689	-0.21933
C	2.88849	-2.56758	-1.56501
C	4.25724	-2.93830	-1.29179
H	5.03843	-3.03346	-2.04460
C	4.34479	-3.17310	0.05316
H	5.21394	-3.49418	0.62548
C	3.03590	-2.91964	0.60960
C	2.76652	-2.92672	1.98733
C	1.48054	-2.68614	2.49927
C	1.18997	-2.56587	3.90991
H	1.93044	-2.63087	4.70585
C	-0.16067	-2.37693	4.02346
H	-0.75290	-2.26940	4.93130
C	-0.69902	-2.38249	2.68315
C	-2.07371	-2.35242	2.40126
C	-2.56802	-2.51084	1.09582
C	-3.97200	-2.63400	0.78075
H	-4.77887	-2.61551	1.51194
C	-4.06422	-2.77446	-0.57758
H	-4.96167	-2.88840	-1.18415
C	-2.71916	-2.69141	-1.10051
C	-2.44171	-2.59321	-2.47346
C	-1.14917	-2.34297	-2.96325
C	-0.85016	-2.11607	-4.35822
H	-1.58762	-2.09388	-5.15908
C	0.50417	-1.94373	-4.45309
H	1.09402	-1.74732	-5.34718
C	1.04365	-2.13000	-3.12577
C	2.41670	-2.24768	-2.84950
N	2.12022	-2.60856	-0.39968
N	0.31823	-2.55767	1.74100
N	-1.79113	-2.55967	-0.06433
N	0.01722	-2.33001	-2.19805
C	-0.19153	1.87645	2.55991
H	0.17758	0.88728	2.27834
C	-0.09602	2.35012	3.87352
H	0.33174	1.70914	4.64930
N	-1.22906	4.17273	-0.61523
C	0.08890	4.79135	-0.91087
C	0.86880	3.91134	-1.86834
C	1.80015	4.41857	-2.78232
H	1.96198	5.49840	-2.85416
C	2.51190	3.52230	-3.59356
H	3.24630	3.89366	-4.31502
C	2.25727	2.14846	-3.47260
H	2.78165	1.41321	-4.08929
C	1.30424	1.71839	-2.54299
H	1.05710	0.65969	-2.42269
N	0.62415	2.57742	-1.74896
O	-0.73744	0.15962	-0.56917
Cu	-0.86199	2.12168	-0.45373
N	-0.71012	2.61611	1.54845
C	-0.53935	3.64924	4.15903
H	-0.46756	4.05702	5.17214
C	-1.06970	4.42399	3.11803
H	-1.42193	5.44484	3.29518
C	-1.15168	3.87240	1.83297
C	-1.79840	4.61628	0.68105
C	-2.19809	4.31302	-1.73340
C	-3.24134	3.21569	-1.64742
C	-4.55992	3.37960	-2.08836
H	-4.88902	4.34712	-2.47961
C	-4.96850	1.06975	-1.50496
H	-5.61729	0.19308	-1.42942
C	-3.63890	0.98680	-1.07425
H	-3.21905	0.06202	-0.66760
N	-2.78831	2.03678	-1.14067
C	-5.43813	2.28721	-2.01879
H	-6.47441	2.38947	-2.35568
H	-0.02113	5.82053	-1.30288
H	0.63944	4.86070	0.04576
H	-2.66386	5.31645	-1.74502
H	-1.63243	4.20255	-2.67706
H	-1.71552	5.71239	0.80836
H	-2.87680	4.37217	0.66553
N	0.26653	-0.53899	-0.06805
O	1.19959	0.08585	0.48105
C	-3.57190	-2.74760	-3.44541
C	3.89035	-3.16622	2.94510
C	3.88569	-4.27940	3.81144
H	3.05012	-4.98710	3.77131
C	4.93373	-4.51525	4.71617
H	4.89480	-5.39580	5.36288
C	6.02022	-3.61812	4.77198
C	6.04002	-2.49562	3.91403
H	6.88498	-1.80173	3.97300
C	4.99230	-2.27916	3.01638
H	5.01671	-1.39941	2.36409
C	7.10975	-4.86274	6.50977
H	6.24503	-4.83908	7.19874
H	8.04132	-4.76792	7.08614
H	7.11379	-5.82053	5.95697
C	-4.03321	-1.66891	-4.22665
H	-3.56459	-0.68492	-4.11553
C	-5.08980	-1.81883	-5.14073
H	-5.41988	-0.95489	-5.72368
C	-5.71154	-3.07572	-5.28682
C	-5.26406	-4.16680	-4.50894
H	-5.75169	-5.13920	-4.63391
C	-4.21241	-4.00018	-3.60445
H	-3.87116	-4.85719	-3.01312
C	-7.22872	-2.26020	-6.95640
H	-7.62468	-1.43543	-6.33492
H	-8.04132	-2.68497	-7.56327
H	-6.43565	-1.87095	-7.62175
O	7.09450	-3.74097	5.61333
O	-6.74654	-3.34206	-6.14477
C	-3.03802	-2.19526	3.53670
C	-3.88977	-3.24636	3.93330
H	-3.83876	-4.20697	3.40854
C	-4.79831	-3.09918	4.99476
H	-5.43699	-3.94150	5.27328
C	-4.86642	-1.87353	5.68828
C	-4.01491	-0.81213	5.30847
H	-4.07817	0.13555	5.85341
C	-3.11682	-0.97563	4.25089
H	-2.46701	-0.14146	3.96364
C	-6.60189	-2.65981	7.14688
H	-7.28456	-2.95479	6.32826
H	-7.18609	-2.24138	7.97918
H	-6.04362	-3.54762	7.49801
C	3.41062	-2.10694	-3.95797
C	3.40201	-2.97633	-5.07666
H	2.65314	-3.77368	-5.13291
C	4.34479	-2.85127	-6.09924
H	4.34039	-3.53309	-6.95596
C	5.33382	-1.84394	-6.03675
C	5.36492	-0.97089	-4.92992
H	6.11919	-0.18346	-4.85261
C	4.41248	-1.11426	-3.90738
H	4.44813	-0.43315	-3.04977
C	7.24298	-0.80952	-7.05770
H	6.81942	0.21198	-7.04905
H	7.82417	-0.95784	-7.97918
H	7.90211	-0.94284	-6.17985
O	-5.71246	-1.61085	6.73388
O	6.20814	-1.80489	-7.09000

***bis*-NO LS**

139

Final complex 2 in acetone

Fe	0.23083	-2.49634	-0.24598
C	2.99168	-2.33999	-1.53369
C	4.38497	-2.59362	-1.23598
H	5.18831	-2.59304	-1.97097
C	4.46585	-2.86182	0.10358
H	5.35019	-3.11801	0.68493
C	3.12818	-2.74321	0.64039
C	2.81765	-2.85645	2.00843
C	1.51551	-2.66053	2.50955
C	1.20424	-2.57313	3.91889
H	1.93326	-2.66029	4.72303
C	-0.14392	-2.35609	4.01907
H	-0.74274	-2.24632	4.92202
C	-0.66775	-2.31843	2.67185
C	-2.04113	-2.23340	2.37272
C	-2.53883	-2.34938	1.06136
C	-3.94811	-2.37667	0.73127
H	-4.75903	-2.29350	1.45344
C	-4.03710	-2.52027	-0.62748
H	-4.93488	-2.57083	-1.24209
C	-2.68264	-2.53546	-1.13971
C	-2.37791	-2.48664	-2.51337
C	-1.07212	-2.27333	-2.99719
C	-0.74984	-2.08605	-4.39377
H	-1.47496	-2.08747	-5.20600
C	0.60477	-1.90298	-4.47383
H	1.20478	-1.71990	-5.36374
C	1.13036	-2.03886	-3.13330
C	2.50601	-2.08349	-2.83089
N	2.23144	-2.44468	-0.37841
N	0.36228	-2.48990	1.75607
N	-1.77561	-2.44471	-0.09425
N	0.08635	-2.21633	-2.23149
C	0.08313	2.23358	2.40363
H	0.40464	1.21882	2.15654
C	0.30682	2.77904	3.67250
H	0.79258	2.17512	4.44410
N	-1.21229	4.38481	-0.79483
C	0.08554	4.92928	-1.24725
C	0.75916	3.95618	-2.19830
C	1.59578	4.37830	-3.23813
H	1.75191	5.44815	-3.40814

C	2.22068	3.41787	-4.04723
H	2.87962	3.72591	-4.86492
C	1.97357	2.06095	-3.79509
H	2.43137	1.27295	-4.39954
C	1.11711	1.71540	-2.74468
H	0.88495	0.66976	-2.52518
N	0.51851	2.63602	-1.95010
O	-0.71696	0.27277	-0.34538
Cu	-0.83739	2.29081	-0.52436
N	-0.51325	2.92147	1.39736
C	-0.08744	4.10200	3.91863
H	0.08270	4.56687	4.89475
C	-0.69777	4.82423	2.88373
H	-1.01593	5.86130	3.03035
C	-0.90696	4.20235	1.64601
C	-1.64470	4.90327	0.51780
C	-2.27293	4.43903	-1.82405
C	-3.29319	3.34014	-1.57953
C	-4.64777	3.48381	-1.90275
H	-5.01217	4.43184	-2.31065
C	-5.00036	1.21296	-1.16294
H	-5.63748	0.34387	-0.97795
C	-3.63651	1.14842	-0.85523
H	-3.18678	0.24488	-0.43366
N	-2.78992	2.18657	-1.05626
C	-5.51751	2.40213	-1.69611
H	-6.58056	2.49175	-1.94075
H	-0.01585	5.93170	-1.70817
H	0.72063	5.04733	-0.34903
H	-2.75992	5.43262	-1.87393
H	-1.78981	4.26599	-2.80409
H	-1.53062	6.00279	0.59160
H	-2.72484	4.68612	0.61809
N	0.34845	-4.15589	-0.46592
O	0.90478	-5.11455	-0.87900
N	0.31777	-0.42834	-0.06165
O	1.34846	0.13213	0.33192
C	-3.50175	-2.62941	-3.49262
C	3.91352	-3.15018	2.98321
C	3.88535	-4.32561	3.76309
H	3.05881	-5.03373	3.63645
C	4.89761	-4.62157	4.68984
H	4.84091	-5.54861	5.26628
C	5.97180	-3.72363	4.85775
C	6.01392	-2.53877	4.08881
H	6.84748	-1.84414	4.23563
C	5.00107	-2.26169	3.16782
H	5.04115	-1.33170	2.59018
C	7.00290	-5.09117	6.53772
H	6.10994	-5.12915	7.18896
H	7.90830	-5.03300	7.15884
H	7.04196	-6.00279	5.91291
C	-3.90331	-1.56325	-4.32337
H	-3.39073	-0.59818	-4.24574
C	-4.95798	-1.70008	-5.24101
H	-5.24159	-0.84624	-5.86190
C	-5.63928	-2.93048	-5.34110
C	-5.25432	-4.00737	-4.51151
H	-5.78894	-4.95883	-4.59976
C	-4.20453	-3.85386	-3.60291
H	-3.91217	-4.70008	-2.97128
C	-7.09711	-2.11599	-7.06370
H	-7.45664	-1.24472	-6.48512
H	-7.92451	-2.52701	-7.65989
H	-6.27900	-1.79863	-7.73685
O	7.01157	-3.90278	5.73093
O	-6.67814	-3.18234	-6.19794
C	-3.00535	-2.05673	3.50470
C	-3.91240	-3.07367	3.86641
H	-3.90977	-4.01888	3.31216
C	-4.81130	-2.91425	4.93410
H	-5.49271	-3.73100	5.18611
C	-4.81397	-1.71081	5.66875
C	-3.91065	-0.68180	5.32036
H	-3.92487	0.24984	5.89552
C	-3.02183	-0.85731	4.25693
H	-2.32967	-0.04901	3.99573
C	-6.57195	-2.46442	7.11677
H	-7.27732	-2.70059	6.29847
H	-7.12619	-2.04948	7.97098
H	-6.04853	-3.38709	7.42915
C	3.50069	-1.92493	-3.93778
C	3.56181	-2.84437	-5.01395
H	2.86861	-3.69222	-5.03822
C	4.50475	-2.70386	-6.03433
H	4.55469	-3.42362	-6.85791
C	5.42374	-1.63056	-6.01173
C	5.38300	-0.70553	-4.94836
H	6.08008	0.13538	-4.90479
C	4.43125	-0.86420	-3.92740
H	4.40944	-0.14016	-3.10532
C	7.26983	-0.51692	-7.06375
H	6.77698	0.47198	-7.10935
H	7.87205	-0.66898	-7.97098
H	7.92451	-0.56160	-6.17369
O	-5.64169	-1.44203	6.72691
O	6.30606	-1.58195	-7.05754

(TMPP)Fe^{II}(NO)

95

Fe	-0.022283	0.025569	0.170534
C	2.995722	-0.038785	0.094107
C	4.142632	0.829757	0.064419
H	5.163409	0.515156	0.221960
C	3.687326	2.082146	-0.205030
H	4.262170	2.990937	-0.303561
C	2.253922	1.999327	-0.299248
C	1.427030	3.116177	-0.455927
C	0.033865	3.044867	-0.348610
C	-0.830984	4.195243	-0.380686
H	-0.506726	5.211519	-0.547044
C	-2.092786	3.749602	-0.142160
H	-2.999521	4.331962	-0.075407
C	-2.018383	2.316232	-0.026264
C	-3.138420	1.488286	0.109393
C	-3.059510	0.092813	0.029877
C	-4.214098	-0.757617	-0.102481
H	-5.238331	-0.415439	-0.096427
C	-3.755862	-2.024533	-0.282929
H	-4.332372	-2.922812	-0.445822
C	-2.318941	-1.964133	-0.221489
C	-1.487914	-3.086705	-0.303176
C	-0.098347	-3.005424	-0.170247
C	0.764612	-4.154326	-0.097851
H	0.438167	-5.179735	-0.186672
C	2.026276	-3.692991	0.112717
H	2.935255	-4.267088	0.214602
C	1.949474	-2.256846	0.151978
C	3.068973	-1.424712	0.268635
N	1.840072	0.690782	-0.118801
N	-0.706702	1.895852	-0.143664
N	-1.902712	-0.657316	-0.047188
N	0.642335	-1.844744	-0.024577
N	0.120438	0.029165	1.983374
O	0.932479	-0.343465	2.772123
C	-2.107803	-4.433722	-0.502276
C	2.070607	4.444801	-0.701925
C	2.068414	5.452728	0.270259
H	1.589259	5.270134	1.228136
C	2.678708	6.689655	0.045655
H	2.659275	7.440146	0.827244
C	3.310696	6.937276	-1.179528
C	3.322940	5.936945	-2.164433
H	3.813347	6.141827	-3.111273
C	2.713425	4.711836	-1.924468
H	2.729362	3.948593	-2.697586
C	3.958389	9.153240	-0.545012
H	2.944124	9.482817	-0.289544
H	4.499653	9.976123	-1.013953
H	4.481946	8.846415	0.368444
C	-1.916301	-5.140883	-1.695834
H	-1.317714	-4.699107	-2.487757
C	-2.483331	-6.401432	-1.901009
H	-2.315069	-6.911304	-2.842355
C	-3.261553	-6.982489	-0.891958
C	-3.461288	-6.288002	0.311818
H	-4.061138	-6.751485	1.089189
C	-2.892458	-5.034427	0.499139
H	-3.050302	-4.513780	1.439515
C	-3.685598	-8.957802	-2.177275
H	-4.093982	-8.428280	-3.046436
H	-4.237119	-9.886930	-2.027144
H	-2.627826	-9.186342	-2.354661
O	3.936262	8.102809	-1.508829
O	-3.860511	-8.203869	-0.979765
C	-4.490104	2.109596	0.271650
C	-5.193031	1.974755	1.475343
H	-4.742344	1.425541	2.297432
C	-6.460347	2.536194	1.652353
H	-6.966410	2.413579	2.602752
C	-7.053672	3.249040	0.603076
C	-6.364955	3.388740	-0.612441
H	-6.838760	3.936358	-1.421504
C	-5.104369	2.826684	-0.771406
H	-4.589752	2.935685	-1.721962
C	-9.031946	3.718583	1.867752
H	-9.247738	2.669466	2.103057
H	-9.967723	4.250352	1.690161
H	-8.505430	4.179777	2.711967
C	4.398088	-2.058828	0.531317
C	4.666174	-2.661369	1.774220
H	3.903581	-2.650370	2.547945
C	5.891331	-3.262689	2.032934
H	6.097065	-3.721305	2.995387
C	6.890827	-3.283069	1.047237
C	6.642051	-2.692152	-0.198036
H	7.391685	-2.698986	-0.980712
C	5.404935	-2.089412	-0.441568
H	5.221341	-1.643337	-1.415111
C	9.107000	-3.949720	0.433597
H	8.800431	-4.501999	-0.462872
H	9.930065	-4.475573	0.919447
H	9.436181	-2.943904	0.146190
O	-8.282432	3.836491	0.660511
O	8.056548	-3.897510	1.396113

[(tmpa)Cu^{II}(NO$_2$)]$^+$

44

C	1.777276	-2.540808	0.888299
H	1.333709	-2.579644	1.875153
C	2.683553	-3.505088	0.459913
H	2.974788	-4.306497	1.129695
N	0.101618	0.239174	-1.516887

C	-0.990768	-0.576704	-2.106883
C	-2.240151	-0.466233	-1.260553
C	-3.521996	-0.596580	-1.788363
H	-3.658709	-0.746635	-2.853979
C	-4.614058	-0.529037	-0.923620
H	-5.623588	-0.628450	-1.309663
C	-4.391421	-0.321865	0.437471
H	-5.213140	-0.254650	1.141621
C	-3.081101	-0.192714	0.885714
H	-2.853789	-0.023382	1.931905
N	-2.027778	-0.268710	0.056418
O	-0.079340	0.029224	2.449548
Cu	-0.018795	-0.024587	0.521278
N	1.381551	-1.523116	0.103030
C	3.187801	-3.421385	-0.837232
H	3.887881	-4.163190	-1.208443
C	2.772579	-2.373682	-1.657741
H	3.137550	-2.279493	-2.675074
C	1.876263	-1.436836	-1.149299
C	1.445124	-0.225284	-1.944066
C	-0.081321	1.690722	-1.779428
C	0.640898	2.510106	-0.732658
C	1.151440	3.780455	-0.985954
H	1.085956	4.205757	-1.981856
C	1.808452	3.899208	1.326200
H	2.260975	4.414755	2.165918
C	1.285313	2.620686	1.495254
H	1.308522	2.110021	2.451821
N	0.715327	1.941776	0.486908
C	1.741797	4.486127	0.062749
H	2.147452	5.478495	-0.107176
H	-1.183741	-0.287299	-3.146440
H	-0.654436	-1.619518	-2.115078
H	0.247926	1.949760	-2.792225
H	-1.153556	1.906524	-1.720725
H	1.469164	-0.423841	-3.021680
H	2.150725	0.589924	-1.750019
N	-0.506911	-0.954104	3.190115
O	-0.853581	-1.964382	2.587114

6.6. References for Supporting Information

(1) Gaussian 09 Revision A.2 Frisch, M. J.; Trucks, G. W.; Schlegel, H. B., Scuseria, G. E., Robb, M. A., Cheeseman, J. R., Scalmani, G., Barone, V., Mennucci, B., Petersson, G. A., Nakatsuji, H., Caricato, M., Li, X., Hratchian, H. P., Izmaylov, A. F., Bloino, J., Zheng, G., Sonnenberg, J. L., Hada, M., Ehara, M., Toyota, K., Fukuda, R., Hasegawa, J., Ishida, M., Nakajima, T., Honda, Y., Kitao, O., Nakai, H., Vreven, T., Montgomery, Jr., J. A., Peralta, J. E., Ogliaro, F., Bearpark, M., Heyd, J. J., Brothers, E., Kudin, K. N., Staroverov, V. N., Kobayashi, R., Normand, J., Raghavachari, K., Rendell, A., Burant, J. C. Iyengar, S. S. Tomasi, J. Cossi, M. Rega, Millam, N. J., Klene, M. Knox, J. E., Cross, J. B., Bakken, V., Adamo, C., Jaramillo, J., Gomperts, R. E. Stratmann, O. Yazyev, A. J. Austin, R. Cammi, C. Pomelli, J. W. Ochterski, R. Martin, R. L., Morokuma, K., Zakrzewski, V. G., Voth, G. A., Salvador, P., Dannenberg, J. J., Dapprich, S., Daniels, A. D., Farkas, O., Foresman, J. B., Ortiz, J. V., Cioslowski, J., and Fox, D. J. Gaussian, Inc., Wallingford CT **2009.**

(2) Becke, A. D. *Phys. Rev. A At. Mol. Opt. Phys.* **1988**, *38*, 3098.

(3) Perdew, J. P. *Phys. Rev. B Condens. Matter Mater. Phys.* **1986**, *33*, 8822.

(4) Ditchfield, R.; Hehre, W. J.; Pople, J. A. *J. Chem. Phys.* **1971**, *54*, 724.

(5) Hariharan, P. C.; Pople, J. A. *Theor. Chim. Acta* **1973**, *28*, 213.

(6) Hariharan, P. C.; Pople, J. A. *Mol. Phys.* **1974**, *27*, 209.

(7) Francl, M. M.; Pietro, W. J.; Hehre, W. J.; Binkley, J. S.; Gordon, M. S.; DeFrees, D. J.; Pople, J. A. *J. Chem. Phys.* **1982**, *77*, 3654.

(8) Rassolov, V. A.; Pople, J. A.; Ratner, M. A.; Windus, T. L. *J. Chem. Phys.* **1998**, *109*, 1223.

(9) Rassolov, V. A.; Ratner, M. A.; Pople, J. A.; Redfern, P. C.; Curtiss, L. A. *J. Comput. Chem.* **2001**, *22*, 976.

(10) Hehre, W. J.; Ditchfield, R.; Pople, J. A. *J. Chem. Phys.* **1972**, *56*, 2257.

(11) Hehre, W. J.; Ditchfield, R.; Pople, J. A. *J. Chem. Phys.* **1972**, *56*, 2257.

(12) Hariharan, P. C.; Pople, J. A. *Theor. Chim. Acta* **1973**, *28*, 213.

(13) Hariharan, P. C.; Pople, J. A. *Mol. Phys.* **1974**, *27*, 209.

(14) Gordon, M. S. *Chem. Phys. Lett.* **1980**, *76*, 163.

(15) Francl, M. M.; Pietro, W. J.; Hehre, W. J.; Binkley, J. S.; DeFrees, D. J.; Pople, J. A.; Gordon, M. S. *J. Chem. Phys.* **1982**, *77*, 3654.

(16) Binning, R. C. J.; L. A. Curtiss *J. Comput. Chem.* **1990**, *11*, 1206.

(17) Blaudeau, J.-P.; McGrath, M. P.; Curtiss, L. A.; Radom, L. *J. Chem. Phys.* **1997**, *107*, 5016.

(18) Rassolov, V. A.; Ratner, M. A.; Pople, J. A.; Redfern, P. C.; Curtiss, L. A. *J. Comput. Chem.* **2001**, *22*, 976.

(19) Handy, N.C.; Cohen, A.J. *Mol. Phys*., **2001**, *99*, 403.

(20) Hoe, W.-M.; Cohen, A.J.; Handy, N.C. *Chem. Phys. Lett*., **2001**, *341*, 319.

(21) Lee, C.; Yang, W.; Parr, R.G. *Phys. Rev. B*, **1988**, *37*, 785.

(22) Miehlich, B.; Savin. A.; Stoll, H.; Preuss, H. *Chem. Phys. Lett*., **1989**, *157*, 200.

Chapter 5:

A Heme/Copper Hyponitrite Species, a Possible Intermediate during Nitric Oxide Reductive Coupling Catalyzed by Cytochrome *c* Oxidase (C*c*O)

This work was accomplished with the aid of the following collaborators:

Ryan E. Cowley, Maxime A. Siegler, Edward I. Solomon, and Kenneth D. Karlin

1. Introduction

Nitric oxide reductase (NOR) is a heme-containing enzyme that catalyzes the two-electron reduction of nitric oxide (NO) to nitrous oxide (N_2O) and this reaction plays a crucial role in the bacterial denitrificatin.[1] The active site of NOR is a dinuclear iron center which consists of a mono-histidine ligated five-coordinate heme and a tris-imidazole ligated distal non-heme Fe_B (Figure 1).[2]

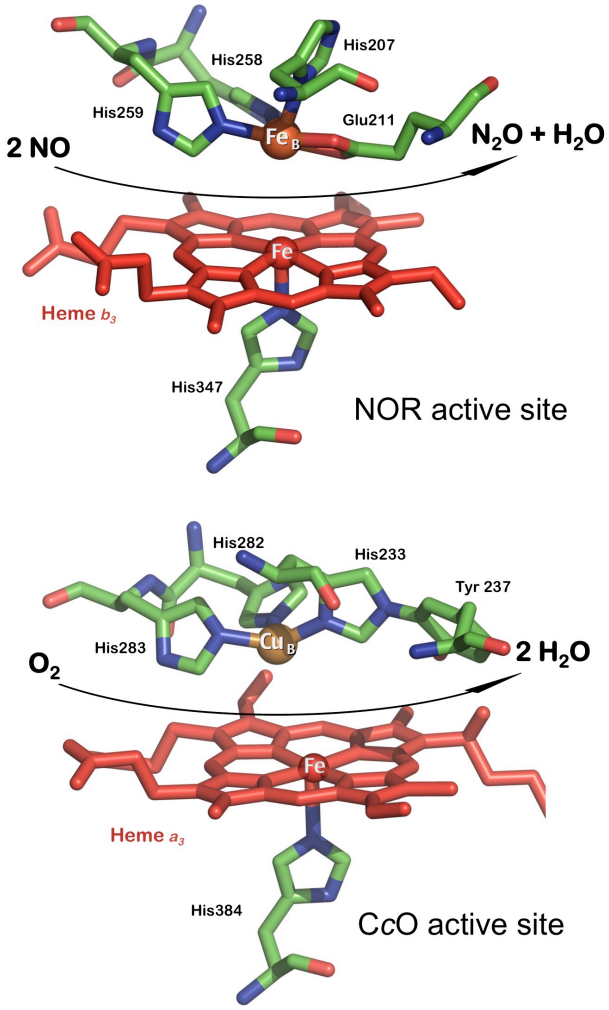

Figure 1. Structures of the bimetallic active sites of: (*top*) NOR presented based on PDB code 3O0R and (*bottom*) C*c*O displayed based on PDB code 1XME.

This active site is structurally homologous to the oxygen reduction site in the enzyme, cytochrome *c* oxidase (C*c*O), where Cu_B occupies the non-heme distal position.[3] Also, a glutamic acid residue coordinates to the Fe_B center in NOR while the tyrosine residue common in C*c*O is absent (Figure 1).[4]

Cytochrome *c* oxidase is the terminal enzyme of the electron transport chain and thus the major site of four-electron reduction of molecular oxygen (O_2) to water in the cell and assists to establish a transmembrane proton gradient that eventually drives ATP production.[5]

NOR and C*c*O are believed to be distant relatives and both are classified as members of the heme-copper oxidase superfamily and are thought to originate from the same progenitor protein.[6] Interestingly, it is also known that some Heme/Cu oxidases and NORs reduce both O_2 and $NO_{(g)}$ with different selectivity.[3a,7] Certain C*c*Os are known to catalyze the reduction of nitric oxide to nitrous oxide as well,[8] a reaction that involves the formation of a N–N bond and cleavage of a N–O bond:

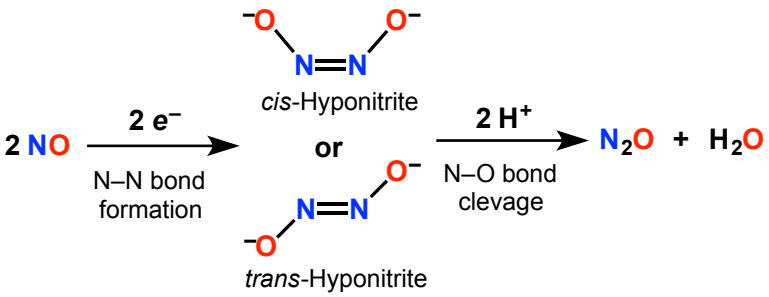

Apparently, two nitric oxide molecules come together at the bimetallic active site and consume two electrons and two protons to form one molecule of nitrous oxide and one water molecule. A full elucidation of the electronic and structural configurations of various intermediates is of great importance to understand the mechanism by which the

enzymes catalyze the formation and cleavage of the N–N and N–O bonds, respectively.[9] However, the molecular mechanism of the reduction of nitric oxide to nitrous oxide by both NOR and C*c*O are poorly understood because of the lack of detection and structural information concerning the short-lived intermediate species.

According to DFT calculations and biophysical studies, all three most commonly discussed mechanisms[10] (Scheme 1) include the coupling of two nitric oxide molecules at the fully reduced binuclear active site followed by the formation of a putative hyponitrite intermediate prior to the generation of nitrous oxide and the resting oxo-briged binuclear active site.[1c,9,11]

Scheme 1. Proposed Intermediates for the Three Putative Mechanisms of Nitric Oxide Reduction by NOR and C*c*O.

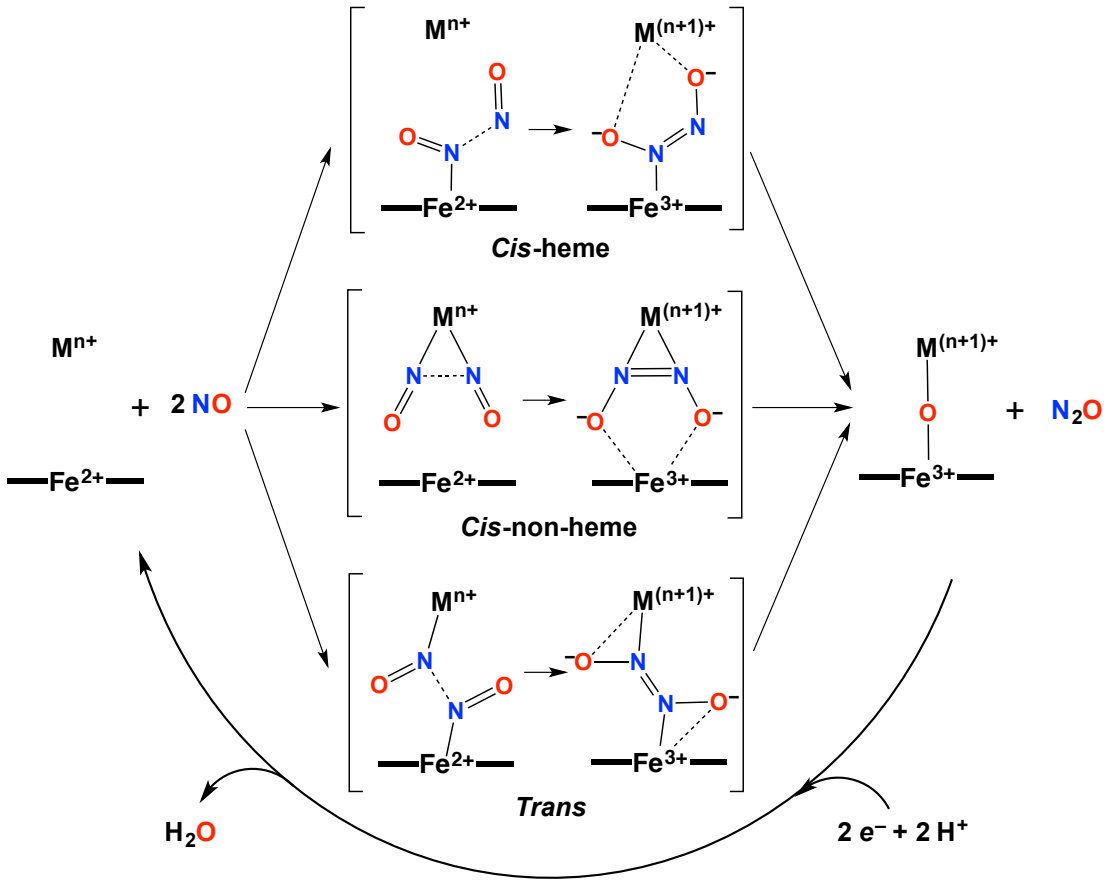

2. Heme/Copper Assemblies Reaction with Hyponitrite ($N_2O_2^{2-}$)

Clearly, synthetic biomimetic model complexes have a vital role to play in providing a straightforward and controlled approach toward understanding the mechanism of this chemical transformation occurring at either enzyme active site.

Previous studies from our research group have demonstrated the nitric oxide reductase activity of some heme-copper synthetic complexes, which resemble heme-copper oxidases, including C*c*O. In our initial study, a dinitrosyl complex (^{6}L)$Fe^{II}(NO)_2$ (^{6}L is a binucleating ligand; also, see below) was reacted with a cuprous ion source and 2 equiv acid to afford nitrous oxide (N_2O) in very good yield (80% based on GC measurements).[12] Later we also reported a similar nitric oxide reductive coupling reaction where a 1:1 mixture of a heme $(F_8)Fe^{II}$ and a copper complex $[(TMPA)Cu^{I}(MeCN)]^+$ are employed as component complexes providing electrons.[13]

The suggested steps in the chemistry described here are as follows: Initially, there occurs attack of the cuprous complex moiety on the second nitric oxide ligand in the heme-dinitrosyl fragment. This may lead to the release of one $NO_{(g)}$ molecule, which now attacks a binuclear heme-$Fe^{II}(NO)\ldots Cu^{I}$ species to form a hyponitrite-type intermediate. Then, protonation, electron-transfer from the copper ion and N–O cleavage may take place in three consecutive steps generating nitrous oxide and water, and the heme-Fe^{III} and Cu^{II} complexes observed. Thus, our heme-copper assemblies efficiently effect reductive coupling of nitric oxide molecules in the same stoichiometry as is known for C*c*O. Since, the formation of a hyponitrite ($N_2O_2^{2-}$) dinuclear intermediate has been postulated and also supported by the structural, spectroscopic, and theoretical studies for

the present systems, we wish to generate and stabilize a possible hyponitrite species that may allow us to deduce details of the coordination chemistry involved.

Using hyponitrous acid ($H_2N_2O_2$) and fully oxidized binuclear complex [(^{6}L)Fe^{III}–O–Cu^{II}][B(C_6F_5)$_4$], we attempted to generate and stabilize a synthetic binuclear heme/Cu hyponitrite ($N_2O_2^{2-}$) species, the proposed short-lived intermediate existing during the $NO_{(g)}$ reductive coupling catalyzed by C*c*O and NOR (Scheme 2). The results indicated that hyponitrous acid ($H_2N_2O_2$) easily breaks the μ-oxo bond of [(^{6}L)Fe^{III}–O–Cu^{II}]$^+$ in the dark at RT, forming the nitrosyl species [(^{6}L)Fe^{II}(NO)...Cu^{II}(OH)]$^+$ when the reaction was carried out with either 1:1 or ½:1 ratio of $H_2N_2O_2$ and [(^{6}L)Fe^{III}–O–Cu^{II}]$^+$ (Scheme 2). The product of the reaction, [(^{6}L)Fe^{II}(NO)...Cu^{II}(OH)][B(C_6F_5)$_4$], was characterized by UV–vis (Figure S1), IR (Figure S2, $\nu_{(NO)}$ = 1685 cm^{-1}) and EPR (Figure S3) spectroscopies as well as ESI mass spectrometry (*m/z* = 1248.3) and elemental analysis. See Supporting Information for additional details.

Scheme 2. Reaction of the Fully Oxidized Binuclear Complex [(^{6}L)Fe^{III}–O–Cu^{II}]$^+$ and Hyponitrous Acid ($H_2N_2O_2$).

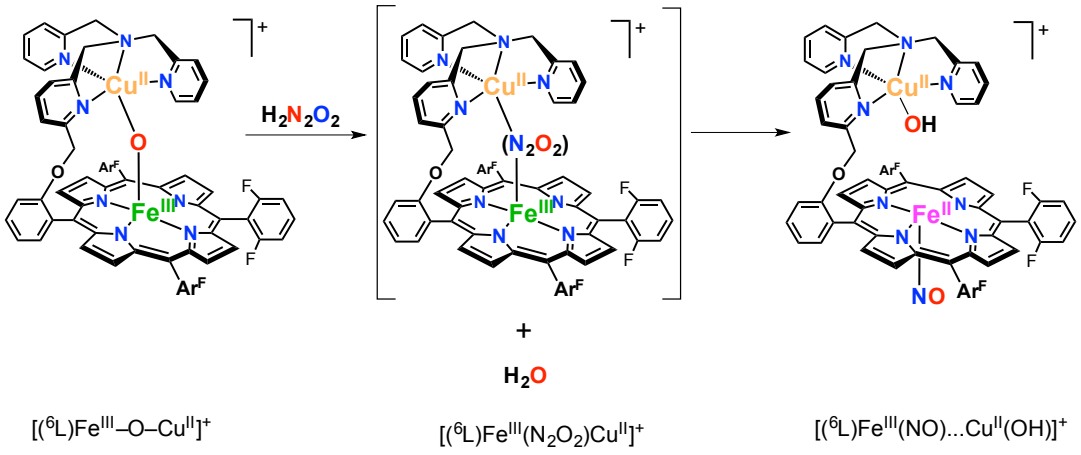

As only half an equivalent of the hyponitrous acid is required for this redox reaction with the μ-oxo complex $[(^6L)Fe^{III}–O–Cu^{II}]^+$, the heme center is exclusively involved in the redox reaction and not the cupric component, pointing to the fact that here hyponitrite bridge may form between two heme centers of neighboring molecules forming a $[(OH)Cu^{II}(^6L)Fe^{III}(N_2O_2)Fe^{III}(^6L)Cu^{II}(OH)]^{2+}$ intermediate. This can be followed by two electron transfers from the bridging hyponitrite to the ferric centers and eventual formation of the ferrous heme nitrosyl product, $[(^6L)Fe^{II}(NO)...Cu^{II}(OH)][B(C_6F_5)_4]$.

In addition, UV–vis monitoring of stoichiometric reactions of the hyponitrous acid with the related μ-oxo porphyrin–iron(III) dimer compounds, $[(F_8)Fe^{III}]_2O$ or $[(TMPP)Fe^{III}]_2O$ in toluene revealed no reaction even after several hours of stirring.

In a second set of experiments, in order to generate and stabilize the proposed hyponitrite intermediate, reactions of silver hyponitrite ($Ag_2N_2O_2$) with chloride precursors/complexes were carried out. In our first approach, the reaction of the fully-oxidized binuclear heme/Cu complex, $[(^6L)Fe^{III}(Cl)...Cu^{II}(Cl)][B(C_6F_5)_4]$ (Figures S4 and S5), and silver salt in THF resulted in formation of heme ferrous nitrosyl compound, $[(^6L)Fe^{II}(NO)Cu^{II}(Cl)]^+$, confirmed by UV–vis (Figure S6), IR ($\nu_{(NO)}$ = 1685 cm^{-1}) and EPR (Figure S7) spectroscopies and ESI mass spectrometry (*m/z* = 1222.2). See Supporting Information for additional details.

The separate reactions of the ferric or cupric mononuclear complexes with silver hyponitrite were also studied. Reaction of half an equivalent of $Ag_2N_2O_2$ with the ferric heme chloride complexes $[(F_8)Fe^{III}(Cl)]$ or $[(TMPP)Fe^{III}(Cl)]$, led to generation of the

corresponding ferrous heme nitrosyl compounds, $[(F_8)Fe^{II}(NO)]$ or $[(TMPP)Fe^{II}(NO)]$, which was confirmed by UV–vis, IR and EPR spectroscopies (Figures S8, S9 and S10, see Supporting Information). Interestingly, in turn, reaction of half an equivalent of the silver hyponitrite with the cupric precursor $[(tmpa)Cu^{II}(Cl)][B(C_6F_5)_4]$ in MeOH resulted in formation of a hyponitrite bridged complex, $[(tmpa)Cu^{II}(ONNO)Cu^{II}(tmpa)]$-$[B(C_6F_5)_4]_2$ which was characterized by UV–vis (Figure S11), EPR (Figure S12), IR (Figure S15), ^{1}H-NMR (Figure S21), resonance Raman (Figure S16) spectroscopies as well as ESI mass spectrometry and elemental analysis. See Supporting Information for details.

This complex shows a d–d band at 875 nm and a shoulder at 682 nm in MeOH (Figure S11), characteristic of Cu(II) ion in a trigonal bypyramidal (TBP) coordination geometry. It is also stable in different alcohols at RT due to the presence of hydrogen bonding interaction with the solvent molecules. However, in the absence of hydrogen bond donation in other organic solvents including THF, MeTHF, MeCN, acetone, etc., it rapidly decomposes to a mixture of different cuprous and cupric species (i.e., $[(tmpa)Cu^{I}(solvent)][B(C_6F_5)_4]$ and $[(tmpa)Cu^{II}(NO_2)][B(C_6F_5)_4]$), as identified by UV–vis Spectroscopy (Figure 2); the copper(I) complex was identified by bubbling the product solution with O_2 which led to the formation of UV–vis absorptions characteristic of the expected trans-peroxo-dicopper(II) species. These observations can be explained as follows: when the hyptonitrite complex is dissolved in a non-hydrogen bonding solvent, electron transfer from the bridging hyponitrite to the cupric centers occurs leading to transient formation of cuprous nitrosyl complex in which the nitric oxide ligand is known to reductively disproportionate to N_2O and nitrite[1b] as shown below, eq 1:

$$3\ NO_{(g)} + \text{ligand-}Cu^{I} \rightarrow N_2O_{(g)} + \text{ligand-}Cu^{II}(NO_2^-) \quad (1)$$

Based on pulse radiolysis studies, one-electron reduction of aqueous $NO_{(g)}$ occurs through the formation of the nitroxyl anion, NO^-, which rapidly concatenates two more molecules of $NO_{(g)}$. Then nitrosyl hyponitrite anion slowly decays ($\tau \approx 3$ ms at 25 ^oC) to the final products.[14] The overall reactions are represented by eqs 2, 3 and 4:

$$NO^- + NO_{(g)} \rightarrow N_2O_2^- \quad \text{(hyponitrite radical)} \quad (2)$$

$$N_2O_2^- + NO_{(g)} \rightarrow N_3O_3^- \quad \text{(nitrosyl hyponitrite)} \quad (3)$$

$$N_3O_3^- \rightarrow N_2O_{(g)} + NO_2^- \quad (4)$$

For the protonated NO^-, HNO, the same reaction sequence occurs but only the first step is much slower. Thus, hyponitrite radical ($N_2O_2^-$) and nitrosyl hyponitrite anion ($N_3O_3^-$) may also be important intermediates in reductive disproportionation happening at a copper center.

UV–vis monitoring after re-dissolution of $[(tmpa)Cu^{II}(ONNO)Cu^{II}(tmpa)][B(C_6F_5)_4]_2$ in THF (Figure 2) shows transient formation of a compound, possibly a Cu^{I}–NO complex or a Cu^{II}–hyponitrite radical species, which finally converts to a mixture of final products, $[(tmpa)Cu^{I}(solvent)]^+$ and $[(tmpa)Cu^{II}(NO_2)]^+$. Electron paramagnetic resonance (EPR) measurements of the dicopper-hyponitrite complex in THF reveal the decay of the cupric signal intensity over time consistent with its gradual conversion to copper(I) (Figures S13 and S14, see Supporting Information).

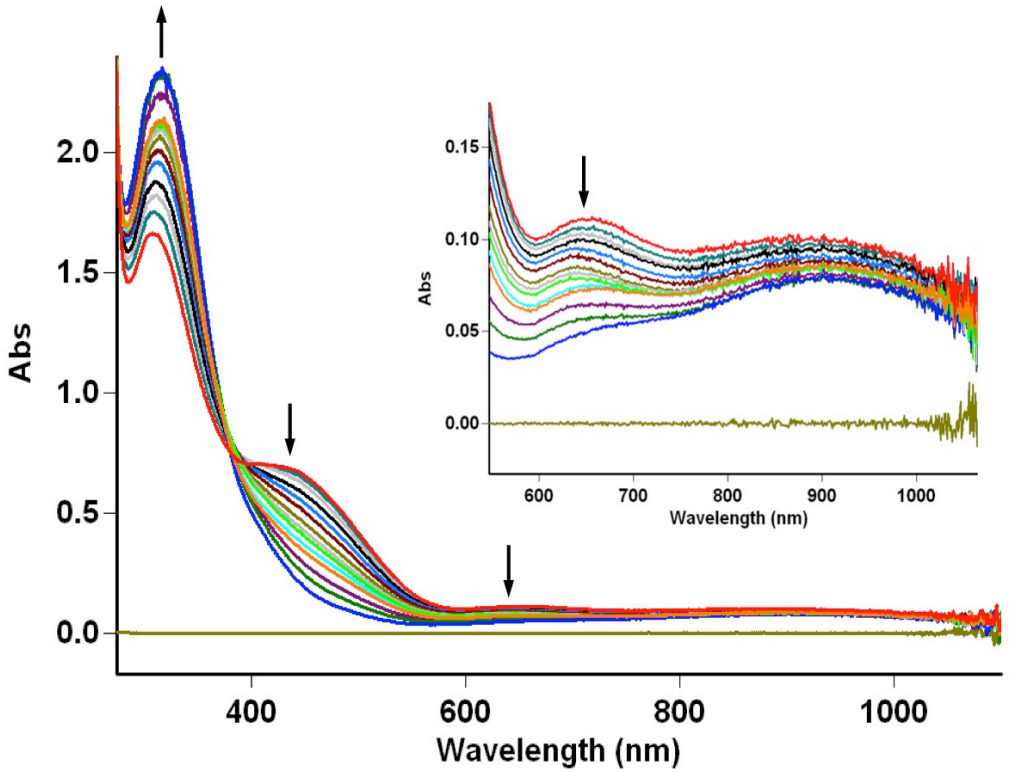

Figure 2. (a) UV−vis spectra of $[(tmpa)Cu^{II}(ONNO)Cu^{II}(tmpa)][B(C_6F_5)_4]_2$ right after dissolution in THF (red, λ_{max} = 308, 420, 656 and 890 nm) and after 30 min (blue, λ_{max} = 317 and 910 nm) (2 mM in a 2-mm cuvette at RT).

For comparison, addition of $NO_{(g)}$ to a solution of $[(tmpa)Cu^{I}(MeCN)]^{+}$ in THF at –80 ^{o}C was also monitored, where formation of an intermediate species were observed (λ_{max} = 311, 400, 627 and 845 nm; this intermediate converts to another species, λ_{max} = 304, 413, 650 and 856 nm exhibiting spectral features very similar to those of the cupric nitrite complex, $[(tmpa)Cu^{II}(NO_2)]^{+}$, Figure S17, see Supporting Information). The spectral resemblence between the intermediate generated from re-dissolution of $[(tmpa)Cu^{II}(ONNO)Cu^{II}(tmpa)]^{+}$ in THF and the intermediate formed by reaction of cuprous complex and $NO_{(g)}$ further supports the involvement of the Cu^{I}–NO/Cu^{II}–hyponitrite radical species in copper mediated reductive $NO_{(g)}$ disproportionation.

Attempts at recrystallization of the isolated complex $[(tmpa)Cu^{II}(ONNO)Cu^{II}(tmpa)][B(C_6F_5)_4]_2$ in different alcohols using slow evaporation by Ar flow or cooling up to –80 ^{o}C were not successful due to the high solubility of the compound and only resulted in formation of amorphous solids. Also, vapor or liquid/liquid diffusion using different antisolvents such as diethylether promoted the redox chemistry where reductive $NO_{(g)}$ disproportionation took place generating a mixture of the cuprous complex and $[(tmpa)Cu^{II}(NO_2)]^{+}$.

However, when using perchlorate as counter anion, $[(tmpa)Cu^{II}(ONNO)Cu^{II}(tmpa)](ClO_4)_2$ crystalized in MeOH at –35 ^{o}C (see Supporting Information); the X-ray crystal structure is depicted in Figure 3 revealing that the bridging *trans*-$N_2O_2^{2-}$ ligand is bound to each cupric center via the η^1-O binding mode. The N–N and N–O bond lengths of 1.257(3) and 1.361(2) Å within the hyponitrite moiety support the notion of an N=N double and N–O single bonds, respectively (cf., 1.256(2) and 1.3622(11) Å in *trans*-$Na_2N_2O_2$).[15] The distance between the cupric centers is 5.56 Å which is shorter than that reported 6.7 Å for Fe centers in the related synthetic hyponitrite-bridged heme complex, $[(OEP)Fe]_2(\mu$-$N_2O_2)$,[16] but still longer than the 4.7–5.1 Å distance between the Cu and Fe centers in the active site of *T. thermophilus* cyt ba_3[17] which is known to exhibit NOR activity.

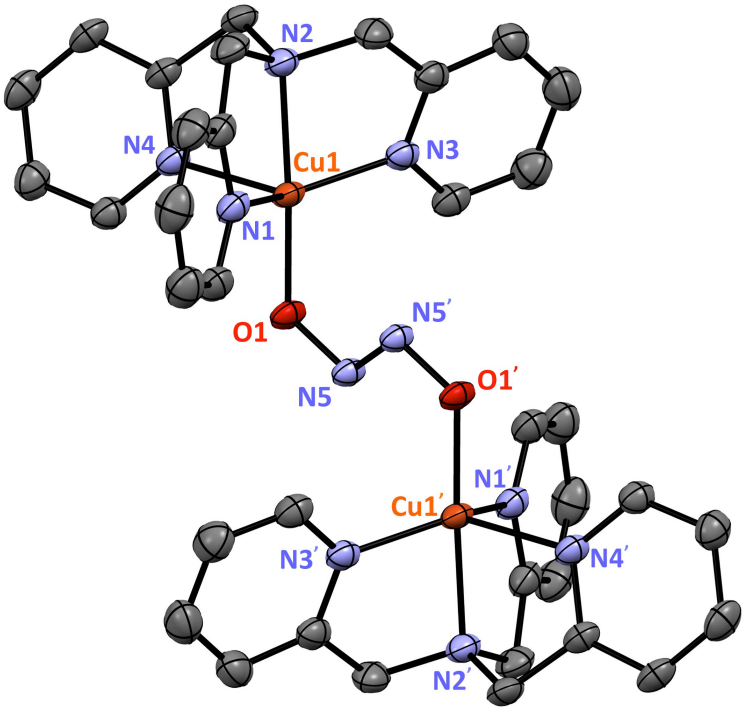

Figure 3. Displacement ellipsoid plot (50% probability level) of the cationic portion of $[(tmpa)Cu^{II}(ONNO)Cu^{II}(tmpa)](ClO_4)_2$ at 110(2) K. Perchlorates and hydrogen atoms have been omitted for clarity. Selected bond lengths (Å) and angles (deg): Cu1–O1, 1.9114(14); Cu1–N1, 2.0304(19); Cu1–N2, 2.0575(17); Cu1–N3, 2.0231(19); Cu1–N4, 2.1499(17); Cu1···N5′, 2.8506(16); N5–O1, 1.361(2); N5–N5′, 1.257(3); O1−Cu1−N2, 174.58(7); N1−Cu1−N3, 140.20(7); N1−Cu1−N4, 99.21(7); N3−Cu1−N4, 113.81(7); Cu1−O1–N5, 120.53(11); N5′−N5−O1, 112.23(19); Cu1···Cu1′, 5.5647(5). (The prime symbol is for the symmetry operation, ⅔ –x, ⅓–y, ⅓–z).

Comparison of the coordination geometry around the pentacoordinated cupric centers of the chloride precursor, $[(tmpa)Cu^{II}(Cl)]^+$, and hyponitrite-bridged cupric complex, $[(tmpa)Cu^{II}(ONNO)Cu^{II}(tmpa)]^+$, shows that cupric center adopts a perfect trigonal bipyramidal (TBP) structure (τ = 1.0) in the former[18] while it adjusts to a very distorted TBP geometry (τ = 0.57) in the latter compound (Figure 3). A closer analysis of the crystal structure of $[(tmpa)Cu^{II}(ONNO)Cu^{II}(tmpa)]^{2+}$ points to existence of an interaction between the copper center and the remote nitrogen of the bridging hyponitrite

ligand (i.e., Cu1···N5' distance is about 2.851 Å and the pyridyl arm trans this nitrogen group of the bridging hyponitrite is elongated to 2.1499 Å compared to other Cu–N bonds of the TMPA scaffold (Figure 3)).

The weak interaction between the cupric center and the remote nitrogen atom of the bridging hyponitrite moiety in $[(tmpa)Cu^{II}(ONNO)Cu^{II}(tmpa)]^{2+}$ can be responsible for the unique redox behavior of this cupric hyponitrite complex in aprotic solvents. This interaction may get strengthened in aprotic solutions (in the absence of hydrogen bonds) resulting in weakening of the Cu–N4 bond to such an extent that the pyridine arm dissociation occurs which can promote the reduction of the metal center and breakage of the N–N bond to generate a Cu^{I}–NO species may be due to the fact that minimum entropic rearrangement is required upon reduction (Scheme 3). Examples of cuprous TMPA complexes with a "dangling" uncoordinated pyridyl arm are known.[19]

Scheme 3. Proposed Mechanism for Conversion of $[(tmpa)Cu^{II}(ONNO)Cu^{II}(tmpa)]^{2+}$ to $2[(tmpa)Cu^{I}(NO)]^{+}$ in Aprotic Solvents.

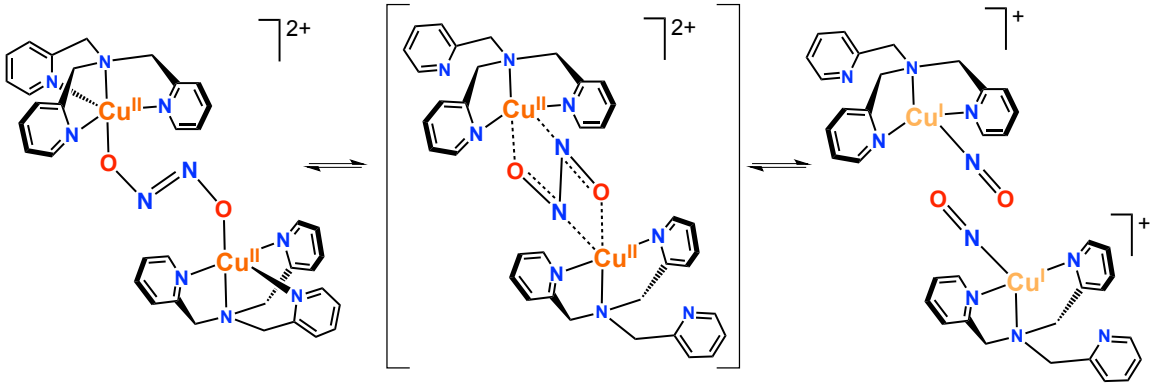

EPR measurement on $[(tmpa)Cu^{II}(ONNO)Cu^{II}(tmpa)]^{2+}$ in MeOH (Figure S12) reveals a typical distorted axial spectrum of copper(II) complex at high field spectra. However, the spectra shows the characteristic signal of a dinuclear species at g = 4.1 (Figure S12, see Supporting Information), due to formally spin-forbidden "half-field" $\Delta M_S = \pm 2$ transitions, and broad lines in the high field part of the spectra (g = 2), which suggest a spin coupling between the two copper ions. These features are interpreted as arising from triplet state phenomena occurring as the result of dimer structure and a weak dipole–dipole interaction due to the large distance between the two copper(II) centers, as also found in similar reported cases.[20] EPR spectra of the complex in frozen THF also give weak "half-field" signals; the spectra are clearly dominated by a spin-triplet dimer (Figures S13 and S14, see Supporting Information). The EPR spectra of the dicopper-hyponitrite complex in either MeOH or THF thus both exhibit Cu(II) species in a TBP geometry, however the g and A values are different (Figure 4; see Supporting Information for further details), suggesting that there are coordination differences at the copper ion in these two solvents (Figure 4).

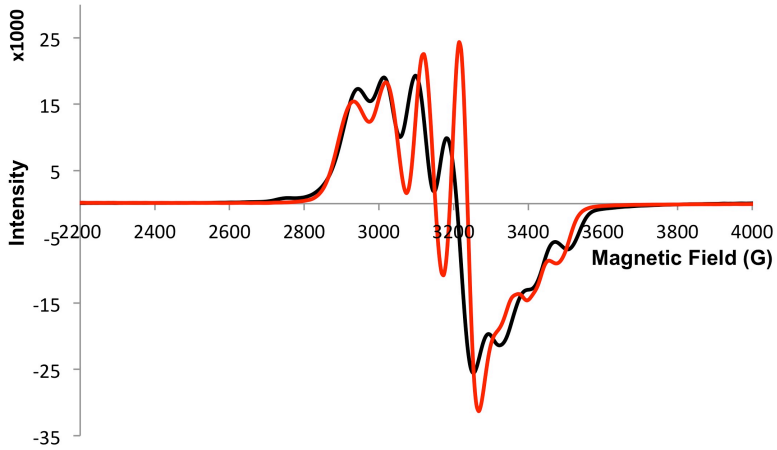

Figure 4. Comparison of EPR spectra of $[(TMPP)Fe^{III}(ONNO)Cu^{II}(tmpa)][B(C_6F_5)_4]$ in MeOH (black) and THF (red). See Suporting Information for details.

The triplet ground state ascribed to $[(tmpa)Cu^{II}(ONNO)Cu^{II}(tmpa)]^{2+}$ by its EPR was also further confirmed with ^{1}H-NMR spectroscopy. As expected, the observed ligand peaks are broad and downfield-shifted and move further downfield, with broadening as the temperature decreases (Figure S21, see Supporting Information) exhibiting an apparent Curie-type temperature dependence. The peaks could be assigned by comparison with values reported for paramagnetic mono-nuclear cupric complexes of the TMPA family (see Supporting Information).[21]

Vibrational spectroscopies were also employed to further characterize this cupric hyponitrite complex. The IR spectrum of $[(tmpa)Cu^{II}(ONNO)Cu^{II}(tmpa)]^{2+}$ reveals no isotope sensitive band upon ^{15}N-labeling of the bridging *trans*-hyponitrite moiety (Figure S15, see Supporting Information), presumably due to centro-symmetric structure of the binuclear complex. The resonance Raman spectrum of this complex in MeOH features an isotope sensitive band at 1085 cm^{-1} which is assignable to the N=N stretch (Figure S16, see Supporting Information). This stretching frequency is in agreement with the theoretical value calculated for a geometry-optimized structure (the N=N bond length from 1.26 to 1.29 Å) for a triplet state, $\nu_{(N=N)}$ = 1076 cm^{-1}. This low value for an N=N stretch compared to those reported for other hyponitrite compounds,[9a,16,22] (see Table 1 for relevant comparisons), points to the fact that in MeOH, the presence of the hydrogen bonds slightly weakens the N=N bond by removal of electron density from the bridging hyponitrite moiety.

Table 1. Vibrational spectroscopic data for some hyponitrite compounds.

Compound	$\nu_{(N=N)}$ (cm^{-1})	$\nu_{as(N-O)}$ (cm^{-1})	$\nu_{s(N-O)}$ (cm^{-1})	Ref
cis-N_2O_2 (gas)		1788[a]	1860[a]	22a
cis-$Na_2N_2O_2$	1314[a]	1047[a]	830[a]	22b
trans-$Na_2N_2O_2$	1392[b]	1035[a]	958[b]	22c
trans-$Ag_2N_2O_2$		1058 [a]		22c
trans-[(OEP)Fe^{III}]$_2$(ONNO)		982[a]		16
trans-[Ph_3Sn]$_2$(ONNO)		1006[a,c]		22d
cis-Pt(PPh_3)$_2$(κ^2-O_2N_2)	1263[a,c]	1001[a,c]	901[a,c]	22e
cis-Pt(PPh_2Me)$_2$(κ^2-O_2N_2)	1286[a,c]	981[a,c]	852[a,c]	22e
cis-Pt(dppf)(κ^2-O_2N_2)	1330[a,c]	974[a,c]	890[a,c]	22e
cis-(bipy)Ni(κ^2-O_2N_2)	1265[a,c]		937[a,c]	22f
cis-[{(bipy)Ni(κ_2-O_2N_2)}η^1:η^1-*N,N*-{Ni(NO)(bipy)}$_2$]$^{2+}$	-	-	-	23
cis-[$(NH_3)_5$Co{μ-N(O)NO}Co$(NH_3)_5$]$^{4+}$	1391[a] 1368[b]	1124[a] 1149[b]	916[a] 933[b]	22g
cis- or *skew*-[$Co_2(CN)_{10}$(μ-N_2O_2)]$^{6-}$	1336,1399[a]	1043[a]	831[a]	22h
trans-[$Ru_2(CO)_4$(μ-H)(μ-P^{t}Bu$_2$)(μ-dppm)(μ-ONNO)]	1482[a]	1099[a]	1025[a]	22i
cis-[(TpRu)$_2$(μ-Cl)(μ-pz){μ-N(=O)−N(=O)-κ^2}		1605[a]		22j
Heme/Cu_B *caa$_3$* oxidoreductase	1330[b]			22k
Heme/Cu_B *ba$_3$* oxidoreductase	1334[b]			9a
Heme *b$_3$*/Fe_B nitric oxide reductase	1332[b]			22l
trans-[(tmpa)Cu^{II}(ONNO)Cu^{II}(tmpa)]$^{2+}$	1085[b]			This work

[a] IR Spectroscopy

[b] Resonance Raman Spectroscopy

[c] The original publications report only IR frequencies, but not assignments.

OEP: octaethylporphyrinate(2−); dppf: 1,1'-bis(diphenylphosphino)ferrocene; dppm: 1,1-bis(diphenylphosphino)methane; Tp: hydridotris(pyrazolyl)borate; tmpa: tris(2-pyridylmethylamine).

Treatment of the ferric heme complex, [(TMPP)Fe^{III}($THF)_2$](SbF_6)[24] with excess (20 equiv) of the dicopper-hyponitrite complex, [(tmpa)Cu^{II}(ONNO)Cu^{II}(tmpa)]$^{2+}$, at −100 °C afforded formation of a new intermediate species, as monitored by UV−vis

spectroscopy (Figure 5). Upon warming to RT, this intermediate, formulated as $[(TMPP)Fe^{III}(ONNO)Cu^{II}(tmpa)]^{+}$, converts to a μ-oxo complex $[(TMPP)Fe^{III}–O–Cu^{II}(tmpa)]^{+}$ [24] in 97% yield with evolution of N_2O in a 88% yield (Scheme 4 and see Supporting Information). As observed by UV–vis monitoring, in the presence of excess dicopper-hyponitrite complex, the starting ferric heme isosbestically converts to the heme/Cu hyponitrite intermediate (Figure S18, see Supporting Information) and this binding appears to be an equilibrium process.

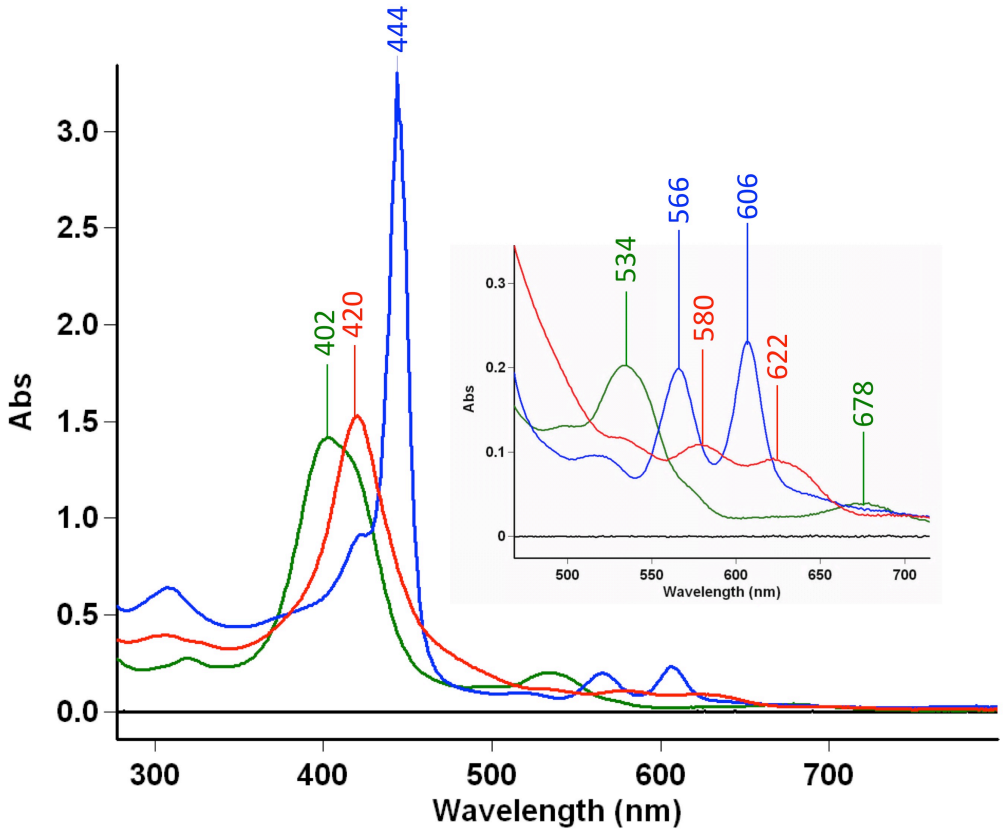

Figure 5. UV−vis spectra of $[(TMPP)Fe^{III}(THF)_2](SbF_6)$ (green) 60 μM in MeTHF in a 2-mm cuvette at −100 °C and the intermediate, $[(TMPP)Fe^{III}(ONNO)Cu^{II}(tmpa)][B(C_6F_5)_4]$, (red) generated upon addition of 20 equiv of $[(tmpa)Cu^{II}(ONNO)Cu^{II}(tmpa)][B(C_6F_5)_4]_2$ in MeOH. Warming to RT and re-cooling back to −100 °C revealed the formation of the μ-oxo complex, $[(TMPP)Fe^{III}–O–Cu^{II}(tmpa)][B(C_6F_5)_4]$, as the final product (blue) in 97% yield.

The nature of this intermediate was further examined using EPR spectroscopy (Figure S19). The starting ferric heme complex, $[(TMPP)Fe^{III}(THF)_2]^+$ exhibits EPR spectra with $g_\perp$ values smaller than 6 ($g_\perp$ = 5.56, Figure S20), which could be interpreted as an admixture of intermediate (S = 3/2) and high (S = 5/2) spin states, which is typical for high-spin ferric hemes with non-coordinating counteranions.[25] However, upon addition of excess cupric hyponitrite complex to the ferric heme, the $g_\perp$ = 5.56 peak disappears and a much less intense but split signal is observed in EPR spectrum of the intermediate (Figure S20, see Supporting Information), possibly representing a departure from tetragonal to a lower symmetry rhombic geometry.[26] The iron center distortion from tetragonal may be consistent with coordination of a hyponitrite moiety to the ferric heme, where both an anionic strong oxygen donor and a more weakly bound *N*-atom coordinate (as we have described (above) for the dicopper-hyponitrite complex). As an aside, it is known that the principal signature of a rhombic field is the so-called "g = 4.3"[27] signal, which we do observe in the EPR spectrum of this intermediate (Figure S20, see Supporting Information), but at this point we do not know if this originates from the Fe(III) or Cu(II) ions.

Scheme 3. Formation of the Heme/Cu Hyponitrite Intermediate, $[(TMPP)Fe^{III}(ONNO)Cu^{II}(tmpa)]^{+}$ at –100 °C and Its Stochiomentric Convesrion to the μ-oxo Complex, $[(TMPP)Fe^{III}–O–Cu^{II}(tmpa)]^{+}$ relasing N_2O at RT.

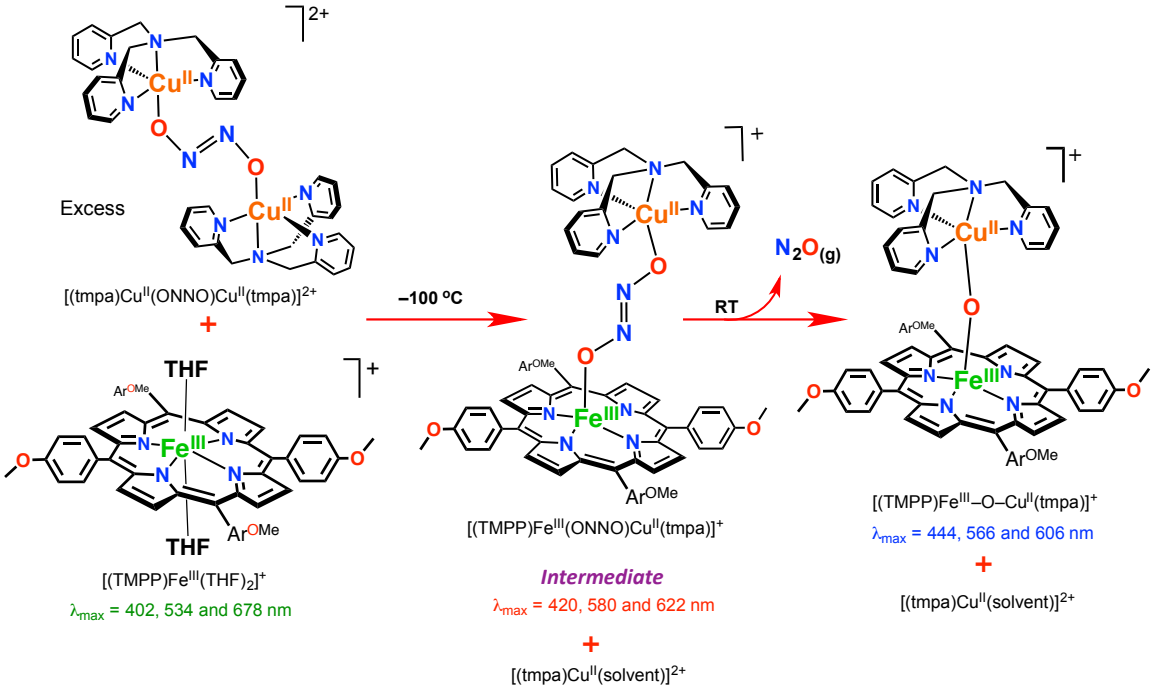

Our further analyses of the heme/Cu hyponitrite intermediate using low temperature ^{1}H-NMR spectroscopy (Figure S22, see Supporting Information) also supported this supposition, that the hyponitrite moiety, as bound to the cupric center, is also coordinated to the ferric heme complex. The pyrrolic protons of the intermediate resonate at larger downfield shifts (δ = 133 ppm, Figure S22) compared to that of the starting ferric heme (δ = 102 ppm, Figure S22). This points to the fact that coordination of cupric hyponitrite moiety to the ferric center results in an increased total spin experienced by the pyrrolic protons[21,25f] in the heme/Cu hyponitrite intermediate. See Supporting Information for further details.

On the basis of the observed hyponitrite coordination mode in the crystal structure of $[(tmpa)Cu^{II}(ONNO)Cu^{II}(tmpa)]^{2+}$, and its solvent-dependent redox chemistries, as well as reactivity of this cupric hyponitrite with a ferric heme complex releasing nitrous oxide, we hypothesize the existence of a new coordination mode for the hyponitrite moiety during the trans mechanism proposed for enzymatic reduction of $NO_{(g)}$ by NOR or C*c*O. As depicted in Scheme 4, in this "Parallel-Trans" mechanism, two $NO_{(g)}$ molecules bind to the ferrous heme and the reduced non-heme center (Fe_B or Cu_B), followed by reduction and formation of the N=N to produce a *trans*-hyponitrite intermediate. The electron transfer to the nitrosyl ligands at the bimetallic active site triggers the change in coordination mode leading to simultaneous binding of the nitrosyls' *O*-atom to the opposite/facing, now oxidized, metal centers. This switching of coordination between the heme and non-heme center is in agreement with accommodating two $NO_{(g)}$ molecules within the very short distance of heme iron and non-heme center reported for both NOR (~ 3.8 – 4.5 Å) and C*c*O (~5 Å).[6e]

Scheme 4. Proposed Parallel-Trans Mechanism for Formation of Hyponitrite Intermediate during Nitric Oxide Reduction by NOR and C*c*O.

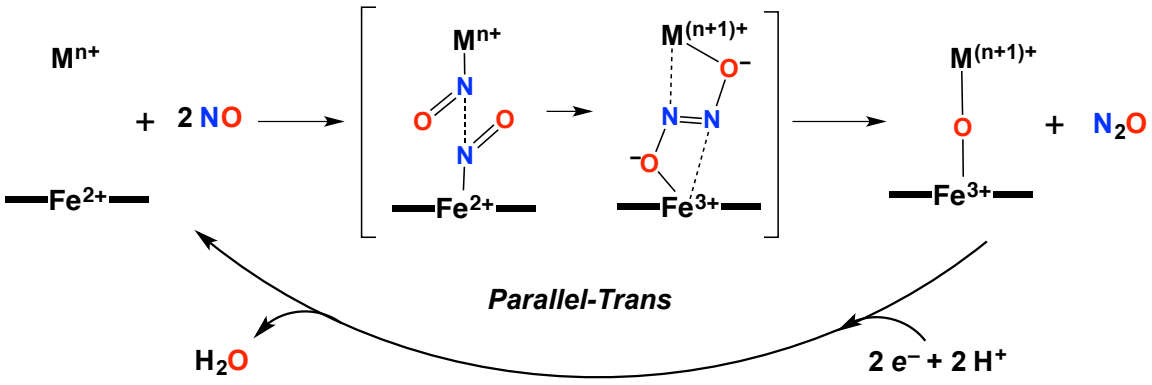

3. Conclusion

In summary, we have reported the first example of a cupric hyponitrite compound and the structural data obtained for this complex confirm the trans geometry for the hyponitrite moiety. The existence of a weak interaction between the cupric center and the remote nitrogen atom of the bridging hyponitrite ion is assigned to be responsible for its unique redox behavior, i.e., the complex's initial transformation to copper(I) plus nitric oxide, in aprotic solvents.

We previously described synthetic heme/Cu assemblies capable of reductive coupling of $NO_{(g)}$ molecules in the same stoichiometry as is known for C*c*Os (and NORs). Here, we introduced a novel heme/Cu hyponitrite intermediate, which converts to a μ-oxo heme-Fe^{III}–O–Cu^{II}(L) compound with stoichiometric loss of nitrous oxide upon warming to RT.

Our future goals include further investigations on the roles of geometry, redox potential, ligand denticity, and hydrogen bonding groups on the stability and reactivity of hyponitrite cupric compounds. For our heme/Cu hyponitrite complexes, we wish to obtain further structural insights concerning the details of the hyponitrite group ligation and other factors such as axial ligand or reducing ability of the heme will also be studied.

4. References

(1) (a) Zumft, W. G. *Microbiol. Molec. Biol. Rev.* **1997**, *61*, 533. (b) Wasser, I. M.; de Vries, S.; Moënne-Loccoz, P.; Schröder, I.; Karlin, K. D. *Chem. Rev.* **2002**, *102*, 1201. (c) Kumita, H.; Matsuura, K.; Hino, T.; Takahashi, S.; Hori, H.; Fukumori, Y.; Morishima, I.; Shiro, Y. *J. Biol. Chem.* **2004**, *279*, 55247. (d) Flock, U.; Thorndycroft, F. H.; Matorin, A. D.; Richardson, D. J.; Watmough, N. J.; Adelroth, P. *J. Biol. Chem.* **2008**, *283*, 3839.

(2) (a) Hendriks, J.; Warne, A.; Gohlke, U.; Haltia, T.; Ludovici, C.; Lubben, M.; Saraste, M. *Biochemistry* **1998**, *37*, 13102. (b) Hino, T.; Matsumoto, Y.; Nagano, S.; Sugimoto, H.; Fukumori, Y.; Murata, T.; Iwata, S.; Shiro, Y. *Science* **2010**, *330*, 1666. (c) Matsumoto, Y.; Tosha, T.; Pisliakov, A. V.; Hino, T.; Sugimoto, H.; Nagano, S.; Sugita, Y.; Shiro, Y. *Nat. Struct. Mol. Biol.* **2012**, *19*, 238.

(3) (a) Cheesman, M. R.; Zumft, W. G.; Thomson, A. J. *Biochemistry* **1998**, *37*, 3994. (b) Wasser, I. M.; Huang, H. W.; Moeñne-Loccoz, P.; Karlin, K. D. *J. Am. Chem. Soc.* **2005**, *127*, 3310. (c) Lin, Y.-W.; Yeung, N.; Gao, Y.-G.; Miner, K. D.; Tian, S.; Robinson, H.; Lu, Y. *Proc. Natl. Acad. Sci. U. S. A.* **2010**, *107*, 8581.

(4) (a) Iwata, S.; Ostermeier, C.; Ludwig, B.; Michel, H. *Nature* **1995**, *376*, 660. (b) Yoshikawa, S.; Shinzawa-Itoh, K.; Nakashima, R.; Yaono, R.; Yamashita, E.; Inoue, N.; Yao, M.; Jei-Fei, M.; Libeu, C. P.; Mizushima, T.; Yamaguchi, H.; Tomizaki, T.; Tsukihara, T. *Science* **1998**, *280*, 1723. (c) Kim, E.; Chufán, E. E.; Kamaraj, K.; Karlin, K. D. *Chem. Rev.* **2004**, *104*, 1077. (d) Flock, U.; Lachmann, P.; Reimann, J.; Watmough, N. J.; Ädelroth, P. *J. Inorg. Biochem.* **2009**, *103*, 845.

(5) (a) Babcock, G. T.; Wikström, M. *Nature* **1992**, *356*, 301. (b) Ferguson-Miller, S.; Babcock, G. T. *Chem. Rev.* **1996**, *96*, 2889.

(6) (a) Saraste, M.; Castresana, J. *FEBS Lett.* **1994**, *341*, 1-4. (b) Pereira, M. M.; Santana, M.; Teixeira, M. *Biochim. Biophys. Acta* **2001**, *1505*, 185. (c) Ducluzeau, A. L.; van Lis, R.; Duval, S.; Schoepp-Cothenet, B.; Russell, M. J.; Nitschke, W. *Trends Biochem. Sci.* **2009**, *34*, 9. (d) Sousa, F. L.;

Alves, R. J.; Ribeiro, M. A.; Pereira-Leal, J. B.; Teixeira, M.; Pereira, M. M. *Biochim. Biophys. Acta* **2012**, *1817*, 629. (e) Sato, N.; Ishii, S.; Sugimoto, H.; Hino, T.; Fukumori, Y.; Sako, Y.; Shiro, Y.; Tosha, T. *Proteins* **2014**, *82*, 1258.

(7) Zumft, W. G. *J. Inorg. Biochem.* **2005**, *99*, 194.

(8) Hayashi, T.; Lin, M. T.; Ganesan, K.; Chen, Y.; Fee, J. A.; Gennis, R. B.; Moënne-Loccoz, P. *Biochemistry* **2009**, *48*, 883.

(9) (a) Varotsis, C.; Ohta, T.; Kitagawa, T.; Soulimane, T.; Pinakoulaki, E. *Angew. Chem. Intl. Ed.* **2007**, *46*, 2210. (b) Pinakoulaki, E.; Varotsis, C. *J. Inorg. Biochem.* **2008**, *102*, 1277.

(10) Xu, N.; Yi, J.; Richter-Addo, G. B. *Inorg. Chem.* **2010**, *49*, 6253.

(11) (a) Schopfer, M. P.; Wang, J.; Karlin, K. D. *Inorg. Chem.* **2010**, *49*, 6267. (b) Hayashi, T.; Caranto, J. D.; Wampler, D. A.; Kurtz, D. M.; Moënne-Loccoz, P. *Biochemistry* **2010**, *49*, 7040.

(12) Wang, J.; Schopfer, M. P.; Sarjeant, A. A. N.; Karlin, K. D. *J. Am. Chem. Soc.* **2009**, *131*, 450.

(13) Wang, J.; Schopfer, M. P.; Puiu, S. C.; Sarjeant, A. A. N.; Karlin, K. D. *Inorg. Chem.* **2010**, *49*, 1404.

(14) (a) Poskrebyshev, G. A.; Shafirovich, V.; Lymar, S. V. *J. Am. Chem. Soc.* **2004**, *126*, 891. (b) Lymar, S. V.; Shafirovich, V.; Poskrebyshev, G. A. *Inorg. Chem.* **2005**, *44*, 5212. (c) Valiev, M.; Lymar, S. V. *J. Phys. Chem. A* **2011**, *115*, 12004.

(15) Arulsamy, N.; Bohle, D. S.; Imonigie, J. A.; Sagan, E. S. *Inorg. Chem.* **1999**, *38*, 2716.

(16) Xu, N.; Campbell, A. L. O.; Powell, D. R.; Khandogin, J.; Richter-Addo, G. B. *J. Am. Chem. Soc.* **2009**, *131*, 2460.

(17) Soulimane, T.; Buse, G.; Bourenkov, G. P.; Bartunik, H. D.; Huber, R.; Than, M. E. *EMBO J.* **2000**, *19*, 1766.

(18) Hematian, S.; Siegler, M. A.; Karlin, K. D. *J. Am. Chem. Soc.* **2012**, *134*, 18912.

(19) (a) Tyeklár, Z.; Jacobson, R. R.; Wei, N.; Murthy, N. N.; Zubieta, J.; Karlin, K. D. *J. Am. Chem. Soc.* **1993**, *115*, 2677. (b) Fry, H. C.; Lucas, H. R.; Narducci Sarjeant, A. A.; Karlin, K. D.; Meyer, G. J. *Inorg. Chem.* **2008**, *47*, 241. (c) Lucas, H. R.; Meyer, G. J.; Karlin, K. D. *J. Am. Chem. Soc.* **2010**, *132*, 12927. (d) Eckenhoff, W. T.; Pintauer, T. *Inorg. Chem.* **2010**, *49*, 10617. (e) Kaur, A.; Ribelli, T. G.; Schröder, K.; Matyjaszewski, K.; Pintauer, T. *Inorg. Chem.* **2015**, *54*, 1474.

(20) (a) Boas, J. F.; Dunhill, R. H.; Pilbrow, J. R.; Srivasta.Rc; Smith, T. D. *J Chem. Soc. A -Inorg. Phys. Theor.* **1969**, 94. (b) Chasteen, N. D.; Belford, R. L. *Inorg. Chem.* **1970**, *9*, 169. (c) Smith, T. D.; Toy, A. D. *J. Am. Chem. Soc.* **1971**, *93*, 3049. (d) Boyd, P. D. W.; Price, J. H.; Smith, T. D.; Pilbrow, J. R. *J. Chem. Phys.* **1972**, *56*, 1253. (e) Smith, T. D.; Pilbrow, J. R. *Coord. Chem. Rev.* **1974**, *13*, 173. (f) Sylvestre, I.; Wolowska, J.; McInnes, E. J. L.; Kilner, C. A.; Halcrow, M. A. *Inorg. Chim. Acta* **2005**, *358*, 1337. (g) Guerra, K. P.; Delgado, R.; Drew, M. G. B.; Felix, V. *Dalton Trans.* **2006**, 4124.

(21) Nanthakumar, A.; Fox, S.; Murthy, N. N.; Karlin, K. D. *J. Am. Chem. Soc.* **1997**, *119*, 3898.

(22) (a) Dinerman, C. E.; Ewing, G. E. *J. Chem. Phys.* **1970**, *53*, 626. (b) Goubeau, J.; Laitenberger, K. *Z Anorg Allg Chem* **1963**, *320*, 78. (c) Kuhn, L.; Lippincott, E. R. *J. Am. Chem. Soc.* **1956**, *78*, 1820. (d) Mayer, T.; Beck, W.; Böttcher, H.-C. *Z Anorg. Allg. Chem.* **2011**, *637*, 345. (e) Arulsamy, N.; Bohle, D. S.; Imonigie, J. A.; Moore, R. C. *Polyhedron* **2007**, *26*, 4737. (f) Wright, A. M.; Hayton, T. W. *Inorg. Chem.* **2015**, *ASAP*, DOI: 10.1021/acs.inorgchem.5b00516. (g) Villalba, M. E. C.; Navaza, A.; Guida, J. A.; Varetti, E. L.; Aymonino, P. J. *Inorg. Chim. Acta* **2006**, *359*, 707. (h) Jeżowska-Trzebiatowska, B.; Hanuza, J.; Ostern, M.; Ziółkowski, J. *Inorg. Chim. Acta* **1972**, *6*, 141. (i) Böttcher, H.-C.; Wagner, C.; Kirchner, K. *Inorg. Chem.* **2004**, *43*, 6294. (j) Arikawa, Y.; Asayama, T.; Moriguchi, Y.; Agari, S.; Onishi, M. *J. Am. Chem. Soc.* **2007**, *129*, 14160. (k) Ohta, T.; Soulimane, T.; Kitagawa, T.; Varotsis, C. *Phys. Chem. Chem. Phys.* **2015**, *17*, 10894. (l) Daskalakis, V.; Ohta, T.; Kitagawa, T.; Varotsis, C. *Biochim. Biophys. Acta* **2015**, *1847*, 1240.

(23) Wright, A. M.; Zaman, H. T.; Wu, G.; Hayton, T. W. *Inorg. Chem.* **2014**, *53*, 3108.

(24) Hematian, S.; Kenkel, I.; Shubina, T. E.; Dürr, M.; Liu, J. J.; Siegler, M. A.; Ivanovic-Burmazovic, I.; Karlin, K. D. *J. Am. Chem. Soc.* **2015**, *137*, 6602.

(25) (a) Maltempo, M. M.; Moss, T. H. *Q. Rev. Biophys.* **1976**, *9*, 181. (b) Reed, C. A.; Mashiko, T.; Bentley, S. P.; Kastner, M. E.; Scheidt, W. R.; Spartalian, K.; Lang, G. *J. Am. Chem. Soc.* **1979**, *101*, 2948. (c) Scheidt, W. R. *Porphyrin Handbook* **2000**, *3*, 49-112. (d) Walker, F. A.; Simonis, U. "Iron Porphyrin Chemistry," In *Encyclopedia of Inorganic Chemistry, Second Edition*; R. B. King, Ed.; John Wiley & Sons Ltd.: 2005; Vol. IV; pp 2390-2521. (e) Yatsunyk, L. A.; Walker, F. A. *J. Porphyrins Phthalocyanines* **2005**, *9*, 214. (f) Yatsunyk, L. A.; Shokhirev, N. V.; Walker, F. A. *Inorg. Chem.* **2005**, *44*, 2848.

(26) (a) Blumberg, W. E.; Peisach, J.; Wittenbe.Ba; Wittenbe.Jb *J. Biol. Chem.* **1968**, *243*, 1854. (b) Peisach, J.; Blumberg, W. E.; Wittenbe.Ba; Wittenbe.Jb; Kampa, L. *Proc. Natl. Acad. Sci. U. S. A.* **1969**, *63*, 934. (c) Yonetani, T.; Drott, H. R.; Leigh, J. S.; Reed, G. H.; Waterman, M. R.; Asakura, T. *J. Biol. Chem.* **1970**, *245*, 2998. (d) Peisach, J.; Blumberg, W. E.; Ogawa, S.; Rachmile.Ea; Oltzik, R. *J. Biol. Chem.* **1971**, *246*, 3342. (e) Ikedasaito, M.; Hori, H.; Andersson, L. A.; Prince, R. C.; Pickering, I. J.; George, G. N.; Sanders, C. R.; Lutz, R. S.; Mckelvey, E. J.; Mattera, R. *J. Biol. Chem.* **1992**, *267*, 22843.

(27) (a) Blumberg, W. E. "The EPR of High Spin Fe^{3+} in Rhombic Fields" In *Magnetic Resonance in Biological Systems*; A. Ehrenberg; B. G. Malmström and T. Vänngård, Ed.; Pergamon: 1967; pp 119-133. (b) Bou-Abdallah, F.; Chasteen, N. *J. Biol. Inorg. Chem.* **2008**, *13*, 15.

5. Supporting Information

5.1. Materials and Methods

All reagents and solvents were of commercially available analytical grade. Methanol (MeOH), diethyl ether (Et_2O), dichloromethane (CH_2Cl_2), and toluene were used after passing them through a 60 cm long column of activated alumina (Innovative Technologies, Inc.) under argon. Tetrahydrofuran (THF) and 2-Methyltetrahydrofuran (MeTHF) (Sigma, 673277, inhibitor free) were purified and dried by distillation from sodium/benzophenone ketyl under argon. Acetonitrile (MeCN) and pentane were dried by distillation over calcium hydride and acetone was distilled over Drierite (anhydrous calcium sulfate) under argon. Dioxygen was dried by passing through a short column of supported P_4O_{10} (Aquasorb, Mallinkrodt). NO gas was obtained from Matheson Gases and purified following methods previously described in the literature.[1] This purified $NO_{(g)}$ was transferred and stored in a 50 mL Schlenk flask capped with a rubber septum. Addition of NO gas to metal complex solutions was effected by transfer via a three-way long syringe needle. Deoxygenation of solvents was effected by either repeated freeze/pump/thaw cycles or bubbling with argon for 45−60 min. Air- and moisture-sensitive compounds were prepared and handled under an argon atmosphere using standard Schlenk techniques or in a Vacuum Atmospheres OMNI-Lab inert atmosphere (<1 ppm of O_2 and H_2O) glovebox filled with nitrogen.

Bench-top low-temperature UV−vis spectra were recorded with a Cary-50 Bio spectrophotometer equipped with a Unisoku USP-203A cryostat using a 2-mm modified Schlenk cuvette. Electron paramagnetic resonance (EPR) measurements were performed

on an Xband Bruker EMX CW EPR spectrometer (~9.4 GHz) controlled with a Bruker ER 041 XG microwave bridge, using 5 mm quartz EPR tubes. Infrared (IR) spectra were obtained using a Thermo Scientific Nicolet Nexus 670 Fourier transform IR (FT-IR) spectrophotometer. Elemental analyses were performed by Columbia Analytical Services (Tucson, AZ). ^{1}H-NMR spectra at RT were recorded at a Bruker Avance 400-MHz spectrometer and low-temperature spectra were acquired using a Bruker Avance 300-MHz spectrometer. Nitrous oxide (N_2O) was purchased from Airgas as a custom mixture, at a concentration of 250 ppm, balanced with dinitrogen at 1 atm. Gas chromatography (GC) analysis was performed on a Varian CP-3800 instrument equipped with a 1041 manual injector, electron capture detector, and a 25 m 5Å molecular sieve capillary column. Single-crystal X-ray data were collected using a SuperNova (Agilent Technologies) diffractometer at the X-ray diffraction facility of the Johns Hopkins University.

The compounds $[(F_8)Fe^{III}]_2O$,[2] $[(F_8)Fe^{III}(Cl)]$,[2] $[(TMPP)Fe^{III}]_2O$,[3] $[(TMPP)Fe^{III}(THF)_2](SbF_6)$,[4] $[(tmpa)Cu^{II}(Cl][B(C_6F_5)_4]$,[5] $[(tmpa)Cu^{II}(Cl](ClO_4)$,[6] $[(tmpa)Cu^{I}(MeCN)][B(C_6F_5)_4]$,[5] silver *trans*-hyponitrite ($Ag_2N_2O_2$),[7] and the reduced binuclear complex $[(^6L)Fe^{II}Cu^{I}][B(C_6F_5)_4]$[8] were synthesized and characterized following methods previously described in the literature. The μ-oxo compound, $[(^6L)Fe^{III}–O–Cu^{II}][B(C_6F_5)_4]$,[8a] was synthesized by bubbling dry dioxygen through a MeTHF solution of reduced binuclear complex at room temperature, similar to that of previously reported for related μ-oxo heme/Cu compounds. The μ-oxo compound is very moisture sensitive, but otherwise stable, and soluble in a variety of solvents. The ethereal solutions of hyponitrous acid ($H_2N_2O_2$) were freshly prepared by reacting silver hyponitrite and

anhydrous hydrochloric acid in ether in the absence of light, similar to the procedure reported by Richter-Addo.[9] Labeled sodium *trans*-hyponitrite hydrate ($Na_2{}^{15}N_2O_2$) was purchased from Eastern Sources, Inc. and labeled silver *trans*-hyponitrite ($Ag_2{}^{15}N_2O_2$) was prepared from *trans*-$Na_2{}^{15}N_2O_2$ using a procedure similar to that used to prepare the unlabeled *trans*-$Na_2N_2O_2$. [(TMPP)Fe^{III}(Cl)] was purchased from TriPorTech (Germany).

5.2. Reactions of Hyponitrous Acid ($H_2N_2O_2$) with μ-oxo Complexes

Preparation of Hyponitrous Acid ($H_2N_2O_2$): The current method is a slightly modified version of procedure reported by Richter-Addo for preparation of hyponitrous acid. Under reduced light, in the glovebox, 1 mL degassed anhydrous diethyl ether was added to $Ag_2N_2O_2$ (10 mg, 0.036 mmol) in a 10 mL Schlenk fask. This mixture was incubated at 0 ºC, followed by dropwise addition of a solution of HCl in Et_2O (20 μL, 2.0 M in Et_2O, 0.040 mmol). This cold reaction mixture was allowed to stir for 1 h under reduced light. The resulting AgCl precipitate and excess $Ag_2N_2O_2$ were removed by filtration under a nitrogen atmosphere, and the colorless filtrate containing the hyponitrous acid was used immediately.

Reaction of $H_2N_2O_2$ with [(^{6}L)Fe^{III}–O–Cu^{II}][$B(C_6F_5)_4$]: In the glovebox, an equimolar amount of freshly prepared solution of $H_2N_2O_2$ in Et_2O was added dropwise to a stirred THF solution (5 mL) of [(^{6}L)Fe^{III}–O–Cu^{II}][$B(C_6F_5)_4$] (37 mg, 0.020 mmol) affording a color change from dark red to dark orange. After stirring for 1 h, solvent was removed under vacuum. The reaction of [(^{6}L)Fe^{III}–O–Cu^{II}][$B(C_6F_5)_4$] with half an equivalent of $H_2N_2O_2$ also resulted in the same final product and this solid product was

dried and used for different analyses. Anal. calcd for $[(^6L)Fe^{II}(NO)...Cu^{II}(OH)][B(C_6F_5)_4]\cdot 3THF$, $C_{99}H_{65}BCuF_{26}FeN_9O_6$: C, 56.60; H, 3.12; N, 6.00. Found: C, 56.53; H, 3.12; N, 6.00. The presence of THF in the reaction product was proved by ^{1}H-NMR spectroscopy on a chemically reduced sample of the binuclear complex (vide infra). UV−vis [λ_{max}, nm (ε_{max}, $M^{-1}cm^{-1}$)]: 411 (148,300) and 547 (17,500) in THF (Figure S1). FT-IR (solid): $\nu_{(NO)}$ = 1685 cm^{-1} (Figure S2) and $\nu_{(OH)}$ = 3360 cm^{-1}. ESI-MS in THF (*m/z* = 1204.2). EPR (Figure S3) spectrum in THF (77 K): the product exhibits signals for both a ferrous heme nitrosyl moiety and a cupric complex found in a distorted square pyrimidal (SP) geometry.

Proof of the Presence of THF: In the glovebox, 12 mg of dried solid product (0.006 mmol) was dissolved in 2 mL of deoxygenated CD_3NO_2 in a small vial, to which 30 equiv (12 mg, 0.180 mmol) of KCN was added. The mixture was stirred at room temperature overnight and filtered into an NMR tube. ^{1}H-NMR (CD_3NO_2, 400 MHz; δ, ppm): 1.60 (m, CH_2(3,4) THF) 3.89 (m, CH_2(2,5) THF).

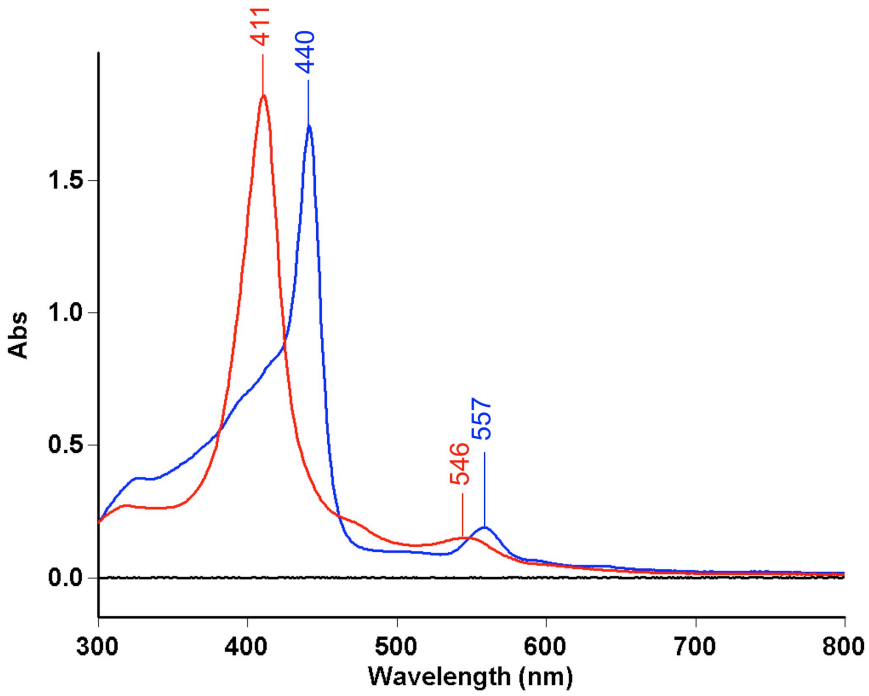

Figure S1. (a) UV−vis spectra of $[(^6L)Fe^{III}–O–Cu^{II}][B(C_6F_5)_4]$ (blue) and the product of its reaction with ½ equiv of $H_2N_2O_2$, $[(^6L)Fe^{II}(NO)...Cu^{II}(OH)][B(C_6F_5)_4]$ (red) (12 μM in THF at RT).

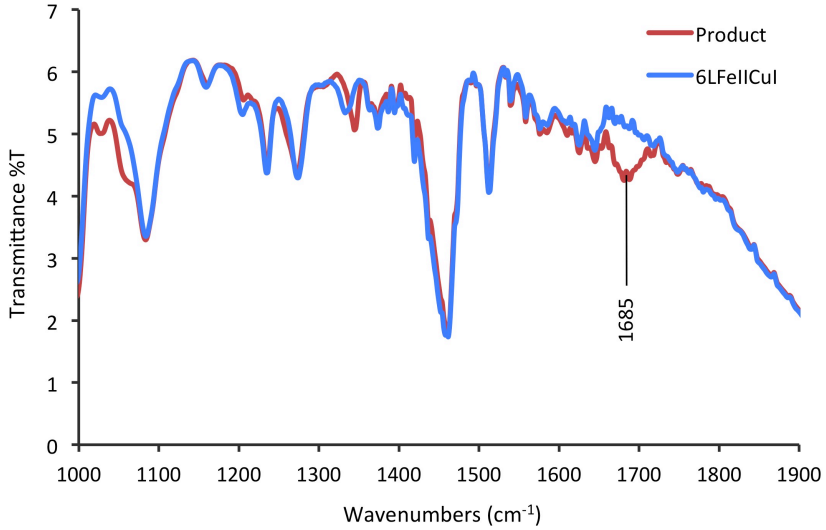

Figure S2. IR spectra (solid) comparison between the product of the reaction of ½ equiv $H_2N_2O_2$ with $[(^6L)Fe^{III}–O–Cu^{II}][B(C_6F_5)_4]$, $[(^6L)Fe^{II}(NO)...Cu^{II}(OH)][B(C_6F_5)_4]$ (red), $\nu_{(NO)}$ = 1685 cm^{-1} and $[(^6L)Fe^{II}Cu^{I}][B(C_6F_5)_4]$ (blue).

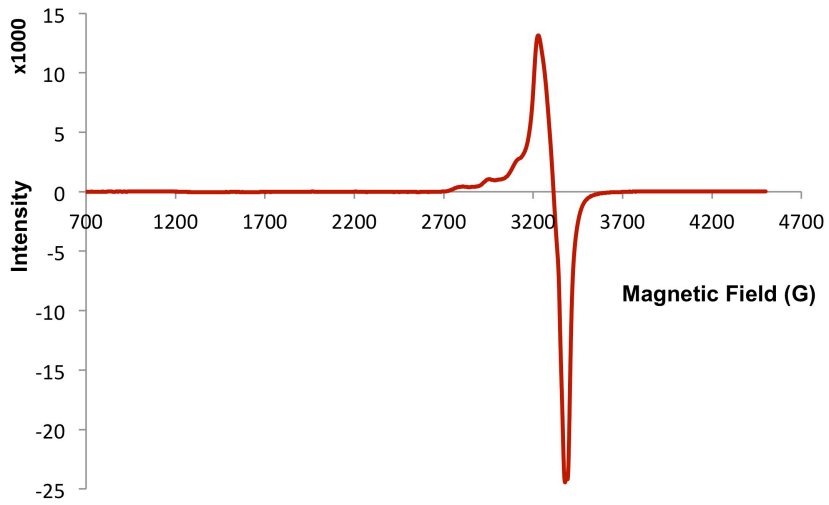

Figure S3. EPR spectrum of the product of the reaction of ½ equiv of $H_2N_2O_2$ and $[(^6L)Fe^{III}–O–Cu^{II}][B(C_6F_5)_4]$, giving signals of ferrous heme nitrosyl and Cu^{II} in MeTHF 1 mM at 77 K.

Stoichiometric Reaction of $H_2N_2O_2$ with $[(porphyrinate)Fe^{III}]_2O$: In the case of stoichiometric reaction of a toluene solution of $[(porphyrinate)Fe^{III}]_2O$ (porphyrinate is either F_8 or TMPP prophyrinate) with freshly prepared solution of $H_2N_2O_2$ in Et_2O at RT, there was no reaction even after one week.

5.3. Reactions of Silver Hyponitrite ($Ag_2N_2O_2$) with Chloride Complexes

Synthesis of $[(^6L)Fe^{III}(Cl)...Cu^{II}(Cl)][B(C_6F_5)_4]$: Under a nitrogen atmosphere, 20 μL of a solution of HCl in Et_2O (2.0 M in Et_2O, 0.040 mmol) was added to a solution of $[(^6L)Fe^{III}–O–Cu^{II}][B(C_6F_5)_4]$ (37 mg, 0.020 mmol) in CH_2Cl_2 (3 mL) affording a color change from dark red to orange-red. After stirring for 20 min, the solvent was removed the solid product was dried under vacuum. UV–vis [λ_{max}, nm]: 370, 412, 507, 575 and

624 in CH_2Cl_2 (Figure S4) and 348, 413, 506, 575, 622 and 653 in MeTHF (Figure S6). ESI-MS in THF (*m/z* = 1227.1). EPR (Figure S5) spectrum in MeTHF (20 K): the product exhibits signals for both a high-spin ferric heme moiety and a cupric complex in distorted square pyrimidal (SP) geometry.

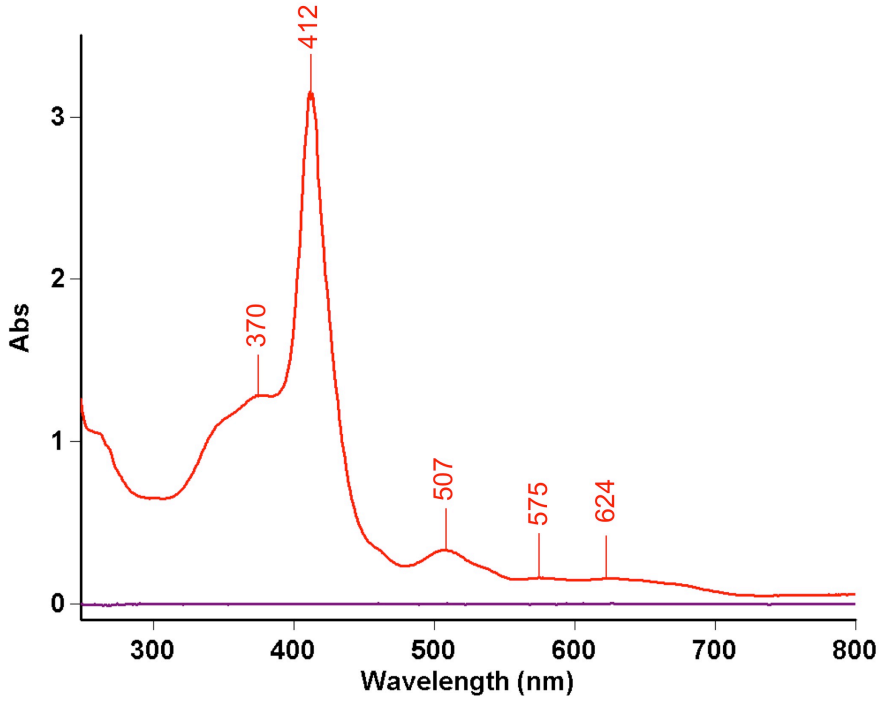

Figure S4. UV−vis spectrum of $[(^6L)Fe^{III}(Cl)...Cu^{II}(Cl)][B(C_6F_5)_4]$ (30 μM) in CH_2Cl_2 at RT.

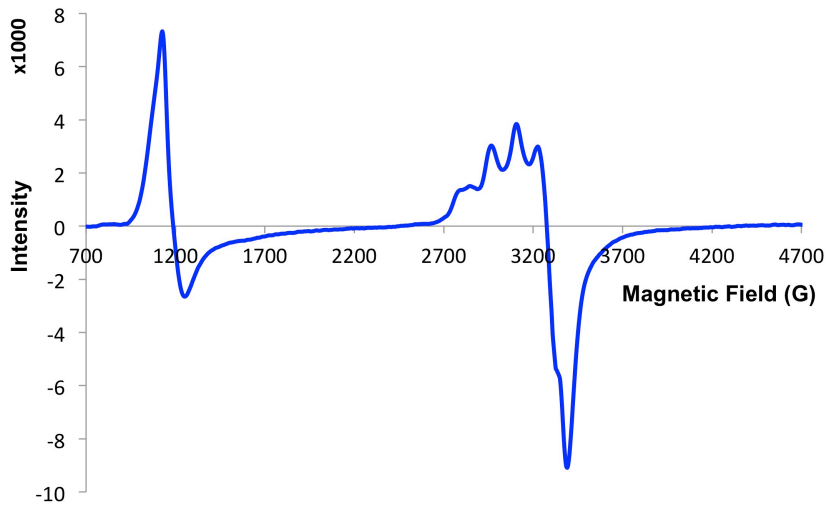

Figure S5. EPR spectrum of $[(^6L)Fe^{III}(Cl)...Cu^{II}(Cl)][B(C_6F_5)_4]$ (1 mM) in MeTHF at 20 K, showing signals for a mixture of (porphyrinate)$Fe^{III}(Cl)$ and Cu^{II} in a distorted SP coordination enviroment, confirmed based on our control experiments using authentic $(F_8)Fe^{III}(Cl)$ and $[(tmpa')Cu^{II}(Cl)][B(C_6F_5)_4]$.

Stoichiometric Reaction of $Ag_2N_2O_2$ with $[(^6L)Fe^{III}(Cl)...Cu^{II}(Cl)][B(C_6F_5)_4]$: In the glovebox, silver hyponitrite ($Ag_2N_2O_2$) (8 mg, 0.029 mmol) was added to a solution of $[(^6L)Fe^{III}(Cl)...Cu^{II}(Cl)][B(C_6F_5)_4]$ (50 mg, 0.026 mmol) in MeTHF (3 mL). The reaction mixture was sonicated for 1 h under reduced light at RT. The solution was then filtered to remove AgCl, and solvent was removed under vacuum. UV–vis [λ_{max}, nm]: 410 and 545 in MeTHF (Figure S6). ESI-MS in THF (*m/z* = 1222.2). FT-IR (solid): $\nu_{(NO)}$ = 1685 cm^{-1}. EPR (Figure S7) spectrum in THF (77 K): the product exhibits signals for both a ferrous heme nitrosyl moiety and a cupric complex in distorted square pyrimidal (SP) geometry.

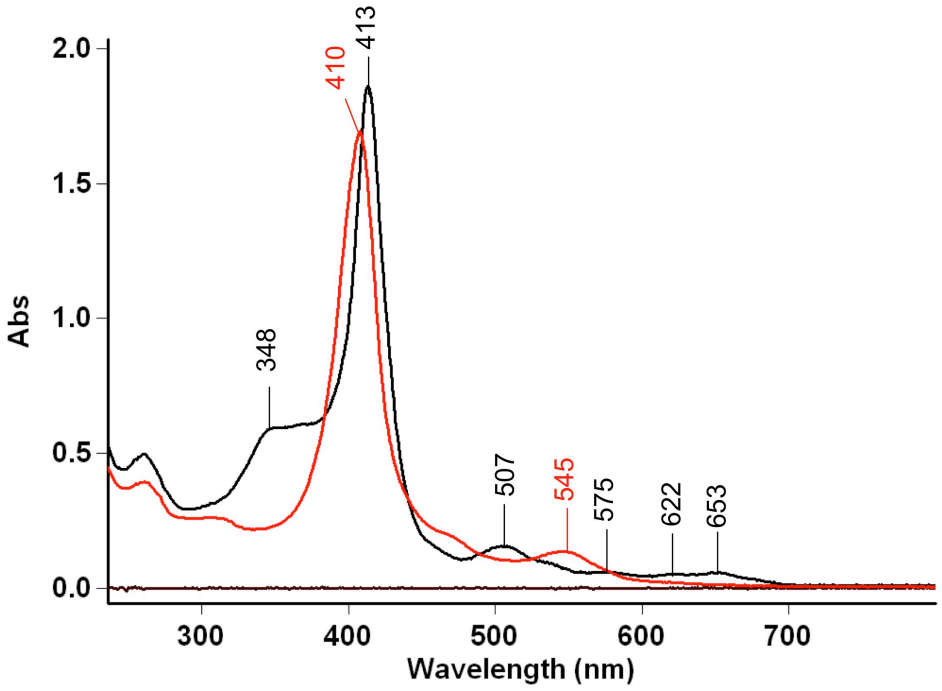

Figure S6. UV−vis spectra of $[(^6L)Fe^{III}(Cl)...Cu^{II}(Cl)][B(C_6F_5)_4]$ (black) and the product of its reaction with 1 equiv $Ag_2N_2O_2$, $[(^6L)Fe^{II}(NO)...Cu^{II}(Cl)][B(C_6F_5)_4]$ (red) (12 μM in MeTHF at RT).

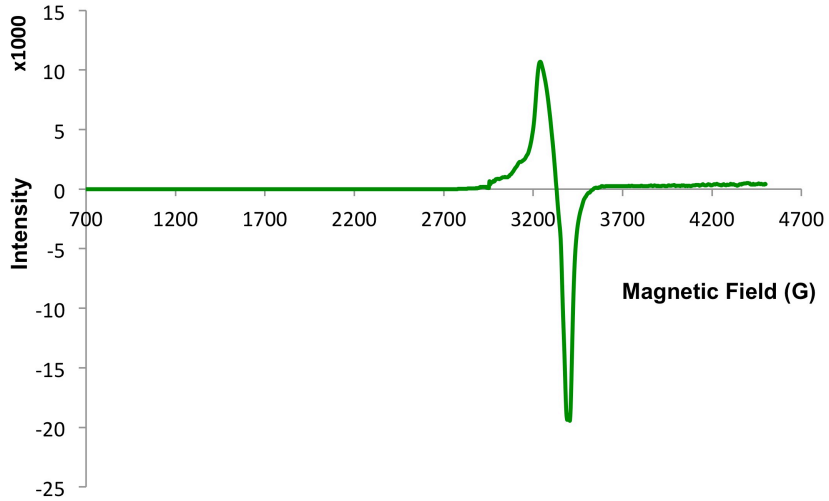

Figure S7. EPR spectrum of the product of the reaction of 1 equiv of $Ag_2N_2O_2$ and $[(^6L)Fe^{III}(Cl)...Cu^{II}(Cl)][B(C_6F_5)_4]$, giving signals of a mixture of a ferrous heme nitrosyl and Cu^{II} species in MeTHF 1 mM at 77 K.

Reaction of $Ag_2N_2O_2$ with [(porphyrinate)Fe^{III}(Cl)]: Reaction of [(porphyrinate)Fe^{III}(Cl)] complexes (porphyrinate is either F_8 or TMPP prophyrinate) with silver hyponitrite in THF at RT resulted in formation of ferrous heme nitrosyl, [(porphyrinate)Fe^{II}(NO)]. For reaction of ½ equiv of $Ag_2N_2O_2$ with: i) [$(F_8)Fe^{III}$(Cl)] generating [$(F_8)Fe^{II}$(NO)]; UV–vis [λ_{max}, nm]: 410 and 545 in THF. ESI-MS in THF (*m/z* = 843.1 for [$(F_8)Fe^{II}$(NO)] + H^+). FT-IR (solid): $\nu_{(NO)}$ = 1685 cm^{-1}. EPR (Figure S8) spectrum in MeTHF (77 K) exhibits a ferrous heme nitrosyl signal. ii) [(TMPP)Fe^{III}(Cl)] generating [(TMPP)Fe^{II}(NO)]; UV–vis [λ_{max}, nm]: 411 and 539 in THF (Figure 9), ESI-MS in THF (*m/z* = 819.2 for [(TMPP)Fe^{II}(NO)] + H^+). FT-IR spectrum in THF: $\nu_{(NO)}$ = 1675 cm^{-1}. EPR (Figure S10) spectrum in MeTHF (77 K) exhibits a ferrous heme nitrosyl signal.

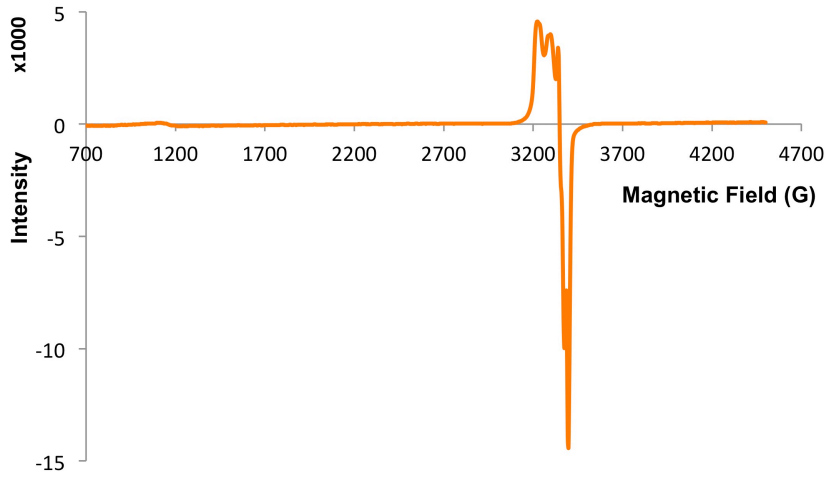

Figure S8. EPR spectrum of the product of the reaction of ½ equiv of $Ag_2N_2O_2$ and [$(F_8)Fe^{III}$(Cl)], giving a ferrous heme nitrosyl signal in MeTHF 1 mM at 77 K.

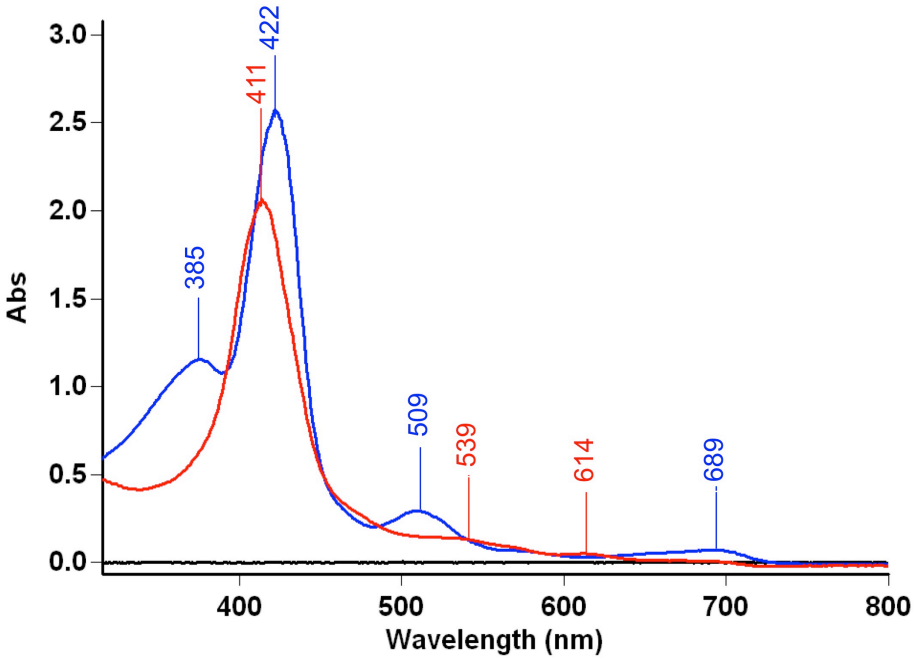

Figure S9. UV−vis spectra of [(TMPP)Fe^{III}(Cl)] (blue) and the product of its reaction with 1 equiv $Ag_2N_2O_2$, [(TMPP)Fe^{II}(NO)] (red) (12 μM in THF at RT).

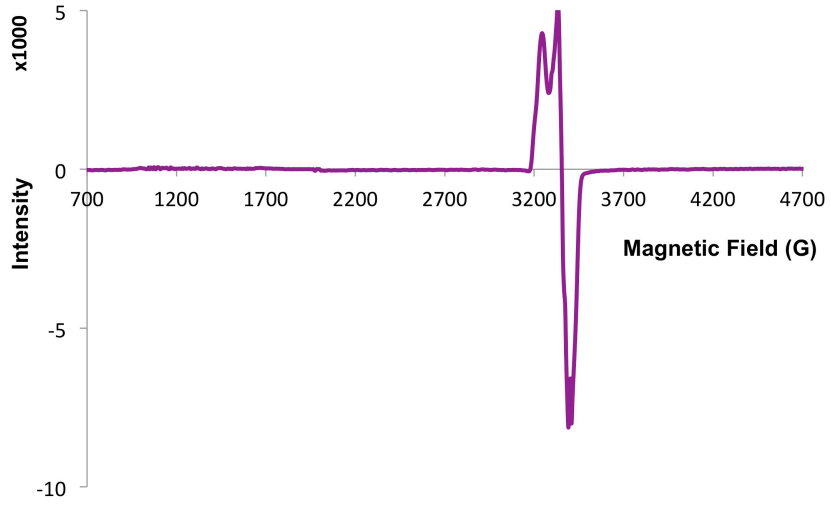

Figure S10. EPR spectrum of the product of the reaction of ½ equiv of $Ag_2N_2O_2$ and [(TMPP)Fe^{III}(Cl)], giving a ferrous heme nitrosyl signal in MeTHF 1 mM at 77 K.

Reaction of $Ag_2N_2O_2$ with [(tmpa)Cu^{II}(Cl)][$B(C_6F_5)_4$]: In the glovebox, silver hyponitrite (56 mg, 0.20 mmol) was added to a solution of [(tmpa)Cu^{II}(Cl)][$B(C_6F_5)_4$] (400 mg, 0.37 mmol) in MeOH (7 mL). Under reduced light, the reaction mixture was sonicated for 1 h to ensure complete precipitation of AgCl, affording a color change from blue to green. The solution was then filtered in the glovebox, and solvent was removd under vacuum. The obtained solid was further dried yielding 330 mg of the greenish gold-brown product (80%). Anal. Calcd for [(tmpa)Cu^{II}(ONNO)Cu^{II}(tmpa)][$B(C_6F_5)_4$]$_2$, $C_{84}H_{36}B_2Cu_2F_{40}N_{10}O_2$: C, 47.46; H, 1.71; N, 6.59. Found: C, 47.46; H, 1.93; N, 5.21. *Note*: The observed value for nitrogen is off by 1.38 which accounts for 2 equiv and this error can be assigned to release of $N_2O_{(g)}$ between weighing and combustion periods during the elemental analysis measuement. UV−vis [λ_{max}, nm (ε_{max}, $M^{-1}cm^{-1}$)]: 310 (4,950), 682 (270) and 875 (390) in MeOH (Figure S11) and 308 (5,500), 420 (2,400), 656 (390) and 890 (310) in THF (Figure S11). EPR spectrum (X-band spectrometer, ν = 9.428 GHz): $g_{\|}$ = 1.999, $A_{\|}$ = 84 G, $g_{\perp}$ = 2.186, $A_{\perp}$ = 78 G in MeOH at 20 K (Figure S12). These data are typical for trigonal bipyramidal copper(II) structures. For EPR measurments of [(tmpa)Cu^{II}(ONNO)Cu^{II}(tmpa)][$B(C_6F_5)_4$]$_2$ in THF, under nitrogen atmosphere, one sample was immediately frozen after dissolution of solid complex in deoxygenated THF and stored in liquid nitrogen, $g_{\|}$ = 2.010, $A_{\|}$ = 70 G, $g_{\perp}$ = 2.170, $A_{\perp}$ = 94 G in THF at 20 K (Figure S13), while the other sample was frozen 1 h after preparation at RT, $g_{\|}$ = 2.007, $A_{\|}$ = 80 G, $g_{\perp}$ = 2.174, $A_{\perp}$ = 86 G in THF at 20 K (Figure S14). EPR spectra of [(tmpa)Cu^{II}(ONNO)Cu^{II}(tmpa)]$^{2+}$ in frozen solutions show weak broad ΔM_s = 2 (“half-field”) signals, in MeOH at g = 4.120 (Figure 12), and in THF immediately frozen at g = 4.120 (Figure 13) and in THF frozen after 1 h at g = 4.291

(Figure 14). This dicopper-hyponitrite complex is unstable in non-hydrogen bonding solvents such as THF, MeTHF, MeCN, acetone, etc., and it rapidly decomposes to a mixture of different cuprous and cupric species. Qulitative gas chromatography analysis (vide infra) of the head space of the dissolved $[(tmpa)Cu^{II}(ONNO)Cu^{II}(tmpa)][B(C_6F_5)_4]_2$ in THF revealed initial release of $NO_{(g)}$ into the headspace after 1 h after dissolution and a very slow generation of N_2O after 3 h. ESI-MS in MeOH (*m/z* = 383.1 for $[(tmpa)Cu^{II}(ONNO)Cu^{II}(tmpa)]^{2+}$ (doubly charged complex, 764.2/2 = 383.1) and other major peak at 353.1 for $[(tmpa)Cu^{I}]^{+}$). FT-IR spectrum (solid) (Figure S15): No isotope-sensitive band was observed in the IR spectrum upon ^{15}N-labeling of the bridging hyponitrite. ^{1}H-NMR (CD_3OD, 400 MHz; δ, ppm): 30.47 (br), 24.34 (br), 10.54. Resonace Raman Spectroscopic measurements revealed the existence of a particularly low N=N stretching vibration, $\nu_{(N=N)}$ = 1085 cm^{-1}, (Figure S16) for the hyponitrite moiety, in agreement with the theoretical value calculated for a geometry-optimized structure (the N-N bond length from 1.26 to 1.29 Å) for a triplet state, $\nu_{(N=N)}$ = 1076 cm^{-1}.

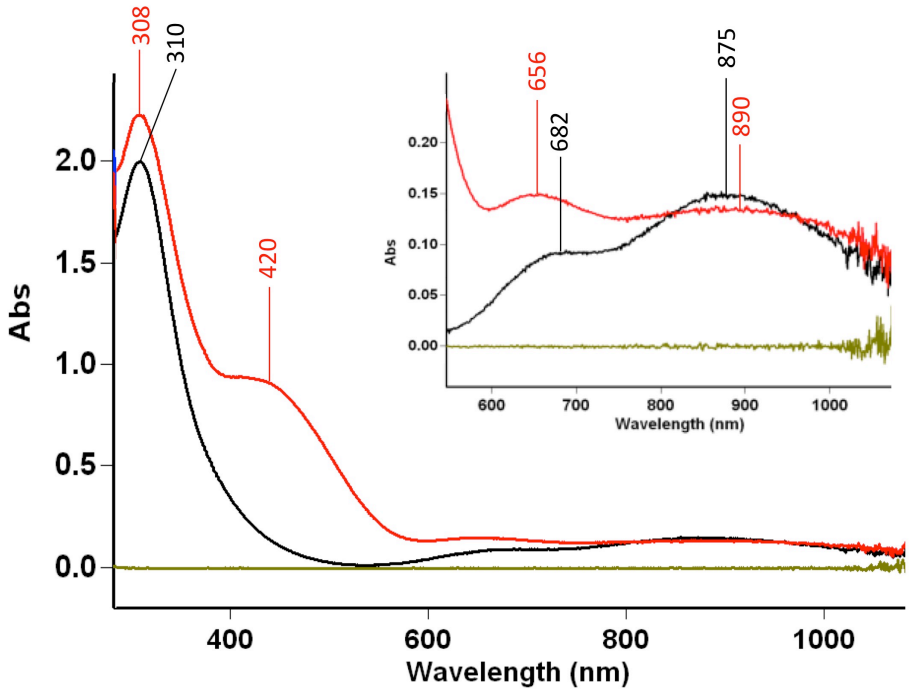

Figure S11. UV−vis spectra of $[(tmpa)Cu^{II}(ONNO)Cu^{II}(tmpa)][B(C_6F_5)_4]_2$ in MeOH (black, 2 mM) and the same complex immediately after dissolution in THF (red, 2 mM) in a 2-mm cuvette at RT.

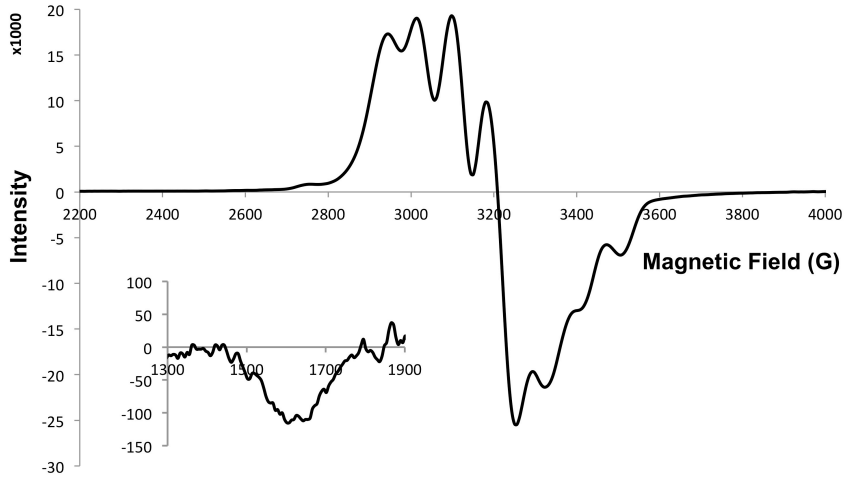

Figure S12. EPR spectrum of $[(tmpa)Cu^{II}(ONNO)Cu^{II}(tmpa)][B(C_6F_5)_4]_2$ (2 mM) in MeOH at 20 K.

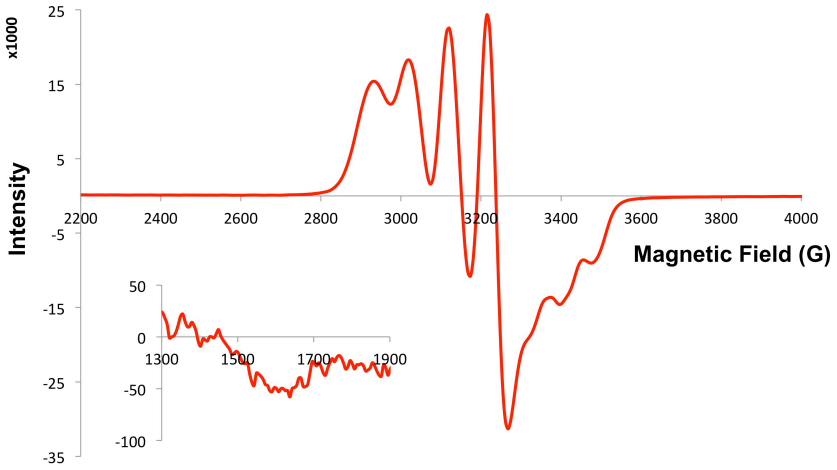

Figure S13. EPR spectrum of $[(tmpa)Cu^{II}(ONNO)Cu^{II}(tmpa)][B(C_6F_5)_4]_2$ (2 mM) immediately frozen after dissolution in THF at 20 K.

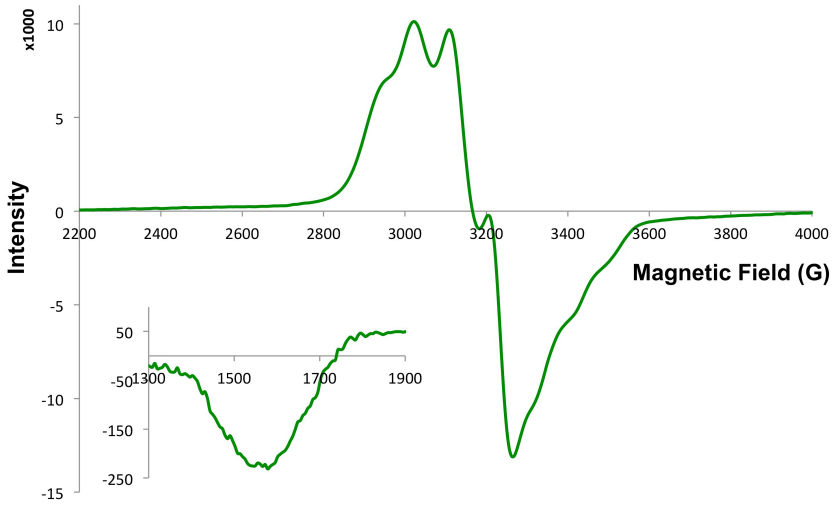

Figure S14. EPR spectrum of $[(tmpa)Cu^{II}(ONNO)Cu^{II}(tmpa)][B(C_6F_5)_4]_2$ (2 mM) frozen 1 h after dissolution in THF at 20 K.

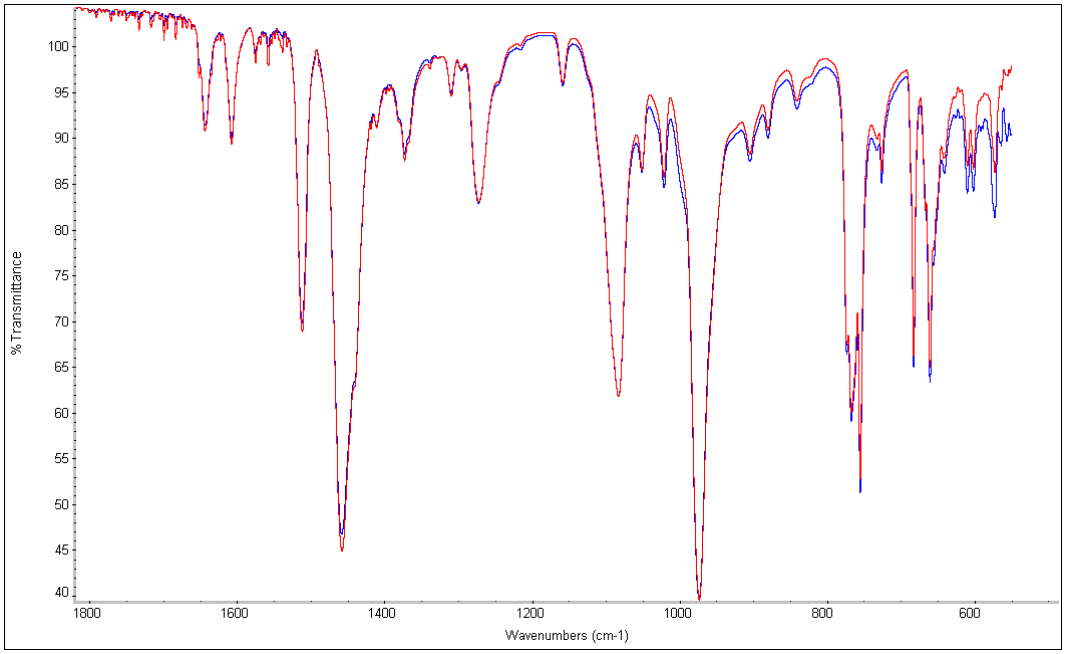

Figure S15. IR spectra (solid) comparison between $[(tmpa)Cu^{II}(ONNO)Cu^{II}(tmpa)][B(C_6F_5)_4]_2$ (blue) and $[(tmpa)Cu^{II}(O^{15}N^{15}NO)Cu^{II}(tmpa)][B(C_6F_5)_4]_2$ (red). The observation that there is no isotope-sensitive band observed in the IR spectrum upon ^{15}N-labeling of the bridging hyponitrite ligand may be due to the high symmetry of the complex.

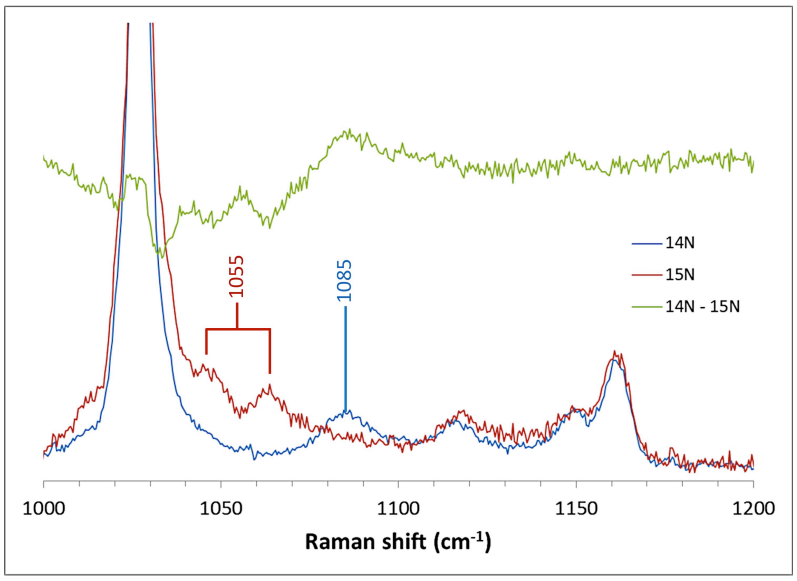

Figure S16. Resonace Raman spectra comparison between $[(tmpa)Cu^{II}(ONNO)Cu^{II}(tmpa)][B(C_6F_5)_4]_2$ (blue) and ^{15}N-labeled hyponitrite complex, $[(tmpa)Cu^{II}(O^{15}N^{15}NO)Cu^{II}(tmpa)][B(C_6F_5)_4]_2$ (red) 2 mM in MeOH with 407 nm excitation collected at 77 K. The data and spectra were provided by our Stanford University collaborators.

Reaction of [(tmpa)Cu^{I}(MeCN)][B(C$_6$F$_5$)$_4$] with excess NO$_{(g)}$: Samples of [(tmpa)Cu^{I}(MeCN)][B(C$_6$F$_5$)$_4$] (2 mM in THF) for UV−vis monitoring were prepared in a 2-mm modified Schlenk cuvette in the glovebox. Upon addition of 1 mL of $NO_{(g)}$ to the cuprous complex solution at –80 ^{o}C, the reaction progressed by an instant formation of a new intermediate. UV−vis: [λ_{max}, nm (ε_{max}, $M^{-1}cm^{-1}$)]: 311(3,100), 400 (3,200), 627 (550) and 845 (150) in THF at −80 °C (Figure S17). This intermediate converts to another species (λ_{max} = 304, 413, 650 and 856 nm), resembeling spectral features of cupric nitrite complexs of the TMPA family. The sample was then warmed to RT and re-cooled to –80 ^{o}C revealing the stoichiometric formation of [(tmpa)Cu^{II}(NO$_2$)][B(C$_6$F$_5$)$_4$] (λ_{max} = 304 (3,000), 413 (1,100) and 856 (280) nm, Figure S17) based on the known extinction coefficients for the authentic compound.[5] Nitrous oxide gas of the headspace was also identified qualitatively by GC analysis. Here, [(tmpa)Cu^{I}(MeCN)]$^{+}$ is capable of reductive disproportionation of 3 equiv of $NO_{(g)}$ to produce $N_2O_{(g)}$ and nitrite.

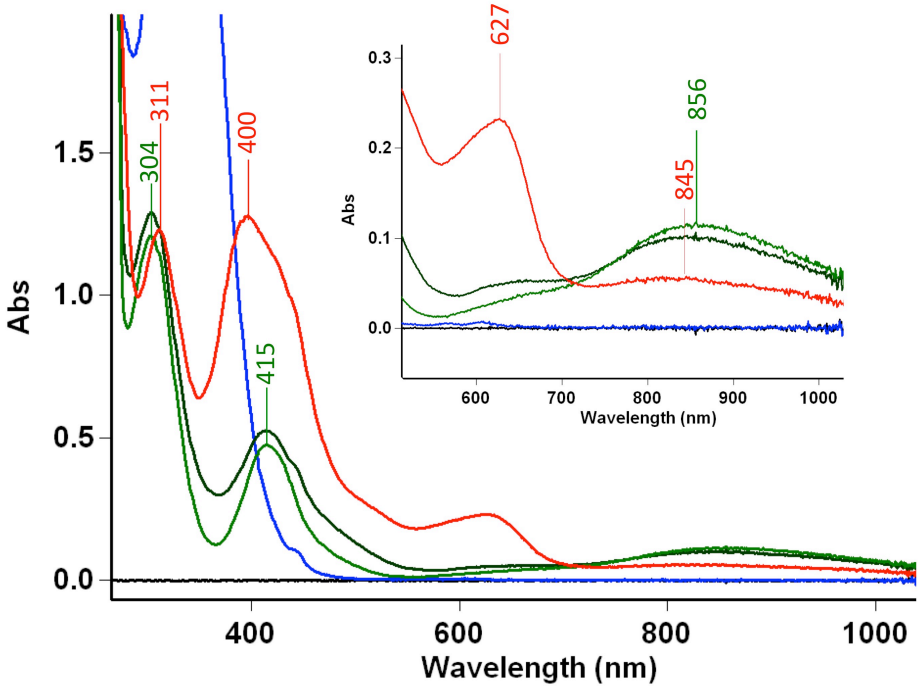

Figure S17. UV−vis spectra of [(tmpa)Cu^{I}(MeCN)][$B(C_6F_5)_4$] (blue), 2 mM in THF in a 2-mm cuvette at −80 °C, the intermediate (red) generated upon addition of 1 mL of $NO_{(g)}$ into the solution. The intermediate converts to another species (dark green) within 10 min which resembeling spectral features of the cupric nitrite complex. Warming to RT resulted in clean production of [(tmpa)Cu^{II}(NO_2)][$B(C_6F_5)_4$] (light green).

5.4. Generation of a Heme/Cu Hyponitrite Complex

Reaction of [(TMPP)Fe^{III}(THF)$_2$](SbF$_6$) with excess [(tmpa)Cu^{II}(ONNO)-Cu^{II}(tmpa)][$B(C_6F_5)_4$]$_2$: In the glovebox, complex [(TMPP)Fe^{III}(THF)$_2$](SbF$_6$).THF (5 mg, 0.003 mmol) was dissolved in 2 mL MeTHF and this solution was cooled to –100ºC using an ethanol/liquid nitrogen bath. Addition of 10 equiv of [(tmpa)Cu^{II}(ONNO)Cu^{II}(tmpa)][$B(C_6F_5)_4$]$_2$ in MeOH to this cold solution resulted in an immediate color change from dark red to dark brown. The reaction mixture was allowed to stir for 2 min at –100 ºC followed by warming to RT which was accompanied by a

color change to dark green indicative of production of the μ-oxo compound, [(TMPP)Fe^{III}–O–Cu^{II}(tmpa)][$B(C_6F_5)_4$]. Gas chromatography analysis (vide infra) of the head space of the reaction products revealed production of significant amount of N_2O (88%) as the gasous product (vide infra). *Note*: The reaction mixture should not be left at RT for longer than 30 min as the excess [(tmpa)Cu^{II}(ONNO)Cu^{II}(tmpa)][$B(C_6F_5)_4$]$_2$ in the solution very slowly releases $NO_{(g)}$ which can further react with the μ-oxo complex produced to generate [(TMPP)Fe^{II}(NO)] and [(tmpa)Cu^{II}(NO_2)][$B(C_6F_5)_4$], as we recently reported.[4]

Characterization [(TMPP)Fe^{III}(ONNO)Cu^{II}(tmpa)][$B(C_6F_5)_4$]: Samples for UV−vis monitoring were prepared in a 2-mm modified Schlenk cuvette. Addition of 20 equiv [(tmpa)Cu^{II}(ONNO)Cu^{II}(tmpa)][$B(C_6F_5)_4$]$_2$ in MeOH directly into the solution of [(TMPP)Fe^{III}(THF)$_2$](SbF_6) in MeTHF at –100 ºC resulted in formation of a new species, [(TMPP)Fe^{III}(ONNO)Cu^{II}(tmpa)][$B(C_6F_5)_4$], UV−vis: [λ_{max}, nm (ε_{max}, $M^{-1}cm^{-1}$)]: 420 (134,000), 580 (10,100) and 622 (8,400) in MeTHF at −100 °C (Figure 5). This intermediate converts to final product, [(TMPP)Fe^{III}–O–Cu^{II}(tmpa)][$B(C_6F_5)_4$] upon warming to RT. Based on the known extinction coefficients for [(TMPP)Fe^{III}–O–Cu^{II}(tmpa)][$B(C_6F_5)_4$], [λ_{max}, nm (ε_{max}, $M^{-1}cm^{-1}$)]: 444 (283,000), 566 (17,600) and 606 (19,800) in MeTHF, the μ-oxo compound was formed in approximately 97% yield (Figure 5). The UV–vis monitoring of reaction of [(TMPP)Fe^{III}(THF)$_2$](SbF_6) with the excess amount (20 eq) of [(tmpa)Cu^{II}(ONNO)Cu^{II}(tmpa)][$B(C_6F_5)_4$]$_2$ in MeTHF at –100 ºC, showed isosbestic conversion of ferric heme to the heme/Cu hyponitrite intermediate, [(TMPP)Fe^{III}(ONNO)Cu^{II}(tmpa)][$B(C_6F_5)_4$] (Figure S18).

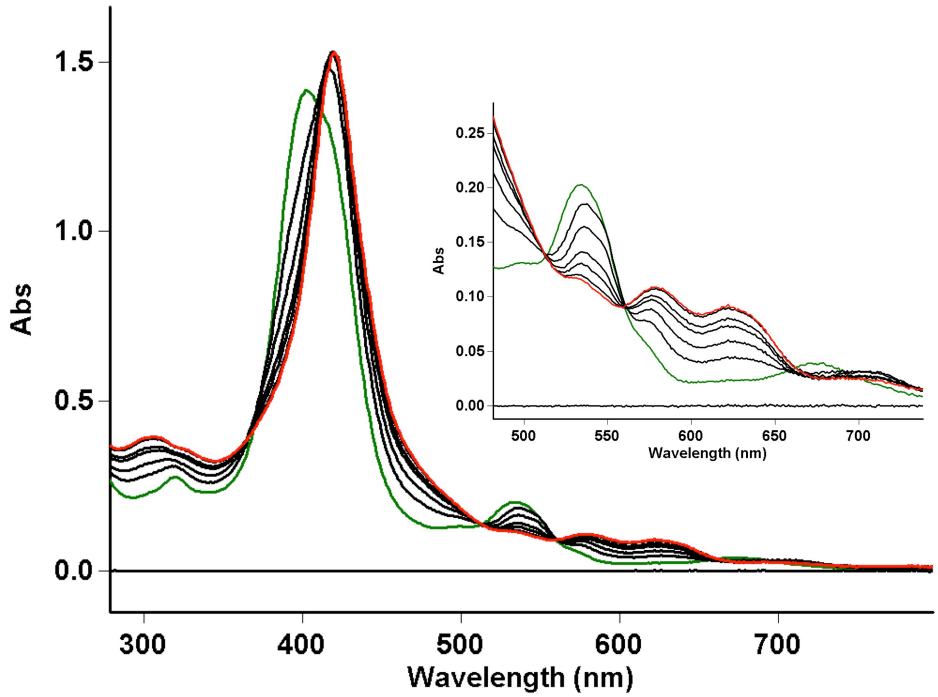

Figure S18. UV−vis spectra of $[(TMPP)Fe^{III}(THF)_2](SbF_6)$ (green) 60 μM in MeTHF in a 2-mm cuvette at −100 °C and its isosbestic conversion to the intermediate, $[(TMPP)Fe^{III}(ONNO)Cu^{II}(tmpa)][B(C_6F_5)_4]$, (red) upon addition of 20 equiv of $[(tmpa)Cu^{II}(ONNO)Cu^{II}(tmpa)][B(C_6F_5)_4]_2$ in MeOH.

EPR samples of the reaction mixture were prepared by addition of 0, 1, 5, 10 equiv of $[(tmpa)Cu^{II}(ONNO)Cu^{II}(tmpa)][B(C_6F_5)_4]_2$ in MeOH to 600 μL of 1 mM solution of $[(TMPP)Fe^{III}(THF)_2](SbF_6)$ in THF/MeTHF (1:9) at –100 ºC (ethanol/liquid nitrogen bath). After mixing for 2 min at –100 ºC, the samples of the intermediate were frozen in liquid nitrogen (Figure S19) while the samples of the final product were warmed to RT and frozen after 30 min. As expected, becuause the final μ-oxo product is EPR silent, the only feature observed in the spectra of the warmed up reaction mixture is the cupric signal originated from excess $[(tmpa)Cu^{II}(ONNO)Cu^{II}(tmpa)][B(C_6F_5)_4]_2$. Addition of 5 or 10 equiv of cuppric hyponitrite complex to the ferric heme resulted in

disappearance of the axial high spin g = 6 ferric signal and appearance of more rhombic signals (g = 4.27 and split/broadened resonances near g = 6) (Figures S20), revealing a change in symmetry around the ferric center as expected in the presence of interaction/coordination of hyponitrite moiety as an axial ligand.

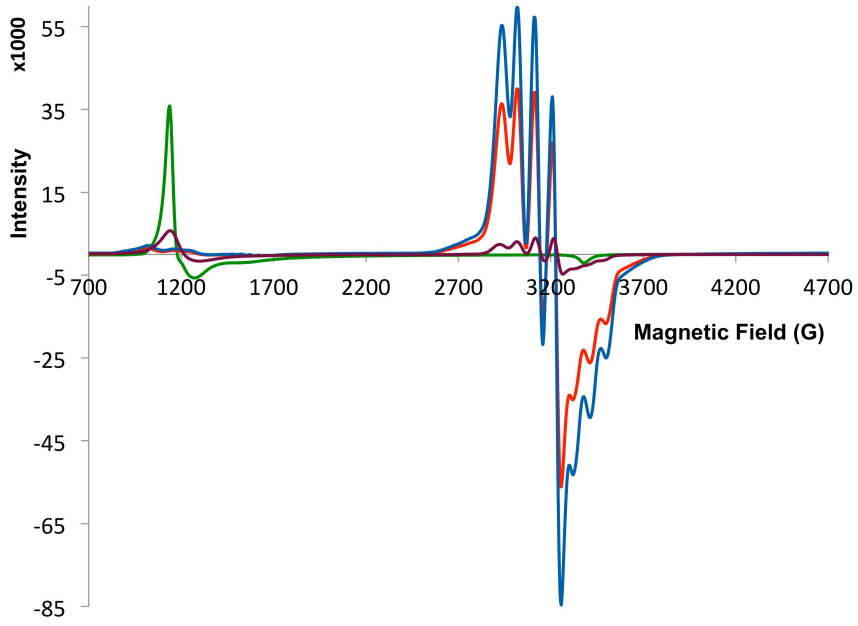

Figure S19. EPR spectra of $[(TMPP)Fe^{III}(THF)_2](SbF_6)$ 1mM in THF/MeTHF (1:9) (green) and after addition of *n* equiv of $[(tmpa)Cu^{II}(ONNO)Cu^{II}(tmpa)][B(C_6F_5)_4]_2$, at –100 ºC, (*n* = 0, green; *n* = 1, purple; *n* = 5, red; *n* = 10, blue), recorded at 20 K.

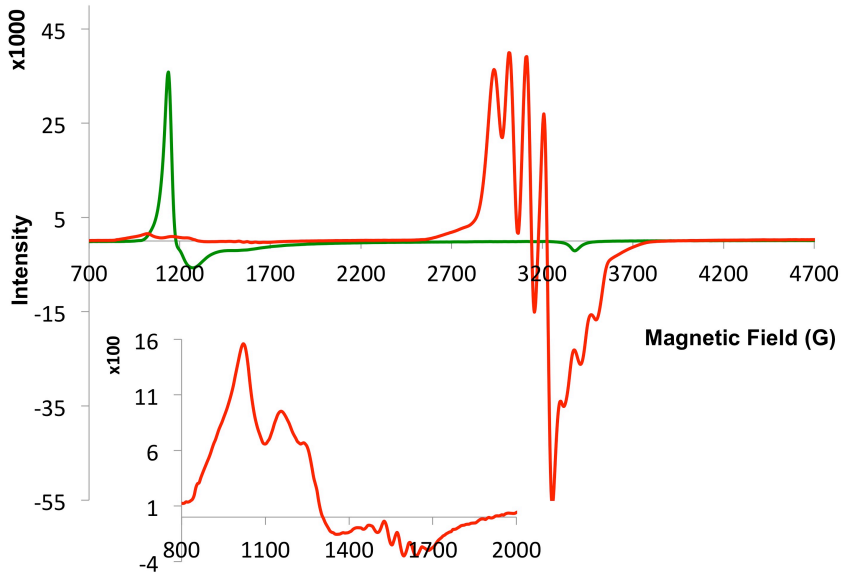

Figure S20. EPR spectra of $[(TMPP)Fe^{III}(THF)_2](SbF_6)$ 1mM in THF/MeTHF (1:9) (green) (g = 6.56) and after addition of 5 equiv of $[(tmpa)Cu^{II}(ONNO)Cu^{II}(tmpa)][B(C_6F_5)_4]_2$, generating $[(TMPP)Fe^{III}(ONNO)Cu^{II}(tmpa)][B(C_6F_5)_4]$ (red) at –100 ºC, recorded at 20 K; for the low field region, g = 6.58, 5.81 and 5.40, for the mid-filed region, the strongest 5 peaks of the multiplet are at g = 4.56, 4.40, 4.27, 4.15, 4.03, i.e. g_{mid} = 4.27.

5.5. Low-Temperature ^{1}H-NMR Spectroscopic Measurements

^{1}H-NMR spectroscopic measurements were performed on a Bruker 300 MHz spectrometer at various temperatures under a N_2 atmosphere in septum-capped NMR tubes. Chemical shifts were reported as δ values relative to internal tetramethylsilane (TMS) standard. In the ^{1}H-NMR spectra of $[(tmpa)Cu^{II}(ONNO)Cu^{II}(tmpa)][B(C_6F_5)_4]_2$, at different temperatures, the observed ligand peaks are broad and downfield-shifted to around 30, 24 and 10.5 ppm and move further downfield, with broadening as the temperature decreases exhibiting an apparent Curie behavior (in the temperature range 55 to –80 ºC). Based on comparison with values reported for mono-nuclear cupric

complexes of TMPA derivatives,[10] the relatively sharp resonance at 10.5 ppm (Figure S21) originates from the pyridyl 4-H of TMPA ligand, which is the furthest removed H-nucleus from the paramagnetic cupric center.

Upon cooling, this peak exhibits a marked downfield shift and splitting of the pyridyl 4-H resonances such that at –30 ºC, there is one sharp peak at 11.4 ppm, one broad peak at 10.0 ppm, with integration values matching a 2:1 ratio (Figure S21). We presume that the pyridyl 4-H peak splitting is due to an asymmetry imposed by the occurrence of a single stereo structure of the $[(tmpa)Cu^{II}(ONNO)Cu^{II}(tmpa)][B(C_6F_5)_4]_2$ at low temperature; probably very similar to what is found in crystal structure, where one pyridyl arm is furthest away from the paramagnetic cupric center experiencing the least interaction with unpaired spin density on the cupric center. Moreover, we suggest that two very broad peaks around 30 and 24 ppm originate from the pyridyl 3-H and 5-H atoms. This area may also include aminomethyl-CH_2-groups of TMPA, which further resolves into three broad components at the higher temperature (i.e. 55 ºC). The closest protons to the Cu center, the 6-pyridyl protons, were not detectable.

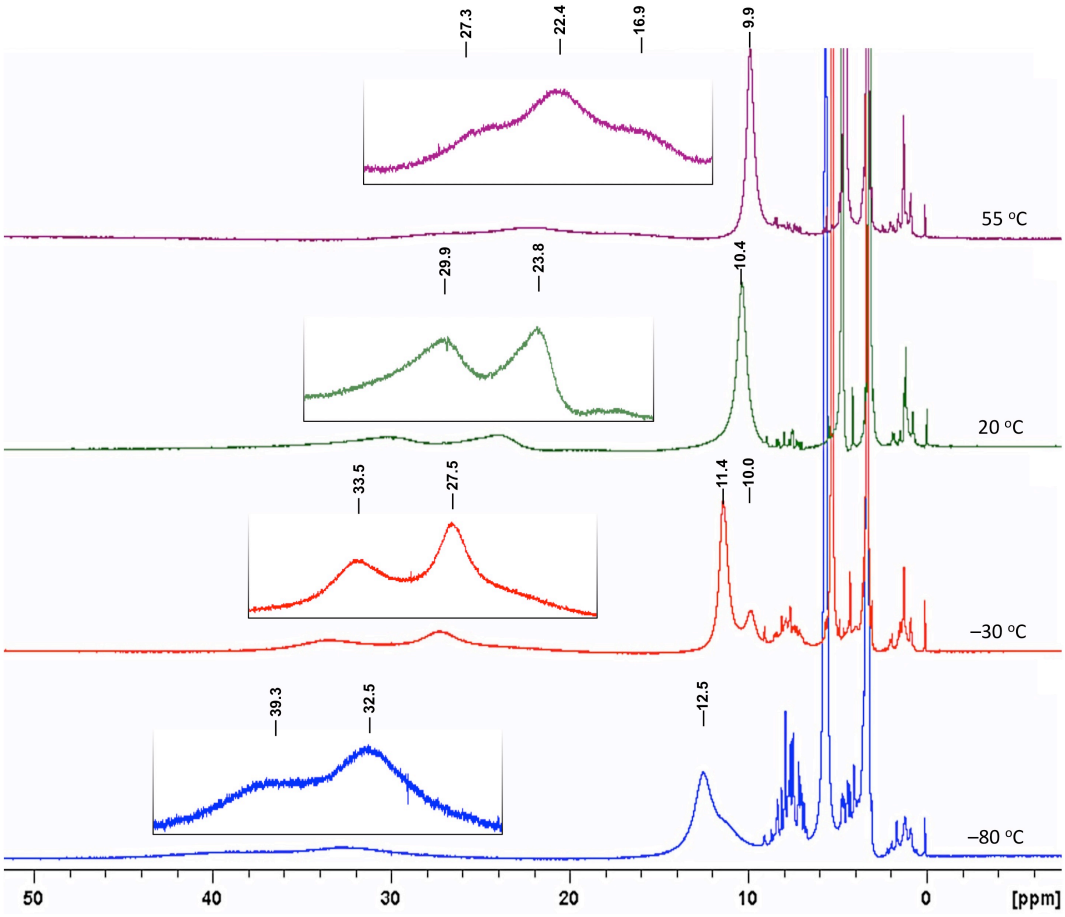

Figure 21. Variable temperature ^{1}H-NMR spectra of [(tmpa)Cu^{II}(ONNO)Cu^{II}(tmpa)]-[B(C$_6$F$_5$)$_4$]$_2$ in CD$_3$OD.

The ^{1}H-NMR samples of the ferric heme and heme/Cu hyponitrite intermediate were prepared at –100 ºC. The ferric heme sample was prepared in THF-*d*$_8$:CD$_3$OD (3:2). Samples of heme/Cu hyponitrite intermediate were generated by addition of excess (3 or 5 equiv) [(tmpa)Cu^{II}(ONNO)Cu^{II}(tmpa)][B(C$_6$F$_5$)$_4$]$_2$ in CD$_3$OD into solution of [(TMPP)Fe^{III}(THF)$_2$](SbF$_6$) in THF-*d*$_8$ via an air-tight syringe at –100 ºC. The broad pyrrole proton resonance of the starting ferric heme appears at 102 ppm (Figure 22). However, upon addition of excess [(tmpa)Cu^{II}(ONNO)Cu^{II}(tmpa)][B(C$_6$F$_5$)$_4$]$_2$, this

pyrrole peak moves further downfield relative to the axially symmetric ferric heme, δ = 133 ppm (Figure S22). This observation is consistant with coordination of cupric hyponitrite moiety to the ferric center which results in an increased total spin experienced by the pyrrolic protons. Note that after addition of only 3 eqiv of the dicopper-hyponitrite complex, some starting ferric heme complex still remains (Figure S22, middle, δ = 107 ppm) which disapears when more [(tmpa)Cu^{II}(ONNO)Cu^{II}(tmpa)][$B(C_6F_5)_4$]$_2$ is added. Thus, conversion of the high-spin Fe^{3+} heme to the heme-hyponitrite-Cu compex appears to be an equilibrium process, lying on the side of the starting heme.

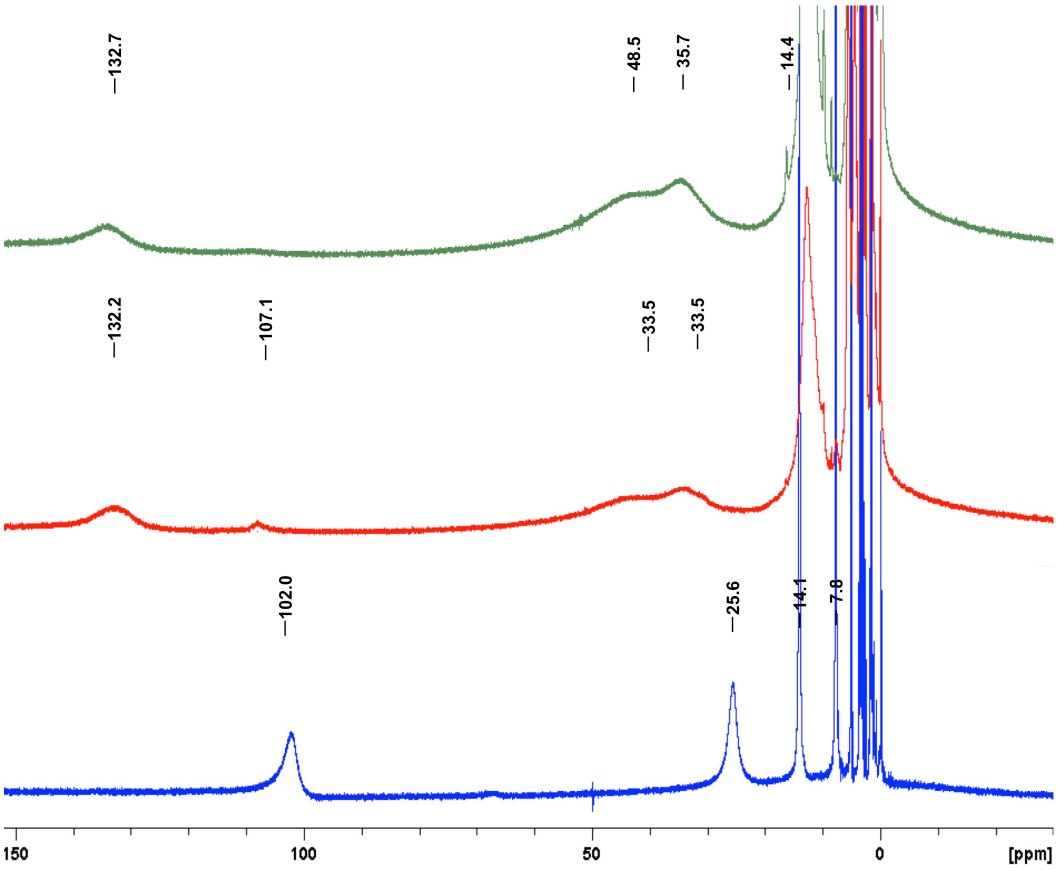

Figure S22. ^{1}H-NMR spectra recorded in THF-d_8:CD_3OD (3:2) at –100 °C. [(TMPP)Fe^{III}(THF)$_2$](SbF_6) (*bottom*) after addition of 3 equiv (*middle*) and 5 equiv (*top*) of [(tmpa)Cu^{II}(ONNO)Cu^{II}(tmpa)][$B(C_6F_5)_4$]$_2$.

5.6. Crystallographic Studies

Crystallization of [(tmpa)Cu^{II}(ONNO)Cu^{II}(tmpa)](ClO$_4$)$_2$: Percholorate cupric hyponitrite complex [(tmpa)Cu^{II}(ONNO)Cu^{II}(tmpa)](ClO$_4$)$_2$, was synthesized using a procedure similar to that used to prepare [(tmpa)Cu^{II}(ONNO)Cu^{II}(tmpa)][B(C$_6$F$_5$)$_4$] by reacting only half an equivalent of $Ag_2N_2O_2$ with a chloride precursor [(tmpa)Cu^{II}(Cl)](ClO$_4$)$_2$. Diffraction quality crystals of the complex were grown from saturated MeOH solution by cooling to –35 ^{o}C in 5 mm glass tubes in the glovebox after three weeks.

X-ray Structure Determinations: All reflection intensities were measured at 110(2) K using a SuperNova diffractometer (equipped with Atlas detector) with Cu *K*α radiation (λ = 1.54178 Å) under the program CrysAlisPro (Version 1.171.36.32 Agilent Technologies, 2013). The same program was used to refine the cell dimensions and for data reduction. The structure was solved with the program SHELXS-2013[11] and was refined on F^2 with SHELXL-2013.[11] Analytical numeric absorption correction based on a multifaceted crystal model was applied using CrysAlisPro. The temperature of the data collection was controlled using the system Cryojet (manufactured by Oxford Instruments). The H atoms were placed at calculated positions using the instructions AFIX 23 or AFIX 43 with isotropic displacement parameters having values 1.2 U_{eq} of the attached C atoms.

The asymmetric unit contains one ordered half of the Cu–O–N=N–O–Cu complex (as the complex is found at sites of inversion symmetry) and two disordered perchlorate counterions (one counterion is found at sites of threefold axial symmetry while the other counterion is found at no special position). Four free variables were used

to refine the occupancy factors of all components of the disordered counterions, and their values are 0.491(2), 0.204(2), 0.1651(19) and 0.1393(19). The SUMP instruction was used to constrain the sum of the four occupancy factors to be equal to 1 as the charge balance must be neutral. The crystal lattice also contains some small amount of lattice disordered solvent molecules (maybe methanol), whose contribution has been taken out in the final refinement (SQUEEZE details are provided in the CIF file, Spek, 2009). *Additional note*: prior to the final refinement, the occupancy factors for O1 and N5 were allowed to refine freely, and their refined values were 1.014(7) and 1.017(9), respectively. In the final refinement, those occupancy factors were set to 1.

Table S1. Experimental Details for $[(tmpa)Cu^{II}(ONNO)Cu^{II}(tmpa)](ClO_4)_2$.

	xs0629a
Crystal data	
Chemical formula	$C_{36}H_{36}Cu_2N_{10}O_2 \cdot 2(ClO_4)$
M_r	966.73
Crystal system, space group	Trigonal, *R*-3
Temperature (K)	110
a, *c* (Å)	24.2966 (2), 18.34987 (19)
V (Å^3)	9381.12 (18)
Z	9
Radiation type	Cu *K*α
μ (mm^{-1})	3.02
Crystal size (mm)	0.19 × 0.17 × 0.10
Data collection	
Diffractometer	SuperNova, Dual, Cu at zero, Atlas diffractometer
Absorption correction	Analytical *CrysAlis PRO*, Agilent Technologies, Version 1.171.36.32 (release 02-08-2013 CrysAlis171 .NET) (compiled Aug 2 2013,16:46:58) Analytical numeric absorption correction using a multifaceted crystal model based on expressions derived by R.C. Clark & J.S. Reid. (Clark, R. C. & Reid, J. S. (1995). Acta Cryst. A51, 887-897)
T_{min}, T_{max}	0.683, 0.808
No. of measured, independent and observed [$I > 2\sigma(I)$] reflections	36353, 4090, 3820
R_{int}	0.041
$(\sin\theta/\lambda)_{max}$ (Å^{-1})	0.616
Refinement	
$R[F^2 > 2\sigma(F^2)]$, $wR(F^2)$, *S*	0.038, 0.115, 1.04
No. of reflections	4090
No. of parameters	362
No. of restraints	441
H-atom treatment	H-atom parameters constrained
	$w = 1/[\sigma^2(F_o^2) + (0.075P)^2 + 19.8987P]$ where $P = (F_o^2 + 2F_c^2)/3$
$\Delta\rangle_{max}$, $\Delta\rangle_{min}$ (e Å^{-3})	0.68, -0.46

5.7. Analysis of Nitrous Oxide by Gas Chromatography

For all the measurements, grade 5.0 nitrogen was used as both the carrier (8 mL/min) and the make-up (22 mL/min) gas. The injector oven and the S4 detector oven were kept at 200 °C and 300 °C, respectively. All nitrous oxide (N_2O) analyses were performed with the column oven held constant at 150 °C. All gas injections were made using a 100 μL gastight syringe with a sample-lock. Samples were prepared in 6 mL Wheaton Clr headspace vials with volumes pre-measured for sample uniformity (actual vial volume ranges from 5.9–6.5 mL). Vials were charged with 3 mL of the reaction solutions in the glovebox, and sealed with rubber septa and 20 mm aluminum seals. For each sample, the headspace (60 μL) was sampled and injected using a gastight syringe with a sample lock and each injection was repeated 3 times. The amount of N_2O in the 60 μL sample was calculated based on a standard calibration curve which was established, and scaled to determine the amount of N_2O in the entire sample.

A first calibration curve was generated in the concentration range needed by injecting various volumes of 267.3 ppm N_2O balanced with nitrogen at 1 atm (purchased from Airgas). This was done using the ideal gas law, PV = nRT, and the N_2O partition coefficient in an organic solvent. The reported value for partition coefficient of N_2O gas in chloroform is 5.13 ($\log L^{chl} = 0.71$),[12] (Assumption: this partition coefficient value was used for calculation of the final amount N_2O for reactions in THF or MeTHF). Gas chromatography analysis of the headspace of the reaction of $[(TMPP)Fe^{III}(THF)_2](SbF_6)$ and $[(tmpa)Cu^{II}(ONNO)Cu^{II}(tmpa)][B(C_6F_5)_4]_2$ (in MeOH) in MeTHF after 1 h revealed that $N_2O_{(g)}$ formed in a yield of 73% using this set of standard calibration curves, the ideal gas law and the N_2O partition coefficient in chloroform.

Another calibration curve was prepared using hyponitrous acid ($H_2N_2O_2$). Standard solutions of hyponitrous acid were prepared in 3 mL THF or MeTHF (vide supra) in 6 mL Wheaton Clr headspace vials and then incubated long enough (overnight) to ensure complete decomposition and equilibration of N_2O into the headspace which were employed to generate a standard calibration curve in each solvent. The N_2O produced from the reaction of $[(TMPP)Fe^{III}(THF)_2](SbF_6)$ and $[(tmpa)Cu^{II}(ONNO)Cu^{II}(tmpa)][B(C_6F_5)_4]_2$, was obtained in a 88% yield, using this calibration curve.

Qualitative gas chromotography headspace analysis were also performed for $[(tmpa)Cu^{II}(ONNO)Cu^{II}(tmpa)][B(C_6F_5)_4]_2$ in THF, where it decomposes to a mixture of cuprous and cupric complexes. This hyponitrite was placed in a 6 mL Wheaton Clr headspace and sealed in the glovebox, followed by addition of 3 mL deoxygenated THF to dissolve the compound. GC analysis revealed initial release of $NO_{(g)}$ (broad leading edge, tR = 1.9 min) into the headspace after 1 h after dissolution and a very slow generation of N_2O (very sharp peak, tR = 6.8 min,) 3 h after dissolution in THF.

5.8. References for Supporting Information

(1) (a) Ford, P. C.; Lorkovic, I. M. *Chem. Rev.* **2002**, *102*, 993. (b) Wang, J.; Schopfer, M. P.; Sarjeant, A. A. N.; Karlin, K. D. *J. Am. Chem. Soc.* **2009**, *131*, 450. (c) Schopfer, M. P.; Mondal, B.; Lee, D.-H.; Sarjeant, A. A. N.; Karlin, K. D. *J. Am. Chem. Soc.* **2009**, *131*, 11304.

(2) Karlin, K. D.; Nanthakumar, A.; Fox, S.; Murthy, N. N.; Ravi, N.; Huynh, B. H.; Orosz, R. D.; Day, E. P. *J. Am. Chem. Soc.* **1994**, *116*, 4753.

(3) Helms, J. H.; Terhaar, L. W.; Hatfield, W. E.; Harris, D. L.; Jayaraj, K.; Toney, G. E.; Gold, A.; Mewborn, T. D.; Pemberton, J. R. *Inorg. Chem.* **1986**, *25*, 2334.

(4) Hematian, S.; Kenkel, I.; Shubina, T. E.; Dürr, M.; Liu, J. J.; Siegler, M. A.; Ivanovic-Burmazovic, I.; Karlin, K. D. *J. Am. Chem. Soc.* **2015**, *137*, 6602.

(5) Hematian, S.; Siegler, M. A.; Karlin, K. D. *J. Am. Chem. Soc.* **2012**, *134*, 18912.

(6) Eckenhoff, W. T.; Pintauer, T. *Inorg. Chem.* **2010**, *49*, 10617.

(7) Arulsamy, N.; Bohle, D. S.; Imonigie, J. A.; Sagan, E. S. *Inorg. Chem.* **1999**, *38*, 2716.

(8) (a) Ju, T. D.; Ghiladi, R. A.; Lee, D.-H.; van Strijdonck, G. P. F.; Woods, A. S.; Cotter, R. J.; Young, Jr., V. G.; Karlin, K. D. *Inorg. Chem.* **1999**, *38*, 2244. (b) Ghiladi, R. A.; Huang, H. W.; Moënne-Loccoz, P.; Stasser, J.; Blackburn, N. J.; Woods, A. S.; Cotter, R. J.; Incarvito, C. D.; Rheingold, A. L.; Karlin, K. D. *J. Biol. Inorg. Chem.* **2005**, *10*, 63.

(9) Xu, N.; Campbell, A. L. O.; Powell, D. R.; Khandogin, J.; Richter-Addo, G. B. *J. Am. Chem. Soc.* **2009**, *131*, 2460.

(10) Nanthakumar, A.; Fox, S.; Murthy, N. N.; Karlin, K. D. *J. Am. Chem. Soc.* **1997**, *119*, 3898.

(11) Sheldrick, G. M. *Acta Crystallogr. Sect. A* **2008**, *64*, 112.

(12) Abraham, M. H.; Platts, J. A.; Hersey, A.; Leo, A. J.; Taft, R. W. *J. Pharm. Sci.* **1999**, *88*, 670.

Vita

Shabnam Hematian, a native of Tehran, Iran, received her B.S. degree in chemistry from National University of Iran and M.S. degree in inorganic chemistry from Sharif University of Technology. In 2010, she joined the research group of professor Kenneth D. Karlin at the Johns Hopkins University to work on heme/Cu/nitrogen oxides chemistry. In 2013, she won a Deans Teaching Fellowship to teach an upper division undergraduate course entitled "Uses of Coordination Chemistry in Medicine". In 2014, Shabnam was awarded a *William Hooper Grafflin* Fellowship by Department of Chemistry in recognition of outstanding academic and research activities.

Starting in September 2015, Shabnam will join professor Jonas C. Peters' research group as a postdoctoral fellow at the California Institute of Technology. Her research interests include metal-mediated small molecule activation.